Author:
Guo, Chuntai

Title:
The electronic properties and structures of some quasi-ionic liquid semiconductors.

The Electronic Properties and Structures of Some Quasi-Ionic Liquid Semiconductors

By Chuntai Guo

Department of Physics, University of Bristol

February, 1995

The Electronic Properties and Structures of Some Quasi-Ionic Liquid Semiconductors

Chuntai Guo

Department of Physics, University of Bristol

February, 1995

A thesis submitted to the University of Bristol in accordance with the requirements for the degree of Doctor of Philosophy in the Faculty of Science.

Acknowledgement

I am particularly grateful to Dr. Adrian Barnes, my supervisor, for the excellent supervision he has provided during the term of my study.

I would like to thank Dr. Robert Mcgreevy for very helpful discussions about reverse Monte Carlo computer simulation.

I would also like to thank Professor Robert Evans for introducing me to the Liquids group, and to thank Professor John Enderby and Dr. George Neilson for their help and encouragement during my Ph. D. study. I am also very grateful to Mr. Stuart Ansell for frequent discussions about computing, and for a lot of help in my daily life.

I sincerely thank the British council and Chinese government for the award of a studentship which has allowed me to have this opportunity to study in the UK.

Finally, I would like to express my deepest thanks to my wife for her support and encouragement throughout the course of my Ph. D. study.

Abstract

The conductivity and thermopower of some liquid quasi-ionic semiconducting alloys and their mixtures with the molten salts have been measured as a function of composition and temperature using a four probe method. These systems were $Mg-Bi$, $(TlCl)_y-(Tl_2Te)_{1-y}$, $(TlCl)_y-(Tl_2Se)_{1-y}$, $(TlCl)_y-(Tl_xTe_{1-x})_{1-y}$, $(TlCl)_y-(Tl_xSe_{1-x})_{1-y}$, $(CuCl)_y-(Cu_2Se)_{1-y}$, $(CuCl)_y-(Cu_2S)_{1-y}$, $(CuCl)_y-(Cu_xSe_{1-x})_{1-y}$, $(CuCl)_y-(Cu_xS_{1-x})_{1-y}$. All the systems except for the mixtures with molten salts are characterised by a minimum conductivity and a p-n transition of the thermopower at the stoichiometric composition, but as the composition is moved away from stoichiometry, their electronic properties behave differently.

Theoretical calculations of the conductivity and thermopower of liquid $Mg-Bi$ and Thallium chalcogenides as a function of composition in the vicinity of stoichiometry were made using the Kubo-Greenwood equations with a rigid band model. The calculations show that the rigid band model is quite applicable to liquid Thallium chalcogenides, but it is completely inadequate to give a satisfactory explanation for liquid $Mg-Bi$.

Neutron diffraction experiments were made on three liquid $Mg-Bi$ alloys, three mixtures of Cu_2Se and $CuCl$ at the total structure factor level, and on three liquid Tl_2Se alloys at the partial structure factor level using isotopic substitution. Reverse Monte Carlo computer simulation (RMC) was successfully applied to the analysis of the diffraction data. It is concluded: (1). the β - Mg_3Bi_2 is a superionic conductor; (2). liquid Mg_3Bi_2, Tl_2Se and Cu_2Se are essentially ionic materials.

The results are discussed in relation to theoretical calculations using the Kubo-

Greenwood equations with a rigid band model. Four cases for the quasi-ionic semiconducting alloys in the vicinity of stoichiometry have been observed as:

1. the ideal case in which the Kubo-Greenwood equations with a rigid band model are applicable;

2. if the 'excess' electrons are in the state of metallic bonding, the Madelung potential will be largely reduced by the electronic screening effect. The conductivity increases dramatically as the band gap collapses, while thermopower is held down and appears to become more metal like;

3. if the 'excess' electrons enter as covalent bonds, the covalent bonding will maintain a low conductivity by keeping the Fermi energy pinned near the mid band gap, while the p-n transition of the thermopower still occurs;

4. if complex ions exist in the liquid (or polyanions), adding the cations will break the complex ions, leaving the electronic structure relatively unaffected.

Declaration

Unless stated otherwise, the work in this thesis is the result of my own research carried out at the University of Bristol and the Rutherford Appleton Laboratory under supervision of Dr. A. C. Barnes from October, 1991 to February, 1995. No part of it has been submitted elsewhere for a higher degree.

Chuntai Guo, February, 1995

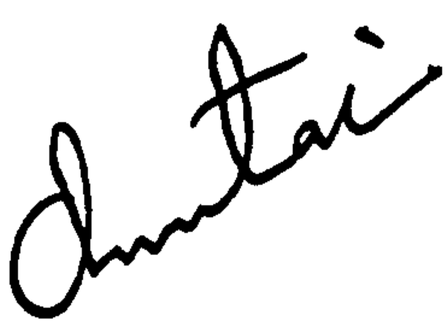

Dedicated to my wife

献给亲爱的妻子

and to the memory of my mother

并纪念敬爱的母亲

Contents

Chapter 1

Introduction

Early studies of liquid semiconductors were based mainly on observing what happens to the electrical behaviour when crystalline semiconductors are melted, but since the liquids can have wide ranges of stoichiometry, liquid semiconductors are better regarded as alloy systems in which the composition is a continuous variable. A broad definition of liquid semiconductors was first given by Ioffe and Regel (1960) and stated as : *liquid semiconductors are electronically conducting liquids with electrical conductivities less than the usual range for liquid metals.*

Enderby and Barnes (1990a) generalised the three regimes of the conductivity for liquid alloys. In the regime 1, a liquid alloy is a simple mixture of two single metals and has a typical conductivity of $\sigma > 5000\ \Omega^{-1}cm^{-1}$. Practically all liquid alloys of this type have a metallic temperature dependence, $d\sigma/dT$ is negative, and the electronic mean free path is $\geq 3\mathring{A}$. The conductivity (σ) and the thermopower (S) can be calculated using the *Ziman formula* which is based on a knowledge of the pseudopotential in momentum space $U(Q)$ and the structure factor $S(Q)$ for the liquid metal in question. The reduction of the conductivity of M due to the addition of A is entirely a diffraction effect and will become marked if the pseudopotential of A differs greatly from that of M. In this 'weak scattering regime' the conductivity is not sensitive to the detail of the density of states at the Fermi energy $N(E_F)$. In the regime 2, the conductivity of liquid alloys is less than $5000\ \Omega^{-1}cm^{-1}$ but greater

than, for example, 500 $\Omega^{-1}cm^{-1}$, the majority of these liquids are characterised by a minimum conductivity at stoichiometry, and have a positive $d\sigma/dT$ in the vicinity of stoichiometry. Liquids in this region are commonly known as liquid semiconductors even though they are statistically degenerate and obey Fermi-Dirac statistics as liquid metals. The observed electrical properties are believed to reflect the electronic density of states directly through the energy dependent conductivity σ(E). Thus, Mott (1969) and others have argued that in the so-called Ioffe-Regel regime in which the electronic mean free path, l, is comparable with the interatomic spacing,

$$\sigma(E) = A[N(E)]^2 \tag{1.1}$$

where A is a constant which is weakly dependent on the specific nature of the liquid alloy. A knowledge of $\sigma(E)$ allows the conductivity (σ) and thermopower (S) to be determined through the Kubo-Greenwood equations based on the kinetic transport coefficients. This regime is of particular interest in liquid semiconductor physics because many alloy systems are characterised by conductivity values in the range of 500-5000 $\Omega^{-1}cm^{-1}$. In regime 3, a gap or very deep minimum in N(E) occurs so that $\sigma(E)$ is zero or very small over a range ΔE which was called the conductivity gap by Enderby and Barnes (1990a). In this regime, the predominant conduction process is the activation of electrons or holes from the valence and conduction band edges.

Enderby (1970), Roth (1975) and Cutler (1977) have progressively developed the *pseudogap model* for explaining the minimum conductivity (σ_0) which usually occurs at a chemical stoichiometric composition M_aA_m. They have all argued that, as the composition of the alloy varies from $M_aA_m + \delta$A to $M_aA_m - \delta$A, where δA is excess of element A, μ (the chemical potential) will move from left to right, and will pass through the deep minimum in the density of states curve. This explains the minimum (σ_0) and the sign change in the thermopower (S) from positive for excess of electronegative element to negative for a deficit through the Kubo-Greenwood equations.

Barnes and Enderby (Barnes, 1993) have generalised the pseudogap model in

quantitative manner using the Kubo-Greenwood equations with a generic model of the energy dependent conductivity σ(E), which is called BE theory in this thesis. The electronic properties of many liquid semiconducting compounds in the vicinity of stoichiometry can satisfactorily be predicted . According to BE theory a narrower definition of a true liquid semconductor is an alloy/compounds in which μ is located within a conductivity gap ΔE defined as $E_C - E_V$ where E_C and E_V are refered to as mobility edges. This group of compounds are refered to as quasi-ionic semiconducting compounds in this thesis because the conductivity gap of those compounds is small ($\Delta E \leq 2kT$) compared with molten salts. The significance of the BE theory is that it can be used as a starting point to explore more physics of liquid semiconductors because it directly involves the electronic density of states, the band gap, the position of the Fermi energy and the temperature.

The origin of the pseudogap of N(E) in these alloys is almost certainly chemical, which reflects a tendency of M to be coordinated to A and vice versa. The nature of the chemical short range order in liquid alloys is best clarified through structural studies at the partial structure factor $S_{\alpha\beta}(Q)$ level or at the partial radial distribution function $g_{\alpha\beta}(r)$ level. The technique of neutron diffraction with isotopic substitution developed by Enderby *et al* (1967) has been successfully applied to many systems to obtain the partial structure factors and partial distribution functions. Conventional analysis of diffraction measurements by direct Fourier transform can not give us three dimensional information of the structure. This limitation has been recently addressed by the reverse Monte Carlo computer simulation (RMC) (McGreevy and Pusztai, 1988) which can produce three dimensional structural models in real space based on the experimental data, instead of an interatomic potential as in the normal Monte Carlo and Molecular Dynamics simulation. Neutron diffraction, combined with the reverse Monte Carlo computer simulation offers us an powerful tool to study the chemical short range order in the liquid.

The pseudogap model and BE theory, however, meet difficulties in explaining the electronic properties of liquid Mg-Bi alloy in the vicinity of the stoichiometric com-

position Mg_3Bi_2. Barnes (1993) pointed out it has a strange anomaly and the rigid band model in this case is totally inadequate. In this case, the transition from liquid semiconductor towards liquid metal must be accompanied by very subtle changes in the mechanism of the electron transport. The electronic conduction processes as the composition crosses stoichiometry, especially in the composition range very near the stoichiometry is still very poorly understood although some models are successful in some situations. Therefore, careful observations of the electronic properties at compositions in the vicinity of stoichiometry are important in producing a better knowledge of the conduction mechanisms in liquid semiconductors.

This research work has focused on the electronic properties of some liquid quasi-ionic semiconducting compounds in the vicinity of the stoichiometric composition. The aims of this research are: (1) to make careful measurements of the conductivity and thermopower, and theoretically calculating the electronic properties using the BE theory; (2) making a comparison between the experiments and the calculations to find out the deviation from the ideal case; (3) conduct the corresponding structural studies at the partial structure factor level to try to give an explanation of any deviation in conjunction with the existing thermodynamic and electronic structure data. Liquid magnesium-bismuth alloys, thallium chalcogenides and copper chalcogenides which are typical liquid semiconductors were chosen for this study. Although they have been the subject of the study of liquid semiconductors for many years, the electronic and structural information in the vicinity of the stoichiometric composition is still far from detailed because of the difficulties in making the measurements.

This thesis can be divided into three parts: (1). chapter 2 and chapter 3 are basic theory of liquid semiconductors and thermal neutron diffraction; (2). chapter 4 and chapter 5 are experimental methods for measuring electronic properties and neutron diffraction; (3). chapter 6, 7, and 8 are the experimental results and discussions of the electronic and structural properties of magnesium-bismuth, thallium chalcogenides, copper chalcogenides, respectively. Chapter 9 gives the main conclusions of this thesis.

Chapter 2

Basic theory of Liquid Semiconductors

2.1 Basic concepts in disordered systems

2.1.1 Electronic density of states

In crystalline materials the wavefunction of the electron can be described in the Bloch form

$$\psi = u(x, y, z)\, exp(i\mathbf{k}.\mathbf{r}) \tag{2.1}$$

where $u(x, y, z)$ has the periodicity of the lattice. The wavevector **k** is a good quantum number for the electron. In disordered materials, especially for liquid semiconductors with strong electronic scattering, **k** is not a good quantum number, and the wavefunctions $\psi(x, y, z)$ no longer has the Bloch form. Nevertheless, solutions of the Schrodinger equation must exist, and therefore the concept of the density of electron states N(E) can be carried over from the theory of crystals to the theory of disordered materials. It is defined so that $N(E)$ dE is the number of eigenstates in unit volume for an electron in the system with given spin direction and with energies between E and E + dE. At a temperature T the number of electrons in the energy

range dE is, for each spin direction, $N(E)f(E)$dE, where $f(E)$ is the Fermi-Dirac distribution function, defined as :

$$f(E) = \frac{1}{exp[(E-\mu)/kT]+1} \tag{2.2}$$

The chemical potential (μ) which is often referred to as the Fermi energy (E_F) is a function of temperature T and tends to a limiting value E_F as T $\rightarrow$ 0, then separating occupied from non-occupied states.

2.1.2 Localised states of electrons

If a system shows sufficient disorder it was shown (Anderson, 1958) that the solution of the Schrodinger equation

$$\nabla^2\psi + \frac{2m}{\hbar^2}(E-V)\psi = 0 \tag{2.3}$$

using the tight binding approximation for a strongly disordered potential leads to electronic states that are strongly localised in real space.

Consider an idealised potential, as shown in Fig.2.1 (a), it is supposed that the potential wells are so far apart that the overlap between the atomic wavefunction $\psi(\mathbf{r})$ (to be taken as a symmetrical function) on adjacent wells is small. The solution of the Schrodinger equation (2.3) for the valence electron in the case (a) on crystalline lattice is described by the normal Bloch wavefunction,

$$\psi_k(x,y,z) = \sum_n exp(i\mathbf{k}.\mathbf{R}_n)\phi(\mathbf{r}-\mathbf{R}_n) \tag{2.4}$$

the suffix n describes the nth well and $\mathbf{R}_n$ its lattice site. The width of the tight binding band is (Mott and Davis, 1971)

$$B = 2zI \tag{2.5}$$

where I is the transfer integral, for a simple cubic lattice with lattice constant a it is given by

$$I = \int \phi^*(r-a_n)H\phi(r-a_{n+1})d^3x \tag{2.6}$$

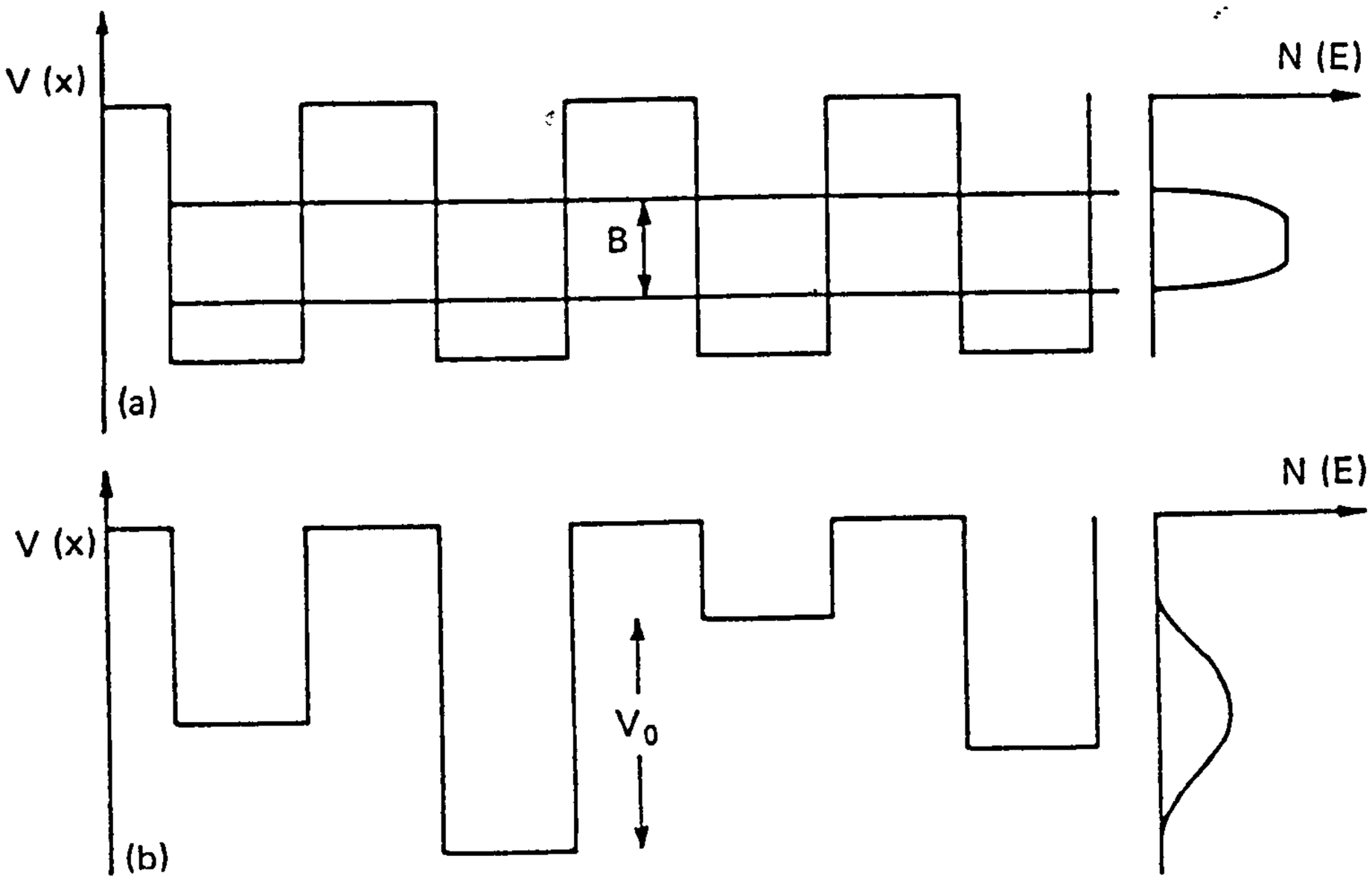

Figure 2.1: Potential energy used by Anderson (1958): (a) without a random potential and (b) with such a potential. The density of states is also shown.

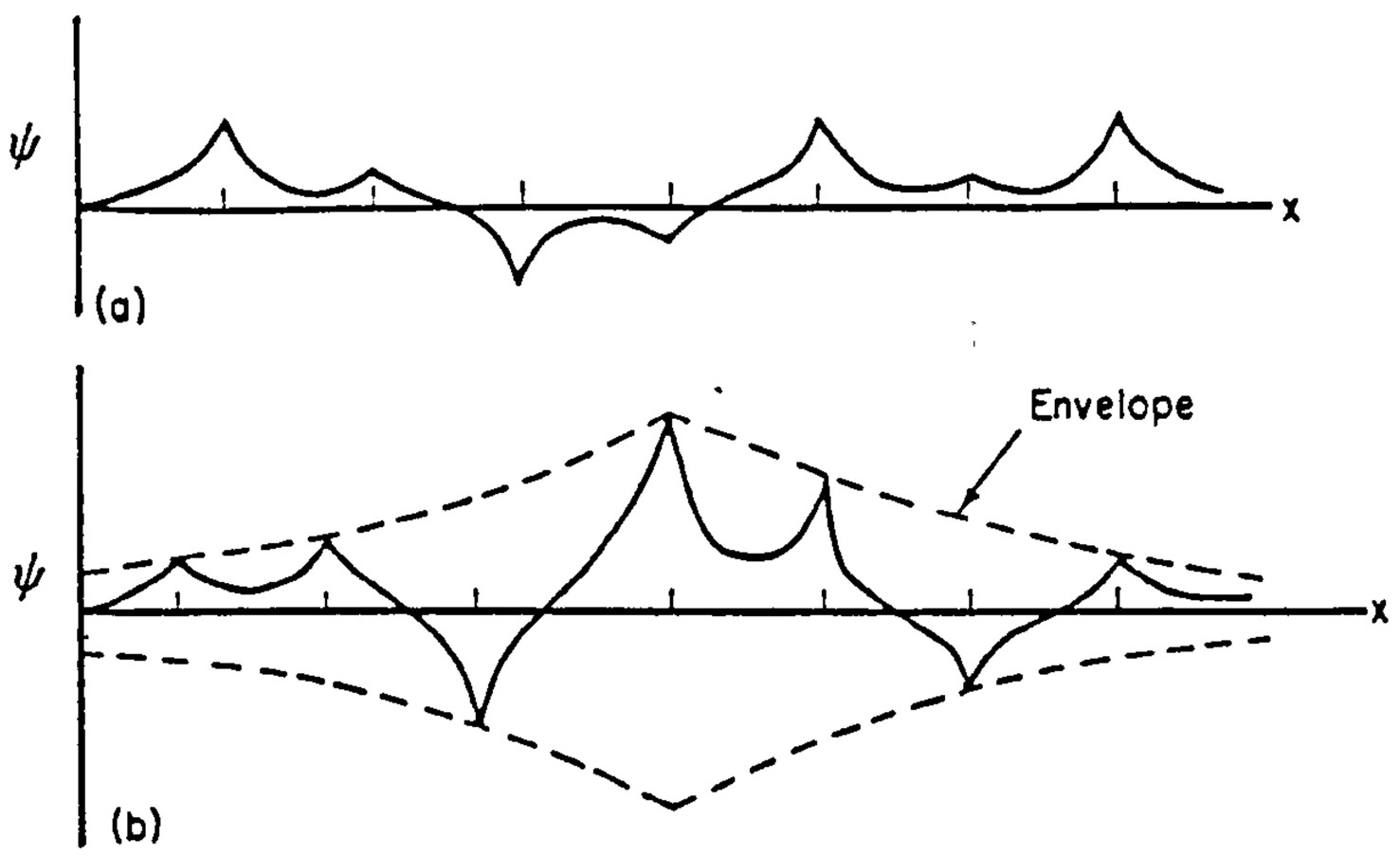

Figure 2.2: Wave function ψ of an electron when $l \sim a$: (a) extended states; (b) weakly localised states.

and z is the coordination number. For the case (b) in Fig.2.1, the wavefunction loses phase memory in going from atom to atom and the fluctuations both in phase and in amplitude become larger as V_0/B, which is called the Anderson criterion, increases. The wavefunction, instead of equation (2.4), has the form

$$\sum_n A_n \phi(\mathbf{r} - \mathbf{R}_n) \tag{2.7}$$

where the A_n have random phases and amplitudes, as shown in Fig.2.2 (a). If V_0/B is very large, the wavefunction for each isolated well would be little perturbed by all the other wells, and so would fall off exponentially with distance, as shown in Fig.2.2 (b). Anderson indicated that at some critical value (V_0/B) the electronic states become localised. The wavefunctions of the localised states can be described as

$$\sum_n A_n \phi(\mathbf{r} - \mathbf{R}_n) exp(-\alpha \mathbf{r}) \tag{2.8}$$

where $exp(-\alpha \mathbf{r})$ is a decay factor, $1/\alpha$ corresponds to the localisation length in the material. When the electronic states are localised at zero temperature the electrons can not diffuse away from their respective lattice sites, so that the conductivity tends to zero.

2.2 Kubo-Greenwood formulation

However complicated the atomic and electronic structures of a metal are, there must be a conduction process which occurs at a corresponding state of energy. It is called the energy-dependent conductivity $\sigma(E)$. An observed conductivity σ can be expressed as the sum of energy-dependent conductivities $\sigma(E)$ for each energy state. Kubo (1956) and Greenwood (1958) deduced an expression for $\sigma(E)$.

Consider a degenerate electron gas at zero temperature, in which the electron states are occupied up to an energy E_F. The eigenfunctions for electrons with energy E in the non-periodic field, with appropriate boundary conditions, are $\psi_E(x, y, z)$,

and are normalised to give one electron in a volume V. An alternating field, $Fcos\omega t$, acts on an electron so that an electron makes a transition from a state with energy E to state with energy $E' = E + \hbar\omega$. The probability of this transition is given by *Fermi*'s golden rule

$$T = \frac{1}{4}e^2F^2\frac{2\pi}{\hbar} \mid X_{E',E} \mid^2_{av} VN\left(E'\right) \tag{2.9}$$

$$X_{E',E} = \frac{\hbar}{m\omega}D_{E',E} \tag{2.10}$$

$$D_{E',E} = \int \psi^*_{E'}\frac{\partial}{\partial x}\left(\psi_E\right)d^3x \tag{2.11}$$

Thus (2.9) becomes

$$T = \frac{\pi e^2\hbar V}{2m^2\omega^2}F^2 \mid D \mid^2_{av} N(E') \tag{2.12}$$

where $N\left(E'\right)$ is the density of states at energy $E' = E + \hbar\omega$. We wish to obtain a conductivity for frequency ω, written $\sigma_E(\omega)$ so that $\sigma_E(\omega)F^2/2$ is the mean rate of energy loss per unit volume. To obtain this, equation (2.12) must be multiplied by $N(E)f(E)dE$, the number of occupied states per unit volume in the energy range dE; by $(1-f(E'))$, the chance that a state with energy E' is unoccupied; by $\hbar\omega$, the energy absorbed in each quantum jump; and by 2 for the two spin directions. $\sigma_E(\omega)$ can be written as

$$\begin{aligned}\sigma_E(\omega) &= \frac{2\pi e^2\hbar^2V}{m^2\omega}\int\{f(E)[1-f(E')]-f(E')[1-f(E)]\} \\ &\quad |D|^2_{av}N(E)N(E')dE\end{aligned} \tag{2.13}$$

The second term in the curly brackets gives the energy emitted in downward jumps. $|D|^2$ is now averaged over all initial and final states. By letting $\omega \to 0$ (that is the d.c. limit) and at T=0 ($E = E_F$) this gives a value for the conductivity of

$$\sigma_E(0) = \frac{2\pi e^2\hbar^3V}{m^2} \mid D_E \mid^2_{av} [N(E)]^2 \tag{2.14}$$

$$D_E = \int \psi^*_{E'} \frac{\partial}{\partial x} \psi_E \, d^3x \tag{2.15}$$

The av represents an average over all states E and all states E' such that $E = E'$, so that at T=0 the conductivity $\sigma_{T=0}(0)$ is given by

$$\sigma_{T=0}(0) = [\sigma_E(0)]_{E=E_f} \tag{2.16}$$

We can write any energy dependent conductivity $\sigma(E)$ as

$$\sigma(E) = \sigma_E(0) = \lim_{\omega \to 0} \sigma_E(\omega) \tag{2.17}$$

At a finite temperature, conductivity σ can be then expressed as

$$\sigma = -\int \sigma(E) \frac{df}{dE} dE \tag{2.18}$$

where f is the Fermi-Dirac distribution function. The equation (2.18) is called the Kubo-Greenwood formula which has universal validity, in the absence of interactions.

2.3 Thermopower

If the electrical conductivity σ is the sum of contribution at different energies $\sigma(E)$ according to the equation (2.18) and if the heat of transport of a charge at energy E is $E - E_F$, then the thermopower S can be expressed in terms of moments of $(E - E_F)/kT$ defined by

$$< (\frac{E - E_F}{kT})^n >= -\int_0^\infty \frac{\sigma(E)}{\sigma} (\frac{E - E_F}{kT})^n \frac{\partial f}{\partial E} dE \tag{2.19}$$

This conclusion can be obtained by using the Kelvin equation $\Pi = ST$, where Π is the Peltier coefficient (Culter, 1972; Fritzsche, 1971; Mott and Davis, 1971).

Since the isothermal current density $J = \sigma F$, where F is the electric field, the differential current density at energy E is

$$dJ = -F\sigma(E)(\frac{\partial f}{\partial E})dE \tag{2.20}$$

The differential heat flux is then

$$dQ = -(1/e)(E - E_f)dJ = (F/e)(E - E_F)\sigma(E)(\frac{\partial f}{\partial E})dE \tag{2.21}$$

Since $Q = \Pi J$ at constant temperature T, integration of (2.21) together with the Kelvin relation for Π gives

$$S = -(k/e) < (\frac{E - E_F}{kT}) > \tag{2.22}$$

So that thermoelectric power S can be written as

$$S = k/e \int \frac{\sigma(E)}{\sigma} \left(\frac{E - E_F}{kT}\right) \frac{\partial f}{\partial E} dE \tag{2.23}$$

Equation (2.23) is expected to be valid in most situations encountered in liquid semiconductors. It is related to equation (2.18) through $\sigma(E)$. These two equations are referred to as the Kubo-Greenwood equations in this thesis.

2.4 Mobility edges and conductivity gap

If the V_0/B, Anderson criterion, is not sufficiently large, it is possible that the electronic states are delocalised at the centre of the band, and localised towards the edges of the band, as shown in Fig. 2.3. The energy dependent conductivity $\sigma(E)$ would then be finite in the middle of the band, but zero at the edge at T=0 ^oC.

In some amorphous and liquid materials, the tails of the conduction and valence band may overlap, such as CFO model (Cohen, Fritzsche and Ovshinsky, 1969) shown in Fig. 2.4. The degree of overlap and the Fermi energy E_F can be varied by changing the composition or temperature. The density of states shows a minimum which is usually called a pseudogap. It is a natural extension of the idea of localised states in band tails to introduce localised states in the pseudogap. E_V and E_C separate the localised states from delocalised states and they are referred to as *mobility edges* in the valence and conduction band respectively. When the energy is below E_C, $\sigma(E)$ will vanish for electrons although $N(E)$ remains finite, and for the case of a hole E_V is the energy above which $\sigma(E)$ vanishes at T = 0 K.

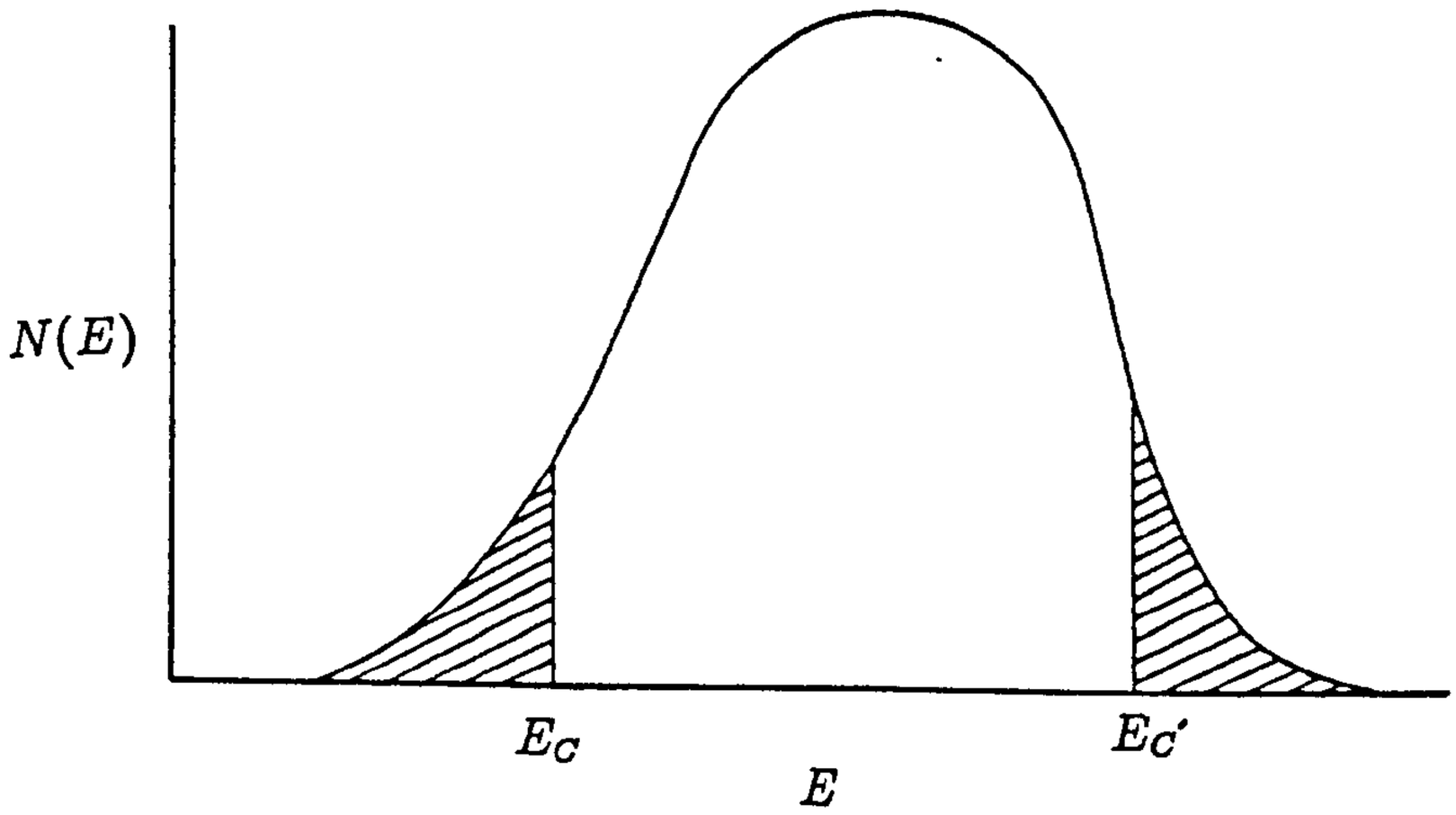

Figure 2.3: Density of states in an Anderson band, with the two mobility edges E_C and $E_{C'}$

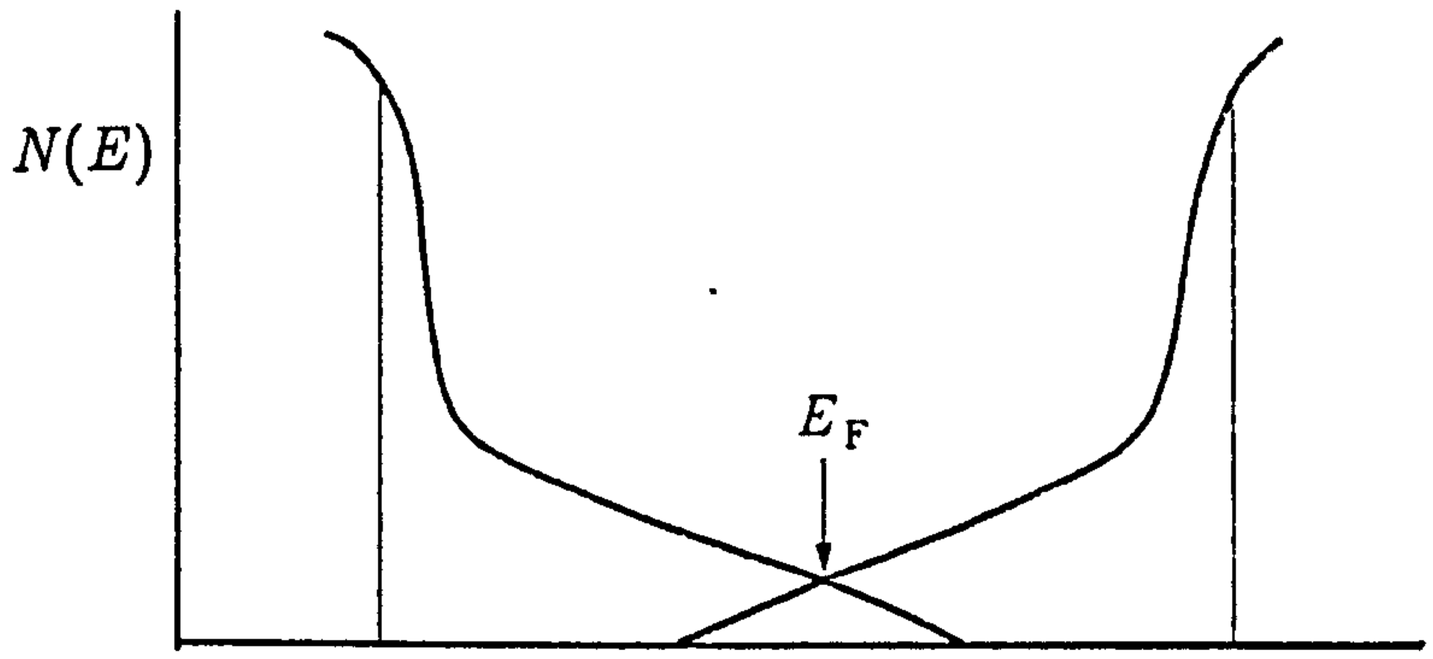

Figure 2.4: Density of states in valence and conduction bands of an amorphous non-metal, with overlapping tails.

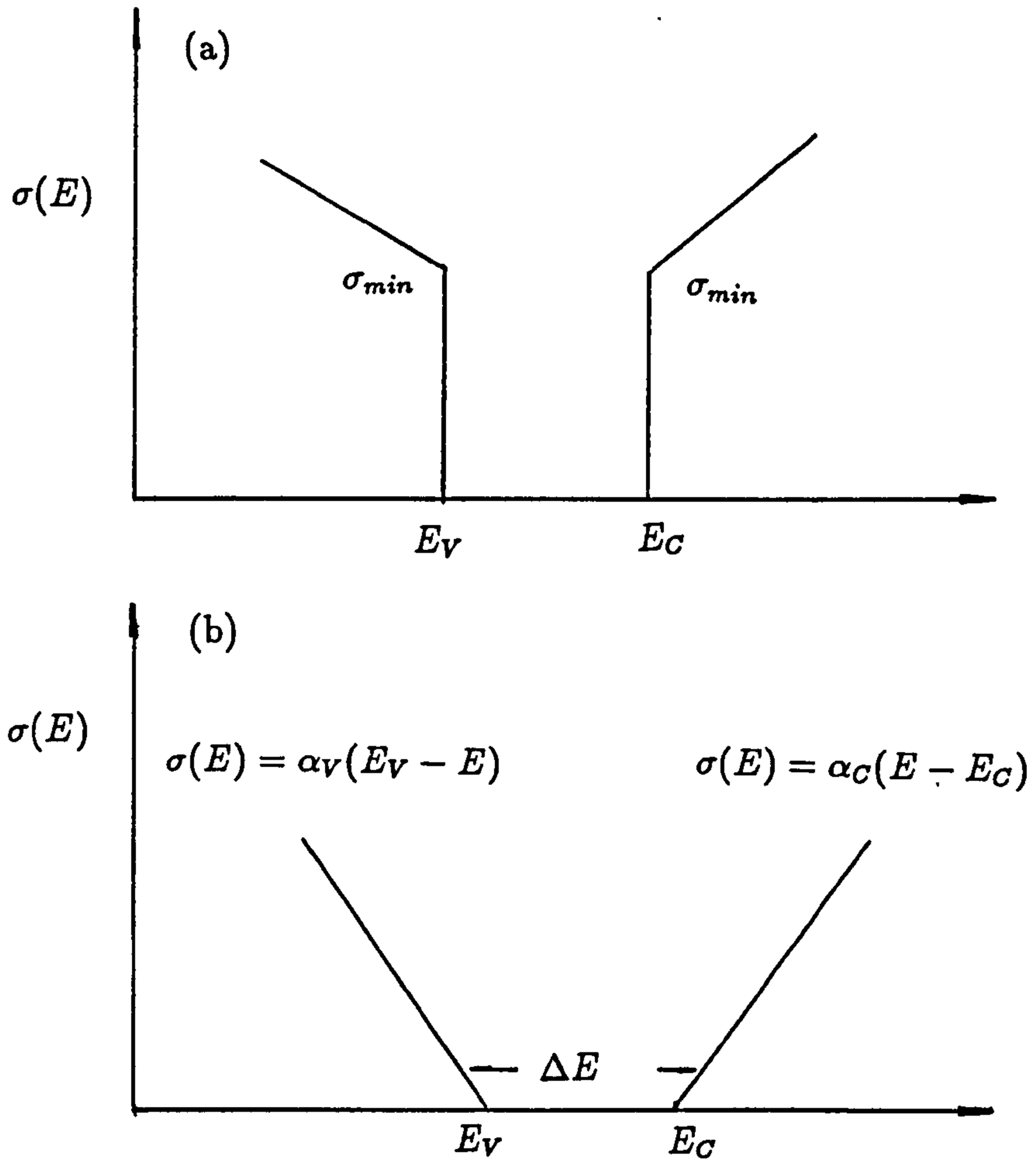

Figure 2.5: Mobility and conductivity close to a substantial in $N(E)$. (a) The original sharp edge model proposed by Mott. σ_{min} was regarded as essentially universal of order 350 $\Omega^{-1}cm^{-1}$. (b) The 'generic' form of $\sigma(E)$ used in this thesis. E_V and E_C are referred to as conductivity edge.

Originally, Mott and Davis (1971) proposed that $\sigma(E)$ was characterised by a minimum value σ_{min} at $E = E_C$ and $E = E_V$. Thus the mobility edges in the bands were, in this picture, very sharp, and then $\sigma(E)$ falls off abruptly from σ_{min} to zero, as illustrated in fig.2.5 (a). However, most workers have abandoned this concept of 'minimum metallic conductivity'. A second model (Enderby and Barnes, 1990a) (fig.2.5 (b)) concludes that for electrons

$$\begin{aligned} \sigma(E) &= \alpha_c(E - E_C)^\nu && E > E_C \\ &= 0 && E < E_C \end{aligned} \tag{2.24}$$

and for holes

$$\begin{aligned} \sigma(E) &= \alpha_v(E_V - E)^\nu && E < E_V \\ &= 0 && E > E_V \end{aligned} \tag{2.25}$$

Cohen *et al* (1985) have argued that in the absence of interactions, ν=1 and α is constant determined by the band width, the interatomic spacing and disorder parameter V_0.

Although the mobility edge picture has been widely used in discussing liquid semiconductors (Cutler, 1977), it is nowadays generally accepted that the effect of finite electron-phonon interactions is to delocalise electrons below E_C and that, at sufficiently high temperature, $\sigma(E)$ is finite unless $N(E)$ is zero (Thomas, 1975). Nevertheless, for liquid semiconductors like $MgTe$ whose total conductivity (ionic and electronic) is only $\sim 9\Omega^{-1}cm^{-1}$ at temperatures in excess of 1400 K, the Kubo-Greenwood equations imply that $\sigma(E)$ must essentially vanish at energies close to E_F in the middle of the band gap. This makes the concept of the mobility edge more obscure. Enderby and Barnes (1990a) proposed a concept of conductivity edge at which σ(E) is zero. They still use E_V and E_C to label the cut off energies at which conductivity, instead of mobility, is zero. Similarly, $\Delta E = E_C - E_V$ is referred to as the 'conductivity gap'.

2.5 Chemical bonding and band structure in alloys

Ionic bonding

Fig. 2.6(a) (Sutton A P, 1993) shows a schematic density of states plot for making an MA ionic compound.There is a finite electronegtive difference between element M and A, M is more electropositive. So element M has a higher on-site energy, E_M^0, than that of element A, E_A^0. The pure A and pure M bands do not overlap. When A and M are mixed in a binary alloy, charge flows from the higher energy states associated with atom M to the lower energy states on atom A. The result is that the lower band is filled and the upper band is emptied. Elements M and A are ionised into cations and anions, respectively. There is a gap between the cation and anion states which is directly related to the Madelung potential. Thus the lower band is associated with the anion sites and the upper band with the cation sites. When the alloy is melted, the fluctuation of the Madelung potential caused by disordering produces the band tails and consequently the upper conduction band can overlap, to some extent, with the lower valence band, forming a 'pseudogap'.

Metallic bonding

If the energy band of the A and M are too close in energy for the above model to apply and a new common band is formed, as shown in Fig. 2.6(b). New common states are formed in the alloy from bonding and antibonding combinations of states on the A and M atoms. The local density of states on the A and M atoms in the alloy thus have a common width, W_{MA}. The centre of gravity, E_{MA}^0, of the common density of states is the average of the centres of gravity of the A and M local densities of states, which remain E_A^0 and E_M^0.

(a)

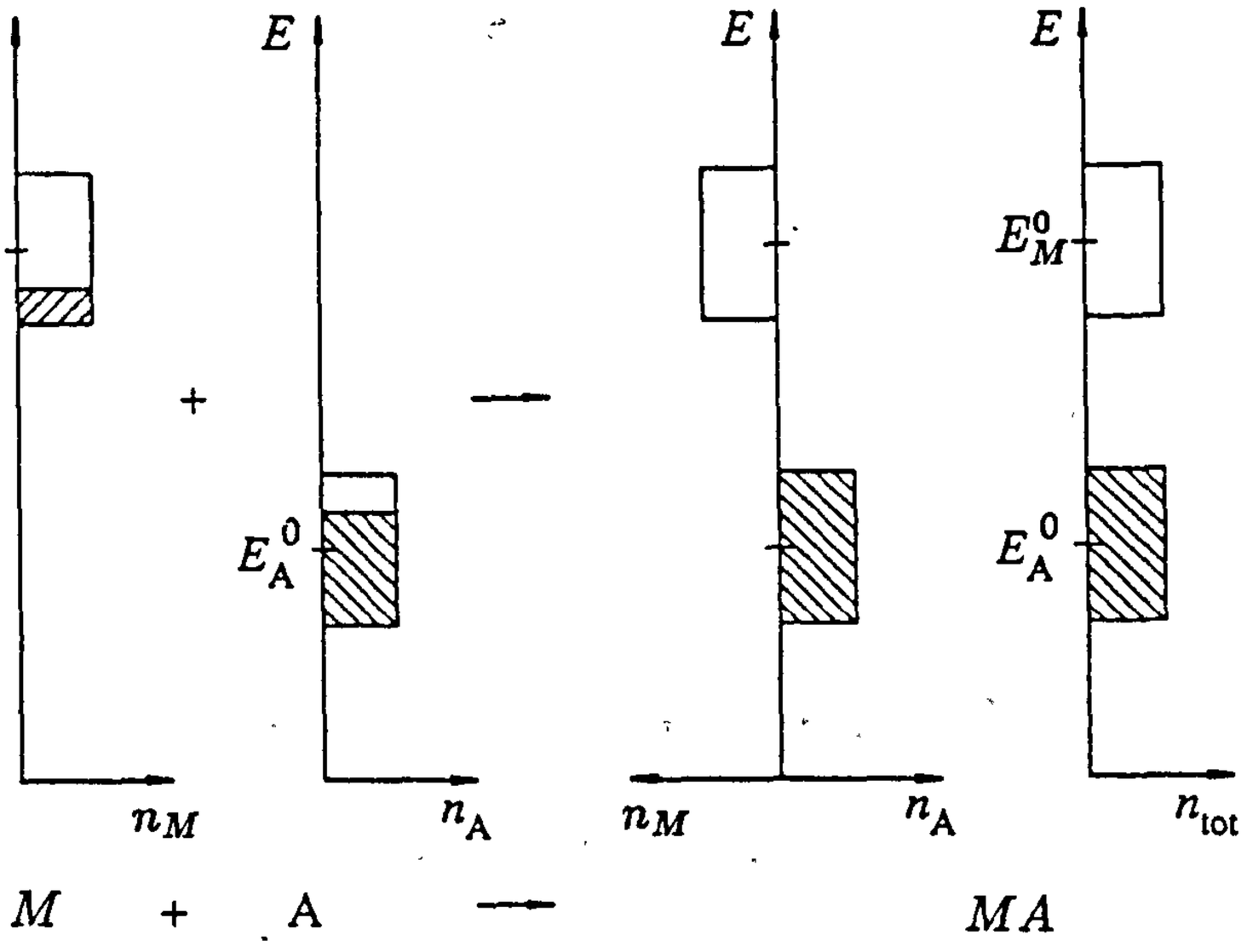

Metallic bond

(b)

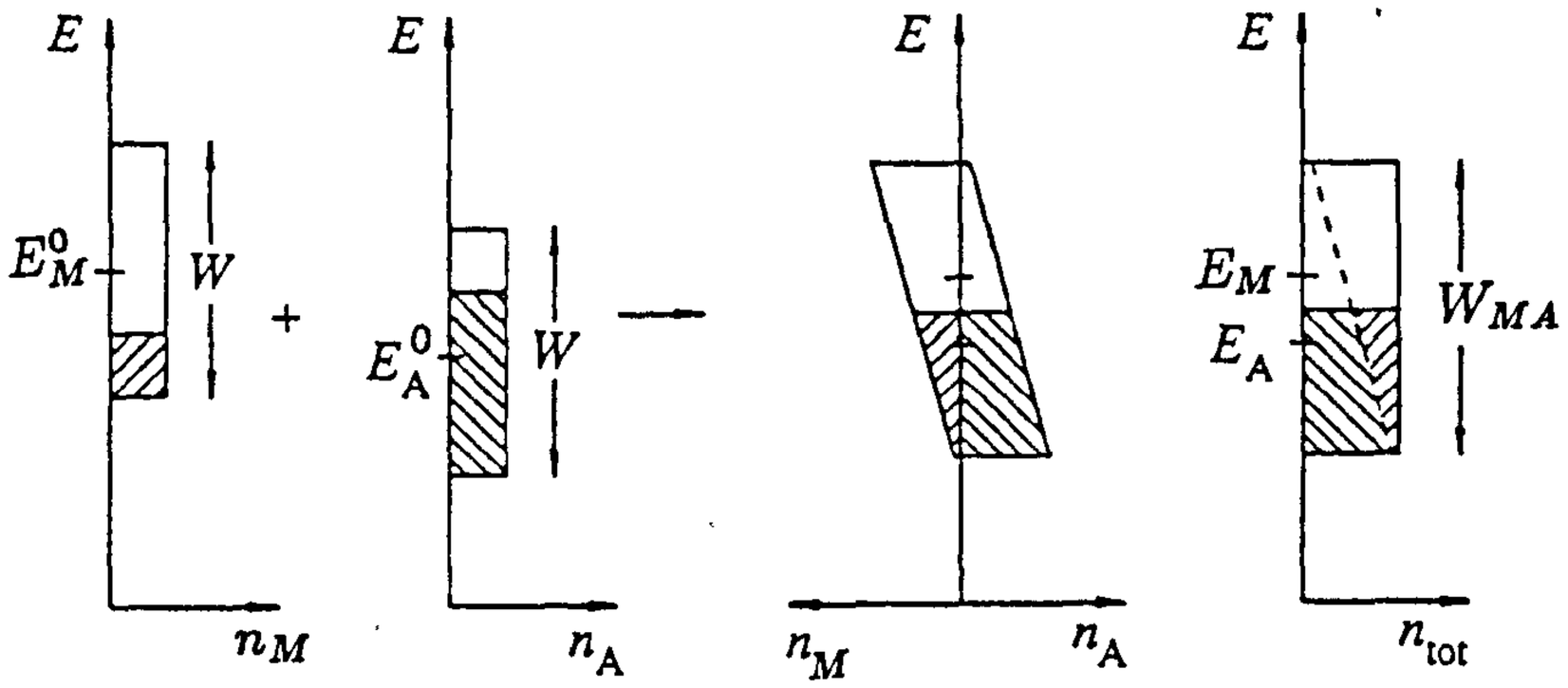

Figure 2.6: Schematic illustrations of the local and total densities of states during the formation of (a) an ionic MA compound and (b) a metallic MA alloy

Covalent bonding

In the case of covalent bonding, the bonding states and antibonding states could not be combined into a common band as in the metallic case, but give two bands separated in energy. The valence electrons go into the bonding states and the anti-bonding states are empty. This can lead to a pseudogap in the same way as that for the ionic case.

2.6 The electronic structure of liquid semiconductors near stoichiometry

2.6.1 Enderby and Collings model

The p-n transition of thermopower and the minimum conductivity at stoichiometry have been observed in many liquid semiconductors of the ionic type M_aA_m. In order to explain this phenomenon a pseudogap model has been developed. This was first suggested by Enderby and Collings (1970). The excess of either M or A over the stoichiometric composition causes the valence electrons of the excess atoms to go into a rigid conduction band, as illustrated in Fig.2.7. On changing composition from excess M to excess A, N(E) decreases to a minimum and then increases. In order to explain the positive thermopower which is frequently found with excess A, they postulated a relatively narrow resonant scattering impurity state in the band just below E_F. Enderby and Barnes (1990a) have modified this model and given a better explanation to the p-n transition of thermopower and the minimum conductivity at the stoichiometry by using Kubo-Greenwood equations The minimum conductivity σ_0 at the chemical stoichiometric composition M_aA_m arises in this model from a deep minimum in the density of state curve. The effect of an increase in temperature is twofold: First, it broadens the Fermi function so that the observed conductivity will, through equation (2.18), show a positive coefficient.

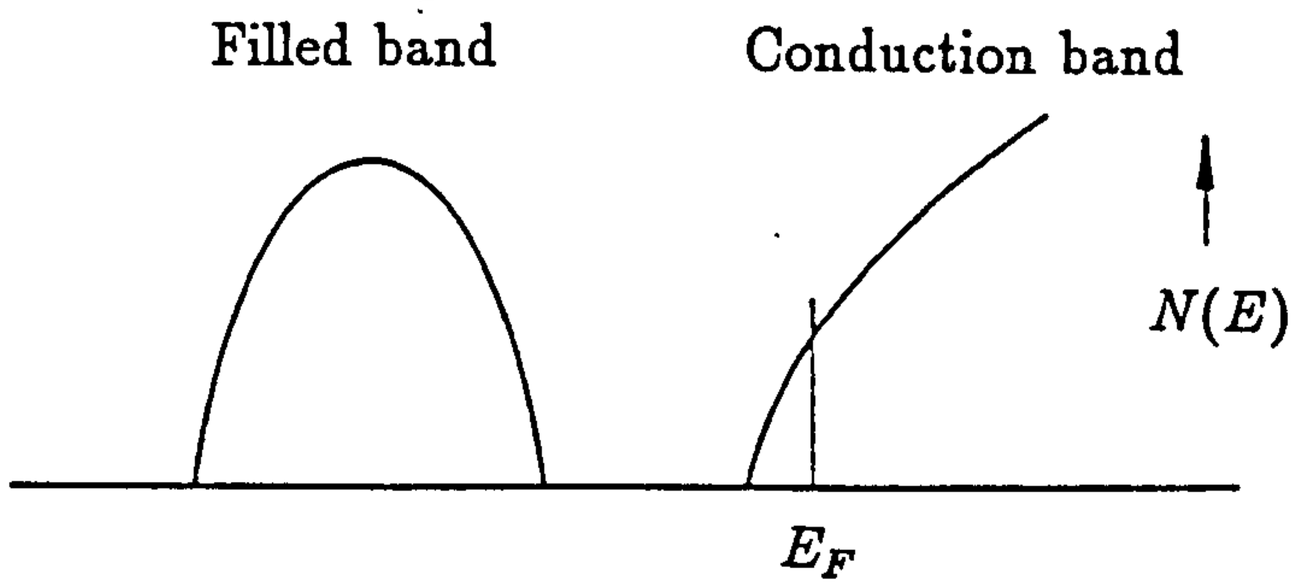

Figure 2.7: Enderby's model for the electronic structure of an MA alloy. E_F always remains in the conduction band and bonding electrons go into the filled band

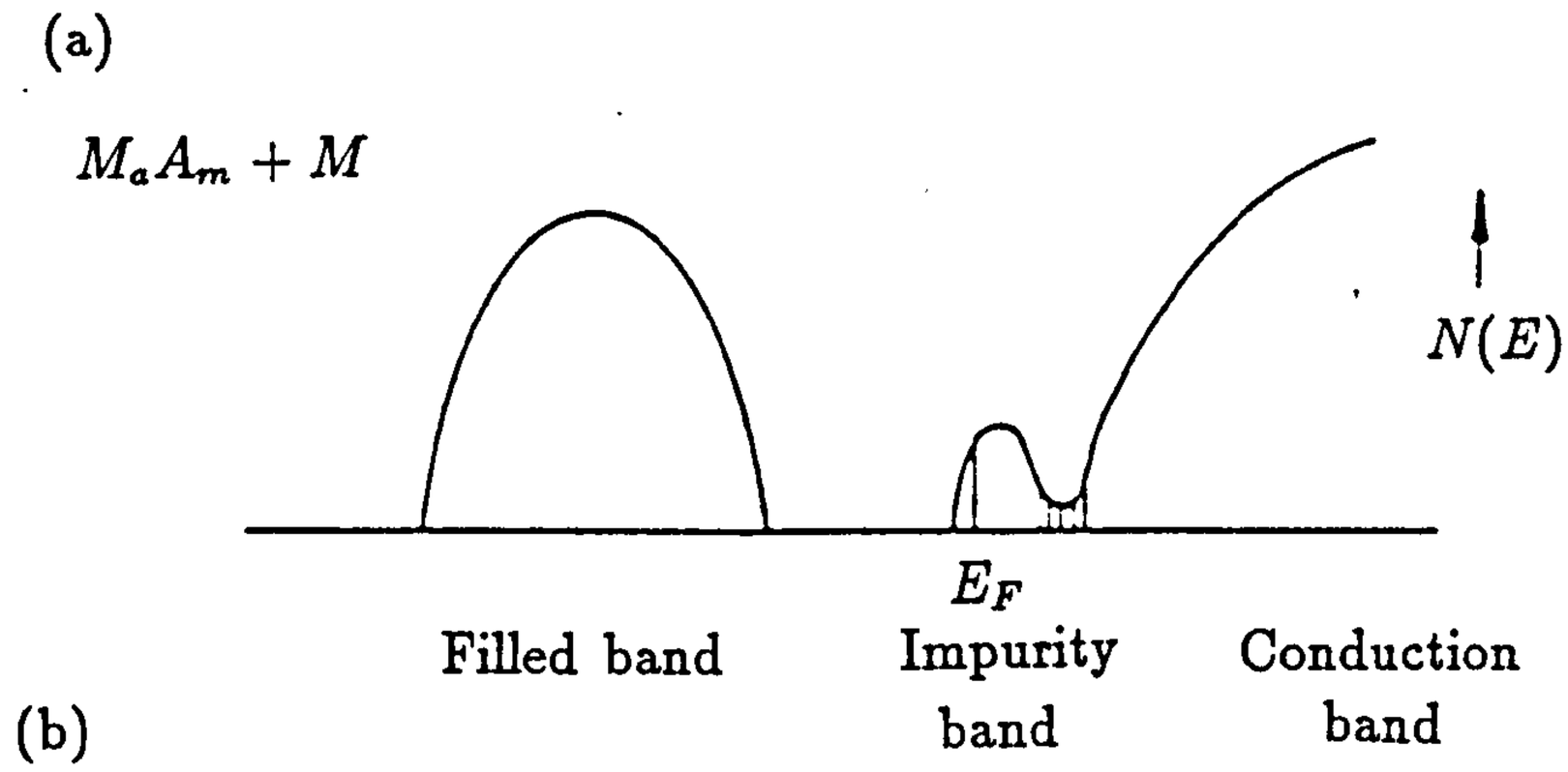

Figure 2.8: Faber's model for the electronic structure of an MA alloy. E_F is always in the impurity band, which grows with increasing concentration of excess M or A. The hatch marks indicate a possible mobility gap between the impurity band and conduction band.

Secondly, the tendency to heterocoordination will be reduced so that the depth of the pseudogap and the minimum conductivity will be less pronounced. These two effects either singly or in combination will lead to an increase in the observed value of σ with temperature. Furthermore, equation (2.23) predicts that if E_F crosses the minimum in $\sigma(E)$, a change in the sign change of the thermopower will occur. As the composition of the alloy varies from $M_aA_m + \delta A$ to $M_aA_m - \delta A$, where δA is excess of element A, E_F move from left to right, thereby explaining the sign change in S from positive for excess of electronegative element to negative for a deficit.

2.6.2 Faber model

Faber (1972) proposed an impurity band model by modifying the Enderby and Collings (1970) model. It was assumed that the excess element forms an impurity band below the bottom edge of the conduction band, as shown in Fig.2.8. The situation is very similar to that in doped semiconductor. With excess M, E_F will be below the maximum of the impurity band, and with A excess, E_F will be above the minimum. Transport is via the impurity band near stoichiometric composition, and the impurity band grows into a full - fledged band with large concentrations of excess M or A. This model can explain the observed behaviour qualitatively, but it is questioned in explaining them quantitatively. Cutler (1977) has argued that an appreciable band gap is necessary if there is to be an impurity band which is not absorbed in to the conduction band.

2.6.3 Roth and Cutler models

Roth (1975) proposed a model for the electronic structure of the M_aA_m alloy, illustrated in Fig.2.9. When a small amount of A is added to M, bonding electrons go into states which are created below E_F and may or may not be separated from the conduction band by a gap. This new band grows with increasing A, and E_F moves downward in the conduction band since each A atom add more states than

the electrons to the lower band. At the stoichiometric composition, E_F is near the centre of the band gap. This is a pure ionic band. An excess of A causes E_F to drop into the valence band, and as the composition changes towards A, the valence band becomes a partially filled band of the pure constituent.

Cutler (1977) has modified the Roth model according to molecular orbital theory by considering ionic bonding as an extreme case of covalent bonding, as shown in Fig.2.10 and Fig.2.11. The charge transfer due to increasing ionicity shifts the potentials of the two atoms toward each other. In the case of Fig.2.10, the nonbonding π electrons (assuming the A atoms have some nonbonding states) are close in energy to the σ bonding electrons. Assuming tight-binding bands, the π and σ bands would overlap strongly in energy and would presumably be merged. Conversely, the antibonding band is close in energy to the original M atomic orbitals. For a small concentration of A in M (Fig.2.11 (a)) the lower A band is split between the σ states and the somewhat higher π states. The antibonding σ^* states must be above E_F in the conduction band, if there is to be bonding. This partial covalent bonding causes removal of M states from the conduction band below E_F to the extent that ionicity is not large. Near the stoichiometric composition (Fig.2.11 (b)) the σ, π and σ^* bands have grown and the original M band has diminished. The M band becomes an impurity band which is either in the band gap between π and σ^*, or is absorbed into the σ^* band. The electronic structure at M_aA_m (Fig.2.11 (c)) shows that the partial covalency causes no quantitative change from ionic bonding up to this point. On going to excess A, however, there is a quantitative difference if the A molecules bond covalently to each other. Assuming that the M atoms have only one valence, the excess A atoms must either bond to other A atoms, which means that the bonding is purely covalent, or else it takes an ionic form, probably sharing its charge with the other A atoms. In the latter case, the sequence is the same as in Roth's model, where E_F moves downward in the valence band. If the A atoms bond to each other, as indicated in Fig.2.11(d) and (e), the valence band remains filled and insulator behavior occurs unless some covalent bonds are broken.

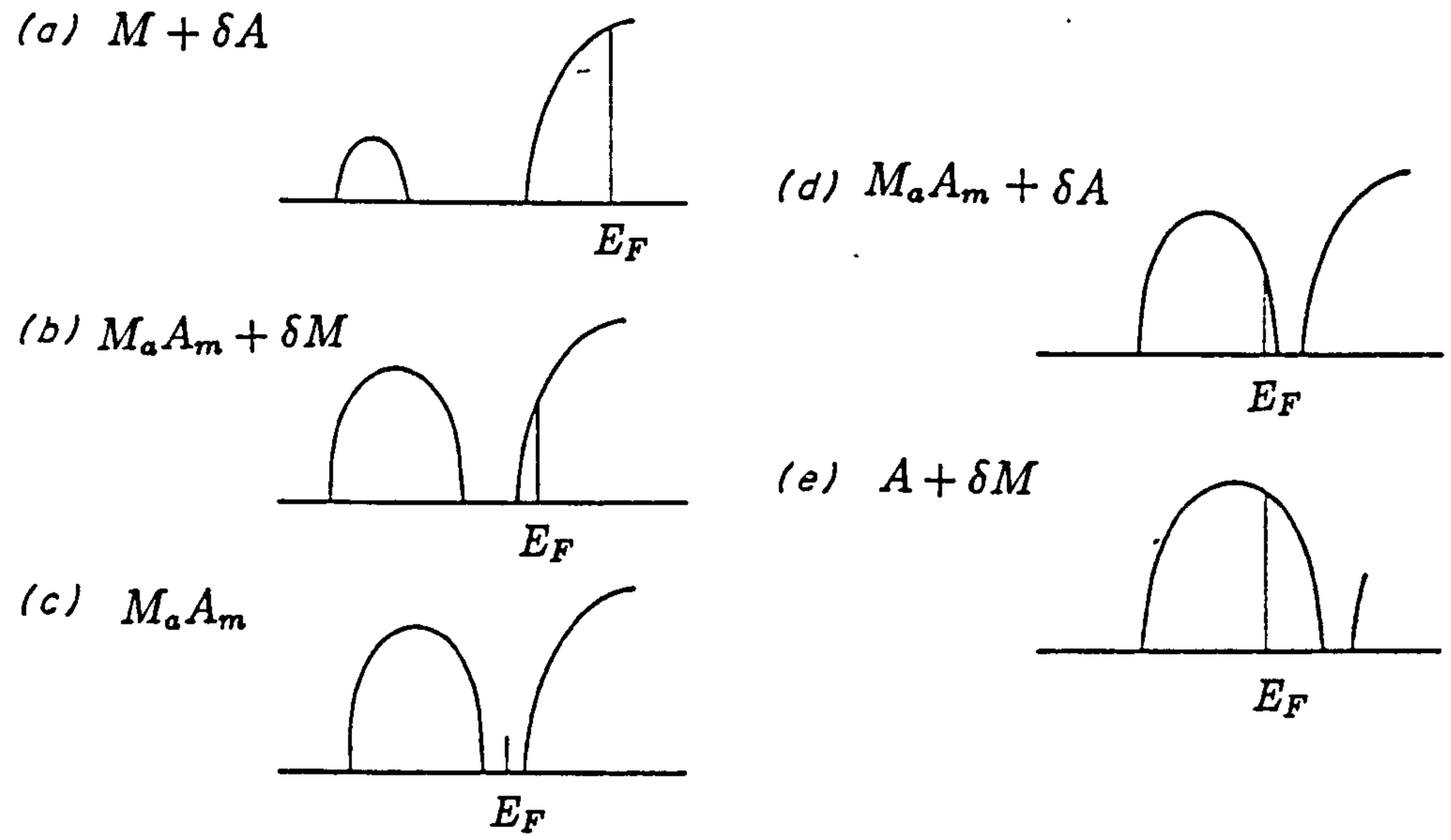

Figure 2.9: Roth's model for the electronic structure of an MA alloy. The lower band is due to A^{a-} ions.

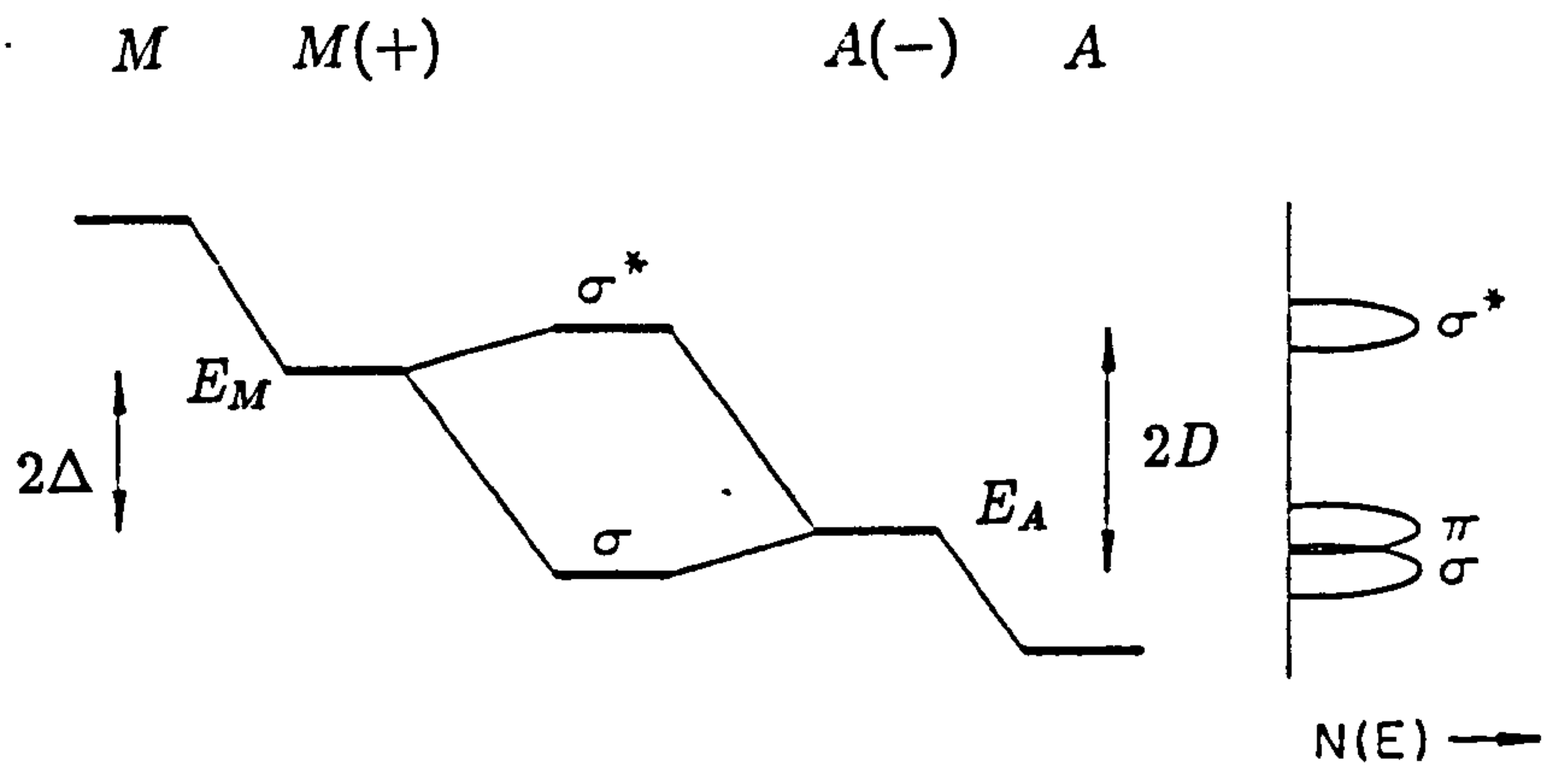

Figure 2.10: Energy level scheme for partially ionic bonds. The M and A levels are shifted to M^+ and M^- as a result of the polarity of the $M - A$ bonds. The tight bonding bands are shown on the right. Assuming that the A atoms have some nonbonding states.

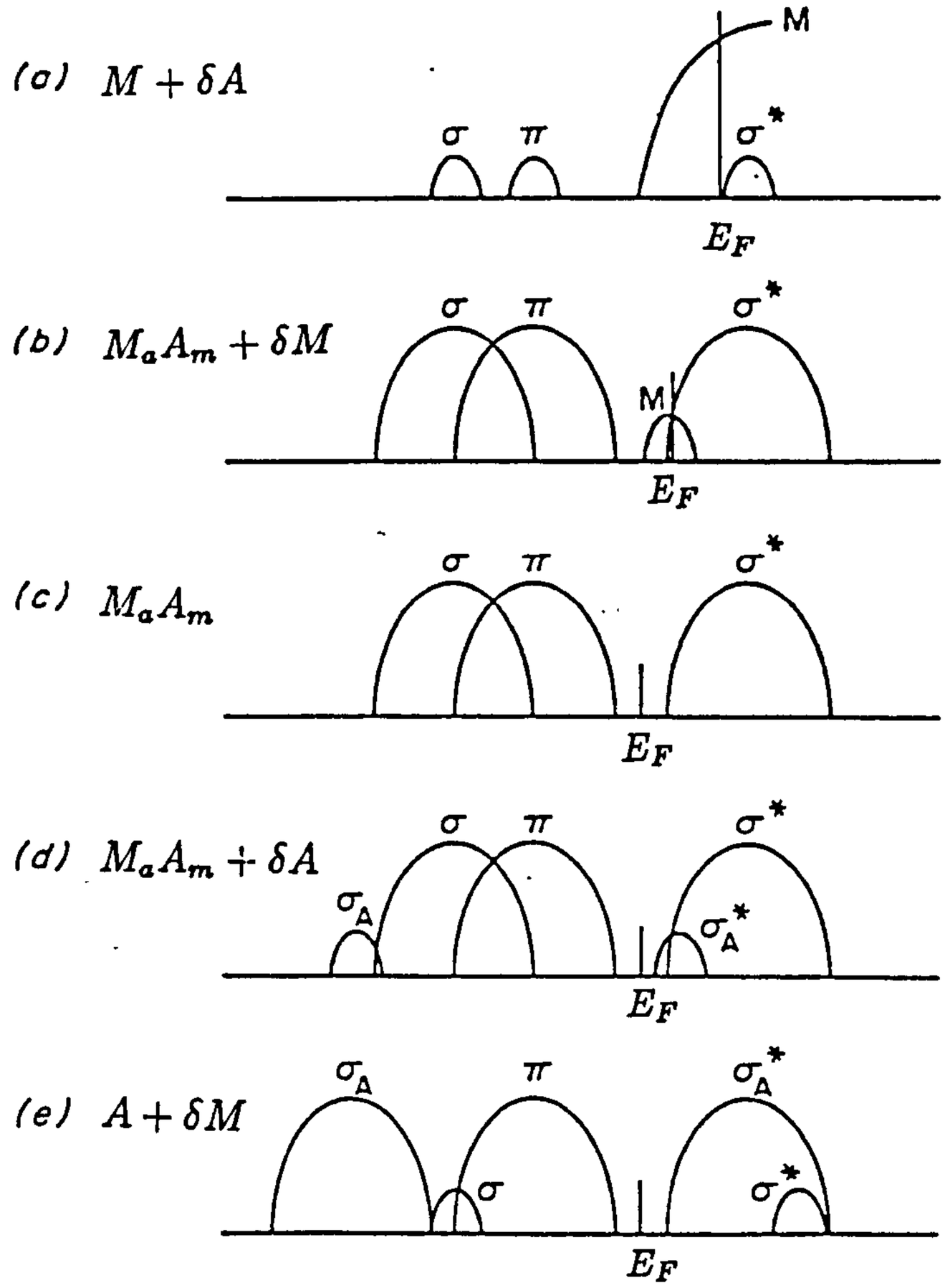

Figure 2.11: Model for the electronic structure of an MA alloy, assuming that excess A bond covalently to itself. (a), (b) and (c) differ from the ionic model Fig. 2.9 only in a partial separation between the σ bonding and π nonbonding states of the valence band. In (d) and (e) the excess A gives rise to σ_A bonding and σ_A^* antibonding states instead of adding electrons and states to the π band.

2.7 Theoretical determination of the conductivity and thermopower near stoichiometry

The concept of the pseudogap model has been introduced through the above discussion. How this model can be put into practice in quantitative manner is a question. Barnes (1993) in conjunction with Enderby has developed a method of calculating the conductivity and thermopower of a liquid ionic semiconductor $M_{1-c}A_c$ on the basis of rigid band model in terms of the Kubo-Greenwood equations. From the equations, it can be seen that if the energy-dependent conductivity $\sigma(E)$ and the chemical potential (Fermi energy) $\mu(T)$ are known, the conductivity and thermopower can be calculated numerically.

The position of the chemical potential near stoichiometry is very sensitive to change in the atomic composition and temperature, and is uniquely determined by the condition

$$Q_{total} = \int_0^\infty N(E)f(E)dE \tag{2.26}$$

where Q_{total} is the total number of electrons per unit volume in the system. The total number of valence electrons per unit volume in the system is given by

$$Q_{total} = [cQ_a + (1-c)Q_c]\rho_N \tag{2.27}$$

where Q_a and Q_c are the original number of valence electrons on the anion and cation, respectively.

A generic model of N(E) is shown in Fig.2.13. The band edges are approximated to be free electron like, such that $N(E)$ is given by

$$N(E) = \begin{cases} k_v(E - E_{vl})^{1/2} & E_{vl} \leq E < E_{vc} \\ k_v(E_{vh} - E)^{1/2} & E_{vc} \leq E \leq E_{vh} \\ k_c(E - E_{cl})^{1/2} & E_{cl} \leq E < E_{cc} \\ k_c(E_{ch} - E)^{1/2} & E_{cc} \leq E \leq E_{ch} \end{cases}$$

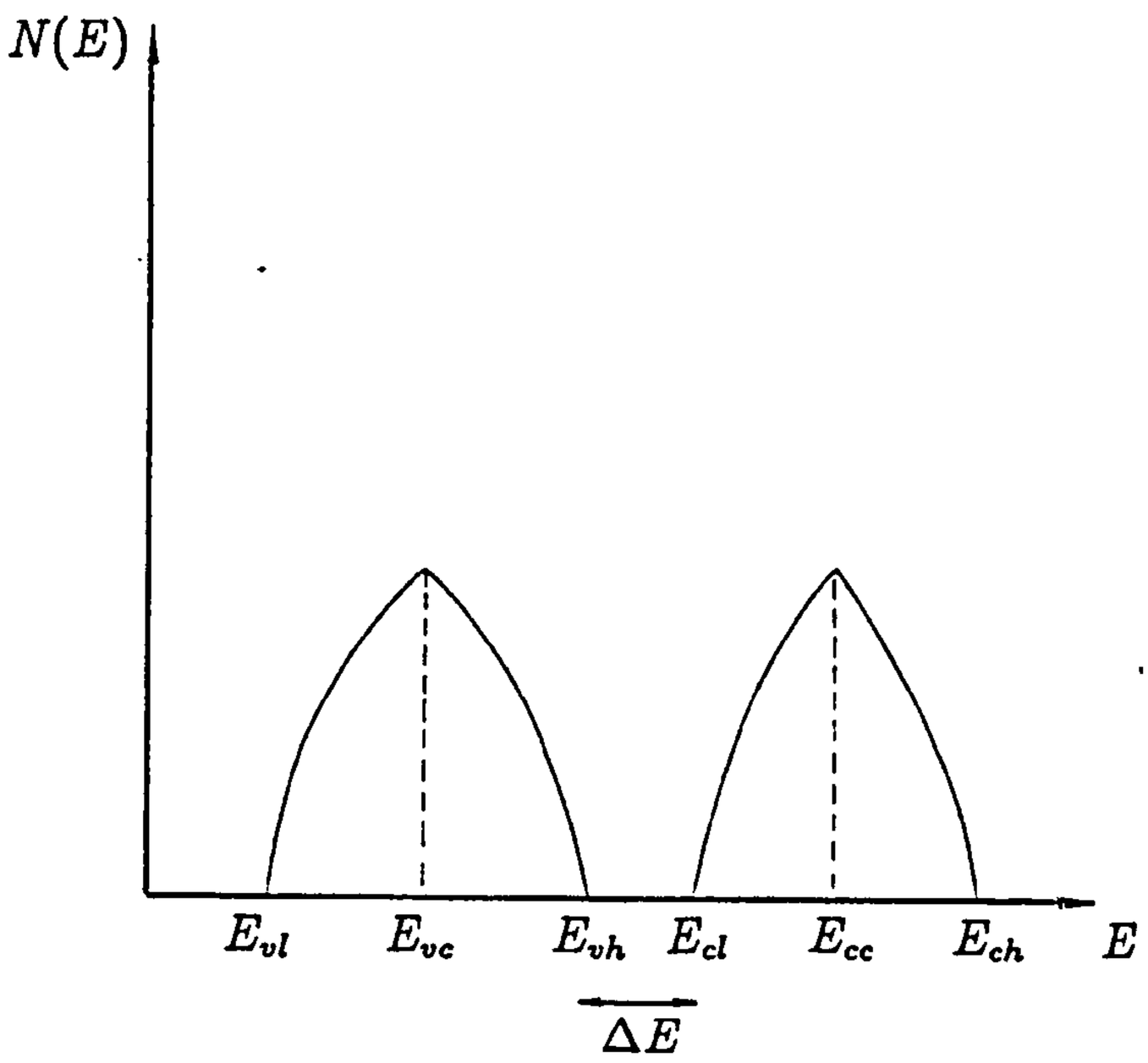

Figure 2.12: The generic model of $N(E)$ used for a charge transfer liquid semiconductor.

and the values of k_c and k_v are given by

$$k = 3(2)^{1/2} n_b / 2(\Gamma)^{3/2} \tag{2.28}$$

where n_b is the total number of electron states per unit volume in the band, and Γ is the band width. For a sample of composition $M_{1-c}A_c$, this gives, for the valence and conduction band, respectively

$$n_v = cN_a\rho_N \tag{2.29}$$

$$n_c = (1-c)N_c\rho_N \tag{2.30}$$

where N_a and N_c are the number of valence electron states on the anion and cation, respectively. From the model density of states $N(E)$ and Q_{total}, the position of the chemical potential is determined uniquely and unambiguously from equation (2.26) for any compositions in this essential rigid band picture.

The next problem is to obtain the energy-dependent conductivity $\sigma(E)$. Assuming, for simplicity, that no electron localisation occurs and using random phase approximation, this gives $\sigma(E)$, for the generic model we have chosen,

$$\begin{aligned} \sigma(E) &= A[N(E-E_c)]^2 \\ &= Ak_b^2(E-E_c) \\ &= \alpha_c(E-E_c) \end{aligned} \tag{2.31}$$

in the conduction band with a similar relationship for the valence band edge. The constant of proportionality, A, can be calculated from the model density of states to give the value of α_c and α_v determined from the data, or can be estimated theoretically, for example, using the simple random phase approximation (Friedman, 1971)

$$A = 1/6(\pi e^2 a^5 \Gamma^2)/\hbar z \tag{2.32}$$

where e is the electronic charge, a is the atomic separation, z is the coordination number. Combined with the (2.31). this gives

$$\alpha = (3\pi e^2 n_b^2 a^5)/(4\hbar z\Gamma) \tag{2.33}$$

Finally, from equation (2.18), (2.23) and (2.31), the conductivity σ and thermopower S can be determined. This method is expected to be most reasonable in the vicinity of stoichiometry where the rigid band model is more applicable.

Chapter 3

Neutron Diffraction

With the advent of nuclear reactors and pulsed sources based on nuclear spallation, thermal neutrons have become a valuable tool for investigating condensed matter. The mass of neutron results in the de Broglie wavelength of thermal neutron being approximately equal to the interatomic spacing in liquids and solids. As a result, interference effects are observed in scattering experiments and these give structural information about the scattering system. Unlike X-rays, the neutron, having no net charges, can penetrate deeply into the target without being affected by electronic cloud. Neutrons are thus scattered by the nuclear force.

Even though neutrons are not electromagnetic waves, the theoretical background for neutron scattering is strongly analogous to light and the X-ray scattering. The neutron is thus viewed through the wave-particle duality as a wave motion with wavelength $\lambda = \hbar/p$, with the momentum given as $p^2 = 2mE$, where m and E are the rest mass and energy of the neutron respectively. The speed of the neutron is related to its wavelength and energy, and is not constant as in the case of electromagnetic waves.

The following review of neutron scattering principles is mainly based on the book < Introduction to the Theory of Thermal Neutron Scattering > (Squires, 1978)

3.1 Scattering cross-section and scattering length

Neutrons of energy E and wavevector k are incident on a target and scattered in some direction (θ, ϕ) with energy E' and wavevector $\mathbf{k}'$. The neutron-nucleus interaction can be described by a scattering cross section, σ, which is obtainable from a neutron experiment. The scattering cross section is usually described at three levels:

(1) The partial differential cross-section

$$\frac{d^2\sigma}{d\Omega dE'} = (\textit{numbers of neutrons scattered per second into a small solid angle } \Omega \textit{ in the direction } \theta,\ \phi \textit{ with final energy between } E' \textit{ and } E' + dE') \,/\, \Phi d\Omega dE' \tag{3.1}$$

where Φ is the incident flux of neutron

(2) The differential cross-section

$$\frac{d\sigma}{d\Omega} = \frac{\textit{number of neutrons scattered per second into } d\Omega \textit{ in direction } \theta\ \phi}{\Phi\ d\Omega} \tag{3.2}$$

(3) The total scattering cross-section

$$\sigma_{tot} = \frac{\textit{total number of neutrons scattered per second}}{\Phi} \tag{3.3}$$

The three cross-sections are related by the following equations

$$\frac{d\sigma}{d\Omega} = \int_0^\infty \left(\frac{d^2\sigma}{d\Omega dE'}\right) dE' \tag{3.4}$$

$$\sigma_{total} = \int_{\textit{all directions}} \left(\frac{d\sigma}{d\Omega}\right) d\Omega \tag{3.5}$$

In the case of scattering of slow neutrons from the nucleus of a bound atom, the differential cross-section can be expressed as

$$\frac{d\sigma}{d\Omega} = b^2(2\pi sin\ \theta d\ \theta) \tag{3.6}$$

and the total scattering $\sigma_{tot} = 4\pi b^2$. The quantity b is known as the neutron scattering length of the nucleus. It is a complex quantity $b \equiv \alpha + i\beta$. The imaginary part is only significant for highly absorbing nuclei. The value of the scattering length depends on the particular nucleus (isotope) and the spin state of the nucleus-neutron system. It can not be calculated, and must be determined experimentally.

3.2 Coherent and incoherent scattering cross - section

Now consider the scattering from a system consisting of a single element where b varies from nucleus to nucleus due to nuclear spin and or the presence of isotopes. If the number of nuclei is large, then the cross-section measured is given by averaging over a set of scattering systems consisting of all possible permutation of the b's over the nuclei. This is written as (Squires, 1978)

$$\frac{d^2\sigma}{d\Omega dE'} = \frac{k'}{k}\frac{1}{2\pi\hbar}\sum_{jj'} b_j b_{j'} \int_{-\infty}^{\infty} < exp[-i\mathbf{Q}\cdot\mathbf{R}_{j'}(0)] \; exp[i\mathbf{Q}\cdot\mathbf{R}_j(t)] > exp(-i\omega t)dt \tag{3.7}$$

Where $\mathbf{Q}=\mathbf{k}-\mathbf{k}'$ is scattering vector and $\mathbf{R}_j(t)$ is the time-dependent Heisenberg operator. It is assumed that there is no correlation between b's values of different nuclei so that

$$\overline{b_{j'}b_j} = (\bar{b})^2 \qquad j' \neq j \tag{3.8}$$

$$\overline{b_{j'}b_j} = \overline{b^2} \qquad j' = j \tag{3.9}$$

where

$$\bar{b} = \sum_i f_i b_i, \qquad \overline{b^2} = \sum_i f_i b_i^2 \tag{3.10}$$

and f_j is the relative frequency of the value b_i.

By use of equation (3.8) and (3.9), (3.7) can be separated into two additive terms. The first of these is known as the coherent cross-section and is defined as

$$\left(\frac{d^2\sigma}{d\Omega dE'}\right)_{coh} = \frac{\sigma_{coh}}{4\pi}\frac{k'}{k}\frac{1}{2\pi\hbar}\sum_{jj'}\int_{-\infty}^{\infty} < exp[-i\mathbf{Q}\cdot\mathbf{R}_{j'}(0)] \; exp[i\mathbf{Q}\cdot\mathbf{R}_j(t)] > exp(-i\omega t)dt \tag{3.11}$$

The second is defined as

$$\left(\frac{d^2\sigma}{d\Omega dE'}\right)_{inc} = \frac{\sigma_{inc}}{4\pi}\frac{k'}{k}\frac{1}{2\pi\hbar}\sum_{j}\int_{-\infty}^{\infty} < exp[-i\mathbf{Q}\cdot\mathbf{R}_j(0)] \; exp[i\mathbf{Q}\cdot\mathbf{R_j}(t)] > exp(-i\omega t)dt \tag{3.12}$$

and is known as the incoherent cross-section. The value σ_{coh} and σ_{inc} are given by

$$\sigma_{coh} = 4\pi(\bar{b})^2, \qquad \sigma_{inc} = 4\pi[\overline{b^2} - \bar{b}^2] \tag{3.13}$$

From (3.11) and (3.12), we see that coherent scattering depends on the correlation between the positions of the same nucleus at different times, and on the correlation between the position of different nuclei at different times. It, therefore, gives interference effects. The incoherent scattering depends only on the correlation between the positions of the same nucleus at different times. It does not give interference effects. Physically, the incoherent scattering arises from the random distributions of the deviation of the scattering length from their mean value. Incoherent scattering can give information only about individual scattering centres, and no direct information about collective motions. Coherent scattering gives information about collective motion and structure present in the liquid.

3.3 Correlation functions

Although equations (3.11) and (3.12) have already given a relation between the cross-section and operators of the scattering system, it is still not easy to see the physics of the scattering system and in particular its structure. A better understanding is achieved by use of the Van Hove correlation function (Van Hove, 1954).

Equation (3.11) can be expressed as

$$\left(\frac{d\sigma^2}{d\Omega dE'}\right)_{coh} = \frac{\sigma_{coh}}{4\pi}\frac{k'}{k}\frac{1}{2\pi\hbar}\int_{-\infty}^{\infty} I(\mathbf{Q},t)exp(-i\omega t)dt \tag{3.14}$$

where

$$I(\mathbf{Q},t) = \frac{1}{N}\sum_{jj'} < exp[-i\mathbf{Q}\cdot\mathbf{R_{j'}}(0)]exp[i\mathbf{Q}\cdot\mathbf{R_j}(t)] > \tag{3.15}$$

and is known as the intermediate scattering function. Another function can be derived from (3.14), namely,

$$S(\mathbf{Q},\omega) = \frac{1}{2\pi\hbar}\int I(\mathbf{Q},t)exp(-i\omega t)dt. \tag{3.16}$$

$S(\mathbf{Q},\omega)$ is known as the scattering law. So equation (3.14) can be rewritten as

$$\frac{d\sigma^2}{d\Omega dE} = \bar{b}^2\frac{k'}{k}S(\mathbf{Q},\omega) \tag{3.17}$$

The scattering law $S(\mathbf{Q},\omega)$ describes the scattering from the samples due to the spatial and temporal correlations of the atoms and consequently contains all the structural information of the system.

3.4 Structure factor $S(Q)$ and radial distribution function $g(r)$

The n^{th} energy moment of the scattering function $S(\mathbf{Q},\omega)$ can be defined as

$$S_n(\mathbf{Q}) = \int_{-\infty}^{\infty} S(\mathbf{Q},\omega)(\hbar\omega)^n d(\hbar\omega) \tag{3.18}$$

Of particular interest is the zeroth moment given by

$$\begin{aligned} S_0(\mathbf{Q}) &= S(\mathbf{Q}) \\ &= \int_{-\infty}^{\infty} S(\mathbf{Q},\omega)d(\hbar\omega) \end{aligned} \tag{3.19}$$

where $S(\mathbf{Q})$ is known as the structure factor, which is *measurable* from a neutron experiment.

The structure factor can be related to the radial distribution function $g(\mathbf{r})$ by (see Squires, 1978)

$$S(\mathbf{Q}) = 1 + \int \rho g(\mathbf{r}) exp(i\mathbf{Q} \cdot \mathbf{r}) d\mathbf{r}, \tag{3.20}$$

where ρ is the atomic number density. In the case of a liquid it is assumed that the scattering system is isotropic. Then the vectors become the scalars. By use of polar angular coordinates, the equation (3.20) then becomes

$$S(Q) = 1 + \frac{4\pi}{Q} \int_0^\infty [g(r) - \rho] sin(Qr) dr \tag{3.21}$$

The subtraction of ρ from $g(r)$ in (3.21) removes the problem of a δ-function that would otherwise occur at $\mathbf{Q}$=0 (lovesey, 1986). Equation (3.21) is then written

$$S(Q) = 1 + \frac{4\pi\rho}{Q} \int_0^\infty [g(r) - 1] sin(Qr) r dr \tag{3.22}$$

By use of Fourier transform

$$g(r) = 1 + \frac{1}{2\pi^2 \rho r} \int [S(Q) - 1] sin(Qr) Q dQ \tag{3.23}$$

It is this definition of $g(r)$ which will be adopted in this work. Given that ρ is the number density of the atoms in the system, the radial distribution function is defined so that $\rho g(r)dr$ is the number of particles in a volume element $d\mathbf{r}$ at a distance r from a particle located at the origin. The mean interatomic distances may be determined from the positions of the peaks in this function. The coordination number N may be determined by integrating over the nearest neighbour peak in $g(r)$. This can be expressed as

$$N = 4\pi\rho \int_{r_1}^{r_2} g(r) r^2 dr, \tag{3.24}$$

where r_1 and r_2 are the positions of the front cut off and first minimum of the peak in g(r).

3.5 The practical derivation of g(r) and S(Q)

The cross-section measured in practice is

$$(\frac{d\sigma}{d\Omega})_{eff} = \int_0^\infty f(E')\frac{d^2\sigma}{d\Omega dE'}dE'$$

$$= \frac{\sigma_{coh}}{4\pi}\hbar N\int_{-\infty}^{E/\hbar} f(E')\frac{k'}{k}S(Q,\omega)d\omega \qquad (3.25)$$

where $f(E')$ is the efficiency of the detector for neutron of energy E'. Equation (3.25) is not generally solvable, and approximations must be used. In the static approximation, any change in neutron energy is assumed to be negligible and the scattering is elastic, namely $k = k'$, E' is constant E_0 and Q is a constant Q_0 (we still denote Q_0 by Q). So that we obtain

$$\left(\frac{d\sigma}{d\Omega}\right)_{eff}^{sa} = \frac{\sigma_{coh}}{4\pi}\hbar f_0 N\int_{-\infty}^{\infty} S(Q,\omega)d\omega$$

$$= \frac{\sigma_{coh}}{4\pi}\hbar f_0 N S(Q) \qquad (3.26)$$

where N is the total number of particles.

Three important equations have so far been obtained, (3.22), (3.23) and (3.26). Equation (3.26) is the quantity measured directly in a neutron diffraction experiment. It is essentially the product of two factors. The first factor σ_{coh} depends on the interaction between the neutron and the individual particles in the scattering system. The second factor is $S(Q)$ which depends on relative position of the particles in the system. The positions of the particles depend on the force between the particles, and on the temperature of the system. So $S(Q)$ gives the structural information of the scattering system. σ_{coh} can be calculated or measured. In practice, several experimental corrections on the measured cross-section have to be made to obtain $S(Q)$. These will be discussed in chapter 5.

3.6 Multi-component systems

So far the discussion has been restricted to a single component system. The extension of the theory to multi-component systems gives the effective cross-section as

$$\frac{1}{N}\left(\frac{d\sigma}{d\Omega}\right)^{sa}_{eff} = \sum_{\alpha} c_\alpha b_\alpha^2 + \sum_{\alpha}\sum_{\beta} c_\alpha c_\beta b_\alpha\ b_\beta\ [S_{\alpha\beta}(Q) - 1]$$

$$= \sum_{\alpha} c_\alpha b_\alpha^2 + S(Q) \tag{3.27}$$

$$S(Q) = \sum_{\alpha}\sum_{\beta} c_\alpha c_\beta b_\alpha\ b_\beta\ [S_{\alpha\beta}(Q) - 1] \tag{3.28}$$

where c_α, c_β is the atomic fraction of component α, β and b_α and b_β are the respective bound coherent scattering lengths. The function $S(Q)$ contains all of the structural information from the scattering system in the form of the partial structure factors $S_{\alpha\beta}$. The partial structure factors are analogous to the structure factor obtained for the single component system.

For a binary liquid alloys of the form $M_a A_m$, equation (3.28) can be written as

$$S(Q) = \left(\frac{a}{a+m}\right)^2 b_A^2 (S_{AA}(Q) - 1)$$

$$+ \left(\frac{m}{a+m}\right)^2 b_M^2 (S_{MM}(Q) - 1)$$

$$+ 2\frac{a\ m}{(a+m)^2} b_A b_M (S_{AM}(Q) - 1). \tag{3.29}$$

To separate out S_{AA}, S_{MM} and S_{AM} from $S(Q)$, b_A, b_M or both must be changed in a systematic fashion. Experimentally, the technique of neutron diffraction with isotopic substitution, which exploits the feature of the variation of the neutron scattering length with isotopic composition, is one of successful methods which have been applied to many systems of liquid semiconductors. As synchrotron sources and the associated instrumentation are further developed, the possibility of changing b_A or b_M by anomalous (resonance) scattering (Waseda, 1984) will be realised.

Likewise the partial structure factors $S_{\alpha,\beta}(Q)$ are related to the partial pair distribution function $g_{\alpha\beta}(r)$ by

$$g_{\alpha\beta}(r) = 1 + \frac{1}{2\pi^2\rho r}\int [S_{\alpha\beta}(Q) - 1] sin(Qr) Q dQ \tag{3.30}$$

The quantity $g_{\alpha\beta}(r)$ is the partial pair distribution function. It measures the probability of finding a β - type particle at a distance r from an α - type particle placed at the origin.

Chapter 4

Experimental Methods for the Electrical Properties

4.1 Principles of measurement of conductivity and thermopower

4.1.1 Conductivity

The electrical conductivity (σ) is defined by Ohm's law, $\mathbf{J} = \sigma\mathbf{E}$, where $\mathbf{J}$ is electrical current density, $\mathbf{E}$ electrical field. The conductivity σ is defined as the reciprocal of the electrical resistivity (ρ), $\sigma = 1/\rho$. Resistivity has units of (Ωcm), so that the conductivity has units of ($\Omega^{-1}cm^{-1}$).

The measurement of the conductivity in this work was based on the four-probe method in which direct electrical contact was made to the sample . A known current (I) is passed through two outer electrodes. By measuring the potential difference (ΔV) across two inner electrodes the sample resistance (R) between them can be determined by the Ohm's law, R=ΔV/I. The resistivity of the sample was determined by calibrating the sample cell with a liquid of known conductivity, so that the conductivity of the sample can be obtained by the reciprocal of the resistivity. By

using a four-probe method and high resistance measurement circuitry, the effects of contact resistance at the interfaces can be eliminated.

4.1.2 Thermopower

When a temperature gradient is maintained across a sample, heat is transported by the electrons from the hot to the cold region. By considering the effects of the current generated thermally and electrically and incorporating interference effects between the two, then the electrical current is given by (Barnard 1972, Ashcroft and Mermin 1976)

$$\mathbf{J} = L^{11}\varepsilon + L^{12}(-\nabla T) \tag{4.1}$$

where $\varepsilon = \nabla\overline{\mu}$, and $\overline{\mu}$ is the electrochemical potential defined by $\overline{\mu} = \mu + eV$, and μ is the chemical potential and V is the electric potential. The L terms are the transport coefficients and relate the primary current flows under primary forces (i.e. L^{11} for J and ε) and the primary current flows with the interference or coupling forces. If no electric current is allowed to flow, J = 0, the equation (4.1) becomes

$$\varepsilon = \frac{L^{12}}{L^{11}}(\Delta T) = |e|S\Delta T \tag{4.2}$$

where S is defined as the absolute thermoelectric power (or thermopower) of the material. S is a fundamental property of a material and determines the sign and magnitude of the various thermoelectric effects.

When a circuit is constructed from two dissimilar metals A and B, with the two junctions held at temperatures T_0 and T_1 , as shown in fig.4.1, a voltage (ΔV) will develop across the points a and b. It is called the Seebeck effect. The magnitude and sign of this voltage is related to the absolute thermopower of the two materials.

From equation (4.2) and integrating

$$\int \varepsilon \cdot d\mathbf{r} = |e| \int_{T_a}^{T_b} S(T)dT = \overline{\mu}^{T_b} - \overline{\mu}^{T_a} \tag{4.3}$$

from which it can be seen that each part of the circuit is in turn

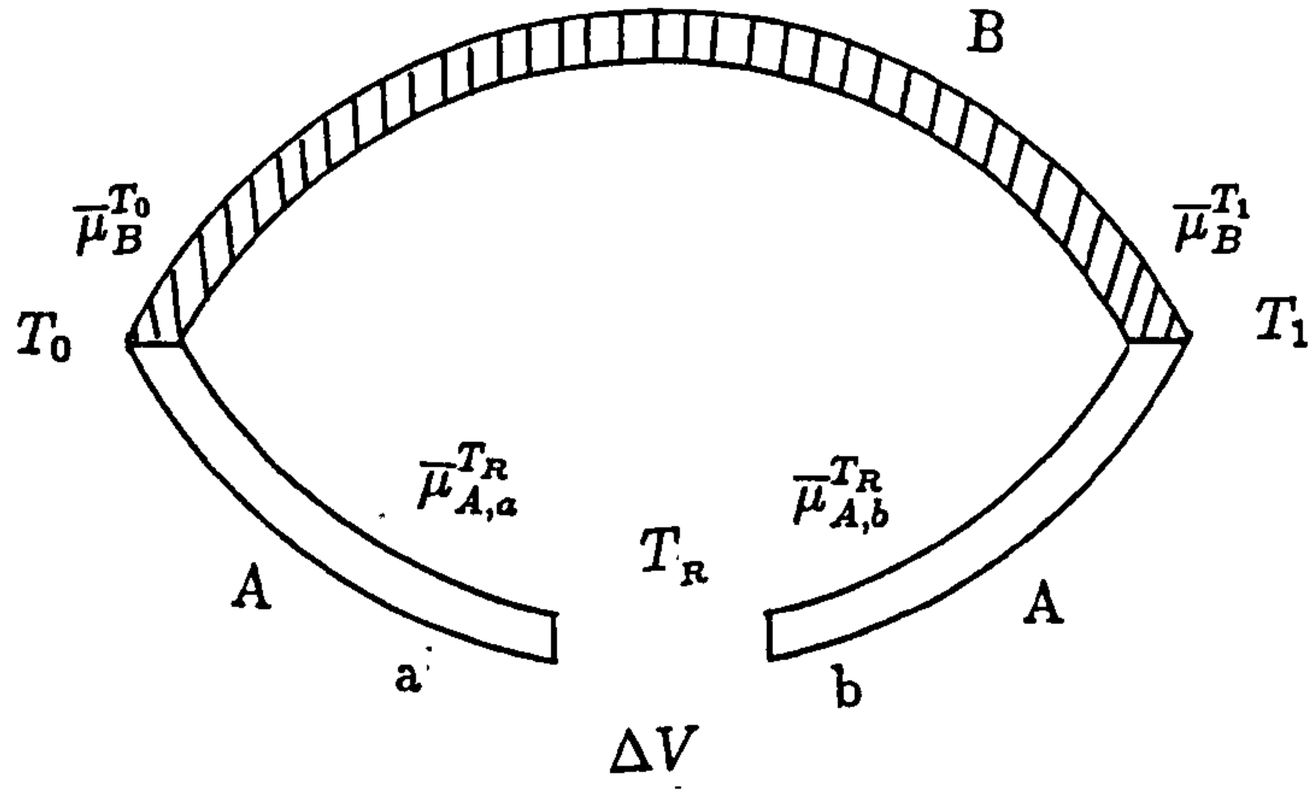

Figure 4.1: The Seebeck effect

$$\overline{\mu}_{A,a}^{T_R} - \overline{\mu}_A^{T^0} = |e| \int_{T_0}^{T_R} S_A(T) dT \tag{4.4}$$

$$\overline{\mu}_B^{T^0} - \overline{\mu}_B^{T_1} = |e| \int_{T_1}^{T_0} S_B(T) dT \tag{4.5}$$

$$\overline{\mu}_A^{T_1} - \overline{\mu}_{A,b}^{T^R} = |e| \int_{T_R}^{T_1} S_A(T) dT \tag{4.6}$$

By summing these together and noting that the electrochemical potentials at the junctions must be equal then

$$\overline{\mu}_{A,a}^{T_R} - \overline{\mu}_{A,b}^{T_R} = |e| \int_{T_0}^{T_1} (S_A(T) - S_B(T) dT \tag{4.7}$$

As $\overline{\mu} = \mu - |e|V$ and μ is independent of temperature,

$$V_b - V_a = \int_{T_0}^{T_1} [S_A(T) - S_B(T)] dT \tag{4.8}$$

By differentiating equation (4.8)

$$\frac{dV(T)}{dT} = S_A(T) - S_B(T) = S_{REF}(T) - S_{SAMPLE}(T) \tag{4.9}$$

In a measurement, one electrode is held at a constant temperature (T) while the temperature of the other electrode is varied. The Seebeck voltages measured between

the two electrodes as a function of temperature can be then used to determine the thermopower of the sample (S_{SAMPLE}(T)) provided the absolute thermopower S_{REF} of a reference material is known.

4.2 Experimental apparatus

4.2.1 The experimental system

The difficult experimental problems in making measurements on liquid semiconductors have undoubtedly dampened progress in this field. The experimental apparatus in this work must contend with the following difficulties:

1. Experimental temperatures in the range of 400-1200 ^{o}C.

2. The chemical elements Selenium, Tellurium and Thallium and the compounds TlCl and CuCl are highly hazard to health.

3. All the samples are very susceptible to oxidisation.

4. Chalcogenides have an appreciable vapour pressure at experimental temperatures.

5. The four-electrode method is used in measuring conductivity and thermopower in the same time. The temperature of the constant temperature region of the furnace should be easily adjustable.

6. The data should be timely collected and stored.

7. In order to obtain high accuracy and to save experimental materials, the compositions of the samples should be adjustable in a single measurement if it is possible.

Under consideration of the above principles, the experimental system used in this work was an improvement of that developed by Howe and Enderby (1967), as shown in Fig.4.2.

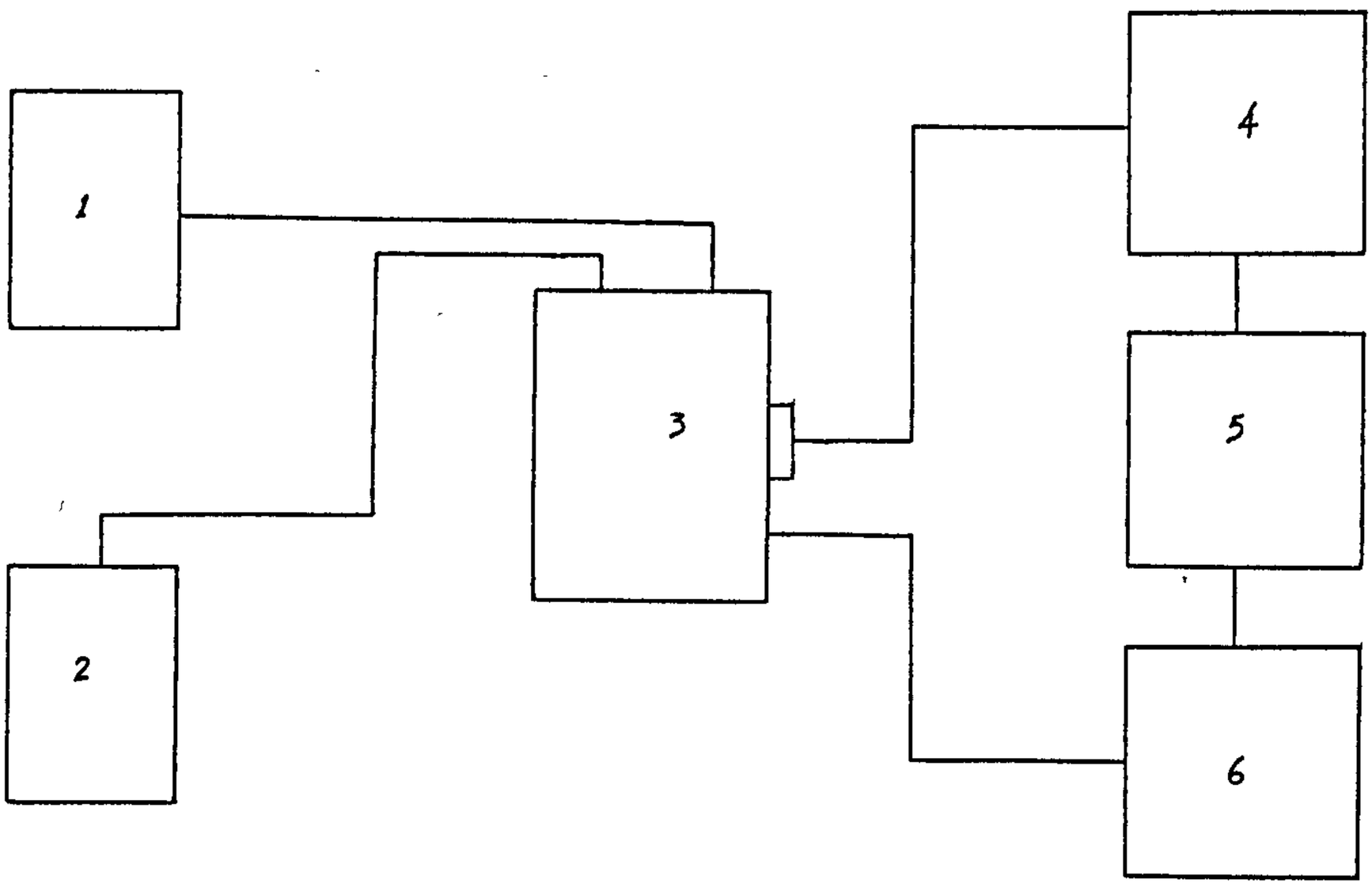

Figure 4.2: The experimental system

1 - Ar 2 - Vacuum 3 - furnace 4 - temperature controller 5 - BBC computer 6 - σ S measurement

It consists of six parts which are: (1). inert gas; (2). vacuum; (3). furnace; (4). temperature controller; (5). BBC computer for programming the measurement and storaging the data; (6) S and σ data collection. These will be described in detail in the following subsections.

4.2.2 Furnace

A twin zone furnace capable of achieving temperature of 1200 ^oC was specially designed for fulfilling measurement of conductivity and thermopower in a single experiment. A diagram of the furnace is shown in Fig.4.3. The twin zone furnace has two sets of Kanthal windings mounted vertically on an alumina tube. The power is quoted as 1.5 KW at 240 V. The wiring diagram is shown in Fig.4.4. The temperature of the twin zone furnace was controlled by two proportional temperature controllers with thyristor output stages. The temperature sensing for this control unit comes from the top and bottom thermocouples on the sample cell. This allows very fine control of the electrode temperatures to obtain an accurate thermopower measurement.

4.2.3 Sample chamber, vacuum and gas systems

The details of the sample cell chamber are shown in Fig.4.5. The sample cell was attached to the end of a neoprene tube and secured in position using a jubilee clip. A tungsten rod of 2mm diameter was passed through a Wilson seal in the top plate. This allowed the sample to be stirred and agitated. The furnace worktube was attached to the mounting with an O-ring compression seal. In order to prevent heat from the furnace affecting this joint, it was cooled by a few turns of copper tubing through which cooling water was continuously circulated. The leads for the electrodes and the thermocouples were passed through glass-metal seals on the top plate. These were terminated under the top plate by connection blocks (of the same material as the electrodes) to facilitate easy connection of the cell wires.

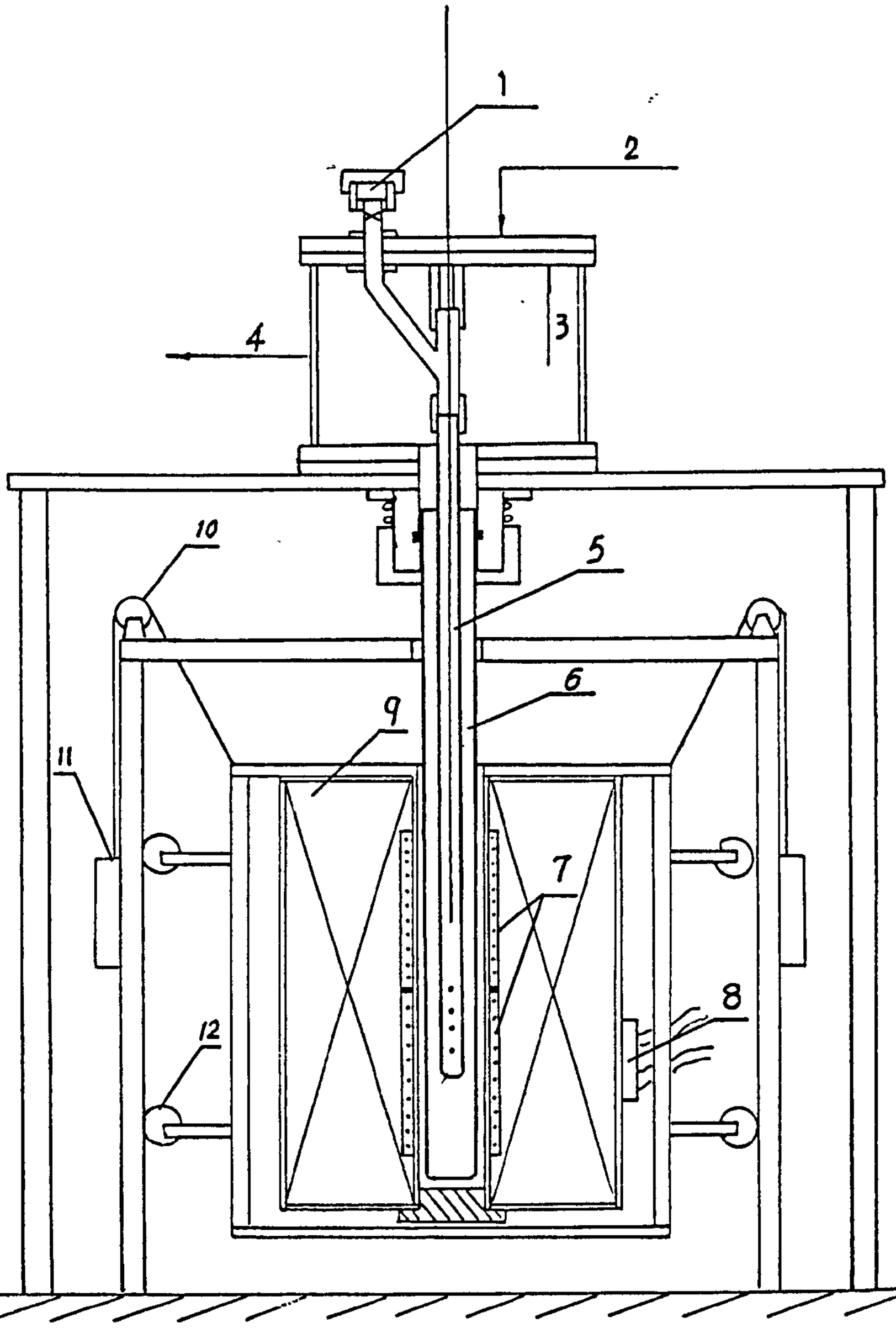

Figure 4.3: Diagram of the furnace and furnace assembly

1 - loading valve 2 - inert gas inlet 3 - cell wires lead 4 - to vacuum 5 - sample cell 6 - work tube 7 - twin windings 8 - power cables 9 - heat-isolation materials 10 - pulley 11 - counterbalance 12 - guidance wheel

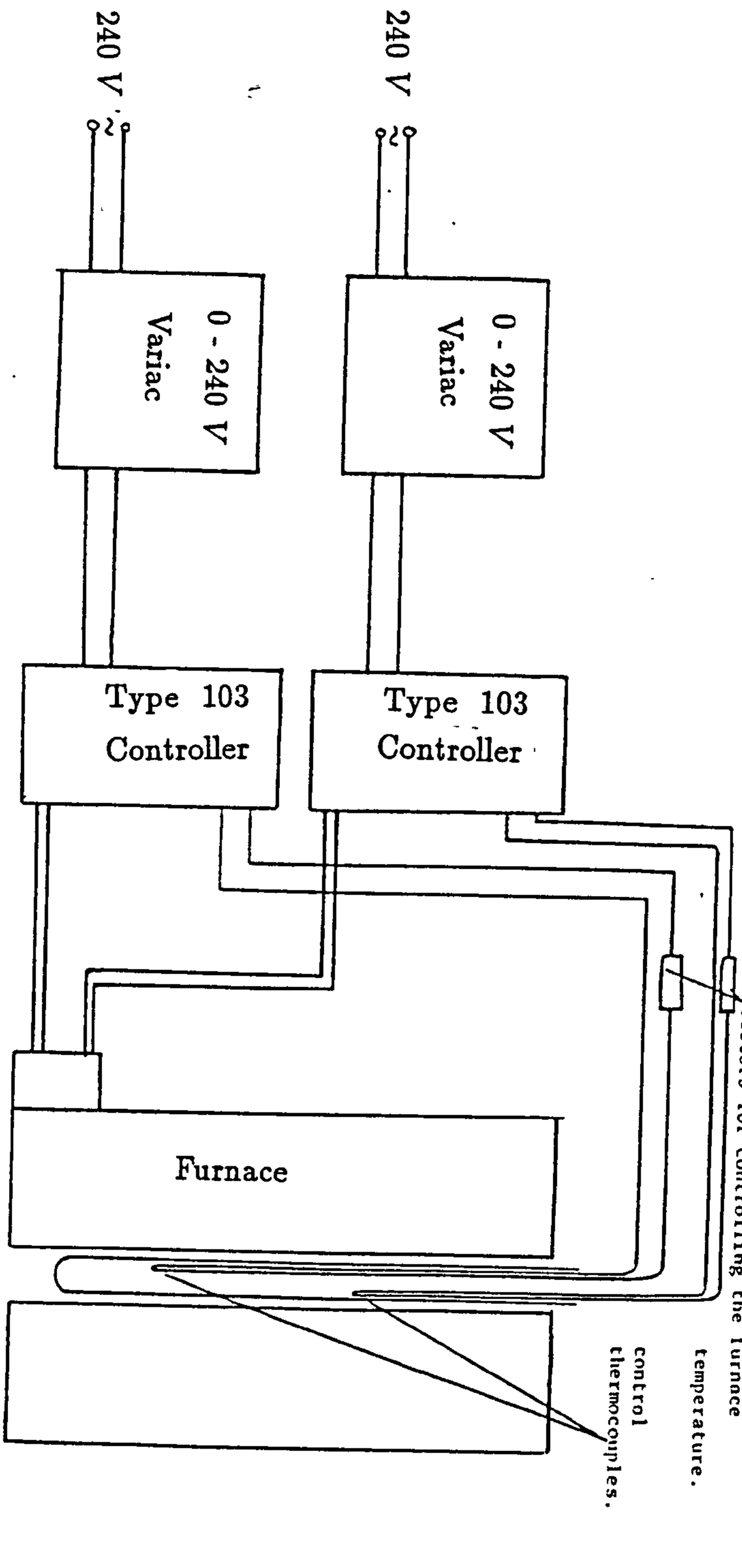

Figure 4.4: Wiring diagram of the furnace

The seals were made vacuum tight by using epoxy resin. Argon could be fed into the sample cell or the whole chamber by using valves A or B. The argon pressure was measured with a Bourdon gauge.

A loading valve was mounted on the sample chamber, through which additional materials can be added into the sample being measured. In this way, the composition of a sample could be changed in a single experiment. This ensured that a set of measurements could be carried out in the same environment, which gives good accuracy and save experimental materials. The valve was specially designed with double seals to prevent gas leakage during loading operations. This loading system was devised and mounted during this work.

A schematic diagram of the vacuum system is shown in Fig.4.6. By using this system the sample chamber could be evacuated to a vacuum of 10^{-4} torr. The vacuum within the worktube of the furnace was measured with a Penning gauge. With the pumping system isolated from the cell chamber, argon could be admitted through the admittance valve. The experiments were conducted with an argon atmosphere pressure above the sample.

4.2.4 Sample cell

Two types of sample cells were used in the experiments, a cell made from vitreous silica for experiments up to 1200 ^oC, and a cell made from Purox recrystallized alumina for Mg_3Bi_2 which is very corrosive to silica at high temperature. Diagrams of the construction and mounting of sample cell are shown in Figs.4.7 and 4.8 respectively.

The silica cells were fabricated from two pieces of silica tube. This consisted of a tube of 500 mm long with an outside diameter of 10 mm, fused to a capillary tube 150 mm long, with an outside diameter of 10 mm and inside diameter 4 mm. The capillary tube was sealed at one end. The capillary tube was ultrasonically drilled with carborundum powder as an abrasive to give four holes spaced 30 mm apart with a nominal diameter of 0.7 mm.

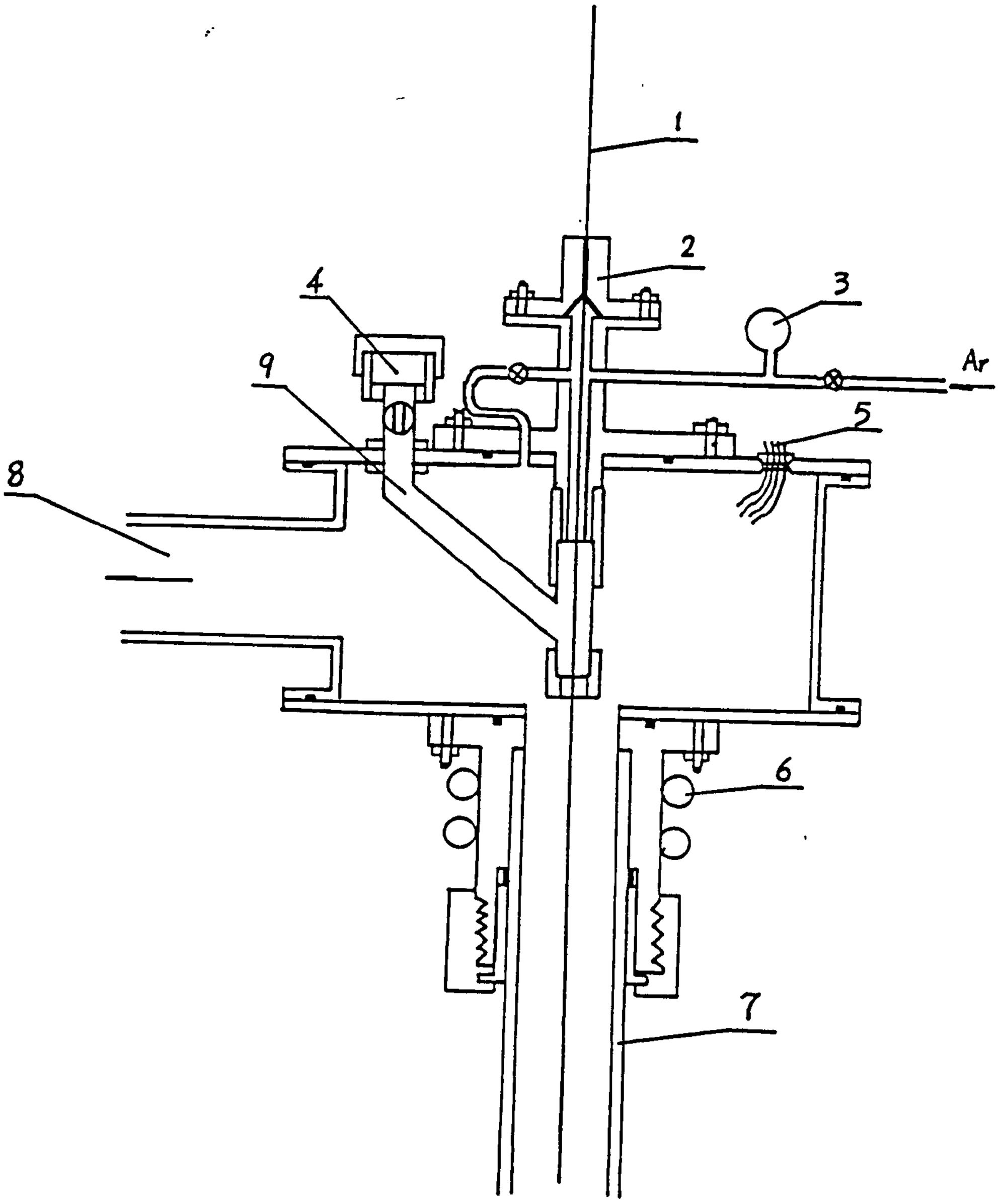

Figure 4.5: Details of the cell mounting assembly

1- Tungsten rod (2.5 mm) 2 - Wilson seal 3 - vacuum gauge 4 - loading valve 5 - lead through for cell wires 6 - cooling tubes 7 - work tube 8 - to vacuum system 9 - loading tube

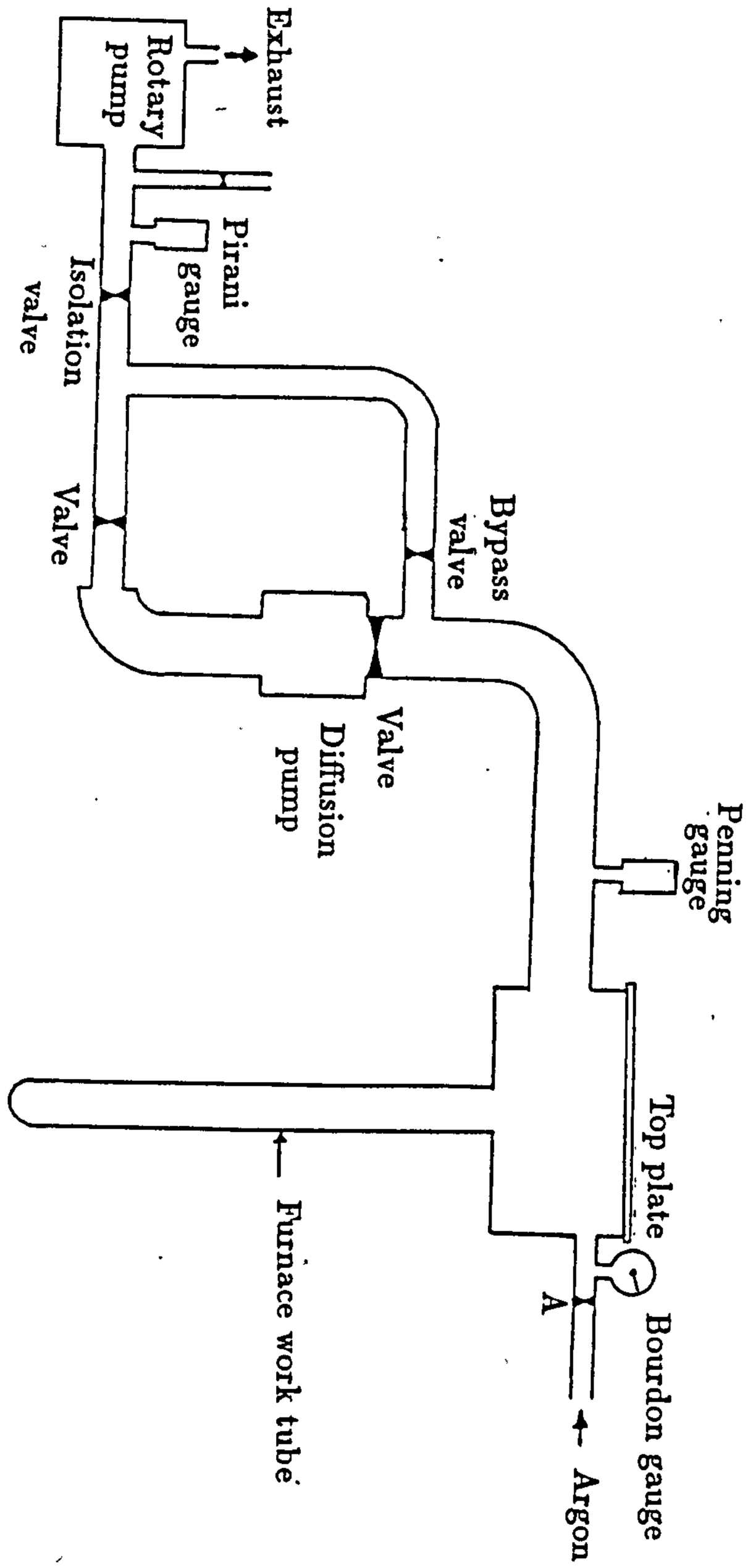

Figure 4.6: Schematic of the vacuum system

These were then ground using a diamond compound to give a 6° tapered hole. This was achieved with a tapered mild steel tool and a diamond mesh size of 60 μm. The graphite barrier plugs were made from 6.3 mm diameter graphite rod. These were accurately turned to give a plug about 5 mm long with 6° degree taper and a tip diameter of 0.5 mm. This ensured that they would fit tightly into the silica tube.These plugs were inserted with a gentle pressure. The top of the plugs were then smoothed down until they were almost flush with the silica surface. If too much of the plug projected the cells were liable to crack during the experiment. Molybdenum was used as the electrode material because of its high melting point, resistance to corrosion and well tabulated thermopower values. The electrode foils was made from 0.1 mm thick molybdenum foil cut into rectangles 20 mm × 50 mm. Each foil was clamped to the cell using stainless steel strips and 8BA stainless steel nuts and bolts. The Purox alumina cells were made from a single piece of alumina tube sealed one end, 650 mm long with an outside diameter of 10 mm and an inside diameter of 6 mm. They were drilled and constructed in a similar fashion to the silica cell.

4.2.5 The control and measurement circuitry

Measurements and temperature control in the experiments were achieved using a BBC microcomputer. The computer controlled the temperature of the furnace, and made measurements of the conductivity and the thermoelectric voltages. The control and measurement system is shown in Fig.4.9. All the voltage measurements were made using a Keithley 181 nanovoltmeter. For voltages between 0 and 2 V this has a quoted input resistance of 1 GΩ and an accuracy of 0.015% with a very low thermal drift. This voltmeter has a built-in IEEE-488 interface allowing it to be directly connected to the BBC. Through this interface the BBC could control the voltmeter ranges and take voltage readings. The wiring diagram is shown in Fig.4.10.

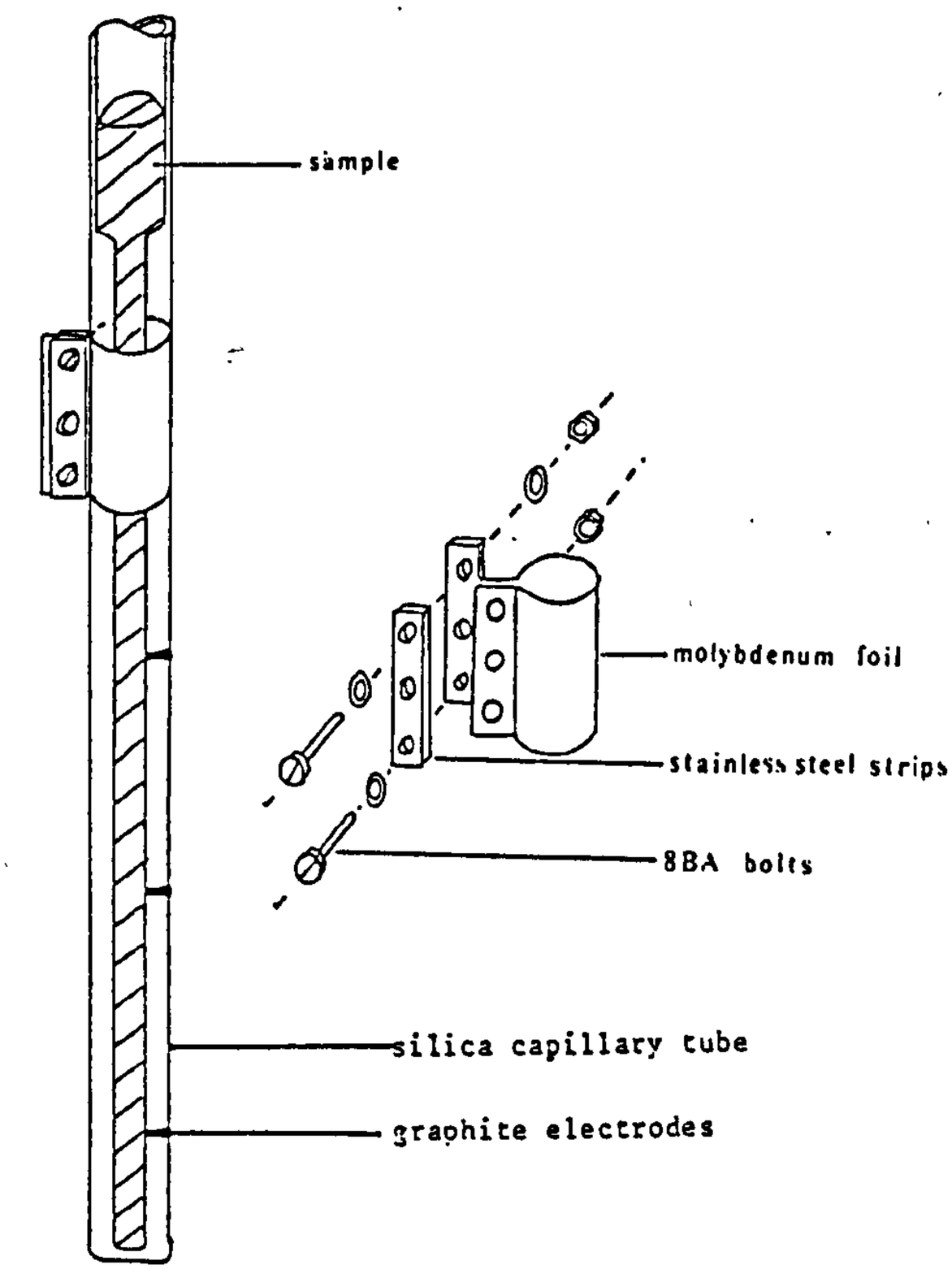

Figure 4.7: Diagram of the construction of the silica sample cells

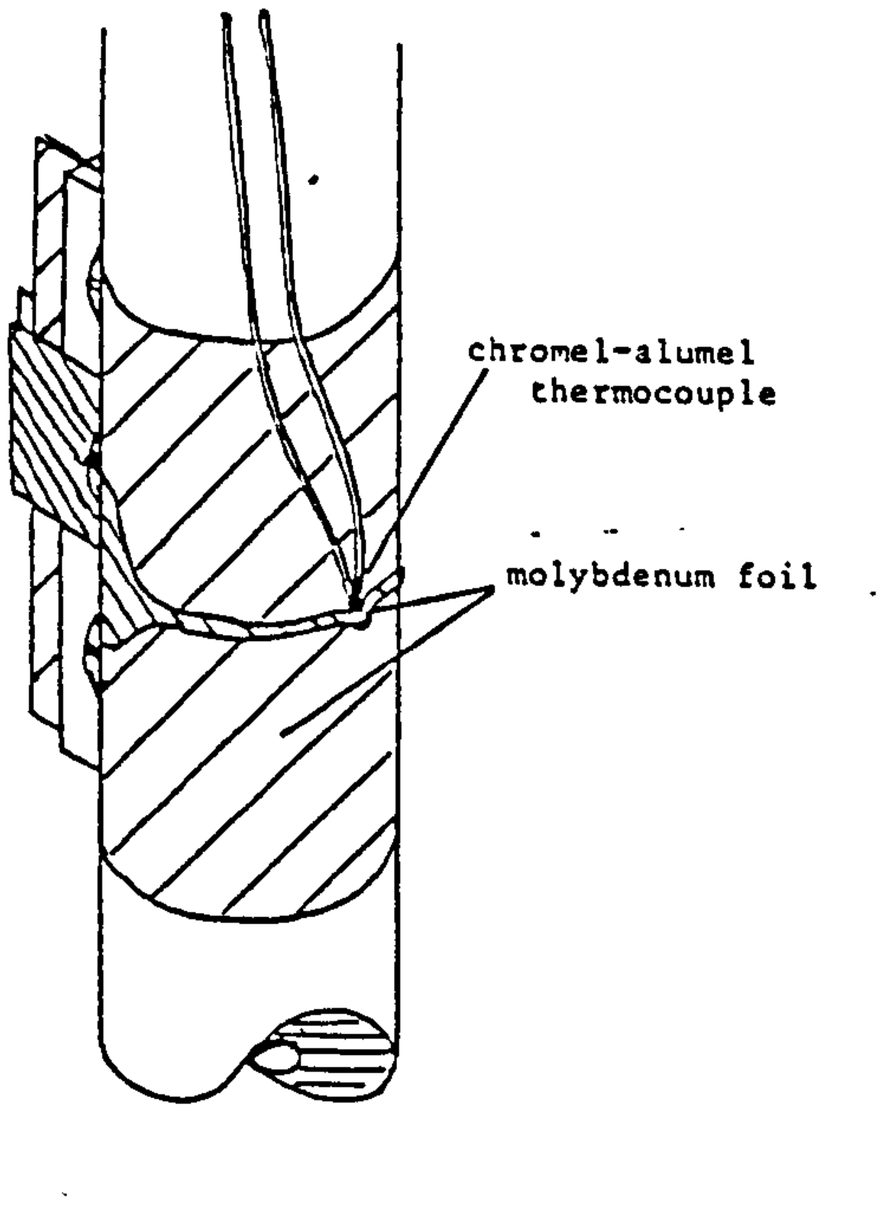

Figure 4.8: The mounting of the silica cells

The circuit consists of twelve relays each of which may be selected through the relay interface circuit. Relays 1-4 are connected to the four thermocouples. Each thermocouple has its own cold reference junction. These are maintained at 0 $°C$ using an ice-water bath. Relay 5 to 7 measured the thermoelectric voltages generated across the chromel wires and corresponded to the voltage developed across electrodes 1-4, 2-4, and 3-4 respectively. Relays 8-10 were wired in a similar manner but measured the voltage across the molybdenum electrodes. Relay 11 was used to measure the potential difference between electrode 2 and 3 when a current was passed through the sample. Relay 12 measured the voltage developed across a nominal 1 Ω resistor in the current source and was used for calibrating the current source. Relays 1-10 were supplied by Keithley Ltd., on a purpose built circuit board(model 7029) and had a guaranteed thermal offset of less than 3 μV. There was also a guard rail to eliminate voltage errors caused by any leakage currents. The output of these relays was connected to the voltmeter.

The temperature controllers have their own cold junction compensation and were connected directly to the thermocouples. Computer control of the temperature was achieved by superimposing an additional voltage onto the thermocouple signal before it was passed to the temperature controllers. This was achieved by passing a small current through a portion of the thermocouple wire before the temperature controller itself. By changing this current with a digital to analogue converter, a temperature offset of 0 to 256 $°C$ with a 1 $°C$ step range could be achieved. This did not produce any observable errors in the temperature readings.

The current source was also constructed using a digital to analogue converter, and could generate currents between +0.3 and −0.3 A in steps of approximately 2.5 mA. In the experiment the current was passed through a nominal 1Ω resistor and the sample itself. The voltage dropped across this resistor approximately gave the current flowing through the circuit in amps. This was a useful check to ensure that the sample connections were not open circuit.

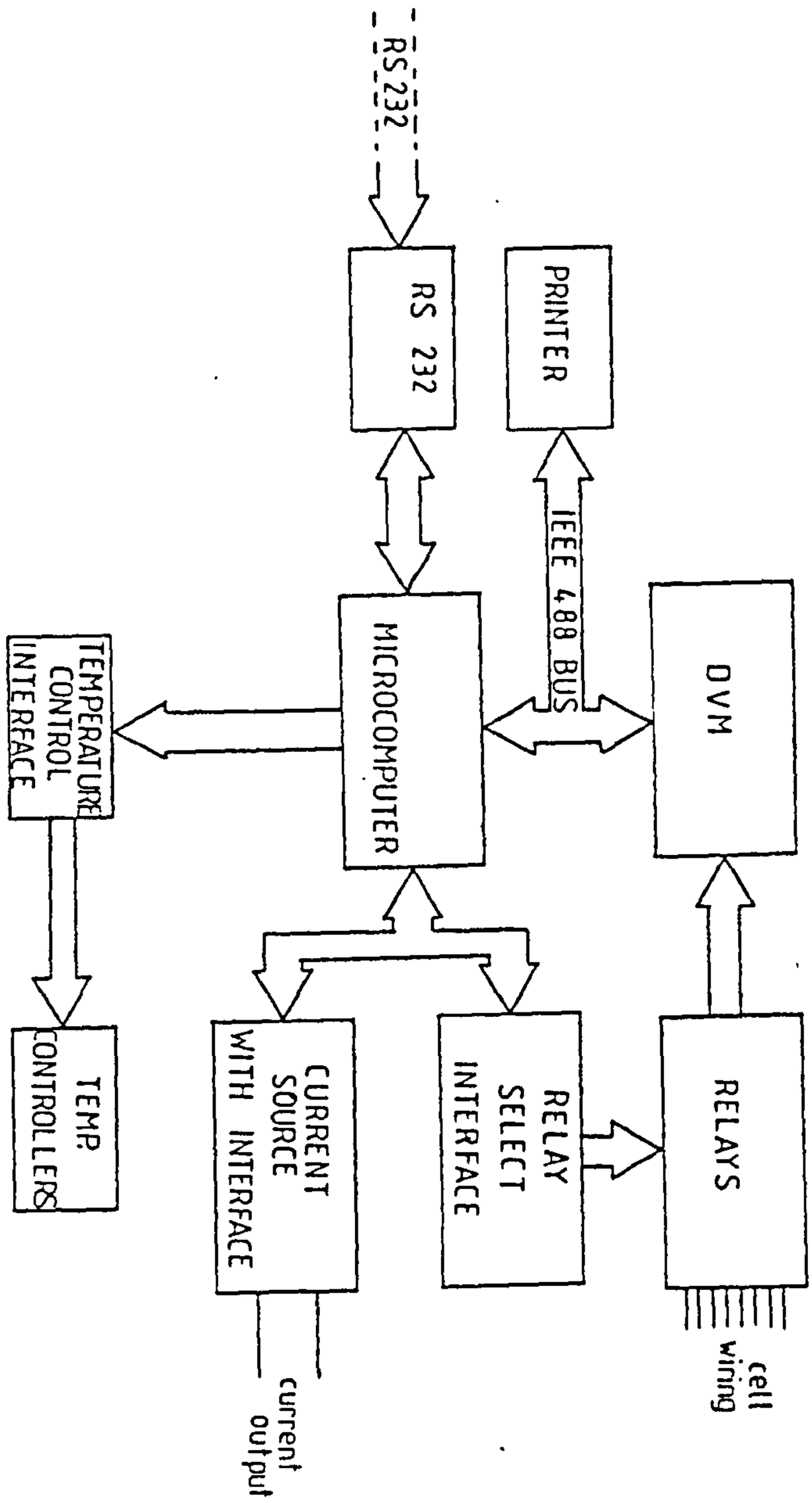

Figure 4.9: Schematic diagram of the computer control system

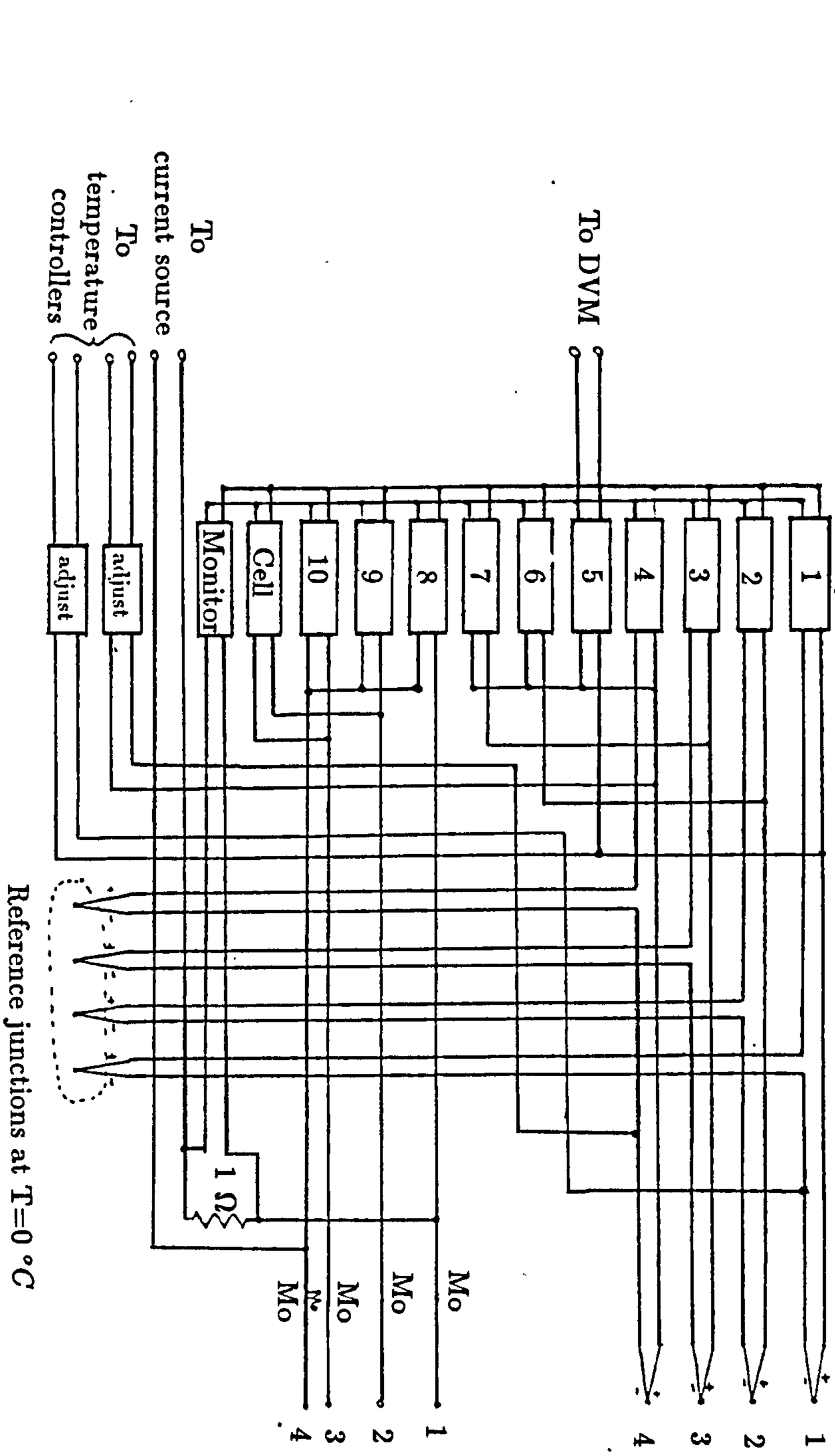

Figure 4.10: Electronic and thermocouple wiring of the furnace

4.3 Calibration of the cell and the current source

In order to produce accurate results for the conductivity the cell had to be calibrated. This was achieved by filling the completed cell with liquid mercury and making a series of measurements. The output from the current source is given by expression of the form

$$I_N = aN - b \tag{4.10}$$

where N is a number between 0 and 255 selected by the microcomputer. a and b are characteristic constants of the current source. When calibrating the current source the voltage generated across the $R_R = 1\Omega$ resistor was monitored. This voltage is given by an expression of the form

$$V_N = I_N \times R_R = aR_RN - bR_R = \alpha N - \beta \tag{4.11}$$

By selecting values of N, and measuring V_N, the computer was programmed to determine α and β by a least squares fitting procedure. The nominal 1 Ω resistor had a very small variation of resistance with temperature. After calibrating the current source a similar process was used to measure the voltages produced across the mercury sample by the current source. These are given by

$$V_{HN} = I_N \times R_H = \frac{V_N R_H}{R_R} = (\alpha N - \beta)\frac{R_H}{R_R} \tag{4.12}$$

where R_H is the resistance of liquid mercury between the two electrodes. The resistance of the liquid mercury will be determined by some geometrical cell constant and its resistivity (ρ_H). This may be expressed as

$$R_H = c\rho_H \tag{4.13}$$

The gradient of the above equation can be determined from a least squares fit to a straight line and a value of R_R/c is calculated. This is the calibration constant. During the experiment, α and β were redetermined to eliminate any changes in the

current source characteristics with time. Then using these redetermined values α' and β', the voltages across the sample are given by

$$V_{SN} = (\alpha' n - \beta')\frac{R_S}{R_R} = (\alpha' N - \beta')\frac{c\rho_S}{R_R} \tag{4.14}$$

where R_S is the sample resistance, and ρ_S the sample resistivity. Again by selecting values of N and measuring V_{SN}, the computer could fit a straight line to this function and determine the gradient (G). This is given by

$$G = \frac{c\alpha'\rho_S}{R_R} \tag{4.15}$$

using this expression and inserting the calibration constant the conductivity ($1/\rho_S$) of the sample could be determined.

4.4 Data collection and analysis

With the twin zone furnace the temperature of the top and bottom electrodes could be controlled independently by the computer. This enables the computer to measure the thermoelectric voltages and conductivity as a function of temperature automatically. During these measurements the screen displayed the temperature for each thermocouple, and the most recent measurements. The conductivity was determined from a least squares fit to the voltage produced by 100 values of the primary current. As each measurement was taken the temperature and results were output to a printer for a permanent record of the results, and written into the computer memory. At the end of each experiment the microcomputer was connected directly to a mainframe computer and data transferred. The data was then analysed.

The conductivity was determined immediately by the BBC, as the data was gathered. The results were output together with an estimation of the random errors from the least squares fit. The Conductivity data needed no further processing.

For the thermopower readings, only the thermoelectric voltages and the temperature were recorded. The thermopower was determined from these measurements after the experiment. The absolute thermopower was obtained from equation (4.9).

Although the bottom electrode was held at a 'constant' temperature, the temperature controllers could only maintain the set temperature to within $\pm 0.5\ ^{o}C$. This caused offset errors in the Seebeck voltage when referred to the steady junction temperature. To compensate for this error the difference in temperature between the two electrodes was calculated. The top junction temperature was then taken as the reference temperature plus this difference. From these values of T and the voltages measured (V) a smooth curve was fitted to the points to give a function of V vs. T. A cubic was generally fitted to the points using orthogonal(Chebyshev) polynomials. From this fit the dV/dT vs. T could be calculated. The absolute thermopowers of molybdenum and chromel were taken from Blatt and Schroeder (1976) and Newport (1979) respectively. To give an indication of the errors in this calculation, straight lines were fitted to the data for point covering 20 ^{o}C intervals. These were then used to give a thermopower measurement for the centre of the 20 ^{o}C interval. These points are plotted along with the fitted line in the results.

4.5 Experimental procedure

After the cell had been calibrated the mercury was emptied from it. The cell was then cleaned using concentrated nitric acid to remove any trace of mercury. It was then rinsed with water and dried by rinsing with methanol and acetone. The sample was then loaded into the cell. The cell was then mounted into the sample chamber and the top plate gently lowered. At this stage the wiring was checked for any short circuits. With the apparatus sealed, the sample chamber and sample cell were evacuated. To remove water from the apparatus, the furnace temperature was raised to 200 ^{o}C. The system was left pumping overnight. Before raising the temperature further, argon was flushed through the apparatus several times. For the experiments the apparatus was filled with argon at a pressure of 0.8 bar.

To start the experiment the temperature of the furnace was raised to approximately 50 ^{o}C above the liquidus temperature of the sample. At this stage the sample

should have filled the bottom of the cell. If necessary the sample was stirred using the tungsten rod to assist this process. After the starting temperature had been reached the system was allowed to stablise for 1 hour. The first step in the experiment was to redetermine the current source constants. At this stage the electrical continuity of the sample could also be checked. After this process was completed, a single measurement of the conductivity of the sample was made. Because the thermopower measurement was critically dependent on the accuracy of the thermocouples these experiments were made first. This minimised any problems due to the drift of the thermocouple readings through chemical attack. These measurements were made by maintaining the bottom electrode at a constant temperature and then increasing the temperature of the top electrode at 5-10 ^{o}C intervals. At each temperature step, the Seebeck voltages at each electrode were measured. The maximum temperature difference used was 100 ^{o}C. After these measurements the temperature of the top and bottom electrodes was equalised and conductivity measurements made. These were made at 5 ^{o}C or 10 ^{o}C intervals. The measurements were generally continued until the cell failed. At the finish of the experiment the furnace was switched off and the apparatus evacuated to remove any noxious gases. The system was then opened to the air and the cell removed. The cell was checked for signs of excessive attack or any other form of failure that might invalidate the results.

During a single experiment the composition of the sample could be changed by adding one of the components through the loading valve. After the loading the sample was stirred using the tungsten rod. The sample was then kept for about 1 hour to stablise before the next measurement.

4.6 Errors

Great care was taken in constructing the apparatus to minimise the errors produced. However, several sources of errors should be considered.

4.6.1 Sample composition

The error in sample composition after preparation was very small ($\pm 0.1\%$). However, during the experiment there was a tendency for the chalcogenide to boil off. their error was estimated to be no more than $\pm 1\%$ after lasting 3 days. This could be checked as a conductivity changed with time.

4.6.2 Temperature

The thermocouples had a quoted accuracy of $\pm 0.5\ ^{o}C$. In the experiments it was found that the chromel-alumel thermocouples underread as they became contaminated. This was typically about 5 ^{o}C after 3 days. The thermopower measurements were always made first to avoid errors produced by this effect. This error is not critical for the conductivity measurements.

4.6.3 Conductivity

The errors produced from the calibration were estimated at $\pm 0.5\%$. The greatest source of error in the measurements was due to bubbles in the sample. These always have the effect of giving a value of the conductivity below the true reading. This error is difficult to estimate. This effect could be noticed by reducing the pressure over the sample and observing the conductivity change or by the change in conductivity after stirring. From these observation the errors produced by this process were estimated to be $\pm 2\%$. This is the dominant error in these measurements.

4.6.4 Thermopower

The error in the thermopower of the reference electrodes was a systematic error on all the results presented and is 1 in $\mu V K^{-1}$. The main error in the thermopower measurements is through mispositioning of the thermocouples and any temperature gradient that may be produced across the graphite. The placement accuracy of

the thermocouple was estimated as ± 1 mm for the chromel-alumel thermocouple. This should give errors in the thermopower of ±1.5%. The errors due to spurious thermoelectric voltage were estimated at ±0.5%. Errors due to the contamination of the reference materials were determined by measuring the Seebeck voltages of used Mo or Chromel wires against unused wires. In this manner the maximum change in the reference electrode thermopowers was found to be 0.3 μVK^{-1}. The total random error in the thermopower measurements is estimated to be about 2% for the measurements with Chromel-Alumel thermocouples.

4.7 Sample preparation

The chemical elements Se, Cu, Te, Tl, Bi and Mg were purchased from Johnson Matthey Ltd, UK. They have the purity of Se (99.999%), Cu (99.999%), Te (99.999%), Tl (99.999%), Bi (99.99%), Mg (99.98%). The compounds CuCl and TlCl were purchased from Aldrich Chemical Company Inc. Their purity is >99% for CuCl and 99% for TlCl. All the elements used are in form of granules or shots, and the compounds in form of fine powder.

The components were weighed to an accuracy of 0.1 mg. The chlorides were weighed in the glove box to prevent moisture absorption. The elemental materials were then mixed and sealed in quartz ampoules under vacuum. The quartz ampoule was put into the furnace and heated up to 50-100 ^oC above the liquidus temperature. This was carried out for at least 5 hours. After this process the samples were cooled in the furnace to the room temperature. The samples were extracted by cracking the ampoule open and removing the bullets. These bullets were convenient for loading into the sample cell.

Mg-Bi samples could not be prepared in this way as the magnesium reacted severely with the quartz at the high temperature. The granules of magnesium and bismuth were put directly into the alumina sample cell of 6mm diameter. The compound was allowed to form at the experimental temperature for at least 6 hours

to make it homogeneous before the measurement. The degree of homogeneity could be checked by observing changes of the conductivity with time.

Chapter 5

Experimental Facilities and Data Analysis For the Neutron Scattering Measurements

5.1 Neutron scattering facility

All the neutron scattering experiments in this work were undertaken at ISIS facility at the Rutherford Appleton Laboratory (RAL). The following instrument data is mainly from User Guide (Boland, 1990).

5.1.1 Neutron source

ISIS is a high intensity spallation neutron source which is primarily based on a 800 MeV high intensity proton synchrotron. The design intensity is 2.5×10^{13} protons per pulse at a pulse rate of 50 H_Z (200μA mean current). The protons hit a uranium target to produce $\sim 4\times10^{16}$ fast neutrons per second. Four moderators close to the target (two ambient water moderators above and one methane at 100 K and one liquid hydrogen at 25 K below the target) slow the fast neutrons down to epithermal and thermal velocities, yielding pulse widths in the range 1 - 100 μs. The moderated

neutrons pass through one of 18 holes in the massive shield of the target assembly to the instruments either directly or through neutron guides.

5.1.2 Neutron scattering instrument

The neutron scattering measurements in this work were performed on the instruments LAD and SANDALS, respectively.

(1). LAD

LAD (Liquid and Amorphous materials Diffractometer) is a total scattering instrument optimised for the study of amorphous solids and liquids. A schematic diagram of LAD is shown in Fig.5.1. Its specifications and instruments are

Specification:

Incident Wavelength	Typically 0.1 - 7.0 $\mathring{A}$
Momentum Transfer	0.2 - 100 $\mathring{A}^{-1}$
Resolution $\Delta Q/Q$	From 0.5% (150°) to 10% (5°)

Instrument:

Moderator	100K CH_4
Sample Position	10m From Moderator
Beam Size	40mm×20mm
Count Rate	$5\times 10^3(5°)$, $7\times 10^4(150°)$
Detectors	10 atm ^3He at 1m at 5°, 10°, 150°
	Scintillator Banks at 20°, 35°, 58°, 90°

(2). SANDALS

SANDALS (Small Angle Neutron Diffraction for Amorphous and Liquid Samples) is a second generation total scattering instrument for the measurement of structure factors of amorphous solids and liquids. There is an extensive low angle bank of detectors which together with the use of high energy neutrons gives a wide Q range, while minimising the inelastic(Placzek) corrections.

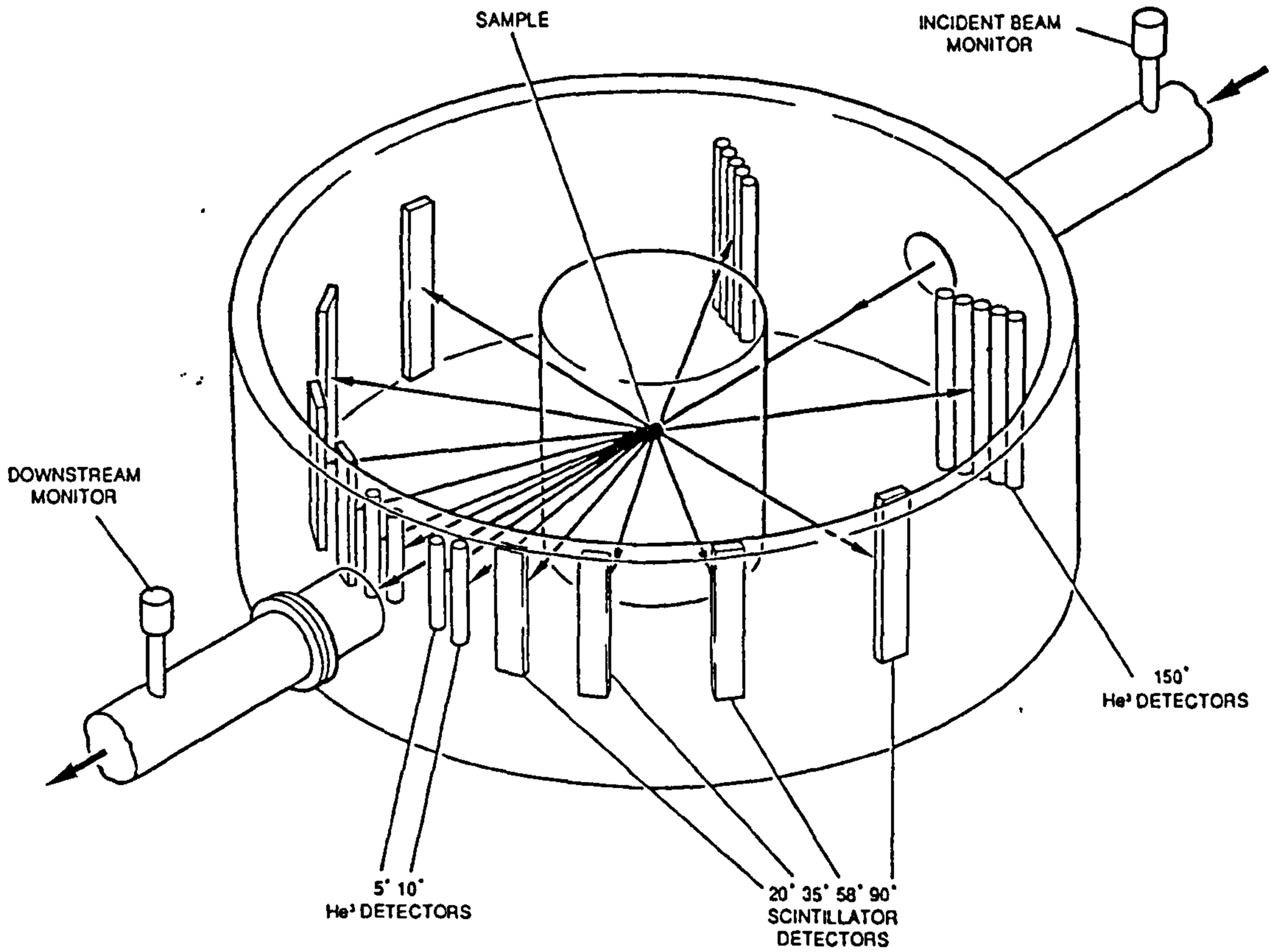

Figure 5. 1: A schematic diagram of LAD

A schematic diagram of SANDALS is shown Fig.5.2. Its specifications and instruments are

Specification:

Incident Wavelength	Typically 0.05 - 4.0 $\AA$
Momentum Transfer	0.05 - 50 $\AA$
Resolution $\Delta Q/Q$	0.01 - 0.2

Instrument:

Beam	N1
Sample Position	11m from moderator
Beam Size	Typically 30mm in diameter

Detectors:

Zinc sulphide scintillator detectors, typically 10 mm wide × 20 mm deep × 200 mm tall. The detectors are arranged in four banks which cover the scattering angle range 3° - 40° in a continuous span. Each bank is divided into modules of 20 detectors each. The detectors in the range $11^\circ - 40^\circ$ are arranged on a surface of constant resolution. The design allows for the provision of detectors up to a scattering angle of 120° when the demand warrants them. A higher resolution, lower count rate option is provided to give a factor of 2 increase in resolution.

5.2 Furnace and sample containers

The measurements were performed at an elevated temperature using a standard RAL furnace. The furnace was mounted at the centre of the diffractometer. The heating element consisted of a cylindrical tube made from vanadium foil with a nominal 0.1mm thickness. It was heated electrically under a vacuum of at least 10^{-5} Torr.

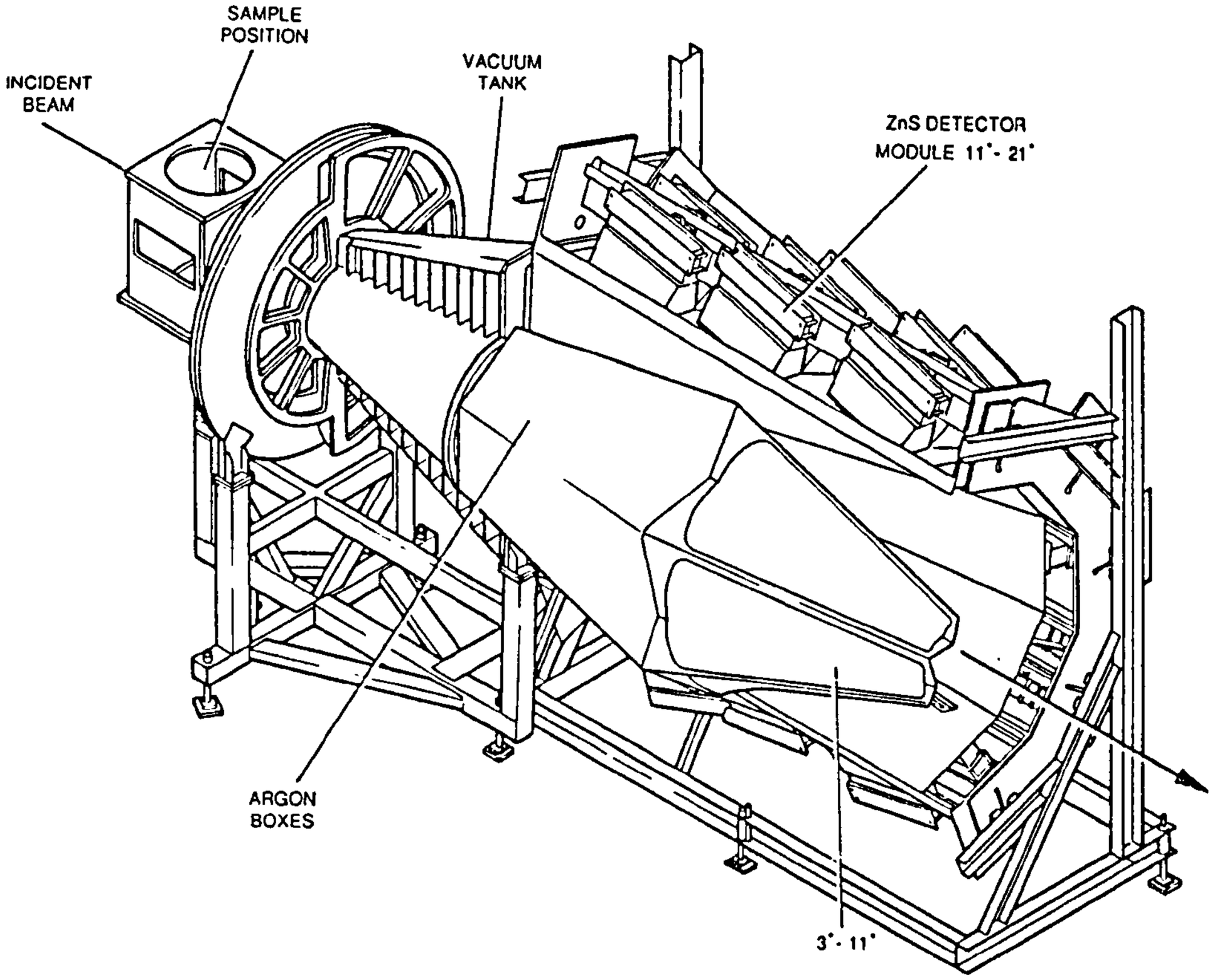

Figure 5. 2: A schematic diagram of SANDALS

Samples of $CuCl - Cu_2Se$ and Tl_2Se were sealed under vacuum in silica tubes with an outside diameter of approximately 5mm which were mounted in a cylindrical vanadium holder with an outside diameter of 10mm and a thickness 0.02mm. The Mg_3Bi_2 sample was sealed directly in the vanadium holder. The temperature of the furnace was measured and controlled by two thermocouples located at the top and bottom of the sample tube.

5.3 The time-Of-flight neutron diffraction experiment

There are seven principal components in a time-of-flight neutron diffraction experiment: (1) production of neutrons in a target; (2) slowing down and thermalisation in a moderator; (3) collimation of the neutrons into a beam; (4) a sample to scatter the neutrons; (5) a detector to analyse the diffraction pattern of the scattered neutrons; (6) a set of data acquisition electronics(DAE) in which the data are stored, initially in fast memory and eventually on computer memory, and finally (7) a data analysis package.

The production of neutrons at ISIS is achieved by accelerating bunches of protons to sufficiently high energies (typically 500-800 MeV) so that when they collide with a target nucleus they produce highly excited nuclear states which decay either immediately or after a delay by throwing off nuclear particles such as neutrons , γ particles, neutrinos, etc. The proton beam is pulsed so that a neutron pulse less than $1\mu s$ wide is produced in the target. These neutrons are not useful however because they typically have energies (wavelength) 10^9 times too high for diffraction effects to be seen. Therefore they are slowed down in a moderator, which scatters the neutrons many times before they escape. Light atoms such as hydrogen-containing materials are used for the moderator since the energy transferred in a collision is greatest when the two particles have the same mass. The neutrons emerge from the moderator in

all directions and so to be useful for diffraction they must be collimated. An essential difference between TOF and reactor diffraction is that there is no monochromator for the TOF experiment which means the full of spectrum of neutron energies, from 800 MeV downwards, is incident on the sample. The collimator defines a neutron beam at the sample position. The scattered neutrons from the sample are detected using one or two types of detector; ^3He gas or scintillators. The data acquisition electronics (DAE) is used to record each neutron event and give it a label corresponding to the number of the detector in which it occurred and its time of arrival at the detector. The clock which measures this time of arrival is started by an electronic pulse which is generated when the burst of protons hits the target. Once the label is generated, a word of memory corresponding to the label is incremented. In this way a histogram of events is built up. The experiment is controlled by a front end minicomputer(FEM) which is a computer to store, manipulate and display the data. After transmission through the sample the unscattered neutron and other particles are absorbed in a beam stop.

The time of arrival, t_0, of a neutron at detector is given by its time-of-flight (TOF) which is the time (in μs) taken by the neutron to travel 1m, multiplied by the total flight path (L) in m. Some relationships can be written down between the neutron's TOF (μs/m), velocity v (in m/s), wavelength λ (in $\mathring{A}$), wavevector (in $\mathring{A}^{-1}$) and energy E (in meV), thus

$$\text{v (m/s)} = 10^6/\text{TOF } (\mu\text{s/m})$$

$$\lambda\ (\mathring{\text{A}}) = 0.0039562\text{TOF} = 0.0039562t_0\ (\mu\text{s})/\text{L (m)}$$

$$t_0\ (\mu s) = 252.77\ \lambda\text{L}$$

$$\text{k } (\mathring{A}^{-1}) = 2\pi/\lambda = 1588.2/\text{TOF}$$

$$\text{E (meV)} = 81.807/\ \lambda^2.$$

In the experiment the scattered intensity is measured as a function of TOF which in turn is proportional to wavelength. In practice, it is represented by the above

relationship as a function of the momentum transfer $\hbar$Q, where for elastic scattering

$$Q = \frac{4\pi sin\theta}{\lambda} \tag{5.1}$$

where 2θ is the scattering angle.

5.4 Experimental procedures

The experimental procedures consisted of :

1. measuring the background intensity without the furnace or sample in place;
2. measuring the scattered intensity from the furnace alone;
3. measuring the scattering from an empty sample tube with the vanadium sample holder and furnace in place;
4. measuring the scattering intensity from a vanadium rod 6mm in diameter with the furnace in position. This was used for the calibration of the sample scattering;
5. measurement of the scattering from the samples themselves.

5.5 Data analysis

The purpose of the data analysis is first, to derive the Time-of-flight Differential Cross Section of the sample (TDCS), $\sum(Q_e, \theta)$, from a set of diffraction data; second, to estimate and subtract the single atom scattering which has no structural information; and last, to derive the radial distribution function (RDF). The data analysis procedures consisted of six main steps : (1). data from equivalent detectors are summed and normalised to monitor count; (2). calculation of the neutron cross section; (3). attenuation and multiple scattering correction; (4). vanadium calibration; (5). merging the data from different detectors to form the structure factor; (6). analysis to radial distribution function.

The data analysis of the neutron scattering experiments was carried out using the data analysis programme package ATLAS (Soper, Howells and Hannon, 1989) and a Fourier Transform programme FOURBRIS (University of Bristol).

5.5.1 Normalisation

The data collected from different detectors are summed and corrected for deadtime. Then the data is normalised to the incident spectrum, which is measured by means of a monitor detector, and combined into the final spectrum after converting from the time-of-flight to wave vector transfer, Q ($Q_e = 2k_e \sin\theta$). A second measurement which is made at the same time as the scattered count rate from the sample is the fraction of neutrons transmitted by the sample. This number is monitored by a transmission monitor placed after the sample. This can provide information on the neutron cross section and density of the sample.

The normalised count rate, NRM(Q_e), and the transmitted intensity, MON(k_e), are obtained:

$$\begin{aligned} NRM(Q_e) &= I(k_e)/I_m(k_e) \\ &= N\sum(Q_e)\frac{E_d(k_e)}{E_m(k_e)}\Delta\Omega \end{aligned} \tag{5.2}$$

$$\begin{aligned} MON(k_e) &= I_t(k_e)/I_m(k_e) \\ &= T(k_e)\frac{E_t(k_e)}{E_m(k_e)} \end{aligned} \tag{5.3}$$

where $I(k_e)$, $I_m(k_e)$ and $I_t(k_e)$ are the detected count rate, monitor detector count rate and transmission count rate, respectively. $\Delta\Omega$ is the detector solid angle. $\sum(Q_e)$ is the TDCS of the sample. $E_d(k_e)$, $E_m(k_e)$ and $E_t(k_e)$ are the detector efficiency, monitor efficiency and transmission monitor efficiency, respectively. $T(k_e)$ is transmission of the sample.

5.5.2 The neutron cross section

The transmission of the sample is dependent on the total neutron cross section of the sample. For any shape of sample the flight path through the sample is a function of position within the beam. If x measures the perpendicular distance from one edge of the beam then the transmission in this case can be written as

$$T(k_e) = \int_0^W \frac{exp[-\rho\sigma_t(\lambda)]dx}{W} \tag{5.4}$$

where W is the width of the beam. From the above equation the total neutron cross section, $\sigma_t(\lambda)$, can be determined because the transmission $T(k_e)$ is known. $\sigma_t(\lambda)$ $= \sigma_s(\lambda) + \sigma_a(\lambda)$, where $\sigma_s(\lambda)$ is scattering cross section and $\sigma_a(\lambda)$ is capture cross section at $\lambda = 1.8\mathring{A}$.

5.5.3 Attenuation and multiple scattering correction

The scattered neutrons in the sample experience an attenuation due to absorption and multiple scattering. The multiple scattering must be removed from the measured scattering intensity. These can be corrected by several methods. The method of Soper and Egelstaff (1980) is used in this analysis. In my experiments in which a sample, container and furnace were used, three experiments were carried out : sample+can+furnace, $I_{SCF}(k_e)$, empty can+furnace, $I_{CF}(k_e)$, and furnace alone, $I_F(k_e)$. These three quantities are each affected by attenuation and multiple scattering and related to the corresponding TDCS by:

$$\begin{aligned} I_{SCF}(k_e) &= \Phi(k_e)[N_S \sum_S (Q_e)A_{F,SCF} + N_C \sum_C (Q_e)A_{C,SCF} \\ &+ N_F \sum_F (Q_e)A_{F,SCF} + M_{SCF}(K_e)]E_d(k_e)\Delta\Omega \end{aligned} \tag{5.5}$$

$$\begin{aligned} I_{CF}(k_e) &= \Phi(k_e)[N_C \sum_C (Q_e)A_{C,CF} + N_F \sum_F (Q_e)A_{F,CF} \\ &+ M_{CF}(k_e)]E_d(k_e)\Delta\Omega \end{aligned} \tag{5.6}$$

$$I_F(k_e) = \Phi(k_e)[N_F \sum_F (Q_e)A_{F,F} + M_F(k_e)]E_d(k_e)\Delta\Omega \tag{5.7}$$

Where $\Phi(K_e)$ is the incident flux. N_S, N_C, and N_F are the number of atoms in the sample, container and furnace in the beam, respectively. The $A_{S,SCF}$, $A_{C,SCF}$, etc are the usual Paalman Pings (1962) attenuation factors. For example, $A_{S,SCF}$ is the attenuation factor for scattering in the sample and attenuation in the sample+can+furnace. The quantities M_{SCF}, M_{CF} and M_F are the total multiple scattering differential scattering cross section for the sample+can+furnace, can+furnace and furnace alone respectively.

5.5.4 Vanadium calibration

A unique characteristic of neutron scattering is the ability to perform an independent measure of the instrumental calibration using Vanadium, which gives almost perfect incoherent scattering. This allows all scattering cross sections to be normalised absolutely by reference to a Vanadium bar of similar geometry in the beam. This calibration consists of the unknown quantities,

$$F_2(k_e) = \frac{E_d(k_e)}{E_m(k_e)}\Delta\Omega \tag{5.8}$$

The normalised spectrum from vanadium is defined as

$$NRM_V(Q_e) = F_2(k_e)[N_V \sum_V (Q_e) A_{V,V} + M_V(k_e)] \tag{5.9}$$

the quantity in square bracket is the vanadium differential cross section which is estimated using exactly the same method as in the previous section. This leads to a vanadium calibration, $CAL_V(Q_e)$, thus

$$\begin{aligned} CAL_V(Q_e) &= NRM_V(Q_e)/[N_V \sum_V (Q_e) A_{V,V} + M_V(k_e)] \\ &= F_2(k_e) \end{aligned} \tag{5.10}$$

5.5.5 Basic algorithm to determine differential cross section

The following is the algorithm to determine the TDCS from the TOF diffraction data. The symbol TOTAL applies to the total scattering, SINGLE applies to the

single scattering, and the suffixes S, C, and B refer to sample, can and background. The sequence is:

(1). Subtract background

$$TOTAL_{SCF}(Q_e) = NRM_{SCF}(Q_e) - NRM_B(Q_e) \tag{5.11}$$

$$TOTAL_{CF}(Q_e) = NRM_{CF}(Q_e) - NRM_B(Q_e) \tag{5.12}$$

$$TOTAL_F(Q_e) = NRM_F(Q_e) - NRM_B(Q_e) \tag{5.13}$$

(2). Normalise to calibration

$$TOTAL_{SCF}(Q_e) => TOTAL_{SCF}(Q_e)/CAL_V(Q_e) \tag{5.14}$$

$$TOTAL_{CF}(Q_e) => TOTAL_{CF}(Q_e)/CAL_V(Q_e) \tag{5.15}$$

$$TOTAL_F(Q_e) => TOTAL_F(Q_e)/CAL_V(Q_e) \tag{5.16}$$

(3). Subtract multiple scattering

$$SINGLE_{SCF}(Q_e) = TOTAL_{SCF}(Q_e) - M_{SCF}(k_e) \tag{5.17}$$

$$SINGLE_{CF}(Q_e) = TOTAL_{CF}(Q_e) - M_{CF}(k_e) \tag{5.18}$$

$$SINGLE_F(Q_e) = TOTAL_F(Q_e) - M_F(k_e) \tag{5.19}$$

(4). Subtract furnace from sample and can

$$SINGLE_{SC}(Q_e) = SINGLE_{SCF}(Q_e) - SINGLE_F(Q_e)\frac{A_{F,SCF}}{A_{F,F}} \tag{5.20}$$

$$SINGLE_C(Q_e) = SINGLE_{CF}(Q_e) - SINGLE_F(Q_e)\frac{A_{F,CF}}{A_{F,F}} \tag{5.21}$$

(5). Apply absorption corrections

$$SINGLE_S(Q_e) = \frac{SINGLE_{SC}(Q_e) - SINGLE_C(Q_e)\frac{A_{C,SCF}}{A_{C,CF}}}{A_{S,SCF}} \tag{5.22}$$

(6). Divide by number of atoms in sample

$$TDCS(Q_e) = \frac{SINGLE_S(Q_e)}{N_S} \tag{5.23}$$

5.5.6 Merging the data to form S(Q)

We have obtained the TDCS which is typically recorded at several scattering angles in a TOF diffraction experiment. For example, on LAD there currently 14 groups of detectors, 7 on each side of the instrument. These separate measurements have different Q ranges and need to be regrouped into one, final TDCS covering the full Q range. A typical approach might be as follows:

1. plot all the spectra on top of each other

2. For each group choose a range of Q values over which this spectrum overlaps with at least one spectrum from a neighbouring group at higher or lower scattering angle. Eliminate any spectra that are inconsistent (this might be due to changes in detector efficiencies, background problems, etc...).

3. merge the selected spectra over the selected Q range. Combine them into one composite structure factor $S(Q)$.

The merging of spectra is achieved by weighting each spectrum with the intensity with which it was measured. The weighting function is obtained from corrected intensity data of the vanadium sample contained in the quantity

$$W_J(Q_e) = CAL_V(Q_e)I_m(k_e) \tag{5.24}$$

where the suffix J is used to label the J'th group of detectors. Hence if $\sum_J(Q_e)$ is the measured differential cross section for the J'th group, the merged differential cross section is obtained by forming the sum

$$\sum_M(Q_e) = \frac{\sum[\sum_J(Q_e)W_J(Q_e)]}{\sum W_J(Q_e)} \tag{5.25}$$

5.5.7 Analysis to radial distribution function

The structure factor $S(Q)$ is given by

$$S(Q) = 1 + 4\pi\rho/Q \int_0^\infty rdr(g(r) - 1)sin(Qr) \tag{5.26}$$

The inversion of the $S(Q)$ data to radial distribution function $g(r)$ was done using numerical Fourier transform method.

5.6 Reverse Monte Carlo computer simulation

The radial distribution function derived from the above process can provide us with the coordination numbers and positions and shape of the peaks which are used in analysis of structure of the system. It is difficult to understand the three dimensional structure of the materials, especially from the data at total structure factors level. In order to assist in understanding diffraction data, the reverse Monte Carlo computer simulation (RMC) technique (McGreevy and Pusztai, 1988 ,and McGreevy, Howe, Nield, Wicks and Keen, 1991) has been tried in this work. This produces a three dimensional model of the structure based on the experimental data, from which further structural information may be deduced.

The conventional approach to an understanding of liquid structure can be summarised as follows:

Diffraction experiment

↓

Structure factor S(Q)

↓

Radial distribution function g(r)

↑

Molecular simulation MC, MD

↑

Interatomic potential

The experimental and simulation results may then be compared with each other in one dimensional g(r). If the comparisons are in good agreement the three dimensional structure produced by the simulation could be examined. There are two disadvantages to this approach. Firstly it is difficult to establish a potential that adequately

reproduces the experimental results. Secondly there is structural information that is apparent in $S(Q)$, for instance the peaks at low Q values, that is not apparent in $g(r)$ since it involves small oscillations with a long r period. The reverse Monte Carlo (RMC) method alleviate some of these problems. It is a method for producing three dimensional models of structure of disordered materials based on experimental diffraction data, either $S(Q)$ or $g(r)$. No interatomic potential is required and data from different sources (X-rays, neutrons, EXAFS) may be combined.

5.6.1 RMC - the basic method

RMC is a variation of the standard Metropolis Monte Carlo (MMC) procedure. The principle of MMC is that we wish to produce a statistical ensemble of atoms (configuration) with a Boltsmann distribution of energies. Rather than simply generating and sampling configurations completely at random, a weighted sampling procedure (Markov chain) is used to satisfy certain requirements. In RMC it is assumed that an experimentally measured structure factor $S^E(Q_i)$ contains only statistical errors that have a normal distribution. The difference between the real structure factor, $S^C(Q_i)$, which can be calculated from a model of the real structure, and that measured experimentally is then

$$e_i = S^C(Q_i) - S^E(Q_i) \tag{5.27}$$

and has probability

$$p(e_i) = \frac{1}{\sqrt{2\pi}\sigma(Q_i)} exp\left(-\frac{e_i^2}{2\sigma(Q_i)^2}\right) \tag{5.28}$$

where $\sigma(Q_i)$ is the standard deviation of the normal distribution. The total probability of S^C is

$$\begin{aligned} P &= \prod_{i=1}^{m} p(e_i) \\ &= \left(\frac{1}{\sqrt{2\pi}\overline{\sigma}}\right)^m exp\left(-\sum_{i=1}^{m} \frac{e_i^2}{2\sigma(Q_i)^2}\right) \end{aligned} \tag{5.29}$$

where m is the number of Q_i points in S^E and

$$\overline{\sigma} = \left(\prod_{i=1}^{m} \sigma(Q_i) \right)^{1/m} \tag{5.30}$$

In order to model the structure of a system using S^E we therefore wish to create a statistical ensemble of atoms whose structure factor satisfies the above probability distribution. Writing the exponent in Equation 5.28 as

$$\chi^2 = \sum_{i=1}^{m} (S^C(Q_i) - S^E(Q_i))^2 / \sigma(Q_i)^2 \tag{5.31}$$

then $P \propto exp(-\chi^2/2)$ and it can immediately be seen that $\chi^2/2$ in RMC is equivalent to U/kT in MMC. The algorithm for RMC is given as follows:

1. Start with an initial configuration with periodic boundary conditions. The positions of the N atoms can be chosen either randomly, or from a known crystal structure, or a configuration from a different model.

2. Calculate the radial distribution function for this old configuration

$$g_0^C = \frac{n_0^C(r)}{4\pi r^2 \Delta r \rho} \tag{5.32}$$

where $n_0^C(r)$ is the number of atoms at a distance between r and $r + \Delta r$ from a certain atom, averaged over all atoms as centres and ρ is the number density. The configuration size L should in principle be sufficiently large that there are no correlations across the cell, so that $g(r > L/2)$=1. The radial distribution function $g(r)$ is only calculated for $r < L/2$ and the nearest image convention is used to determine the atomic separations.

3. Transform to the total structure factor

$$S_0^C(Q) - 1 = \frac{4\pi\rho}{Q} \int_0^\infty r(g_0^C(r) - 1) sinQr dr \tag{5.33}$$

where Q is the momentum transfer.

4. Calculate the difference between the measured total structure $S^E(Q)$ and that determined from the configuration $S^C(Q)$

$$\chi_0^2 = \sum_i (S^C(Q_i) - S^E(Q_i))^2 / \sigma(Q_i)^2 \tag{5.34}$$

where the sum is over the m experimental points and $\sigma(Q_i)$ is the experimental error. In practice a uniform σ is normally used since the distribution of systematic errors is unknown.

5. Move one atom at random. calculate the new radial distribution function, $g_n^C(r)$ and total structure factor, $S_n^C(Q)$, and

$$\chi_n^2 = \sum_i (S_n^C(Q_i) - S_n^E(Q_i))^2 / \sigma(Q_i)^2 \tag{5.35}$$

6. If $\chi_n^2 < \chi_0^2$ the move is accepted and the new configuration becomes the old configuration. If $\chi_n^2 > \chi_0^2$ then the move is accepted with probability $exp(-(\chi_n^2 - \chi_0^2)/2)$. Otherwise it is rejected.

7. Repeat from step 5.

As this process is iterated χ^2 will initially decrease until it reaches an equilibrium value above which it will fluctuate. The resulting configuration should be a three dimensional structure that is consistent with the experimental total structure factor within experimental error. Statistically independent configurations may then be collected.

5.6.2 multiple data sets

The algorithm described in the previous section is specially for modelling a single set of diffraction data which could be obtained using either neutrons, X-rays or electrons. For a multi-component system where the fit is to several different total structure factors $S(Q)$ (indicated by index k) it has

$$\chi^2 = \sum_k \chi_k^2 = \sum_k \sum_{i=1} (S_k^C(Q_i) - S_k^E(Q_i))^2 / \sigma_k(Q_i)^2 \tag{5.36}$$

For neutron diffraction

$$S_k^E(Q_i) = \sum_\alpha \sum_\beta c_\alpha c_\beta \overline{b_{\alpha k}}\ \overline{b_{\beta k}}(S_{\alpha\beta}(Q_i) - 1) \tag{5.37}$$

where c_α is the concentration and $\overline{b}_{\alpha k}$ the coherent scattering length for species α in sample k. $S_{\alpha\beta}(Q_i)$ are the partial structure factors.

Chapter 6

The Structural and Electronic Properties of the Mg-Bi System

6.1 Introduction

As stated in chapter 2, the pseudogap models and BE theory can explain the observed electronic properties of a variety of liquid semiconducting alloys whose conductivity is characterised by a minimum value at stoichiometry. It rationalises the apparent conflict between a 'semiconductor' description (positive $d\sigma/dt$ and a clear p-n transition of the thermopower) and a 'metallic' description (relatively small Hall coefficients and significant Knight Shifts). Accordingly, the broad ($\Delta E < 0$) and narrow ($\Delta E > 0$) definitions of liquid semiconductors can be clearly separated.

The BE theory based on the rigid band can not however, explain the electronic properties of the liquid Mg-Bi system at and near to the stoichiometric composition Mg_3Bi_2. Enderby and Collings (1970) measured the conductivity and thermopower of liquid Mg-Bi. It was pointed out by Enderby and Barnes (1990a) that this system shows unusual electronic properties. The conductivity shows a very deep minimum at stoichiometry which would imply a large conductivity gap, ΔE, and consequently a very large value of ΔS ($> 400\ \mu V K^{-1}$) at the p-n transition. The observed

transition over quite a large composition range was in fact only ΔS=20 $\mu V K^{-1}$. On the other hand, for Mg-Bi amorphous films a large p-n transition ($\Delta S = 200 \mu V K^{-1}$ at 200 K) in the thermopower has been observed at stoichiometry (Ferrier and Herrell, 1969 and 1970, and Ferrier, 1974). Mott and Davis (1979) have interpreted these results in terms of the pseudogap model.

Theoretically, the sharp p-n transition is predicted to occur within 1 or 2 *at.*% over stoichiometry using the BE theory. The data of Enderby and Collings were only taken at 5 *at.*% intervals. It is therefore entirely possible that the large thermopower values associated with the transition were missed. In order to confirm the strange properties of liquid Mg-Bi a further detailed study of the electronic properties of Mg-Bi system in the vicinity of stoichiometry is necessary. It is of particular interest for a better understanding of electronic conduction process in liquid semiconductors especially as a test of the Kubo-Greenwood relations.

The aims of this work were

1. confirming the unusual properties by making more careful measurements at composition intervals as small as possible and comparing the experiments with theoretical calculation.

2. trying to obtain a better understanding of the electronic properties of the liquid through the structural studies.

Careful measurements of the conductivity and thermopower of Mg-Bi in the vicinity of the stoichiometric composition Mg_3Bi_2 have been carried out at an interval of 0.5 *at.*%. Theoretical calculations of conductivity and thermopower were made using the BE theory. The structures of Mg_3Bi_2, $Mg_{2.9}Bi_{2.1}$ and $Mg_{3.1}Bi_{1.9}$ samples were determined by means of neutron scattering on the LAD diffractometer at ISIS. The diffraction data was further treated using reverse Monte Carlo computer simulation.

6.2 The electronic properties of Mg-Bi system

6.2.1 Measurements of conductivity and thermopower

The conductivities and thermopowers of Mg-Bi in the vicinity of the stoichiometric composition Mg_3Bi_2 at intervals of 0.5 $at.\%$ and at a temperature of 920 ^oC are shown in Fig. 6.1 and 6.2, respectively. The temperature dependence of the conductivity is shown in Fig.6.3. It is clear that the conductivity shows a deep minimum at stoichiometry Mg_3Bi_2 and is very sensitive to a small changes of the composition. As the composition changes by 1 $at.\%$ away from stoichiometry, the conductivity jumps by almost two order of magnitudes, while the thermopower changes slowly and steadily across stoichiometry from the negative, Mg-rich side, to the positive, Bi-rich side at a speed of about 2 μV^oC^{-1} for 1 $at.\%$ of composition changes. The temperature coefficient $d\sigma/dT$ in the vicinity of stoichiometry is positive, showing semiconducting behaviour.

6.2.2 Theoretical determination of the conductivity and thermopower

The electronic properties of Mg-Bi system were calculated under different conditions using the Kubo-Greenwood equations and a generic $N(E)$ model (Barnes, 1993) which has been reviewed in chapter 2. The calculation for composition dependence of conductivity σ, thermopower S and chemical potential μ (the Fermi energy at a finite temperature) were made at the compositions near stoichiometry Mg_3Bi_2 where the rigid band picture might be expected to be a good approximation. The band gap and mobility edge in the calculations were chosen by considering of two typical situations:

1. $E_g = E_{cl} - E_{vh}$ was given as 0.4 eV according to the optical measurement for annealed amorphous Mg_3Bi_2 compound by Watson *et al* (1984). Given E_g=0.4 eV, the mobility edge was considered for two cases:

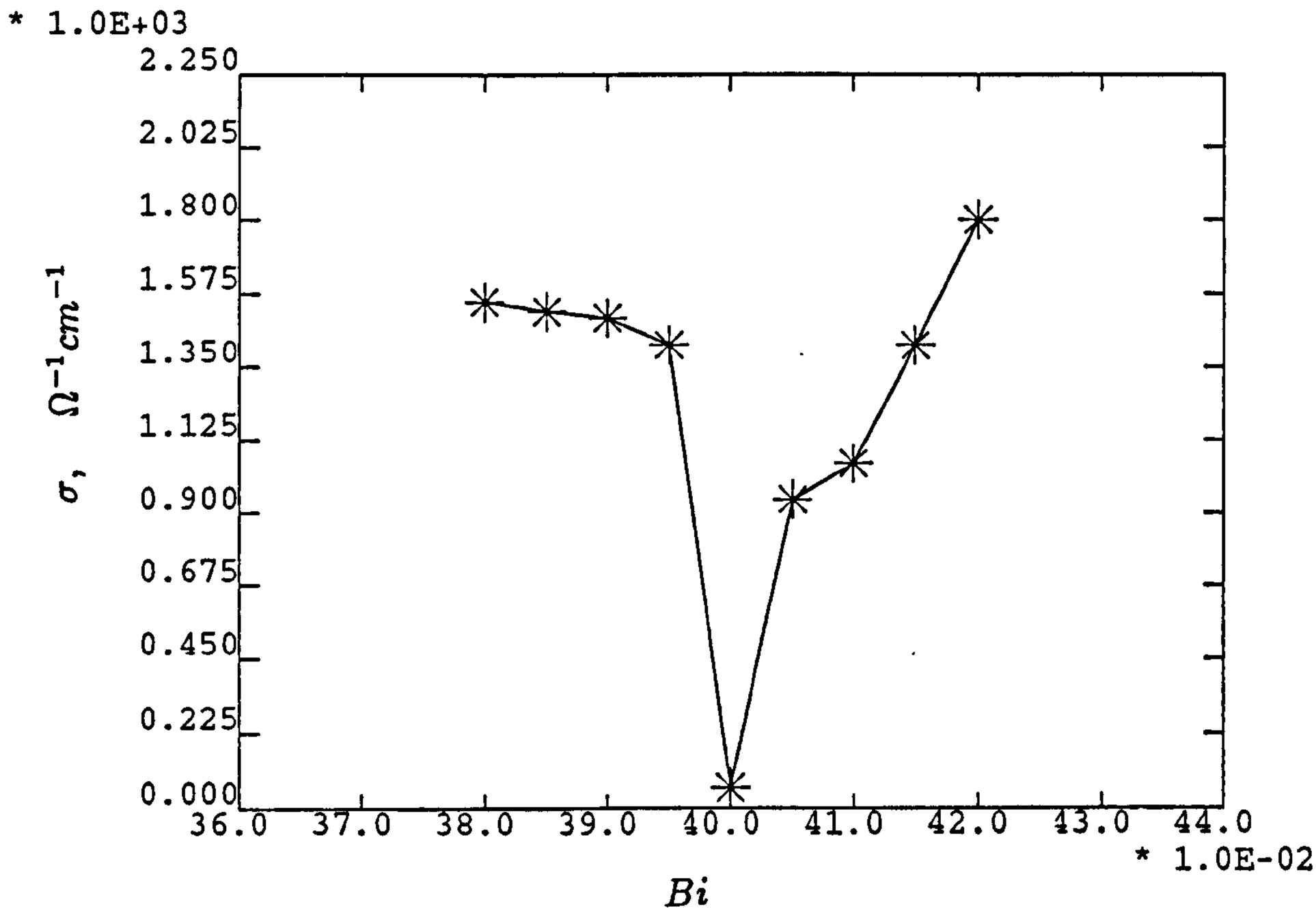

Figure 6.1: The conductivity of liquid $Mg-Bi$ as a function of composition at 920 ^oC.

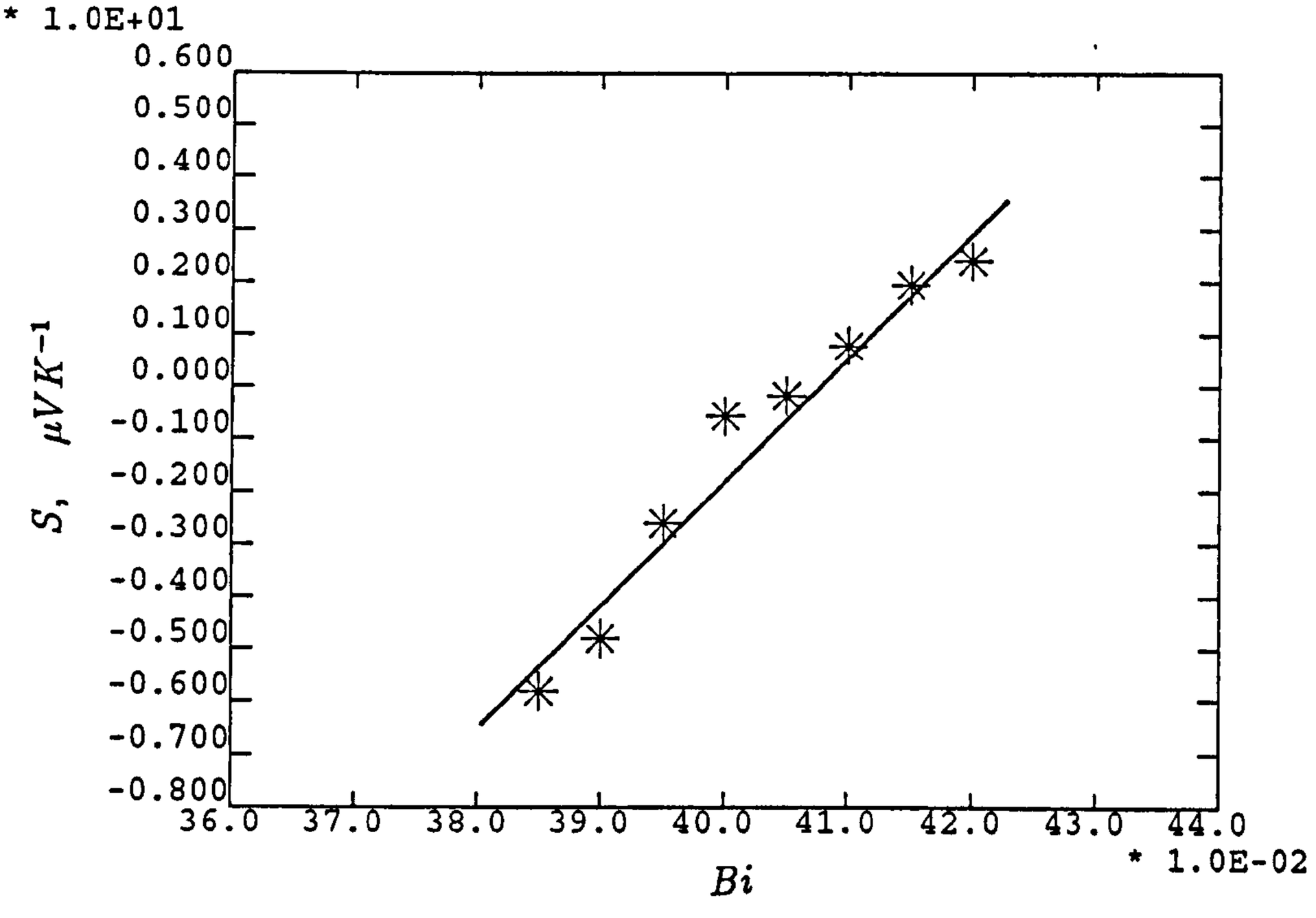

Figure 6.2: The thermopower of liquid $Mg-Bi$ as a function of composition at 920 ^oC.

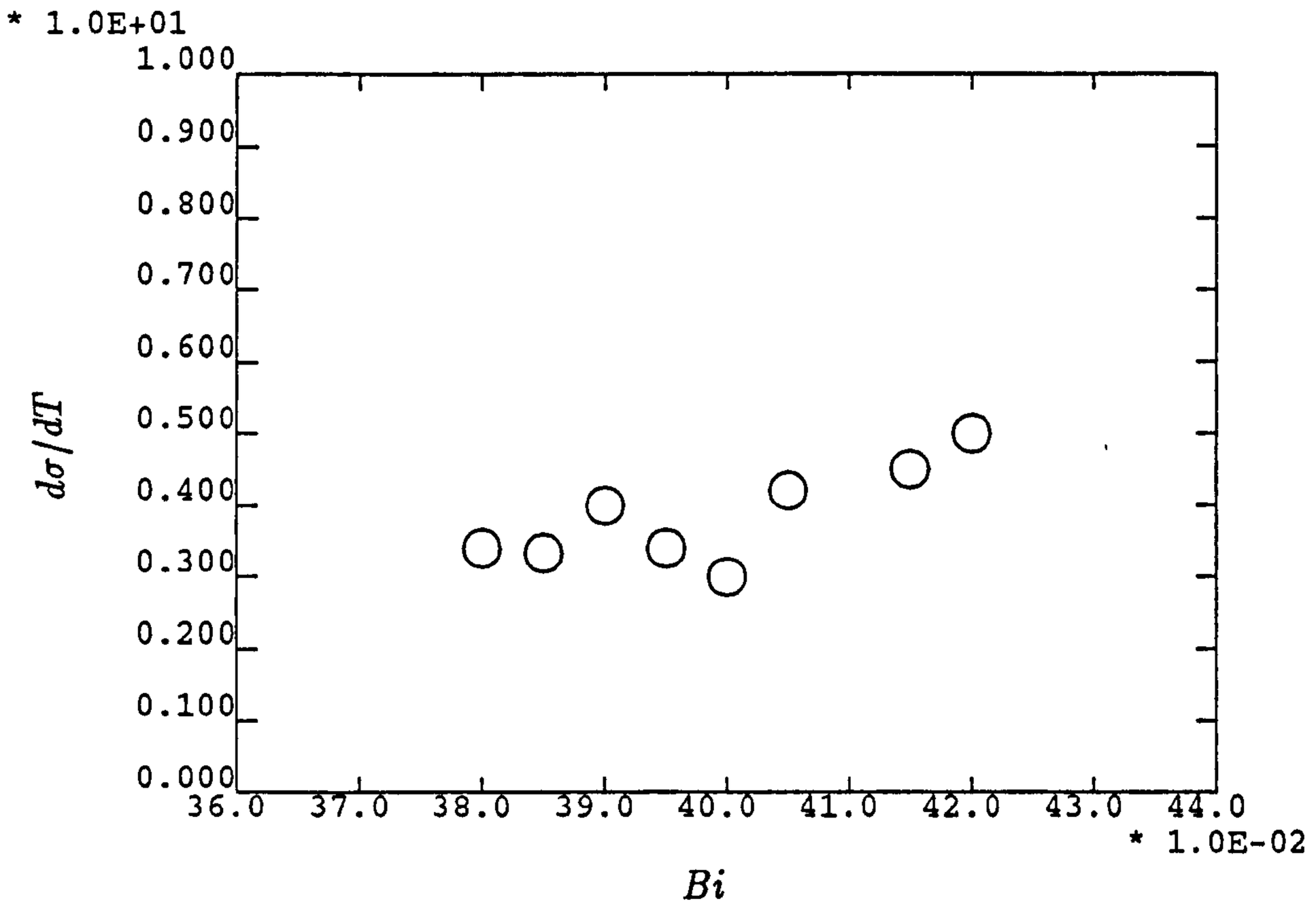

Figure 6.3: The temperature dependence $d\sigma/dT$of the conductivity of liquid $Mg - Bi$ as a function of composition.

i) no electron localisation occurs in the bands, the mobility edge is equal to the band edge, $E_V = E_{vh}$ and $E_C = E_{cl}$; ii) that electron localisation occurs, the mobility edges were chosen as $E_V = E_{vh} - 0.1$ and $E_C = E_{cl} + 0.1$.

2. the band gap was chosen as just closed, $E_C = E_V$, $E_g = 0$. This is an extreme case for semiconductors. For the zero band gap the mobility edge was chosen the same as the above.

The calculated conductivity, thermopower and chemical potential as a function of the composition at 1200 K are drawn in Fig.6.4, 6.5 and 6.6, respectively. It can clearly be seen that at stoichiometry the conductivity shows a minimum and the thermopower has a sharp p-n transition. For the bigger band gap the conductivity minimum is much deeper, but show a broader dependence with composition. The thermopower behaves in a similar way to the conductivity, but depends more strongly on the band gap. The p-n transition of thermopower for the band gap of 0.4 eV is four times larger than that for the zero gap. The mobility edge gives the same effects as the band gap. Beyond the composition range of about 5 % away from the stoichiometry the effect of the mobility edges and band gap disappears in the calculations.

6.2.3 Comparison between the experiment and calculation

Two major differences can be seen when comparing the experimental data in Fig.6.1 and Fig.6.2 with the calculations in Fig.6.4 and 6.5 :

1. The experimental data shows a much deeper and steeper minimum for conductivity than that of the calculations for compositions in a range $\pm$ 1 $at.\%$ about stoichiometry.

2. The p-n transition of the experimental thermopower ($\Delta S \simeq 8\ \mu V K^{-1}$) is far smaller than the calculated value ($\Delta S \simeq 650\ \mu V K^{-1}$) as the composition of

Bi changes from 38 % to 42 %. Even for $E_g = 0.0\ eV$ the p-n transition for the calculation is still much larger than the experimental data.

In conclusion, the electronic properties of liquid $Mg-Bi$ near the stoichiometric composition shows a very different behaviour from, for example, other quasi-ionic semiconducting compound, like Tl_2Te whose electronic properties could be understood by BE theory. The results of these experiments support the conclusions of Enderby and Barnes, (1990) that Mg-Bi has special electronic properties. It has not been possible to reproduce this behaviour using a theoretical model based on rigid band behaviour, which suggests that the electronic structure of Mg_3Bi_2 changes rapidly on moving away from stoichiometry.

6.3 Neutron diffraction

Because of the special electronic properties of Mg-Bi system the thermochemical , thermodynamic and structural properties have been well studied (Cohen and Sak, 1972; Michael *et al.*, 1979 and Egan, 1959). Michael *etc.* (1979) measured , at the total structure level, the structures of liquid Mg-Bi with the Bi compositions from 10 *at.*% to 100 *at.*% at intervals of 10 % using X-ray and neutron diffraction. All the evidence shows that there is chemical ordering at the stoichiometric composition Mg_3Bi_2. Studies of the structure close to stoichiometry have not yet been made. The following experiments were made to overcome the lack of information.

In this work neutron scattering measurements of three samples (Mg_3Bi_2, $Mg_{3.1}Bi_{1.9}$, $Mg_{2.9}Bi_{2.1}$) were performed using LAD at the Rutherford Appleton Laboratory, UK. The measurements were made at the total structure level because suitable isotopes are not available. Reverse Monte Carlo computer simulations were employed to further analyse the diffraction data to obtain the structure factors at the partial level which could better give the evidence for the local interactions and the bonding properties.

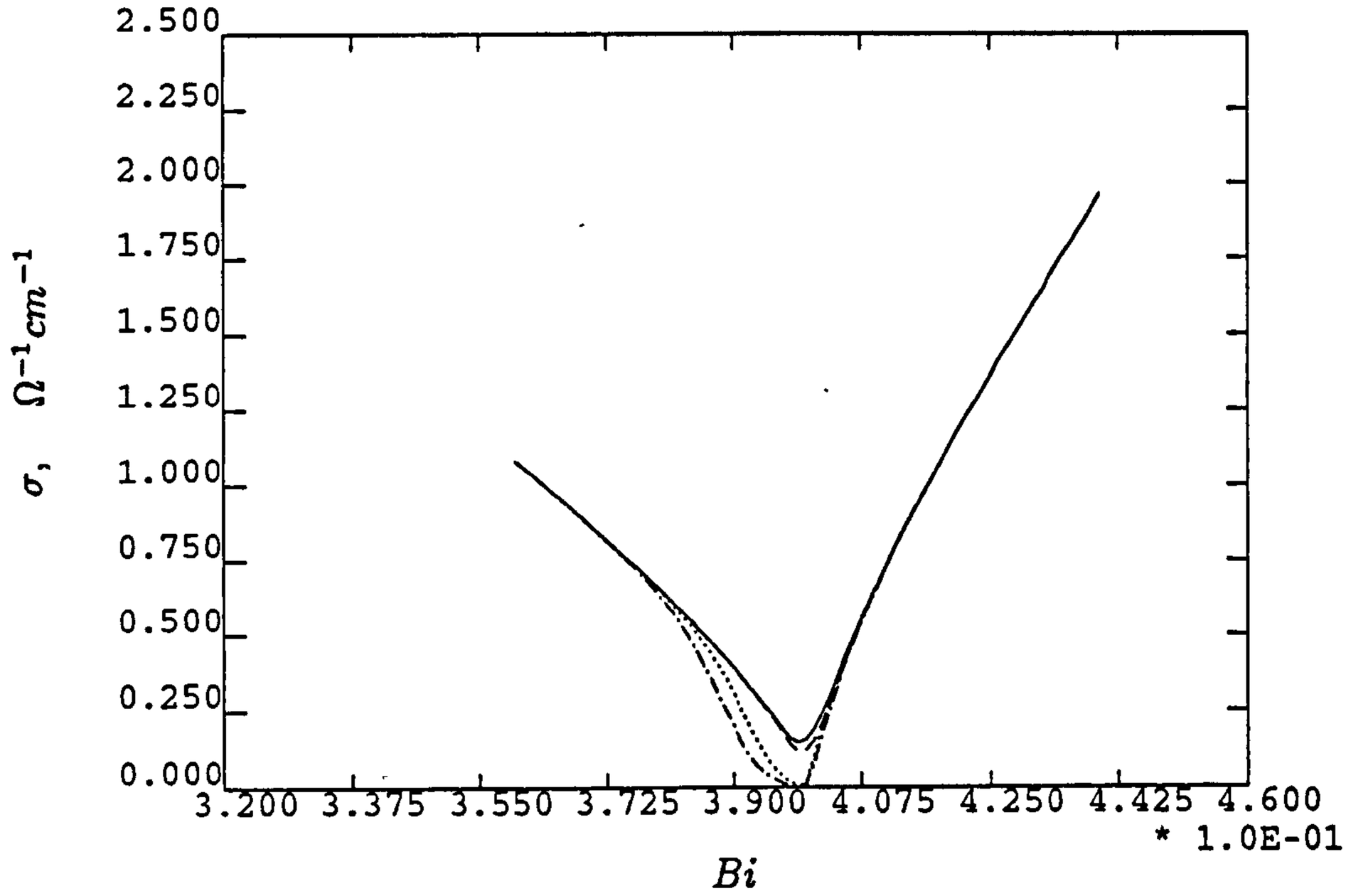

Figure 6.4: The calculated conductivity of liquid $Mg - Bi$ as a function of composition. Full line - $E_g = 0.0$ $E_V = E_C = 0.0$; Broken line - $E_g = 0.0$ $E_V = -0.1$ $E_C = 0.1$; Dotted line - $E_g = 0.4$ $E_V = 0.0$ $E_C = 0.4$; Dot-dash line - $E_g = 0.0$ $E_V = -0.1$ $E_C = 0.5$, where the valence band edge is used as zero coordination. T=900 ^oC.

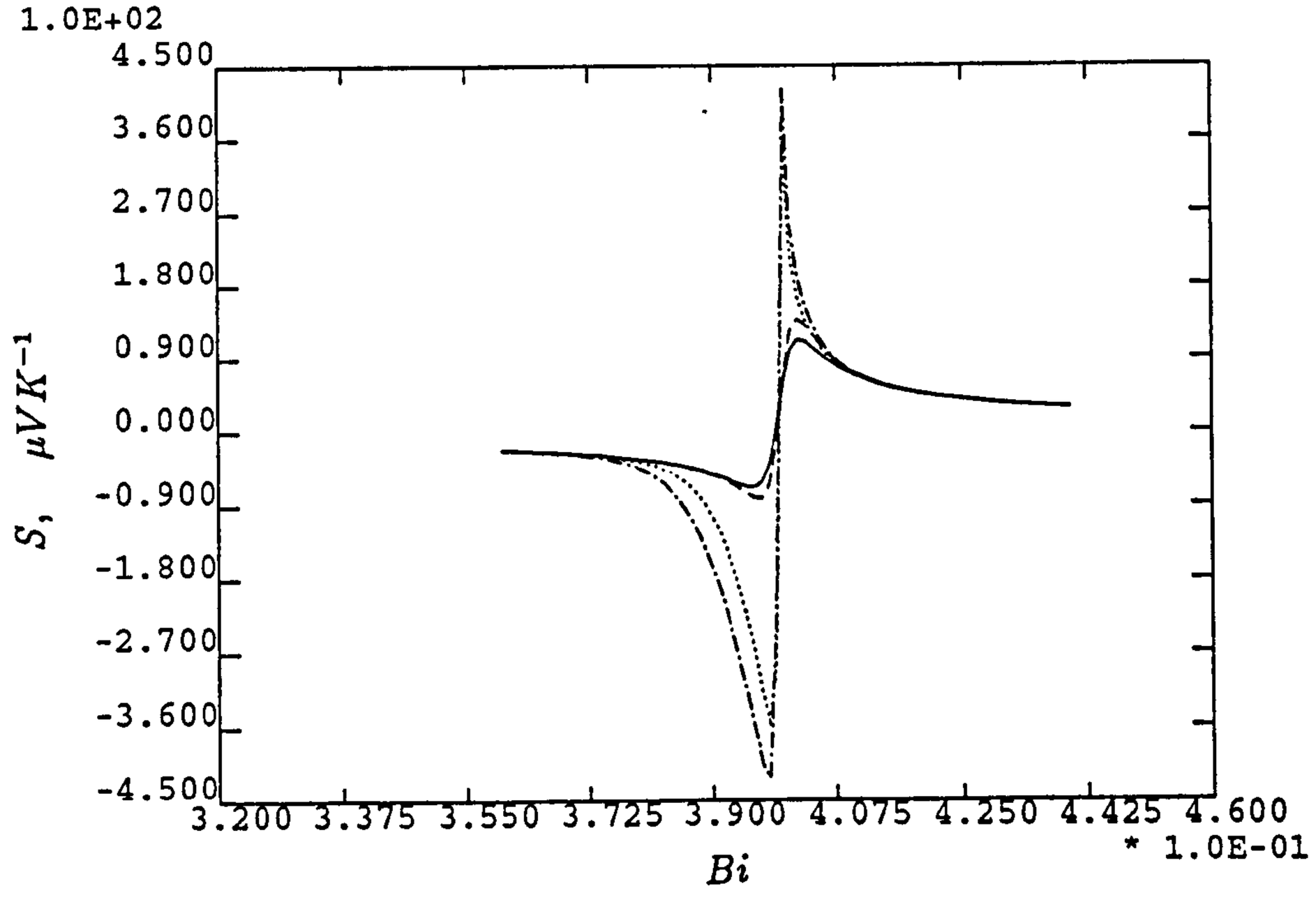

Figure 6.5: The calculated thermopower of liquid $Mg - Bi$ as a function of composition. The conditions are the same as Fig. 6.4.

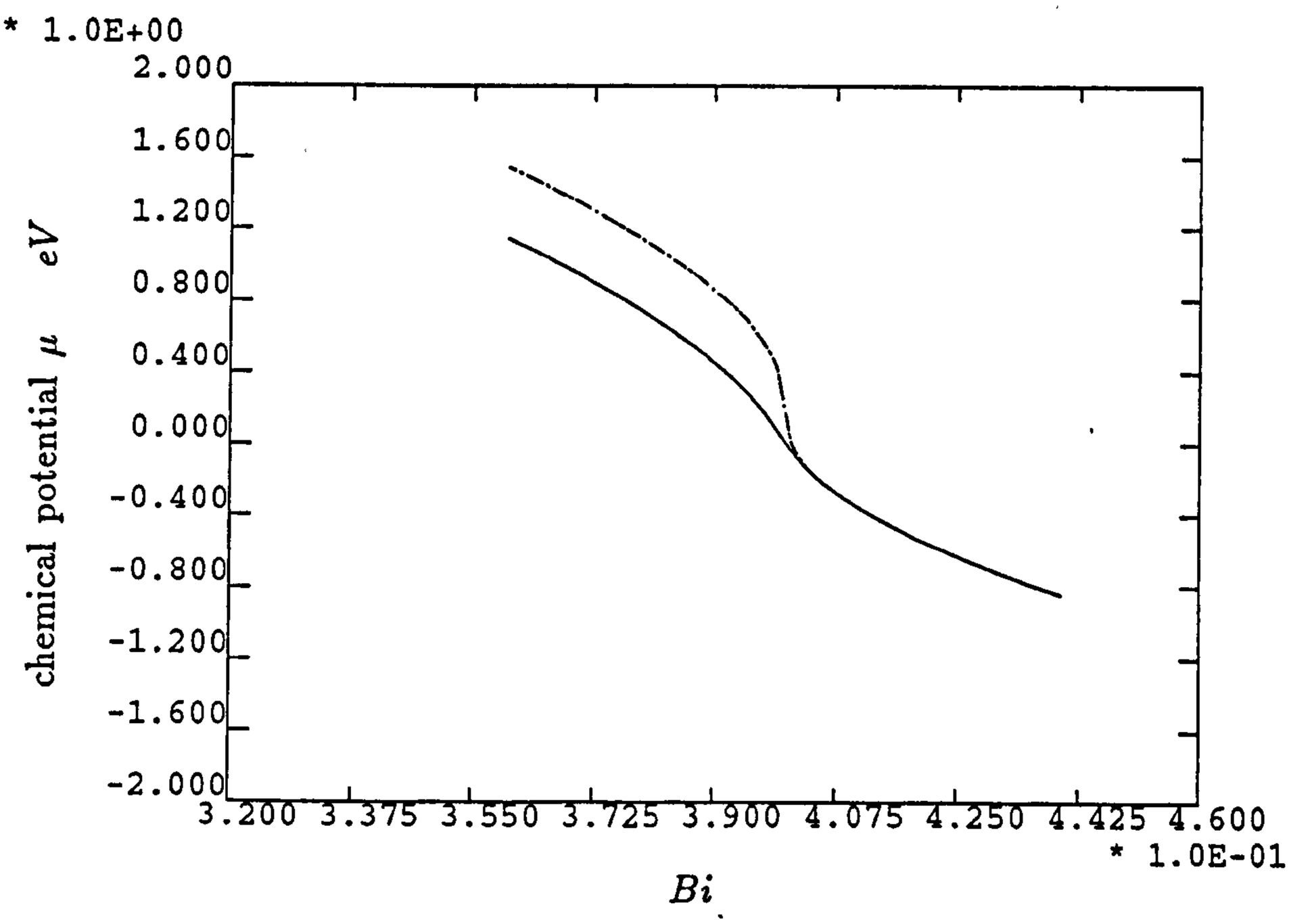

Figure 6.6: The calculated chemical potential of liquid $Mg-Bi$ as a function of composition at 900 $^{\circ}C$. Full line - $E_g = 0.0$; Dot-dash line - $E_g = 0.4$.

6.3.1 Diffraction of the solid α- and β-phase of Mg_3Bi_2

The phase diagram of Mg-Bi system is reproduced in Fig.6.7. It can be seen that the compound Mg_3Bi_2 has a polymorphic phase transformation with increasing temperature. The α-phase transforms to the β - phase at a temperature of 703 ^oC and melts congruently at 821 ^oC. The α-phase has hexagonal lattice with a = b =4.675 c = 7.415 Å and $\alpha = \beta = 90^o$, $\gamma = 120^o$. The structure of the β-phase has not been determined to date. Enderby and Barnes (1990a) showed that crystal structure of a material just below its melting point is often closely related to the structure of liquid. It is therefore of particular importance to study the structure of the β phase in order to understand the liquid.

6.3.1.1 Experimental results

Neutron diffraction measurements on these two phases were carried out at temperature 150 ^oC and 740 ^oC, respectively. The diffraction patterns obtained from the α-phase and β-phase for the LAD 150° angle is shown in Fig. 6.8 as a function of d-spacing. The diffraction peaks of the α-phase are tagged according to the trigonal ($p\bar{3}ml$) structure reported by Zintl and Husemann (1933) and show a good agreement with reported structure. There is a very clear change on moving to the β-phase. It is immediately apparent that in this phase there is a high symmetry structure which is characterised by a large diffuse background. Figure 6.9 shows the structure factors of the α- and β-phase as a function of momentum transfer Q along with the diffraction pattern of the sample after melting. Figure 6.10 shows the radial distribution functions obtained by direct Fourier transform of the fully corrected β-Mg_3Bi_2 data along with the liquid phase. It is apparent that the β phase is characterised by Bragg peaks of a periodic structure on a liquid like background. Clear similarities between the diffuse background in the β phase and the liquid are observed.

Table 6.1 shows the d-spacings for the diffraction peaks observed in the β phase.

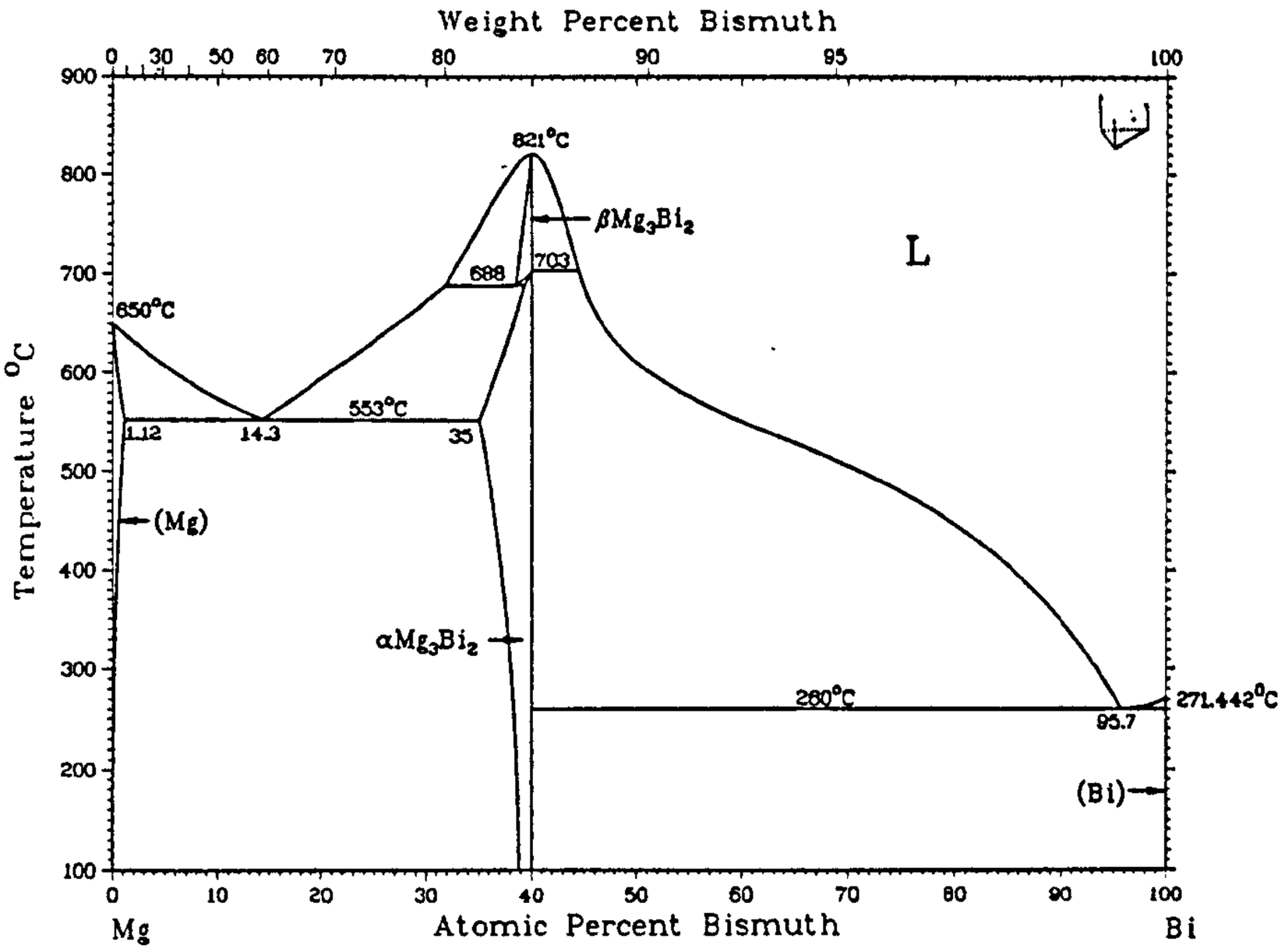

Figure 6.7: $Mg - Bi$ phase diagram

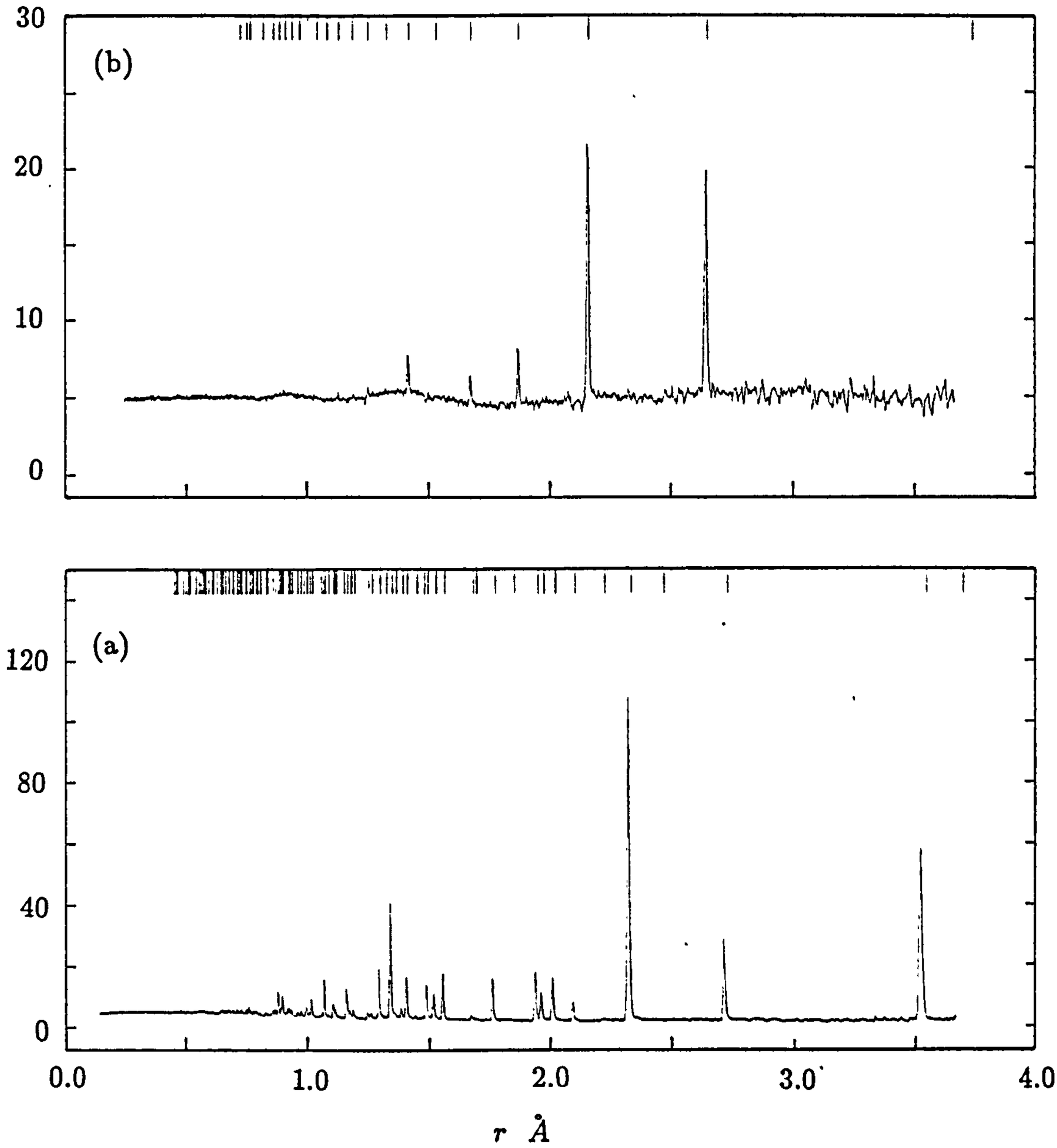

Figure 6.8: The diffraction pattern of α- and β-phase of Mg_3Bi_2 in d-spacing. (a). α-phase; (b). β-phase

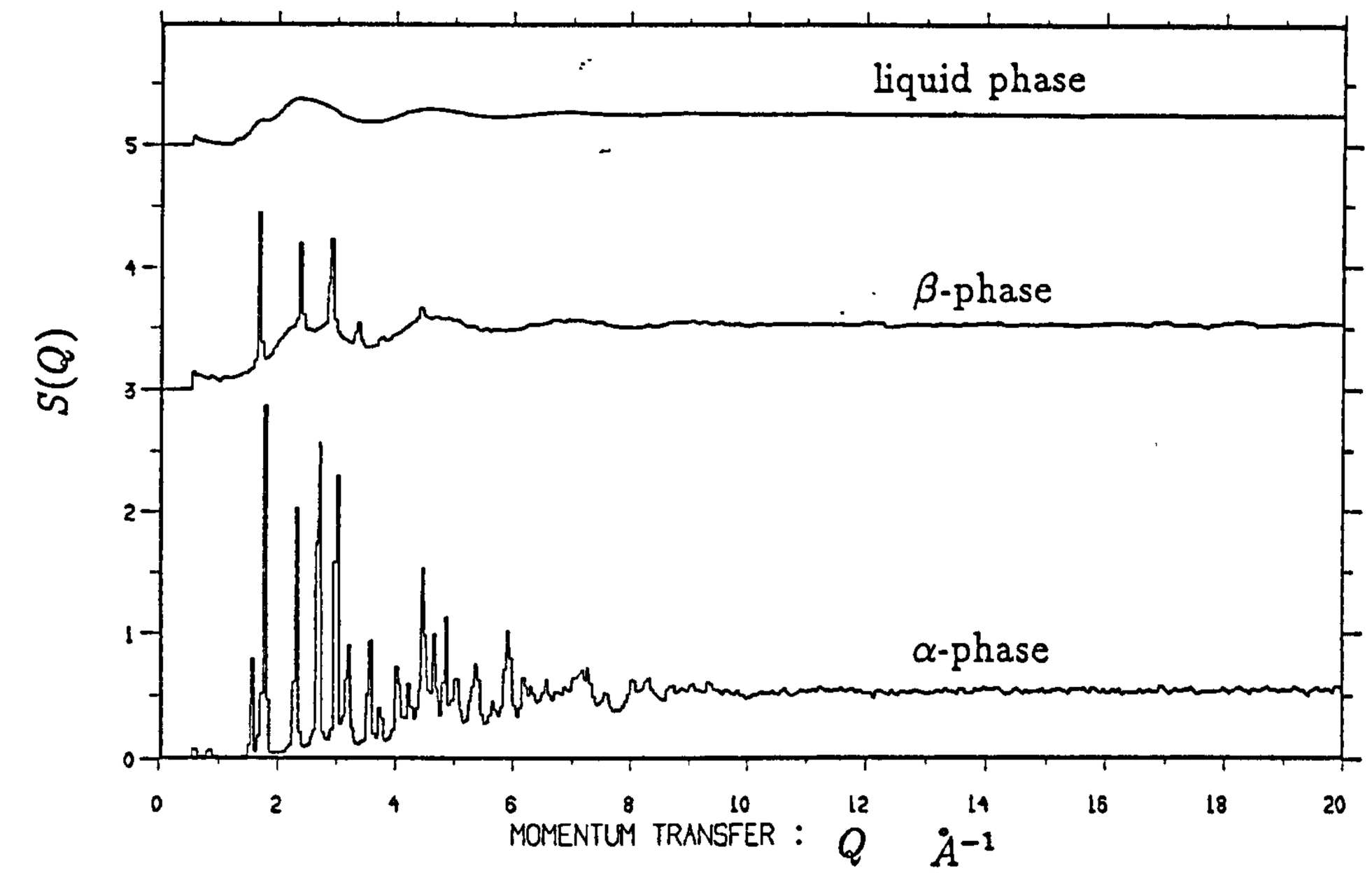

Figure 6.9: Total structure factor $S(Q)$ of α-, β- and liquid phase of Mg_3Bi_2. $T = 150°C$ (α- phase), T=740 $°C$ (β- phase) and T=950 $°C$ (liquid phase).

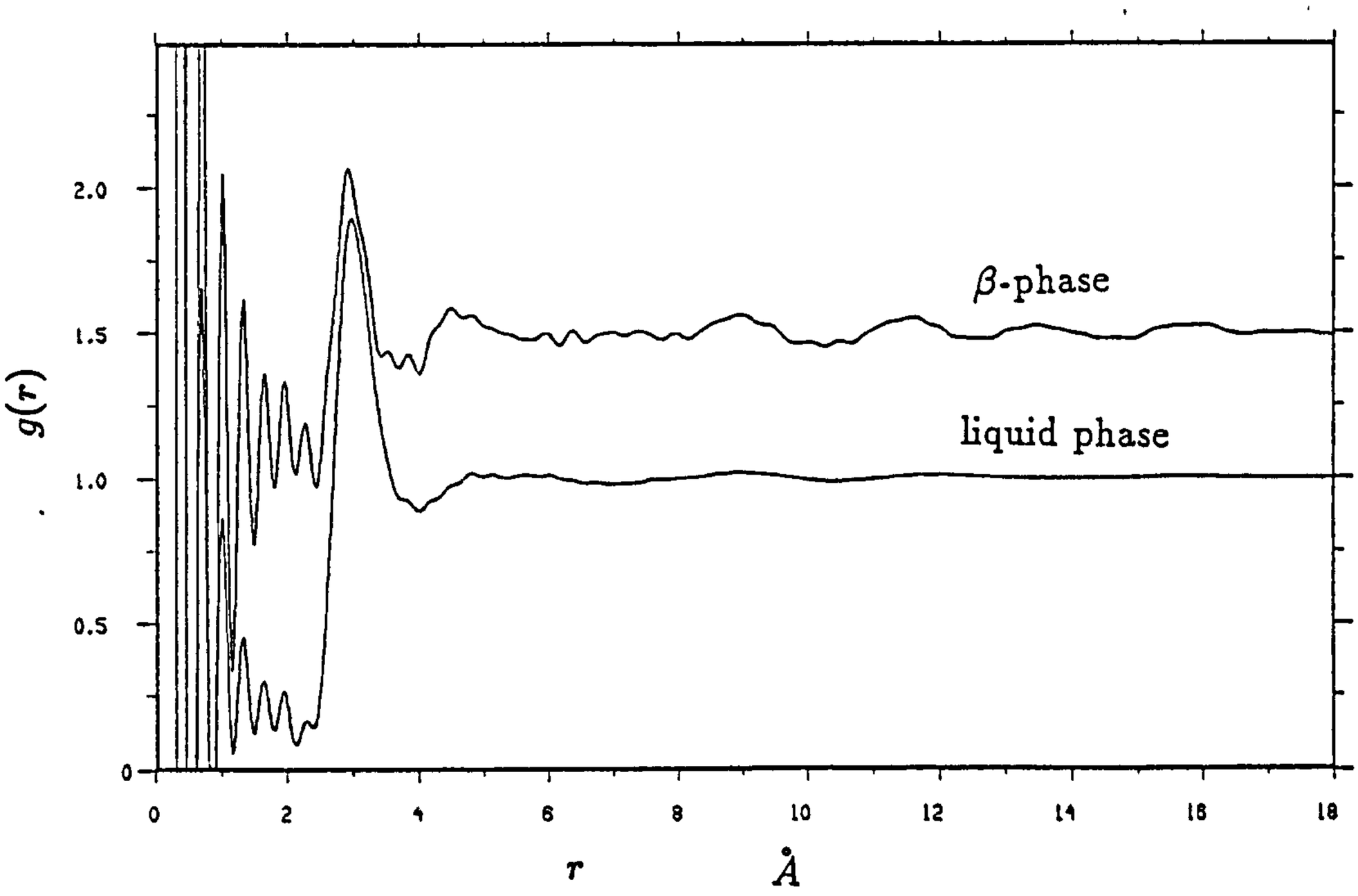

Figure 6.10: Radial distribution function $g(r)$ of β- and liquid phase of Mg_3Bi_2.

Table 6.1 The d-spacing and assignment of the Bragg peaks observed in β-Mg_3Bi_2

Assignment	110	200	211	220	310	222	321
d-spacing /Å	3.741	2.647	2.162	1.874	1.675	unresolvable	1.417

These can be indexed to a body centred cubic structure with the peak assignments, as shown in Fig. 6.8. The 222 reflection is predicted to have a low intensity and is not resolvable within the statistics of the experiment. The unit cell dimension corresponds to $a = 5.297 \pm 0.0004$ Å. The very large and liquid-like diffuse background observed in the β-phase is characteristic of a superionic (fast ion) conductor and is similar to that of α-AgI and α-Ag_2Se which also have body centered cubic structure (Salamon, 1979). Due to the large size of the Bi^{3-} ion and the smallness of the Mg^{2+} ion we conclude that β-Mg_3Bi_2 is a superionic conductor in which magnesium is mobile ion. This structure is fully consistent with the atomic number density of the system.

6.3.1.2 Reverse Monte Carlo computer simulation on β-Mg_3Bi_2

In the last section the total structure factor and their direct Fourier transform g(r) including both Bragg peaks and diffuse scattering was shown for the β - Mg_3Bi_2. In order to make clear how the atoms contribute Bragg peaks and diffuse scattering, information on the partial level is needed. I have used the Reverse Monte Carlo technique (RMC) to produce detailed local structures.

The principles of the RMC method have been reviewed in detail in chapter 5. In the application of this technique to β-Mg_3Bi_2 a special initial configuration was created. The basic structure of the configuration is described as cubic with the lattice constant $a = 5.297$ Å. The bismuth atoms were put on the b.c.c sites and magnesium atoms on the f.c.c sites. The unit cell atom position is as follows:

$$\begin{vmatrix} 0 & 0 & 0 \\ 1/2 & 1/2 & 1/2 \\ 1/2 & 0 & 1/2 \\ 0 & 1/2 & 1/2 \\ 1/2 & 1/2 & 0 \end{vmatrix}$$

In order to ensure lattice periodicity, the sides of the unit cell were taken to be $L = na$, where n is an integer and a is the unit cell parameter. A configuration of $L = 5a$ (625 atoms) was used in the simulation. Theoretically, a larger configuration should be used to achieve a better fit to both the long-range order and short-range disorder. However, because of a smaller r-spacing 0.05 Å used in this simulation, 625 atoms is the most sensible when considering computing time. The allowed distances of r_{Mg-Mg}, r_{Mg-Bi} and r_{Bi-Bi} were set as 2.9, 2.4, 3.8 Å which is determined according to the analysis in last section.

The fit to the total structure factor and the calculated partial distribution functions are shown in Fig. 6.11 and 6.12, respectively. Figure 6.11 shows the fit is fairly good, but not perfect as a result of the small size configuration. This is most noticeable in the center of the Bragg peaks. It is very clear from figure 6.12 that the bismuth has kept its crystalline periodicity, where as the Mg-Mg has lost its periodicity resulting in a liquid like diffuse scattering pattern and consequently the Mg-Bi pair is less crystal like than the Bi-Bi pair, but still showing a periodical structure. The positions of the first peaks of Mg-Mg, Mg-Bi and Bi-Bi pairs are 3.0, 2.9, and 4.5, respectively. The coordination numbers of Mg were calculated according to the area of the first peak of Mg-Bi pair as 4.07.

Fig.6.13 is the average density distribution of the magnesium and bismuth in the unit cell of an equilibrium structure constructed by RMC. This visualisation of the structure shows clearly that the bismuth sits in the normal b.c.c position, while the magnesium in the faces of the unit cell is mobile, diffusing along the 100 direction via the octahedrally coordinated sides. This result is consistent with that derived from the structure factors and distribution functions.

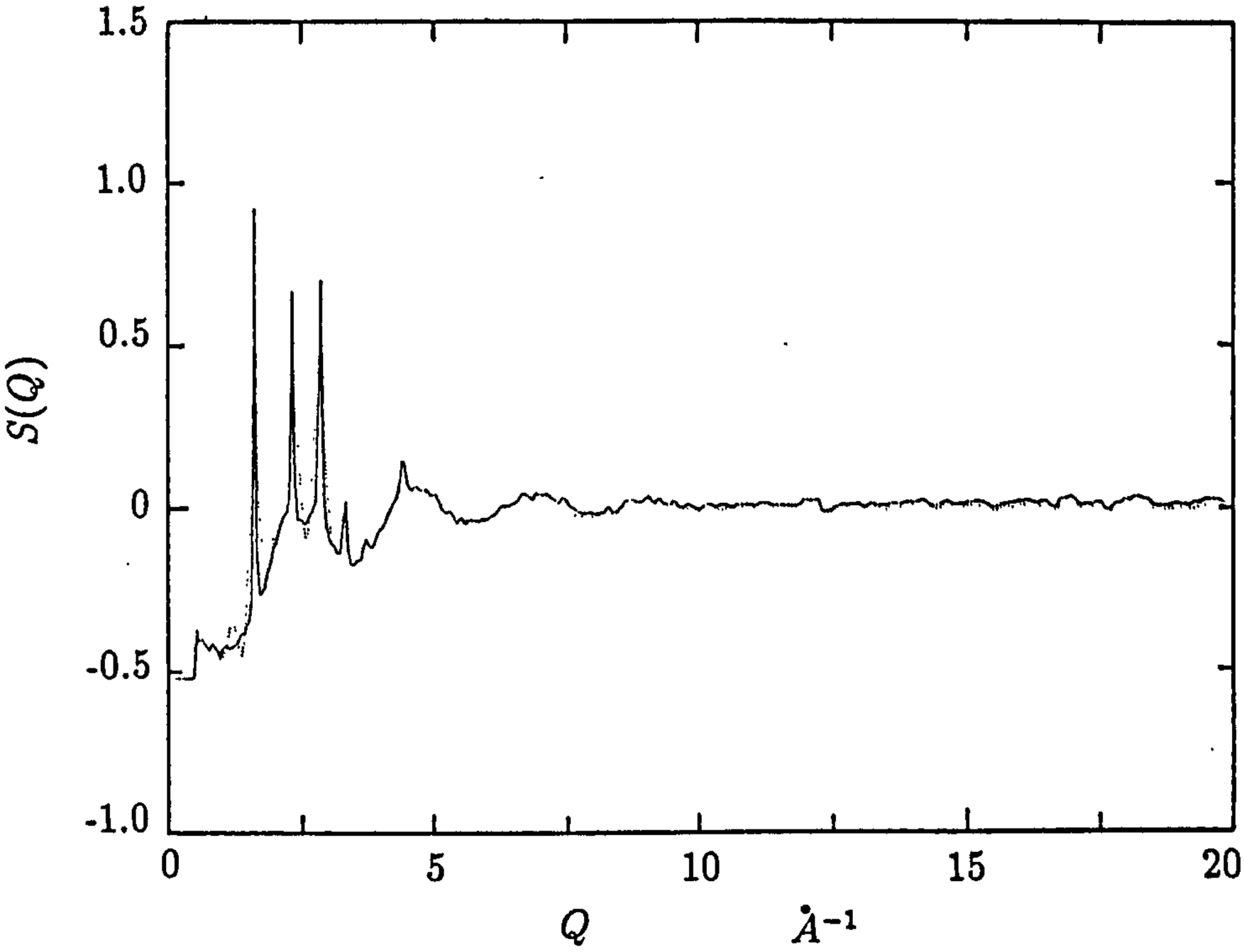

Figure 6.11: The fit of total structure factor $S(Q)$ of β- Mg_3Bi_2. Full line - Experiment; Dotted line - RMC fit.

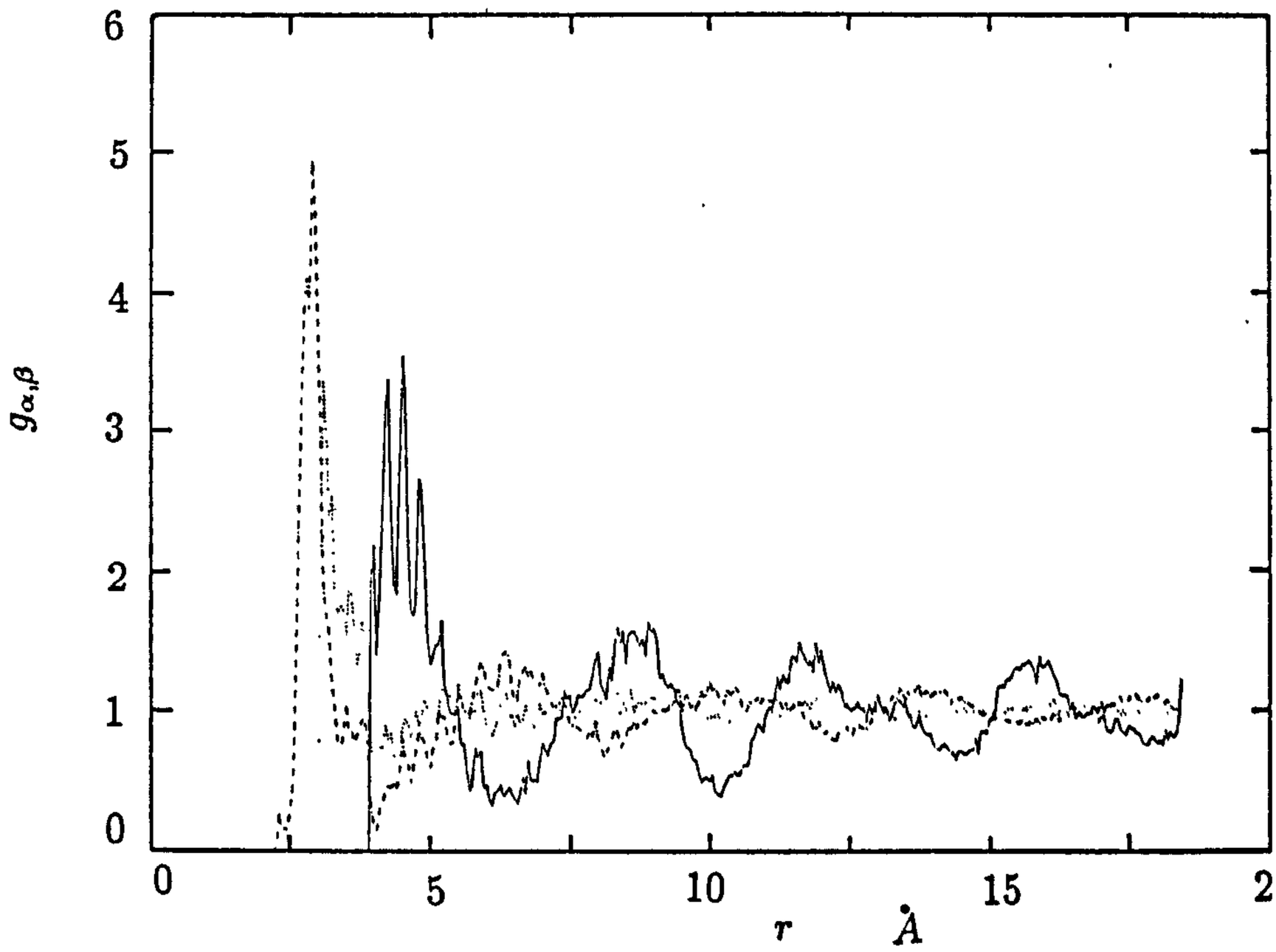

Figure 6.12: The calculated partial radial distribution function $g_{\alpha,\beta}(r)$ of β - Mg_3Bi_2. Full line - $g_{Bi-Bi}(r)$; Dotted line - $g_{Mg-Mg}(r)$; Dot-dash line - $g_{Mg-Bi}(r)$.

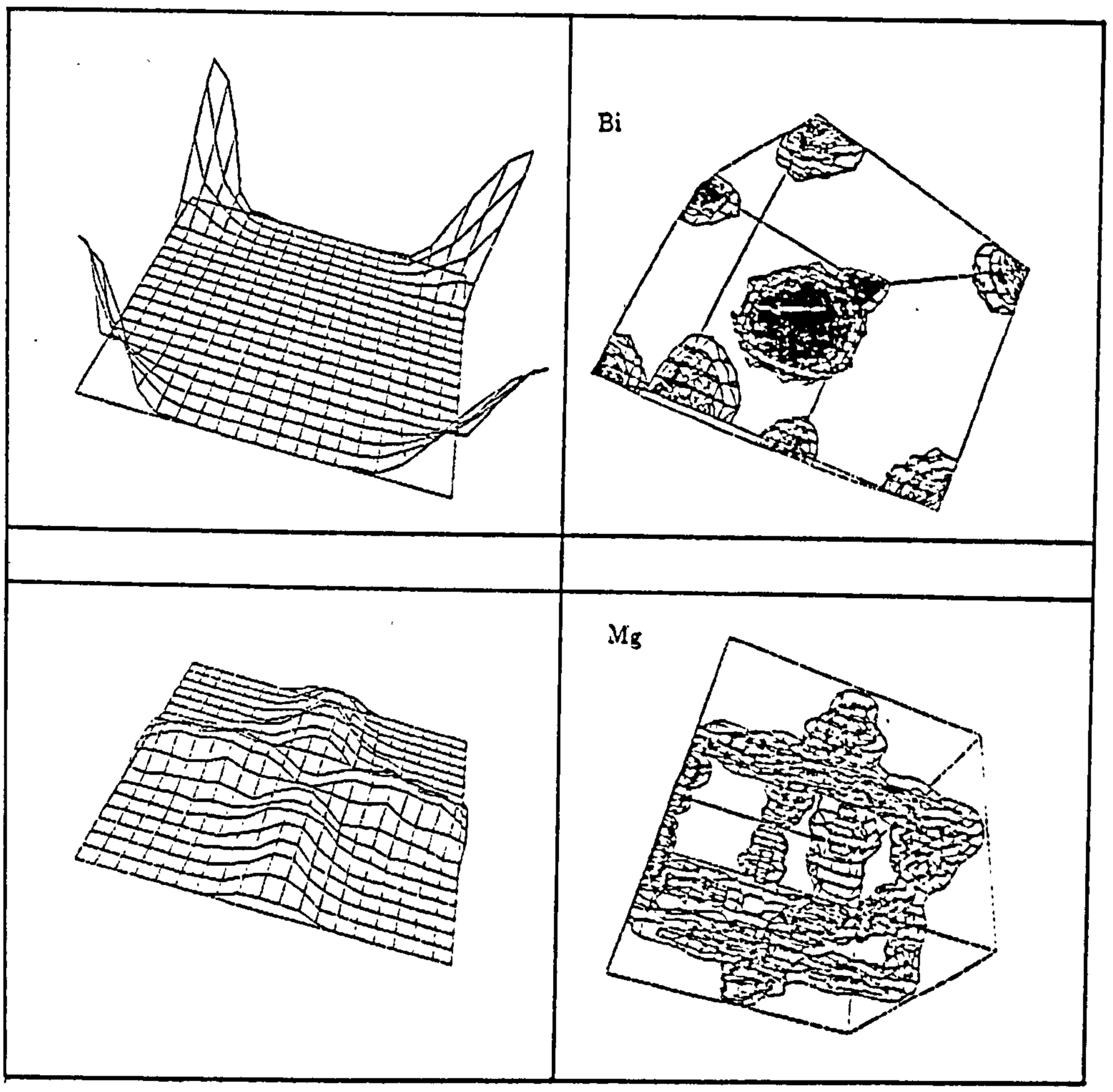

Figure 6.13: The everage density distribution of the Mg and Bi in the unit cell in the equilibrium cubic structure of β-phase of Mg_3Bi_2.

It is concluded that the Bismuth structure gives rise to the Bragg peaks as expected, while the Mg-Mg contributes to the diffuse scattering background. β-Mg_3Bi_2 has a superionic structure.

It has been noted (Armstrong, 1972) that in a material in which the cation is the mobile ion, the following conditions should be met:

i) There must be a large number of connected and vacant sites in the crystal structure.

ii) The difference in the energies of the cation-anion interactions on different sites should be small.

iii) The cation should be stable with a coordination number of 4 or less.

iv) The fast ion should be small and singly charged.

The first three conditions are met well in this case. It is interesting that the cation Mg of β-Mg_3Bi_2 should be divalent if it is recognised as an ionic compound, which suggests a new kind of superionic conductor.

6.3.2 Diffraction experiment of liquid states

The total structure factors $S(Q)$ of the three samples Mg_3Bi_2, $Mg_{3.1}Bi_{1.9}$ and $Mg_{2.9}Bi_{2.1}$ have been obtained from the scattered intensity after the corrections stated in chapter 5. The total radial distribution functions $g(r)$ were deduced by direct Fourier transform of the total structure factors. They are shown in Fig 6.14 and 6.15, respectively.

For this multi-component system the total structure factor can be expressed with the partial structure factors S_{Mg-Mg}, S_{Mg-Bi} and S_{Bi-Bi} with their own weights according to the equation (3.29) as follows:

(1) for the sample Mg_3Bi_2

$$\begin{aligned} S(Q) &= 10.40(S_{Mg-Mg}(Q)-1) + 21.99(S_{Mg-Bi}(Q)-1) \\ &+ 11.63(S_{Bi-Bi}(Q)-1) \end{aligned} \tag{6.1}$$

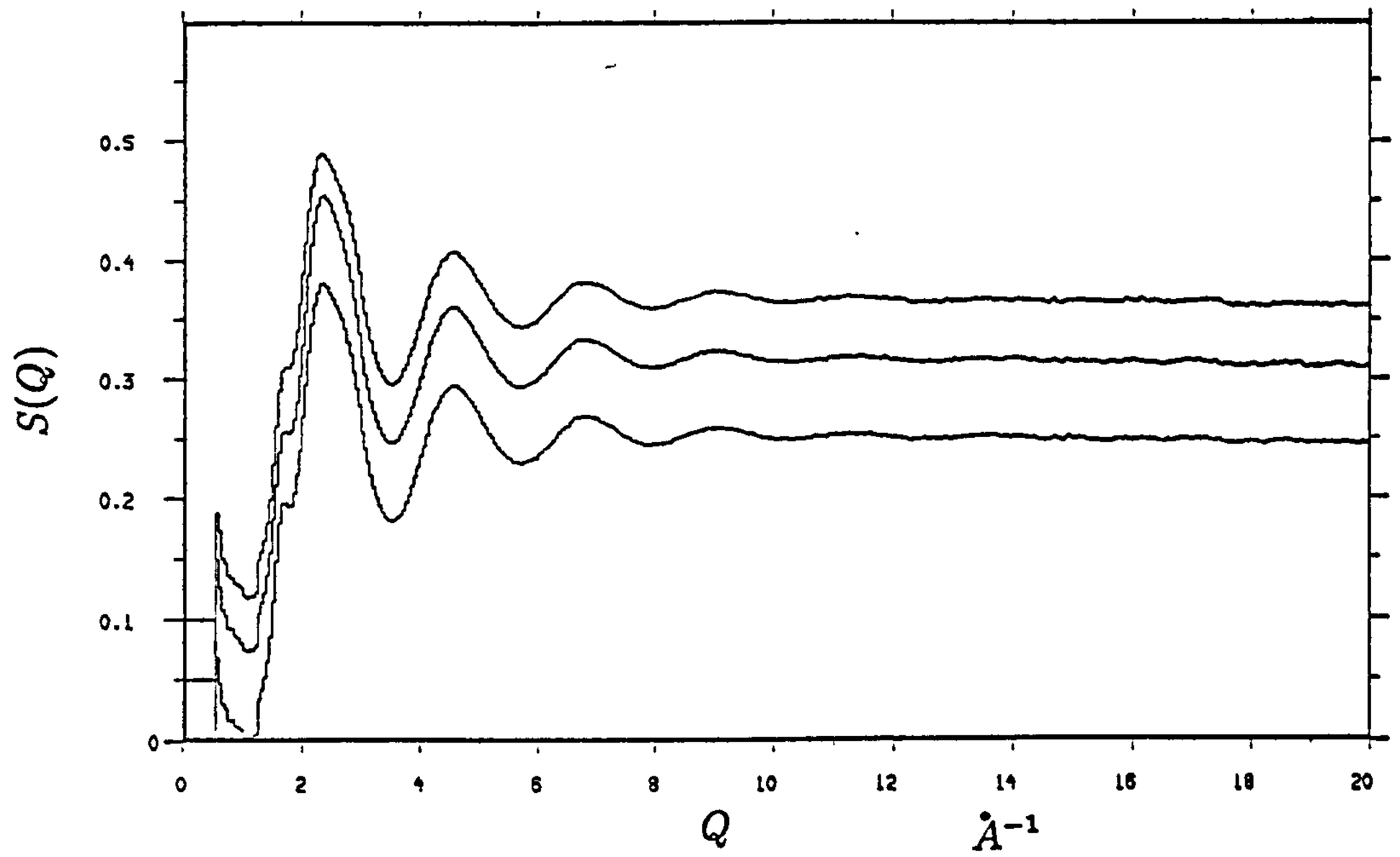

Figure 6.14: Total structure factor $S(Q)$ of liquid $Mg_{2.9}Bi_{2.1}$ (upper line), Mg_3Bi_2(middle line) and $Mg_{3.1}Bi_{1.9}$ (lower line) at 950 ^oC.

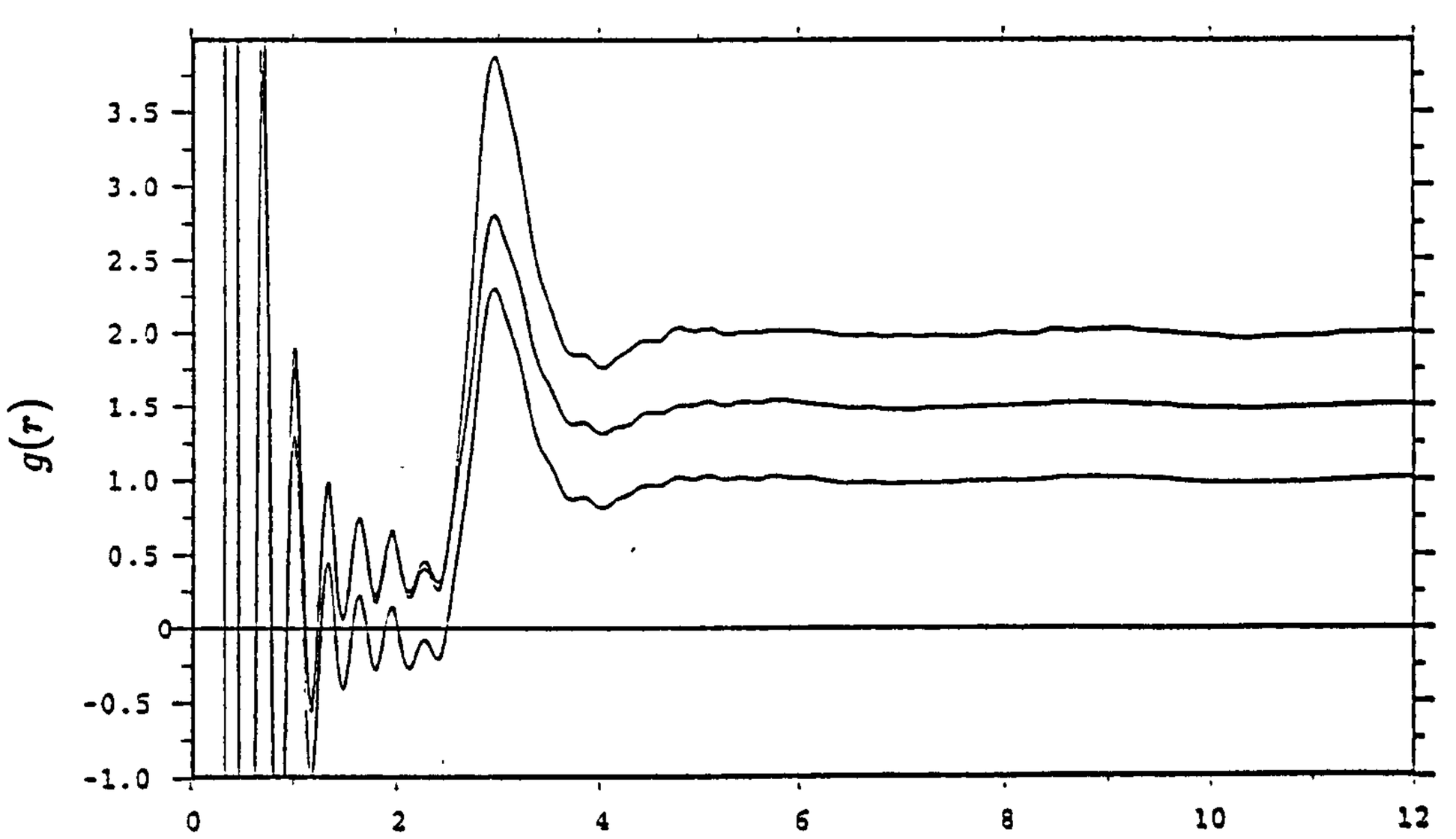

Figure 6.15: Total radial distribution function $g(r)$ of liquid $Mg_{2.9}Bi_{2.1}$ (upper line), Mg_3Bi_2 (middle line) and $Mg_{3.1}Bi_{1.9}$ (lower line) at 950 ^oC.

(2) for the sample $Mg_{3.1}Bi_{1.9}$

$$\begin{aligned} S(Q) &= 11.10(S_{Mg-Mg}(Q)-1)+21.55(S_{Mg-Bi}(Q)-1) \\ &+ 10.49(S_{Bi-Bi}(Q)-1) \end{aligned} \tag{6.2}$$

(3) for the sample $Mg_{2.9}Bi_{2.1}$

$$\begin{aligned} S(Q) &= 9.71(S_{Mg-Mg}(Q)-1)+22.32(S_{Mg-Bi}(Q)-1) \\ &+ 12.81(S_{Bi-Bi}(Q)-1) \end{aligned} \tag{6.3}$$

The bound coherent scattering lengths in the calculation are $b_{Mg} = 5.375\ fm$, $b_{Bi} = 8.526\ fm$ (Sears 1984). The above equations show that $S_{Mg-Bi}(Q)$ gives twice contribution of $S_{Mg-Mg}(Q)$ and $S_{Bi-Bi}(Q)$ to the total structure factor $S(Q)$. Because we could not do an isotope substitution experiment the partial structure factors can not be determined at this stage. It can be seen from the Fig.6.14 and 6.15 that the change of composition of 2 $at.\%$ does not produce a dramatically different structure despite the huge change of the electronic properties. Both the structure factors and the radial distributions show that ordered structures are quite short ranged, the peaks disappear beyond 5 $\mathring{A}$ for $g(r)$ and 5 $\mathring{A}^{-1}$ for $S(Q)$. From the β-Mg_3Bi_2 data it is apparent that the transition from the solid β phase to the liquid state occurs through the collapse of the long-range order of $Bi-Bi$ pairs. The features of the short-range order in the β-Mg_3Bi_2 are inherited and the physicochemical properties of β-Mg_3Bi_2 are likely to be similar in the effective local interaction. As the temperature is increased from room temperature to 50 ^oC above the melting point, the compound Mg_3Bi_2 experiences three states: (1) pure solid state - α-phase; (2) 'semi-liquid' or 'semi-solid' state - β-phase with superionic behaviour; and (3) liquid state. It is clear from Fig.6.14 that the total structure factor is characterised by the 'Coulomb' shoulder at 1.7 $\mathring{A}^{-1}$. Evans and Telo da Gama (1980) suggested this kind of Coulomb shoulder could be one of the 'bench marks' of liquid ionic semiconducting alloys. The position of the first peak in $g(r)$ is at 2.95 Å which agrees with the sum of $r_{Mg^{2+}}$ and $r_{Bi^{3-}}$, but it also agrees with the sum of their covalent

radii shown in table 6.2. The information obtained at the total structural level is not sufficient to determine the bonding details.

Table 6.2 Structure data of Mg and Bi

Elements	Metallic radius / Å	Covalent radius / Å	Ionic radius / Å
Mg	1.60	1.37	0.75 (0.66) [2^+]
Bi	1.55	1.52	2.13 [3^-]
			1.20 [3^+]
			0.74 [5^+]

The ionic radius is the Goldschmidt radius, [ ] indicates the valence state, ( ) indicates the Pauling radius.

6.3.3 RMC computer simulation on liquid states

6.3.3.1 Process of the calculation

It is impossible to unambiguously determine the three partial structure factors from only one experimental total structure factor, $S^E(Q)$. To produce partial structure factors consistent with the experimental data, I used the RMC computer simulation which has been reviewed in chapter 5.

The RMC calculation starts with an initial configuration of the crystal structure of β-Mg_3Bi_2 type which is the most reasonable according to the conclusion deduced in the last section. The atomic positions in the unit cell are the same as that used in the simulation of the β-phase. The numbers of the particles in the configurations for the three samples are listed in table 6.3.

Table 6.3 The numbers of the particles in the configuration

Systems	Total	Mg	Bi
$Mg_{2.9}Bi_{2.1}$	3471	2013	1458
Mg_3Bi_2	3645	2187	1458
$Mg_{3.1}Bi_{1.9}$	3527	2187	1340

The number densities of the systems in the liquid were adopted with assumption that it is about 20 % less than in the solid at room temperature, (0.027-0.029 $\dot{A}^{-1}$). The cubic box size of the configuration is about A=B=C 60 Å̇These dimensions ensure that the calculated $g^C(r)$ can be transformed directly from the calculated $S^C(Q)$ with $g(r > L/2)$=1, L is the size of the box. The constraints of the closest approach distances of two atoms have been used to prevent the particles approaching each other to unphysical distances. These were chosen assuming that the features of the short range structure of β-phase is kept in the liquid when the temperature is just over the melting point. Therefore, the closest approach distances of two atoms were chosen as Mg-Mg=2.6 Å Mg-Bi=2.4 Å and Bi-Bi=3.8 Å according to the crystal structure data derived in the above section. The program takes about 5 hours on a computer VAX workstation 3100.

6.3.3.2 Structure factors and R. D. F

The calculated and measured total structure factors are shown in Fig. 6.16, 6.17 and 6.18 for the samples Mg_3Bi_2, $Mg_{2.9}Bi_{2.1}$ and $Mg_{3.1}Bi_{1.9}$, respectively. It can be seen that the fit is satisfactory. The Coulomb shoulder at low Q and structures at higher Q are simulated well within the experimental errors. A small deviation appears in the first peak due to the fact that the experimental data has a slight downward slope with momentum transfer Q.

The partial structure factors and partial radial distribution functions obtained from the simulation are shown in Fig.6.19 - 6.24. The configuration adopted in the simulation is big enough to enable the calculation of partial radial distribution function up to r=24 Å which is the same as the experiment. Nevertheless, the oscillations in $g_{\alpha\beta}(r)$ are still sufficiently large to cause truncation ripples in the transform to $S_{\alpha\beta}(Q)$ at low Q. This will not alter the short range structure in which we are interested. The partial structure factors of the three samples are shown in Fig. 6.19 - 6.21.

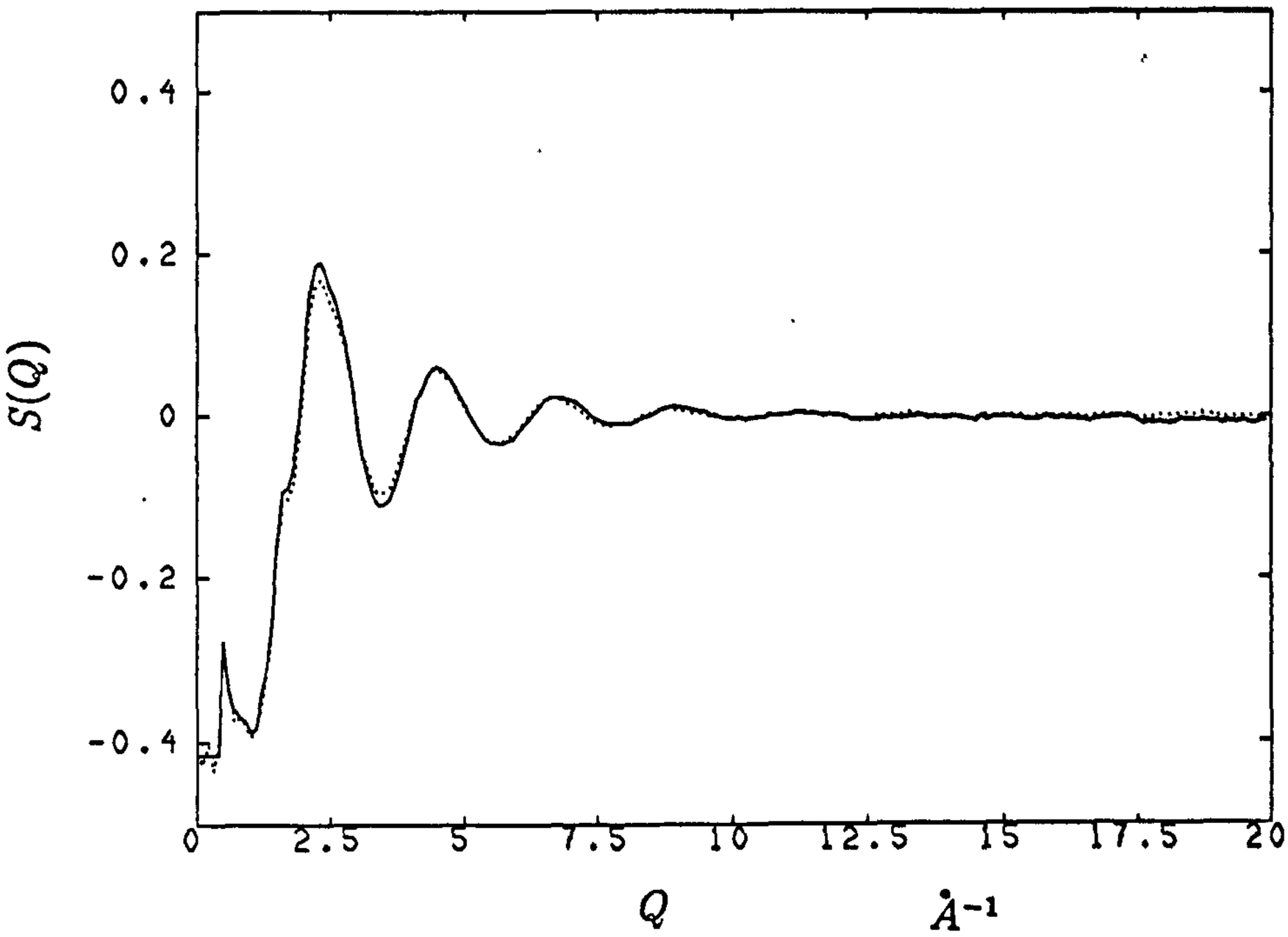

Figure 6.16: The fit of total structure factor $S(Q)$ of liquid $Mg_{2.9}Bi_{2.1}$. Full line - Experiment; Dotted line - RMC fit.

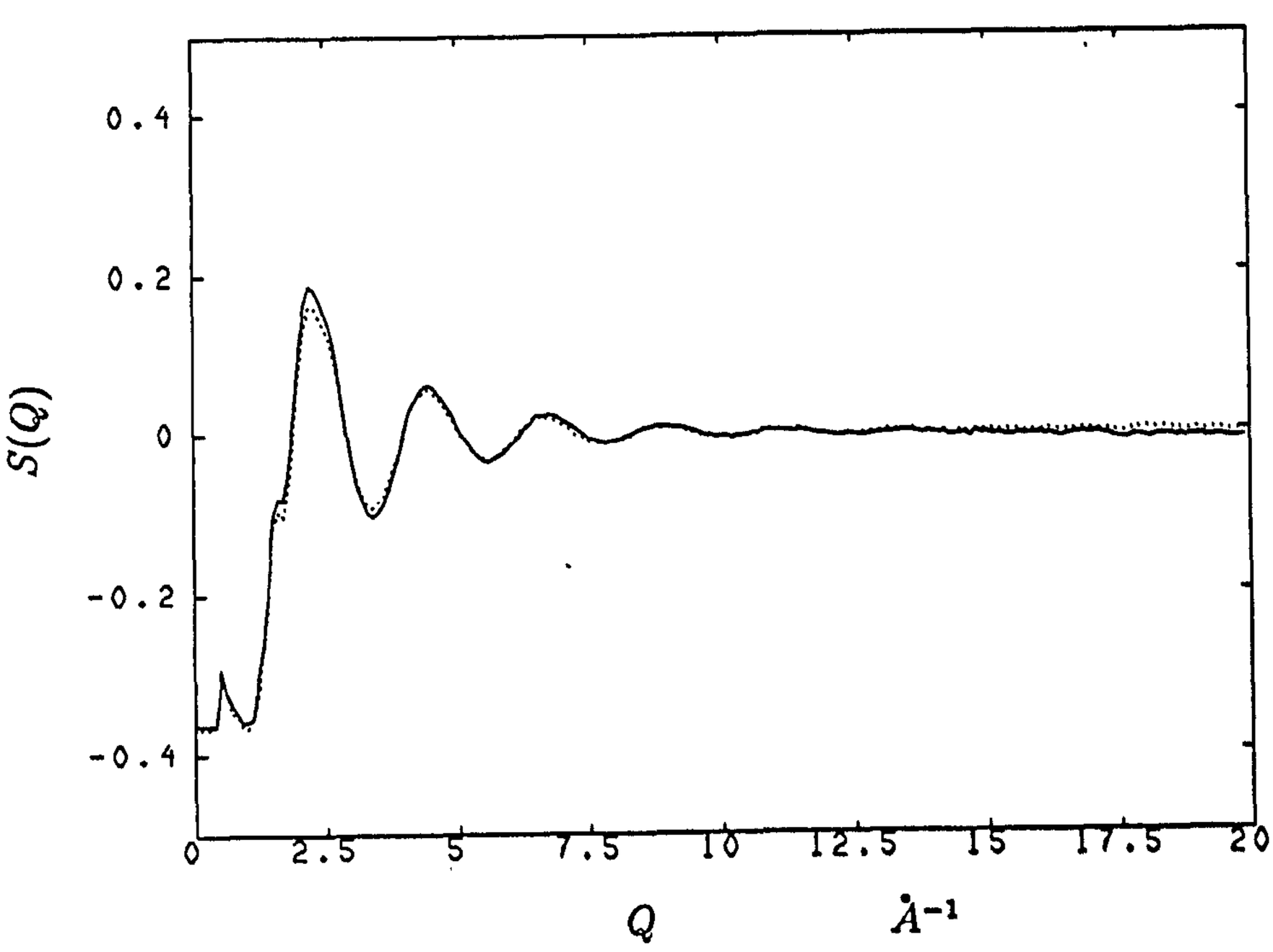

Figure 6.17: The fit of total structure factor $S(Q)$ of liquid Mg_3Bi_2. Full line - Experiment; Dotted line - RMC fit.

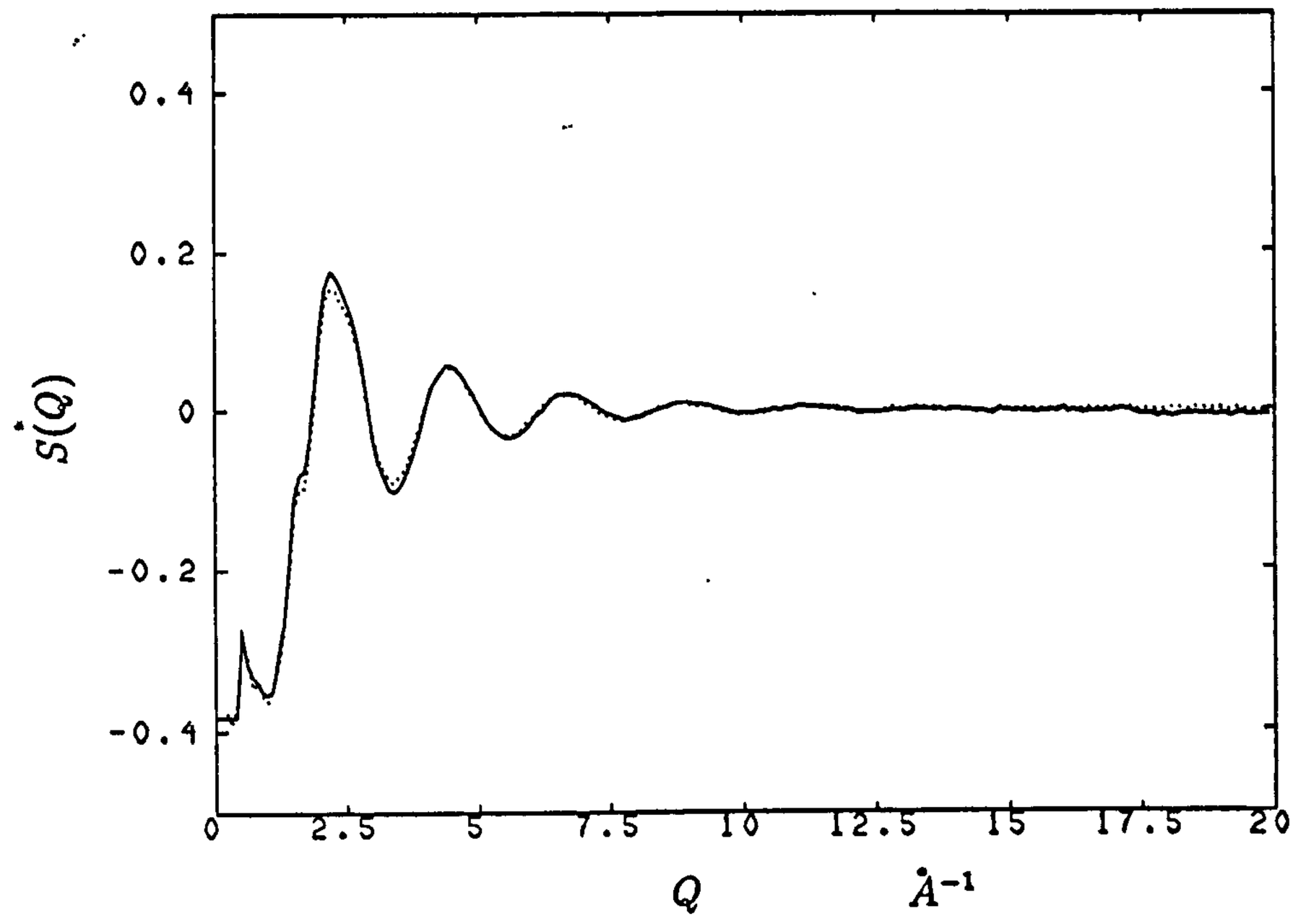

Figure 6.18: The fit of total structure factor $S_{\alpha,\beta}(Q)$ of liquid $Mg_{3.1}Bi_{1.9}$. Full line - Experiment; Dotted line - RMC fit.

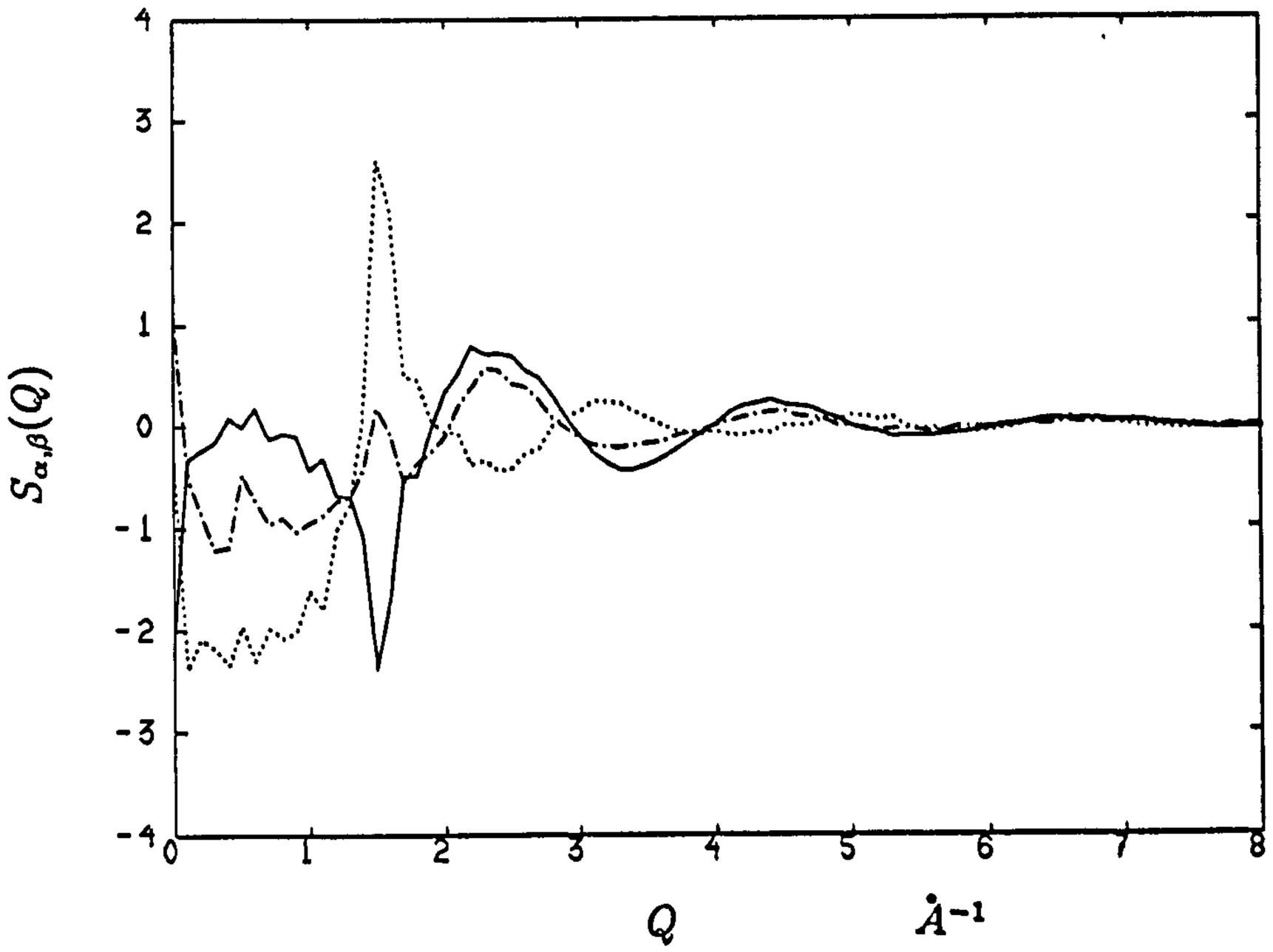

Figure 6.19: The partial structure factor $S_{\alpha,\beta}(Q)$ of liquid $Mg_{2.9}Bi_{2.1}$. Full line - $S_{Mg-Bi}(Q)$; Dot-dash line - $S_{Mg-Mg}(Q)$; Dotted line - $S_{Bi-Bi}(Q)$

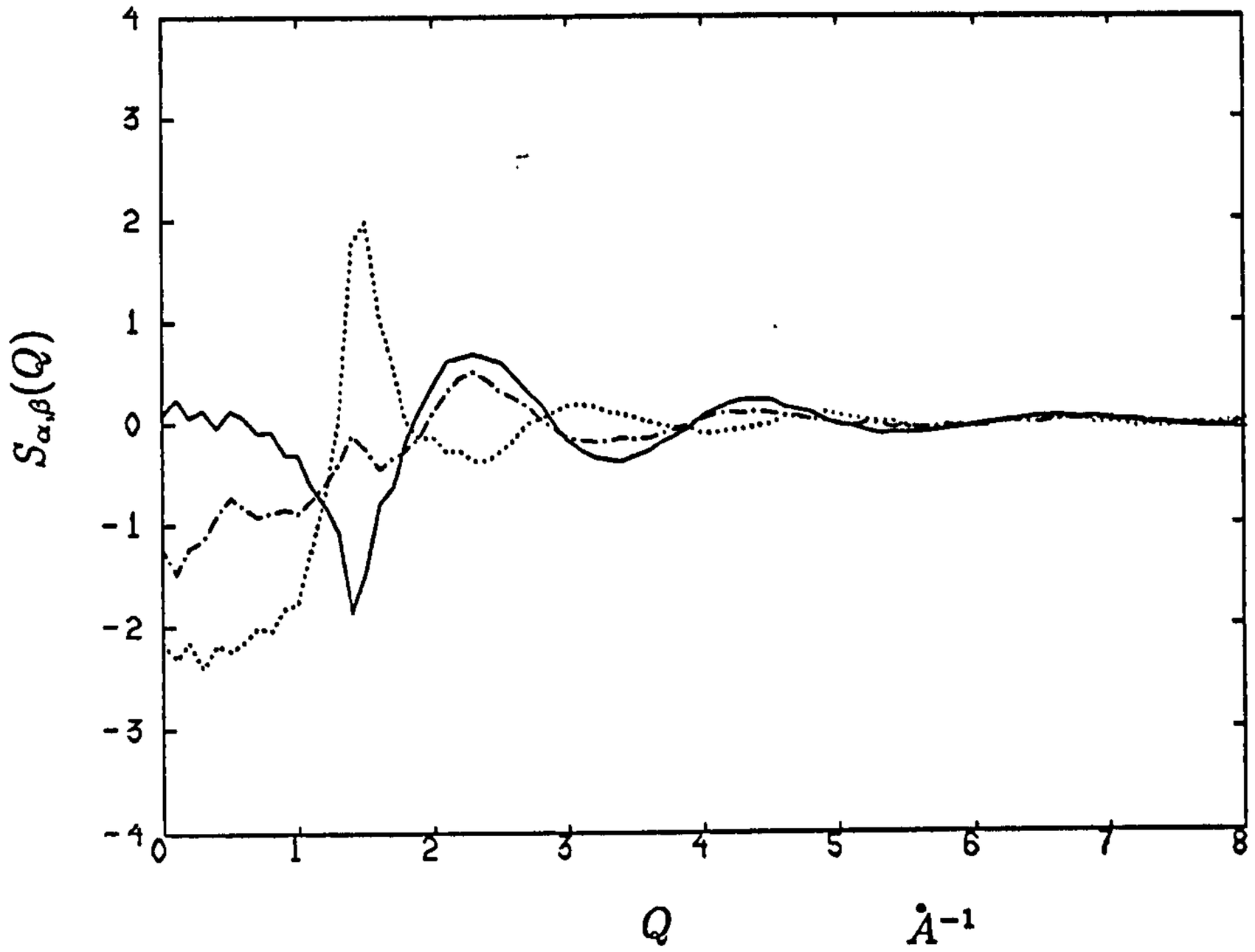

Figure 6.20: The partial structure factor $S_{\alpha,\beta}(Q)$ of liquid Mg_3Bi_2. Full line - $S_{Mg-Bi}(Q)$; Dot-dash line - $S_{Mg-Mg}(Q)$; Dotted line - $S_{Bi-Bi}(Q)$

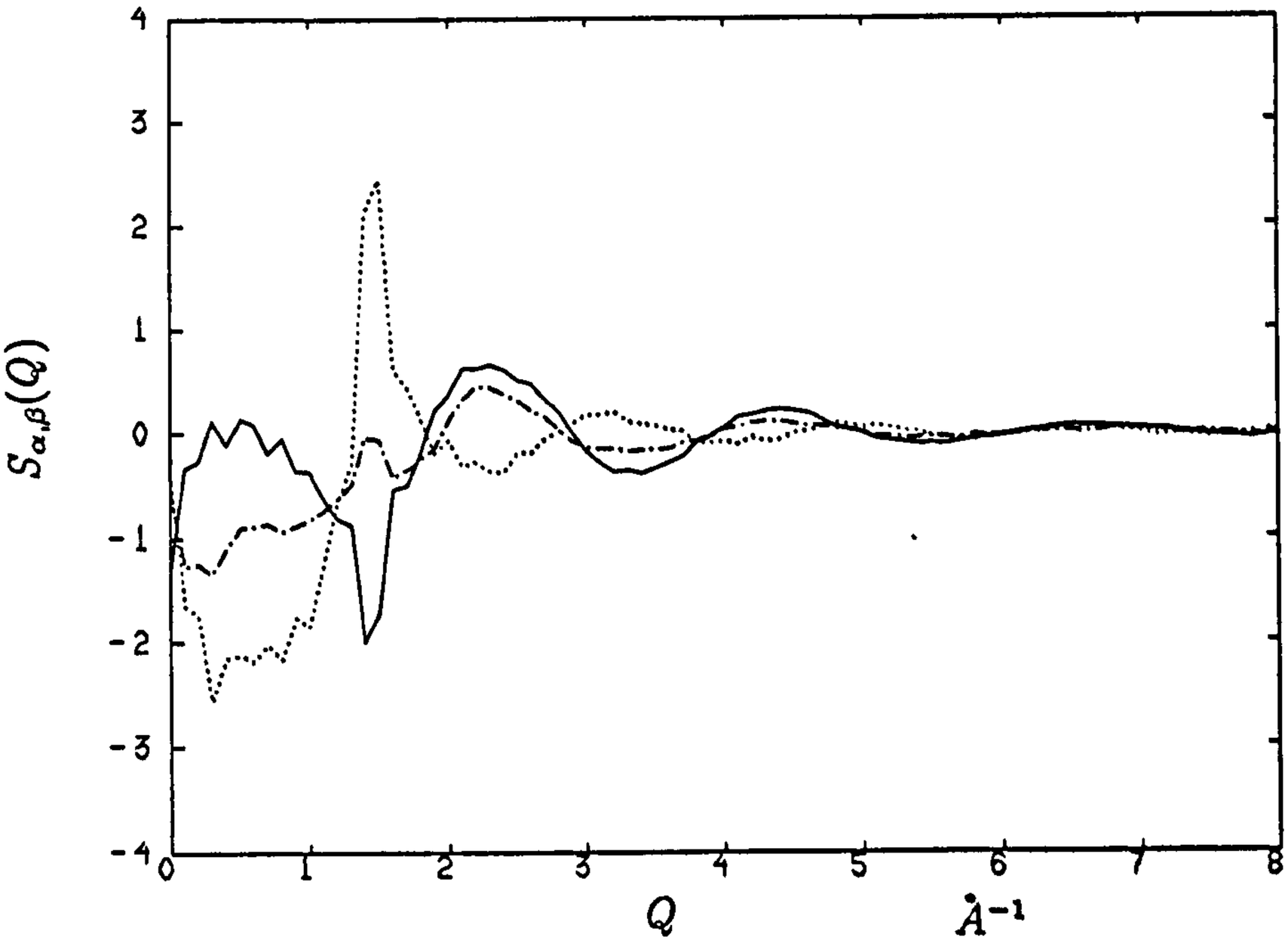

Figure 6.21: The partial structure factor $S_{\alpha,\beta}(Q)$ of liquid $Mg_{3.1}Bi_{1.9}$. Full line - $S_{Mg-Bi}(Q)$; Dot-dash line - $S_{Mg-Mg}(Q)$; Dotted line - $S_{Bi-Bi}(Q)$

It can be seen that a composition change of 2 *at.*% does not cause a significant change of the structure. All the three samples have a similar structural pattern which is summarised as follows:

1. $S_{Mg-Bi}(Q)$ has a large negative-going peak at low Q at about 1.5 $\AA^{-1}$;

2. for the same value of Q, $S_{Bi-Bi}(Q)$ has its positive maximum;

3. $S_{Mg-Mg}(Q)$ shows a small positive peak.

These structures show a similarity to those of molten $ZnCl_2$ (Biggin and Enderby, 1981), but with notable differences between $S_{Zn-Zn}(Q)$ and $S_{Mg-Mg}(Q)$. The three partial structure factors in this work are almost exactly the same as those of Tl_2Te obtained experimentally by Nguyen *et al* (1982). The structural arrangements with the negative peak of $S_{+\ -}(Q)$ and the positive peaks of $S_{+\ +}(Q)$ and $S_{-\ -}(Q)$ at low Q is thought to be a signature of ionic ordering because the ions arrange themselves to maximise ionic screening. As a result the heterocoordination in an ionic system is driven by charge cancellation. This situation happens in alkali halides with cubic arrangement.

The partial radial distribution functions in Fig. 6.22 - 6.24 show that the first peak of $g_{Mg-Bi}(r)$ is very well defined and the first peak for $g_{Mg-Mg}(r)$ and $g_{Bi-Bi}(r)$ is not defined as well as that of S_{Mg-Bi} because there are several interatomic distances of Mg-Mg (or Bi-Bi) in this distance range. The short range structure of g_{Bi-Bi} is longer than that of g_{Mg-Mg} and g_{Mg-Bi}. The positions of the first peaks for all the three samples are 2.9 Å for g_{Mg-Bi} and 3.0 Å for g_{Mg-Mg} and 4.2 - 4.5 for g_{Bi-Bi}, which are much similar to that of β-Mg_3Bi_2. This implies that the features in the structures of β-Mg_3Bi_2 are kept when it is melted and the liquid short-range structure is similar to its high temperature crystal phase as stated by Enderby and Barnes (1990). It is also noticed that the first peak of $g_{Mg-Mg}(r)$ penetrates deeply into that of $g_{Mg-Bi}(r)$. This is reflected in its structure factor by the absence of a sharp positive peak corresponding to the negative peak in $S_{Mg-Bi}(Q)$

at low Q. This feature shows that the liquid Mg_3Bi_2 has moved away from the fully heterocoordinated ionic compounds, such as the alkali halides. This penetration may play an important role in the band structures and consequently affect the electronic properties.

6.3.3.3 Coordination number and neighbour distribution

One of the advantages of RMC is that it can give an estimate of probability of different coordinations in the liquid, besides the normal coordination number $n_{\alpha\beta}$ derived from $g_{\alpha\beta}(r)$. This can be deduced from the the RMC configuration. The precise definition of the coordination shell then becomes less important. The first coordination shell is defined in this calculation as being ions within the first minimum in $g_{\alpha\beta}(r)$ (i.e. within 3.8 Å of a Mg and 5.0 Å of a Bi). Neighbours are defined as those in the first shell in this calculation. The distributions of the number of neighbours of the three samples around the Mg and Bi in the first coordination shell are shown in fig.6.25 - 27. The most probable coordinated number ($n_{\alpha,\beta}$) in the first shells are listed in table 6.4

Table 6.4 Most probable coordination numbers in the first shells

Systems	n_{Mg-Mg}	n_{Mg-Bi}	n_{Bi-Mg}
$Mg_{2.9}Bi_{2.1}$	3.4	3.7	5.0
Mg_3Bi_2	3.3	3.3	5.1
$Mg_{3.1}Bi_{1.9}$	3.3	3.1	5.1

$n_{\alpha-\beta}$ is the nearest neighbour coordination for which the α is coordinated by β.

It is interesting that the Bi is only coordinated by the Mg ($n_{Bi-Mg} \sim 5$), while the Mg atoms are coordinated with both themselves and the Bi in the first coordination shell. The Mg atoms in all three samples have about 3.3 Mg atoms and Bi atoms as its nearest neighbours. As the composition is changed, the opposite neighbours have slight changes, accordingly. No dramatic changes have been observed.

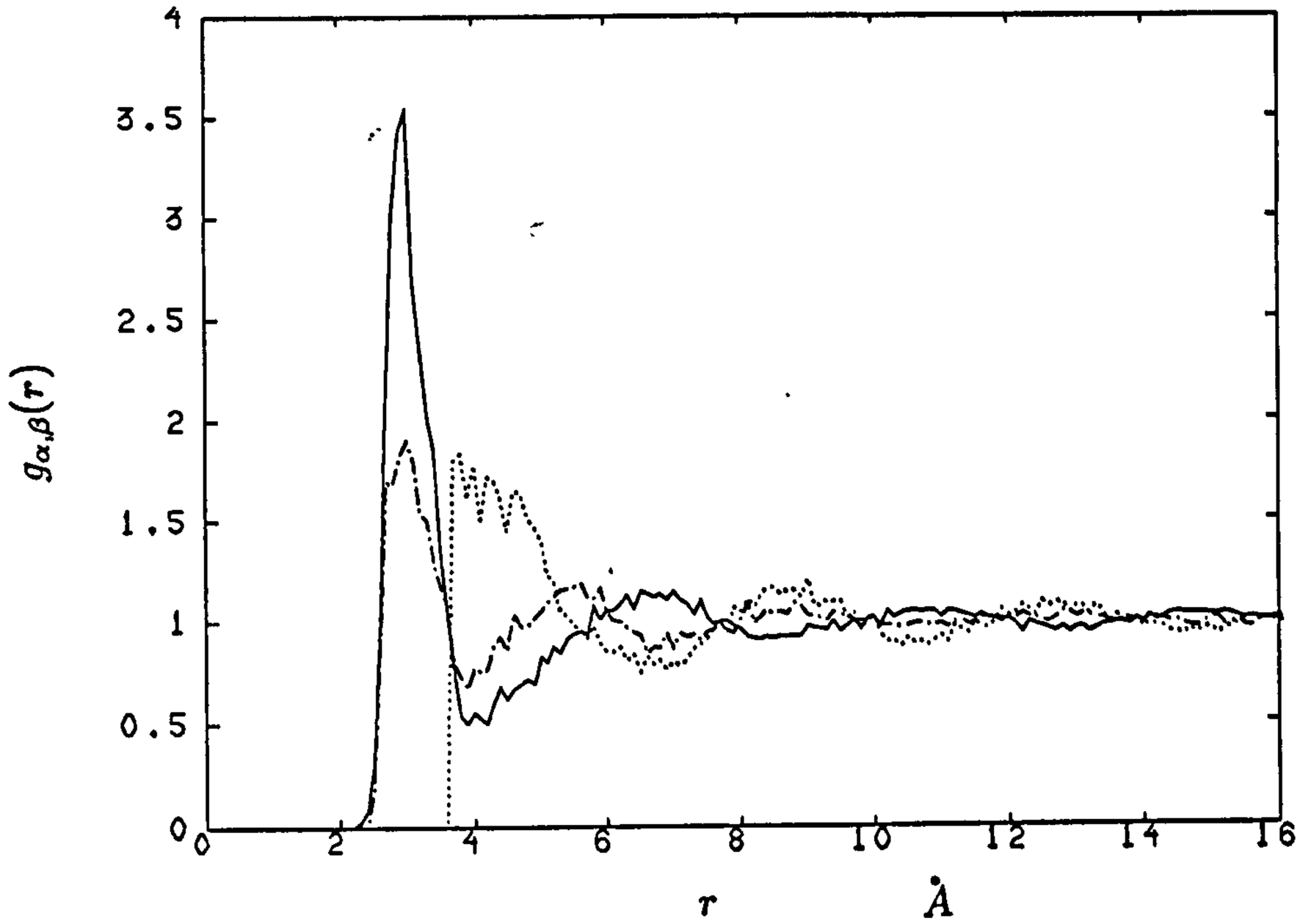

Figure 6.22: The partial radial distribution function $g_{\alpha,\beta}(r)$ of liquid $Mg_{2.9}Bi_{2.1}$. Full line - $g_{Mg-Bi}(r)$; Dotted line - $g_{Bi-Bi}(r)$; Dot-dash line - $g_{Mg-Mg}(r)$

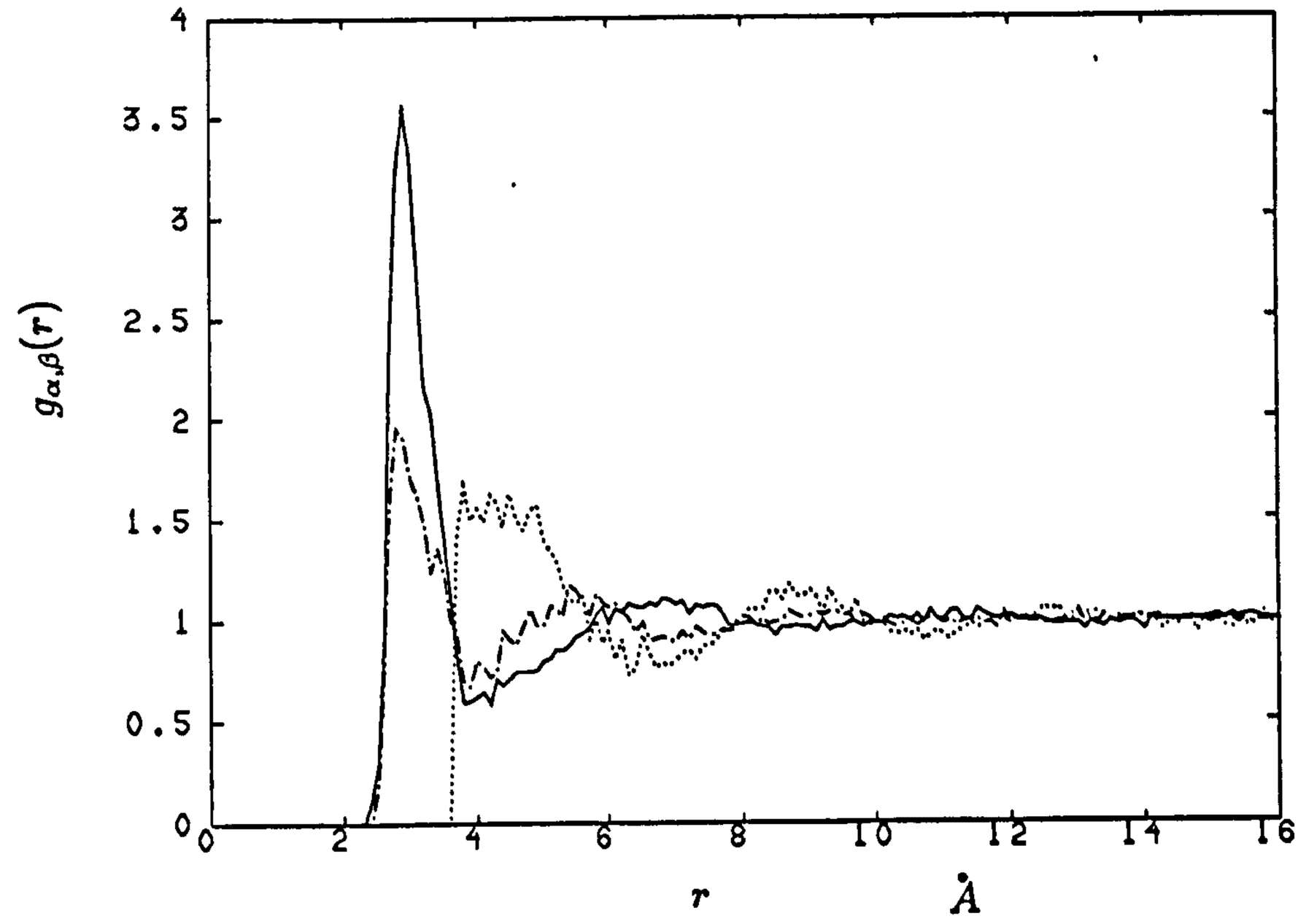

Figure 6.23: The partial radial distribution function $g_{\alpha,\beta}(r)$ of liquid Mg_3Bi_2. Full line - $g_{Mg-Bi}(r)$; Dotted line - $g_{Bi-Bi}(r)$; Dot-dash line - $g_{Mg-Mg}(r)$

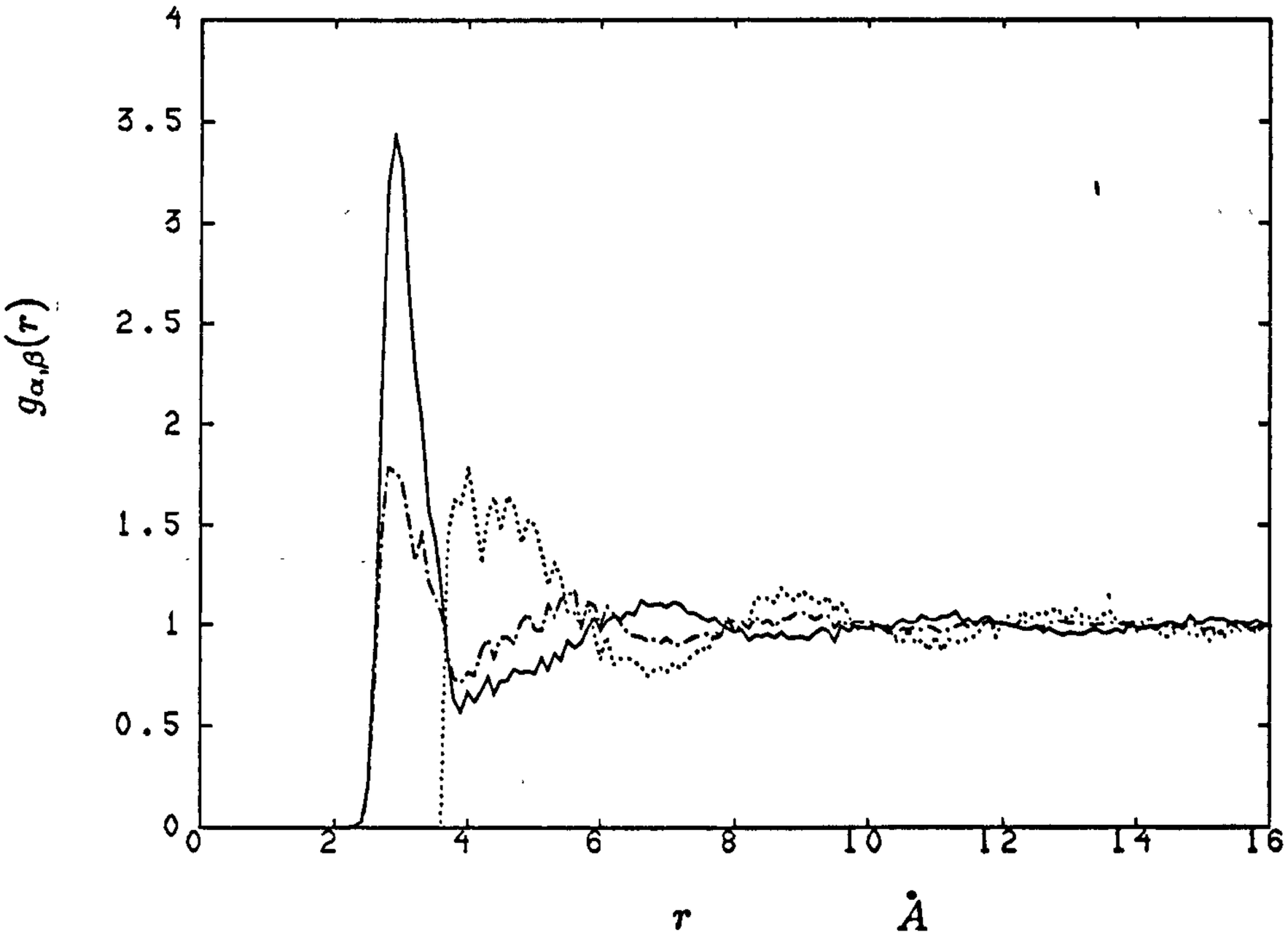

Figure 6.24: The partial radial distribution function $g_{\alpha,\beta}(r)$ of liquid $Mg_{3.1}Bi_{1.9}$. Full line - $g_{Mg-Bi}(r)$; Dotted line - $g_{Bi-Bi}(r)$; Dot-dash line - $g_{Mg-Mg}(r)$

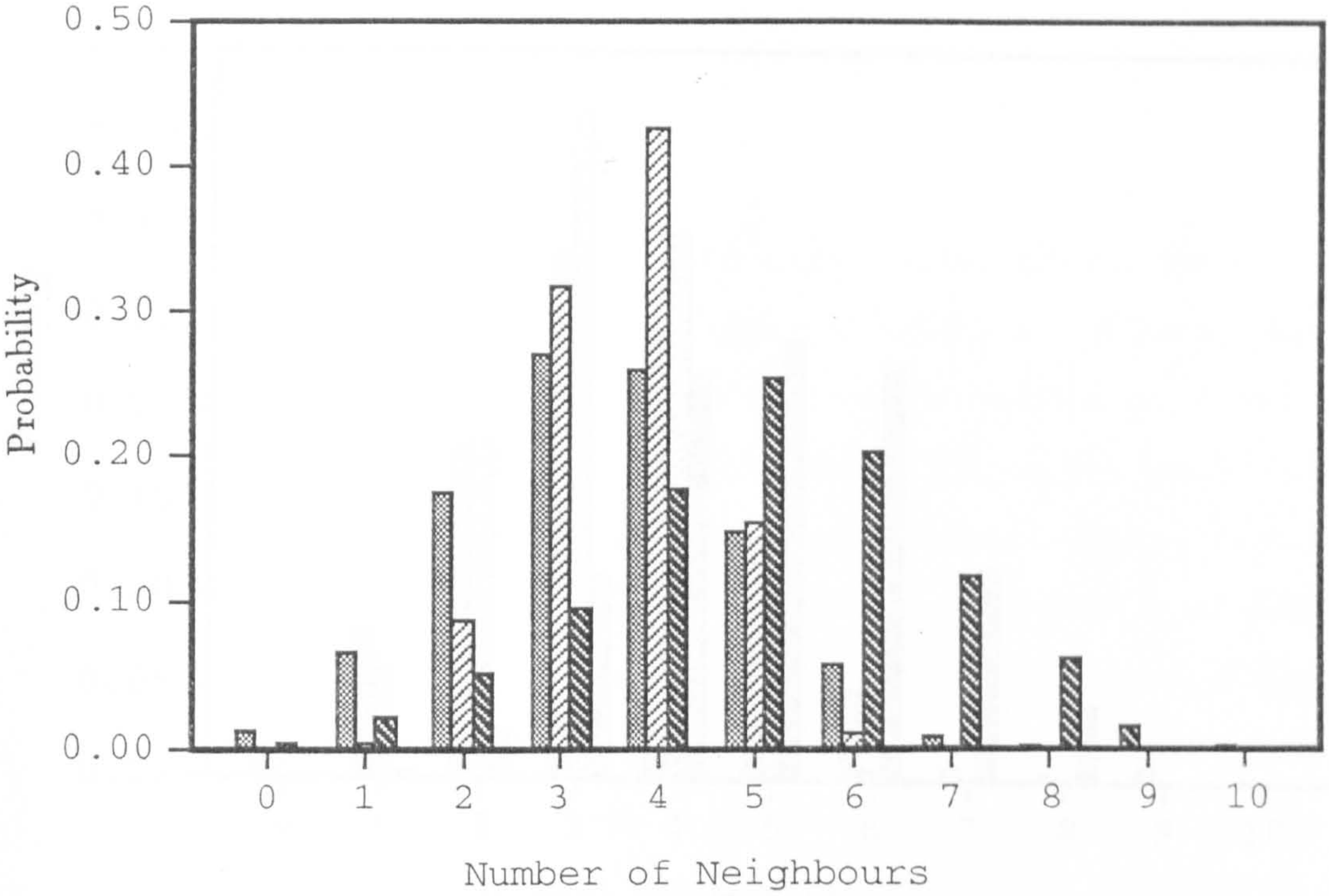

Figure 6.25: The distribution of the number of neighbours in liquid $Mg_{2.9}Bi_{2.1}$.

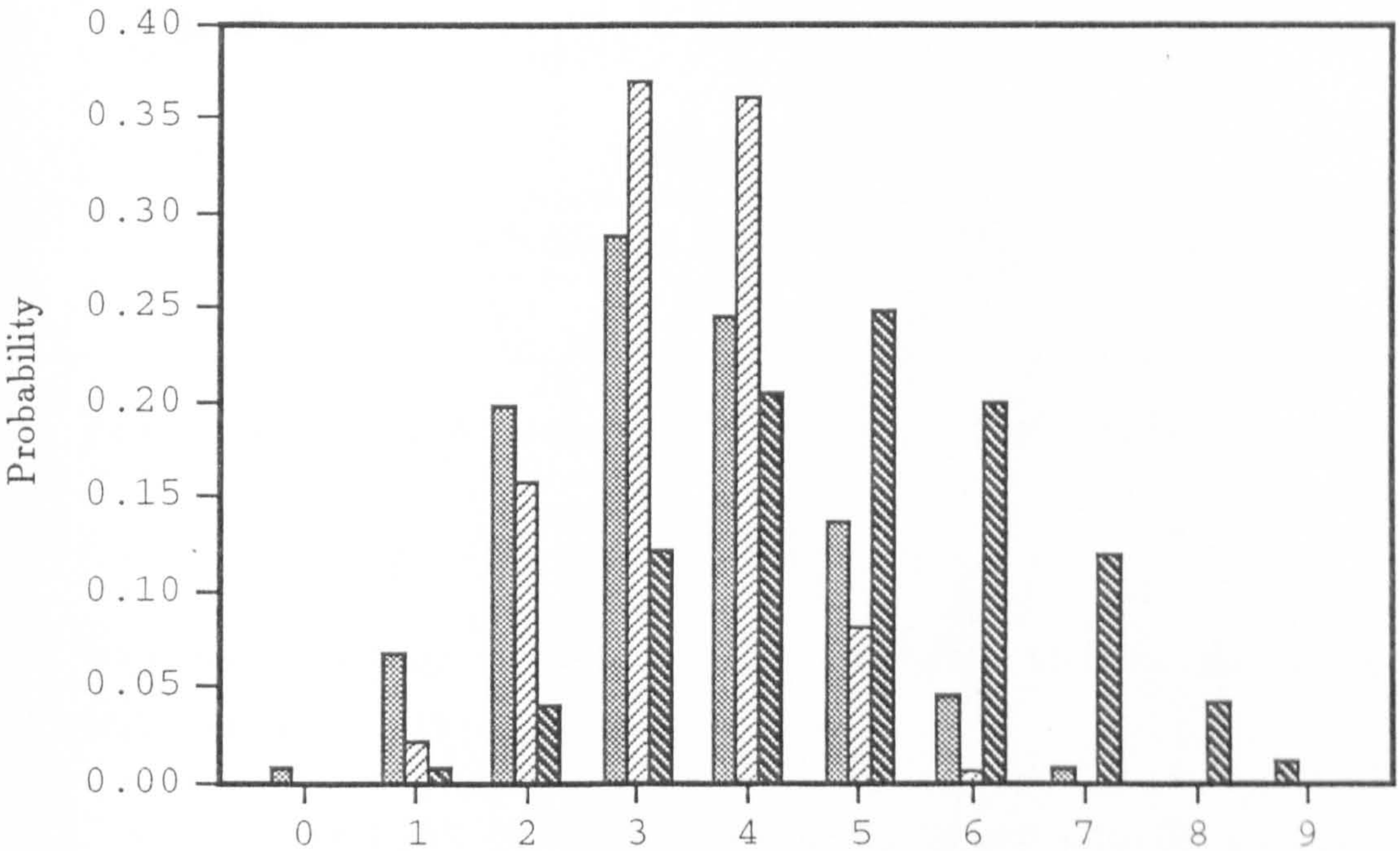

Figure 6.26: The distribution of the number of neighbours in liquid Mg_3Bi_2.

n_{Mg-Mg} n_{Mg-Bi} n_{Bi-Mg}

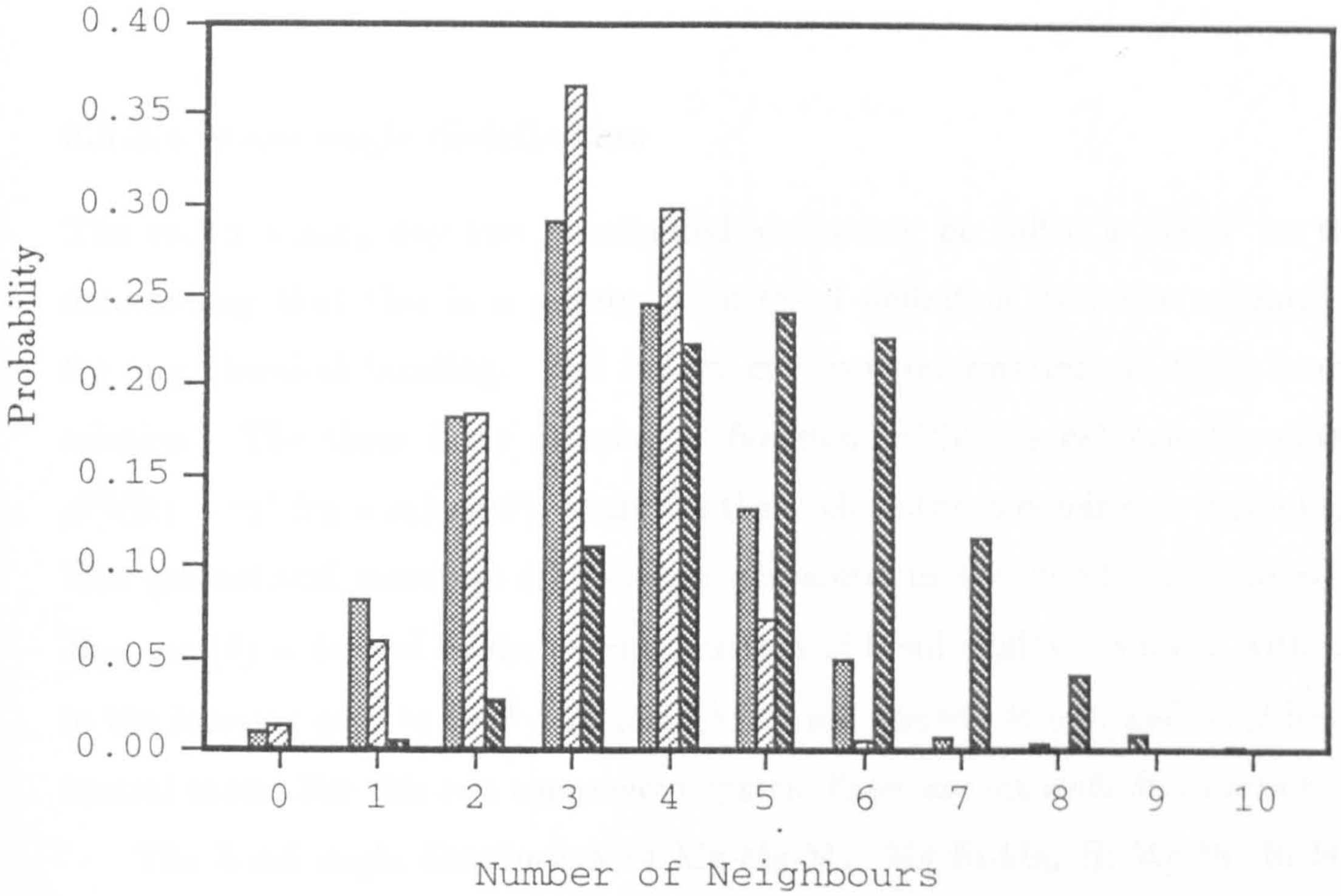

Figure 6.27: The distribution of the number of neighbours in liquid $Mg_{3.1}Bi_{1.9}$.

6.3.3.4 Bond angle distribution

The vector joining any two coordinated atoms can be called a 'bond' on the understanding that this is a purely geometrical definition and has no implication for any chemical bonding. But it can give you information on three body correlation. The three body correlation function $g^{(3)}(\mathbf{r_1}, \mathbf{r_2}, \mathbf{r_3})$ can be written as $g^{(3)}(|\mathbf{r_1} - \mathbf{r_2}|, |\mathbf{r_2} - \mathbf{r_3}|, cos\theta)$, where θ is the angle between bonds $\mathbf{r_1} - \mathbf{r_2}$ and $\mathbf{r_2} - \mathbf{r_3}$. The geometrical structure is therefore contained in the bond angle distribution. $B_{\alpha\beta\gamma}\ cos(\theta)$ is defined as the average number of bond angles per ion β with cosines in the interval $cos\theta$ to $cos\theta + \Delta(cos(\theta))$, for ion triplets of α, β and γ, β being the central atom. For this two component system there are six such distributions.

The bond angle distribution of Mg-Mg-Mg, Mg-Bi-Mg, Bi-Mg-Bi, Bi-Mg-Mg, Bi-Bi-Mg and Bi-Bi-Bi for the three samples are shown in fig. 6.28 - 6.33. All the three samples have almost exactly the same distribution patterns. The values of the bond angles are listed in Table 6.5.

Table 6.5 Bond angle

Mg-Mg-Mg	Mg-Bi-Mg	Bi-Mg-Bi	Bi-Mg-Mg	Bi-Bi-Mg	Bi-Bi-Bi
60° 120°	60°	90°	60°	30°	60°

Table 6.5 shows that the structural characteristic of β-Mg_3Bi_2 persists in the liquid.

A Summary of the structure studies:

From the experiments and RMC computer simulation, the following features of the studied systems could be concluded:

- When the α-phase of Mg_3Bi_2 transforms to the β-phase at a temperature of 703 ^oC, the lattice pattern changes from the trigonal to the cubic type. We have discovered that β-Mg_3Bi_2 has superionic structure.

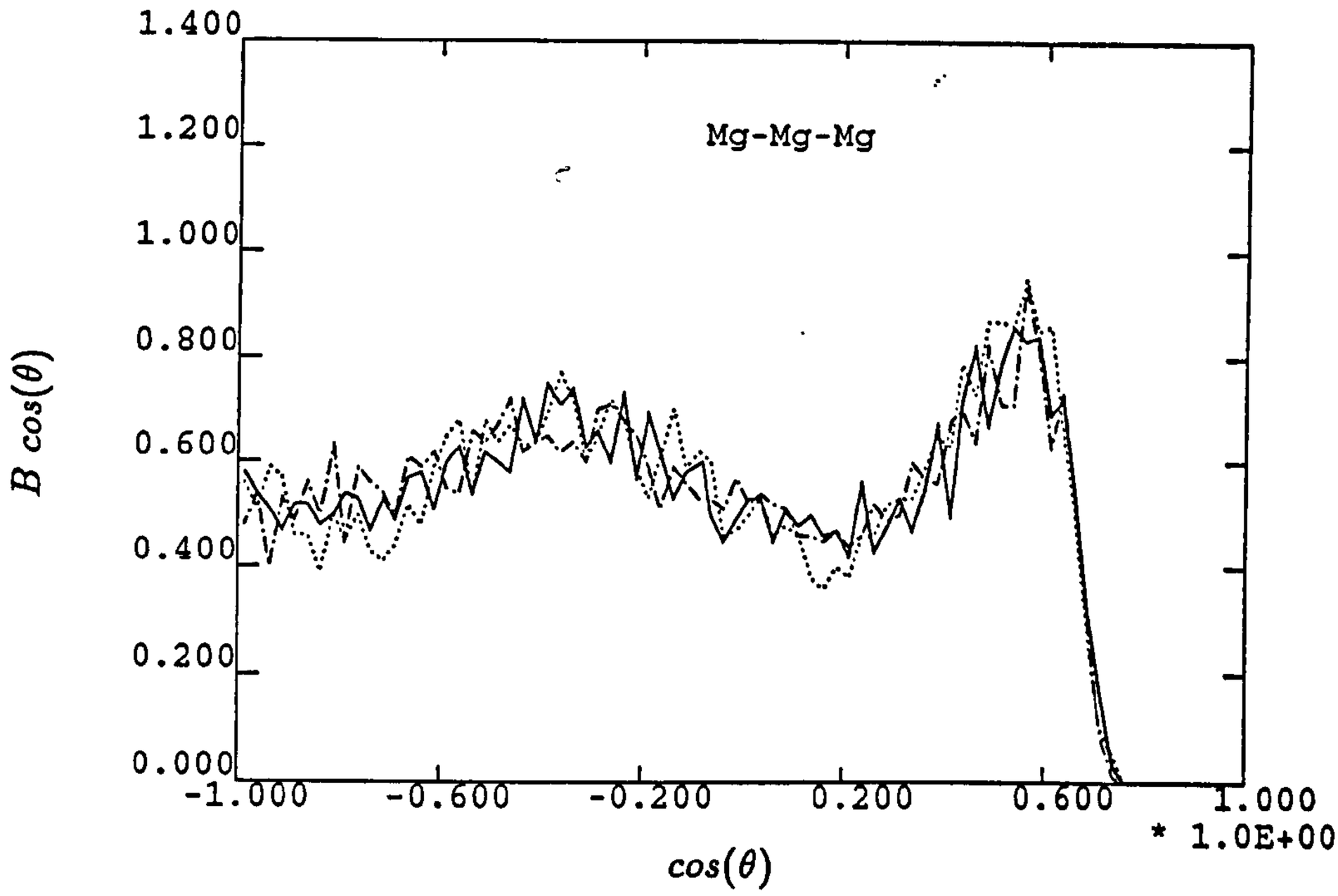

Figure 6.28: Distribution of the bond angle $Mg - Mg - Mg$ of liquid $Mg_{2.9}Bi_{2.1}$ (full line), Mg_3Bi_2 (dotted line) and $Mg_{3.1}Bi_{1.9}$ (dot-dash line).

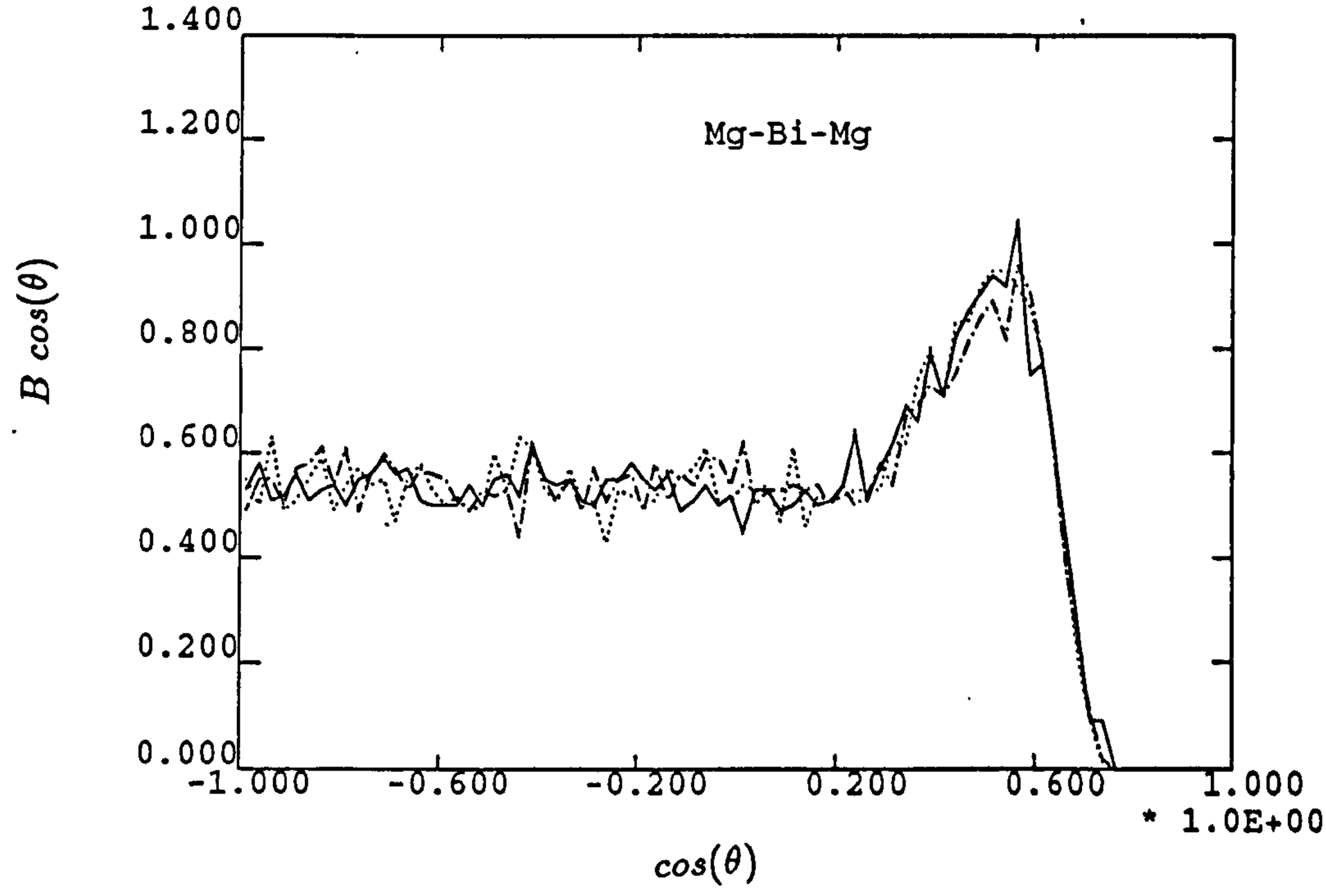

Figure 6.29: Distribution of the bond angle $Mg - Bi - Mg$ of liquid $Mg_{2.9}Bi_{2.1}$ (full line), Mg_3Bi_2 (dotted line) and $Mg_{3.1}Bi_{1.9}$ (dot-dash line).

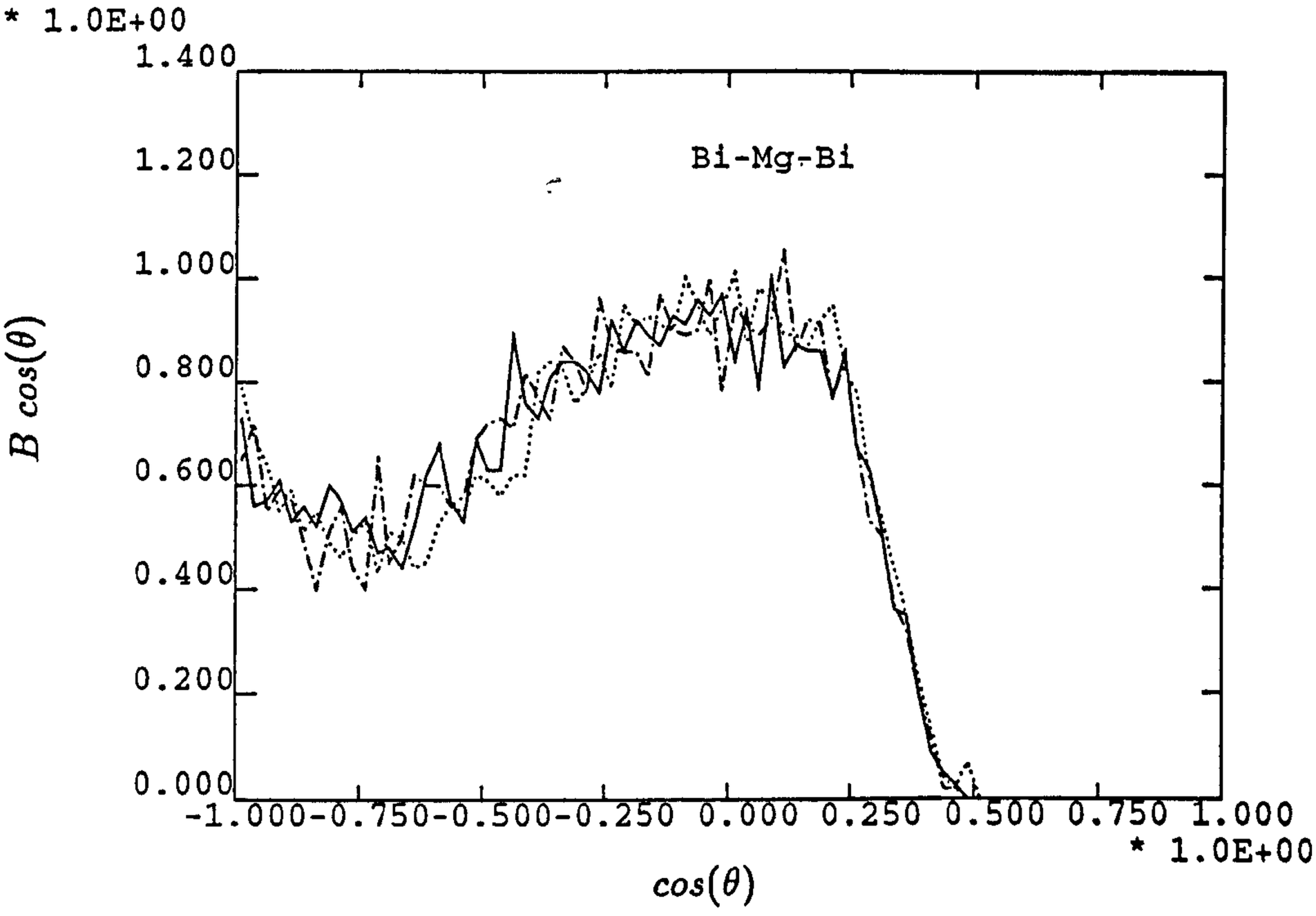

Figure 6.30: Distribution of the bond angle $Bi-Mg-Bi$ of liquid $Mg_{2.9}Bi_{2.1}$ (full line), Mg_3Bi_2 (dotted line) and $Mg_{3.1}Bi_{1.9}$ (dot-dash line).

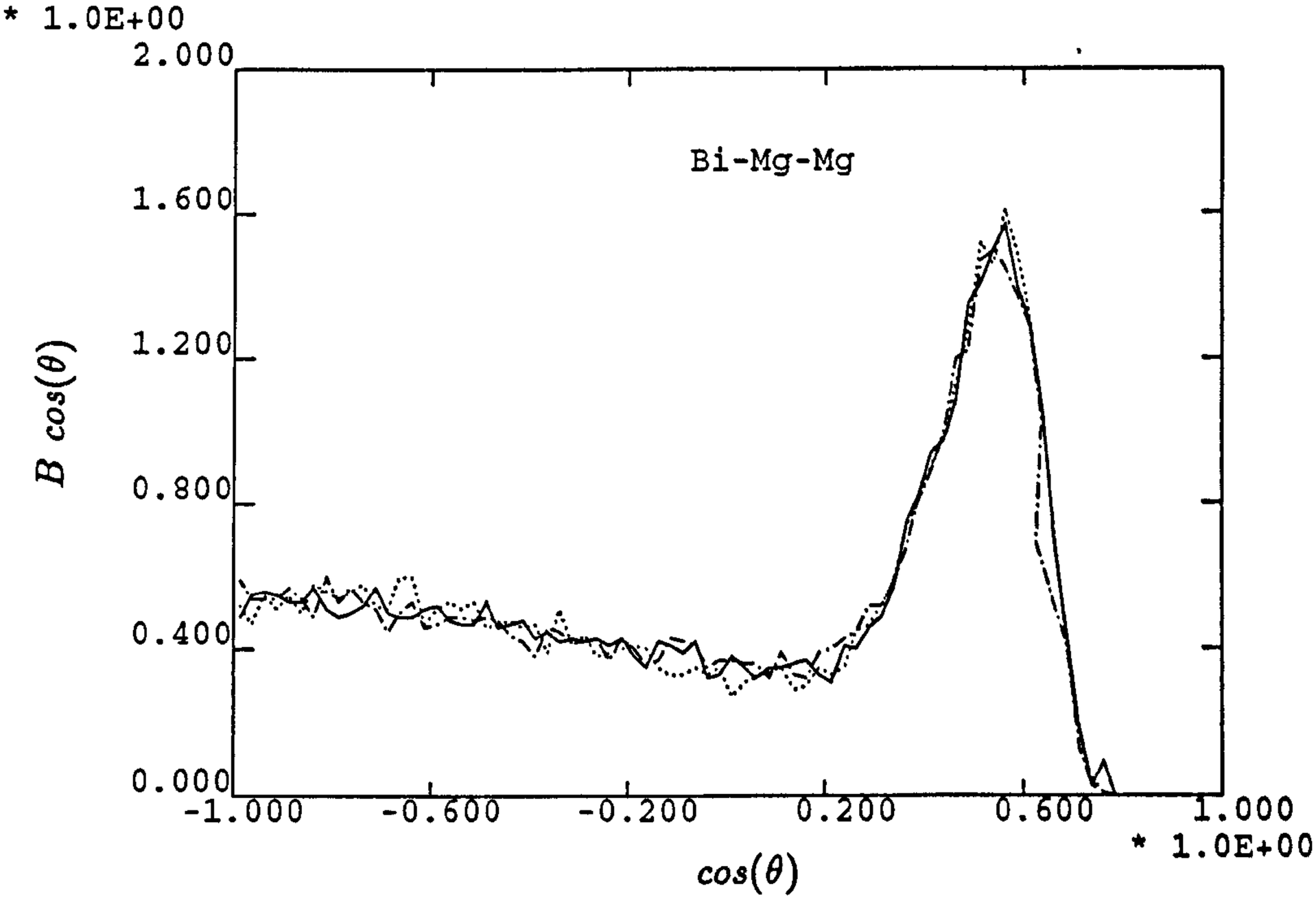

Figure 6.31: Distribution of the bond angle $Bi-Mg-Mg$ of liquid $Mg_{2.9}Bi_{2.1}$ (full line), Mg_3Bi_2 (dotted line) and $Mg_{3.1}Bi_{1.9}$ (dot-dash line).

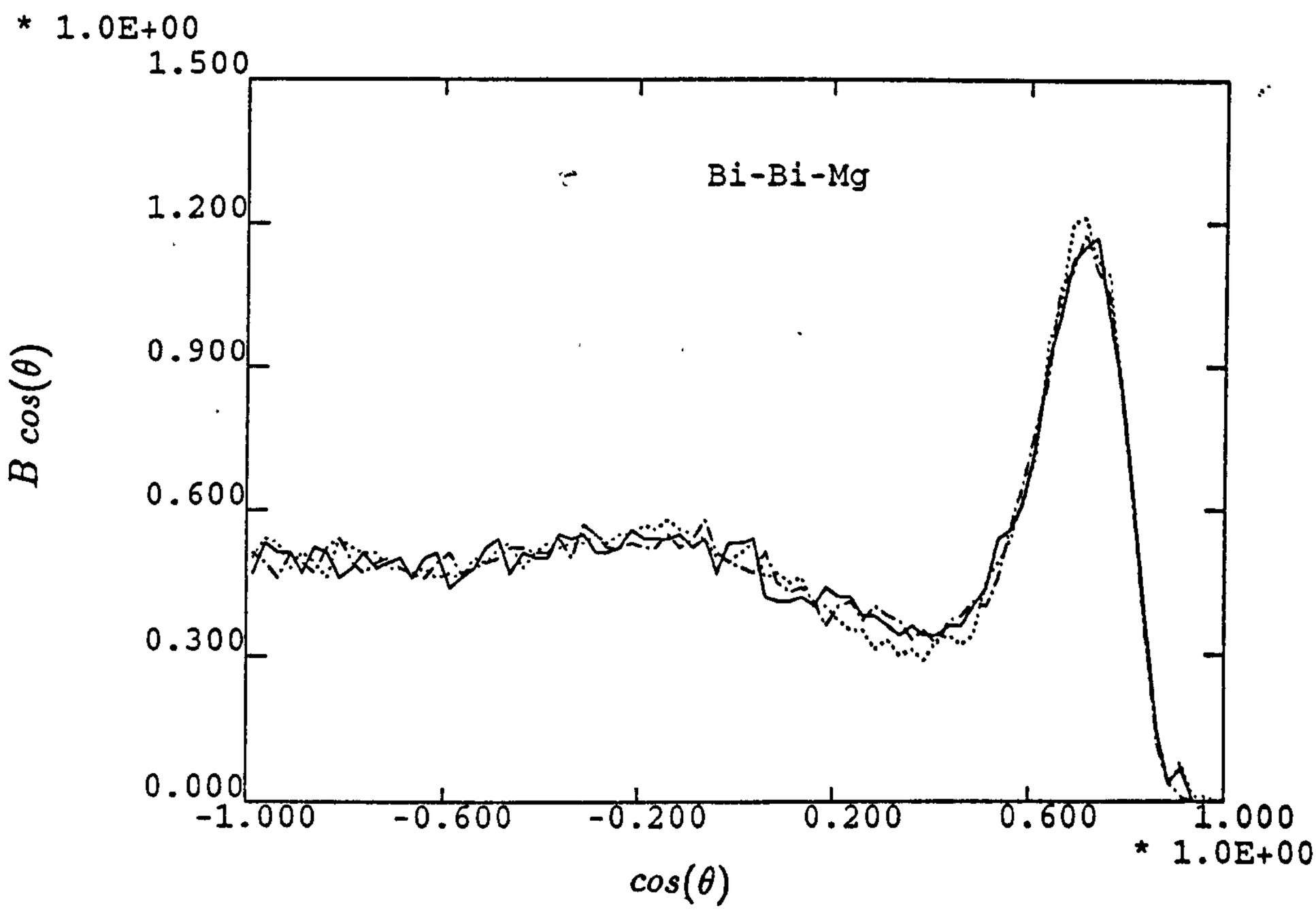

Figure 6.32: Distribution of the bond angle $Bi-Bi-Mg$ of liquid $Mg_{2.9}Bi_{2.1}$ (full line), Mg_3Bi_2 (dotted line) and $Mg_{3.1}Bi_{1.9}$ (dot-dash line).

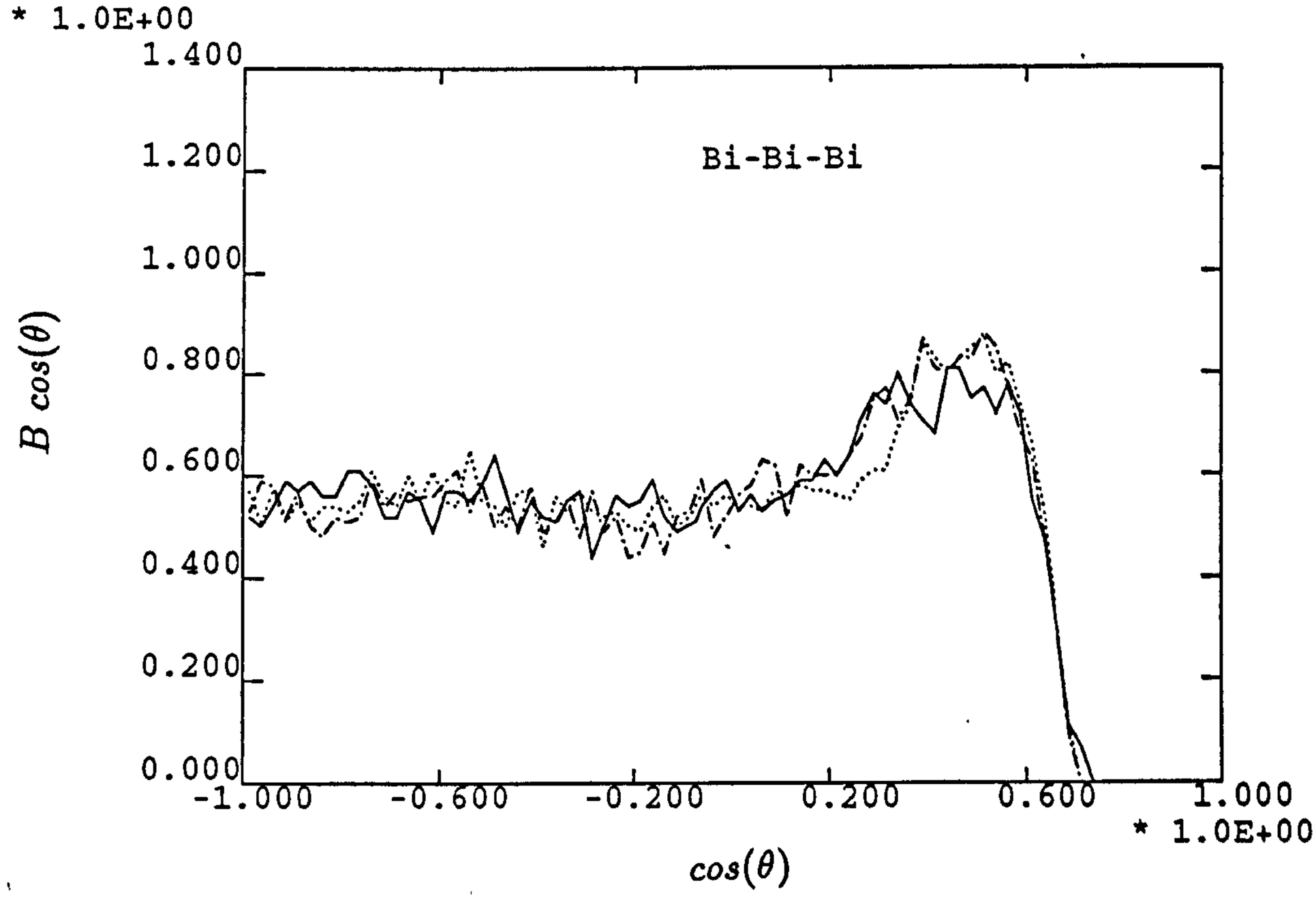

Figure 6.33: Distribution of the bond angle $Bi-Bi-Bi$ of liquid $Mg_{2.9}Bi_{2.1}$ (full line), Mg_3Bi_2 (dotted line) and $Mg_{3.1}Bi_{1.9}$ (dot-dash line).

- The features of crystal structure of β-Mg_3Bi_2 persist in the liquid at short range.

- A composition change of 2 $at.\%$ from the stoichiometry Mg_3Bi_2 in either component cause no dramatic structure change in comparison to the structure of Mg_3Bi_2.

- The total structure factors show a Coulomb shoulder which is generally accepted as one of the features of ionic compounds. The partial structure factors show the 'bench mark' of ionic compounds.

- The Bi is nearly heterocoordinated, having about 5 Mg atoms as its neighbours. The Mg is partially heterocoordinated with the neighbours of about 3 Bi atoms and 3 Mg atoms. In the $g(r)$, the incomplete heterocoordination is observed by the deep penetration of the first peak of $g_{Mg-Mg}(r)$ into the first peak of $g_{Mg-Bi}(r)$.

- The positions of the first peak of $g_{Mg-Bi}(r)$ for the three samples are about 2.9 Å which is approximately the sum (2.88 Å) of radii of Mg^{2+} and Bi^{3-}, but it is also close to the sum (2.87 Å) of the their covalent radii. The positions of the $g_{Mg-Mg}(r)$ are at about 3.1 Å which are roughly equivalent to the sum (3.2 Å) of their metallic radii.

6.4 Discussion

6.4.1 Relationship between ΔS and σ and E_g

It was demonstrated by Enderby and Barnes (1990a) that by using the Kubo-Greenwood equations and letting r=(α_C/α_V)=1 (symmetrical hole and electron conduction), for the case of $E_g >> kT$, σ , S and ΔS can be obtained analytically within the Boltzmann approximation. They are described by the E_g as

$$\sigma(T) = 2\alpha_V kT exp(-E_g/2kT) cosh(E_F/kT) \tag{6.4}$$

$$S(T) = -\frac{k}{e}\left[tanh\left(\frac{E_F}{kT}\right)\left(\frac{E_g}{2kT}+2\right) - \frac{E_F}{kT}\right] \tag{6.5}$$

$$\Delta S = \frac{(\frac{2k}{e})[-(\beta-1)^{1/2} + \beta^{1/2} tanh^{-1}((\beta-1)/\beta)^{1/2}]}{\beta^{1/2}}, \tag{6.6}$$

where $\beta = E_g/2kT + 2$. It is shown from equation (6.6) that ΔS depends only the conductivity gap (or the band gap) E_g for a given temperature. For values of E_g which are too small for the equation (6.6) to apply, the numerical integrations of the Kubo-Greenwood equations gives the E_g versus S, and the minimum conductivity σ_{min} shown in Figs. 6.34 and 6.35 respectively. It can be seen that the p-n transition ΔS increases almost linearly with the conductivity gap, and the conductivity decreases quickly as the conductivity gap is enlarged. The small conductivity requires a large band gap, while the small p-n transition ΔS of the thermopower needs small band gap. This conclusion clearly contradicts the experimental results of liquid $Mg - Bi$ in the vicinity of stoichiometry. The Kubo-Greenwood equations themselves may not be incorrect, as the problem could arise from the rigid band model which may not be applicable here. However it still helps as a starting point to pursue an understanding of liquid $Mg - Bi$.

According to the calculations the anomalous properties could be explained thus: when the composition is slightly away from stoichiometry, the electronic energy band no longer keeps its 'rigidity' and changes considerably; the band gap rapidly collapses within the change of composition of order of 0.1 - 0.5 *at.*% from stoichiometry; the chemical potential (or the Fermi energy) only shifts slightly.

In order to understand these changes, the intraatomic and interatomic structures of the system will be examined in the following sections.

6.4.2 Local structure and chemical bonding

Evidence for chemical compound formation in a liquid is usually based on three types of data: thermodynamic, structural and transport.

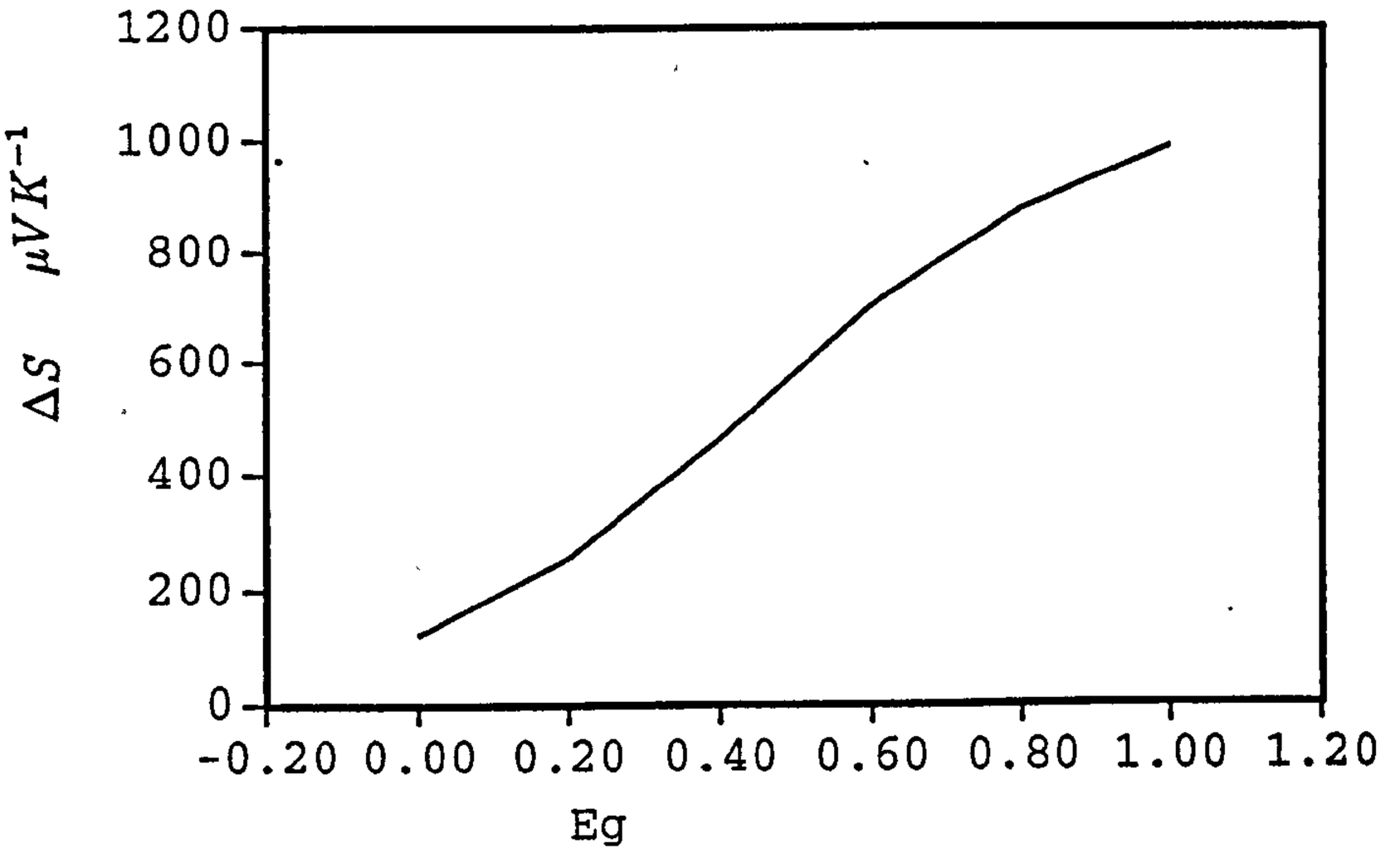

Figure 6.34: Relationship between the band gap E_g and the p-n transition ΔS of the thermopwer

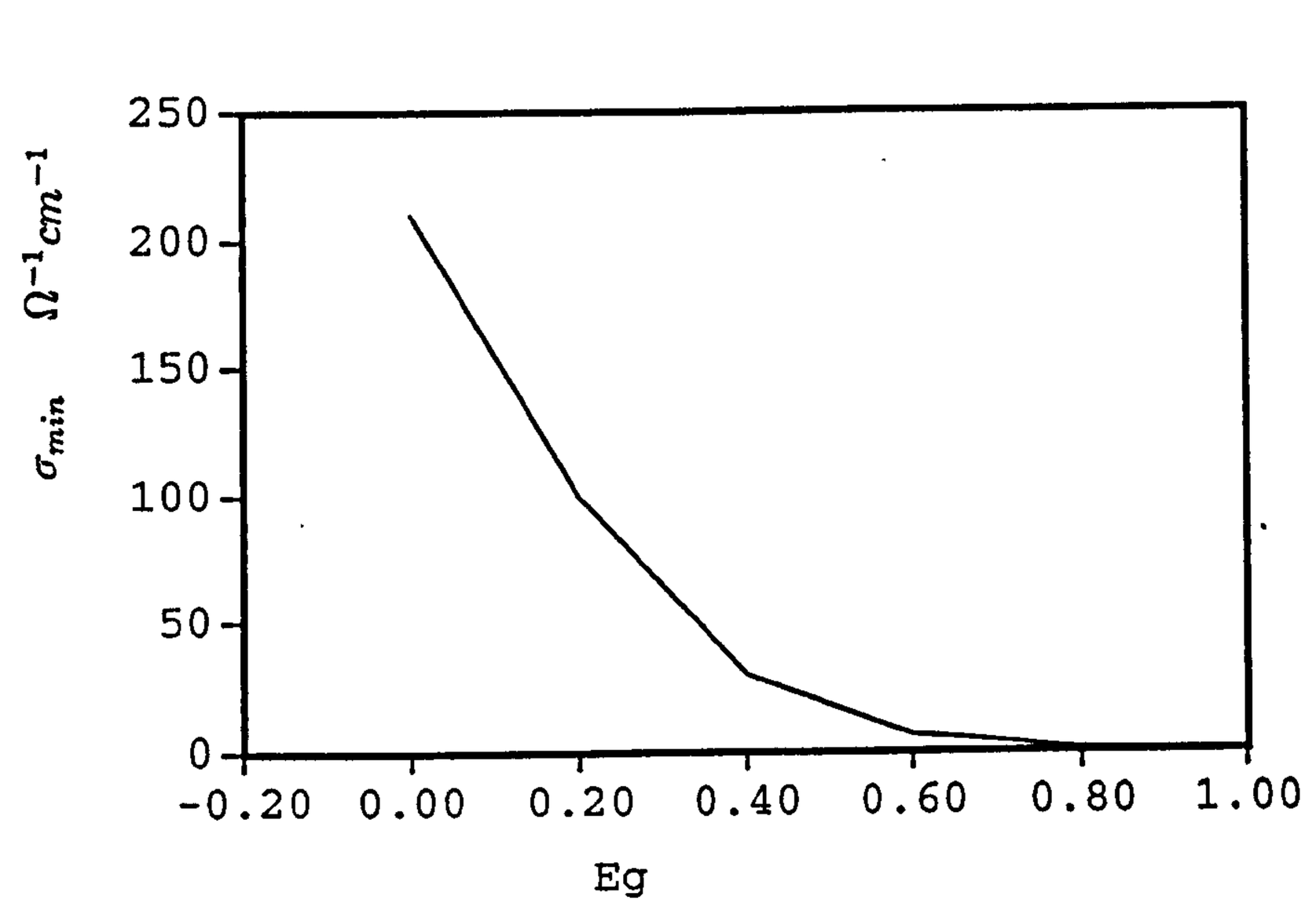

Figure 6.35: Relationship between the band gap E_g and the minimum conductivity σ_{min}.

In the thermodynamic case, the equilibrium phase diagram and the molar quantities including the entropy, enthalpy, and free energy can be used as the first evidence for the formation of a compound, but they can not be used to predict the nature of the bonding . An ideal confirmation of ionic bonding would be total and partial structure factors. The transport data can be used as supporting evidence for the formation of the compound and also for the nature of chemical bonding.

6.4.2.1 Thermodynamic evidence for the formation of the chemical compound Mg_3Bi_2

The equilibrium phase diagram Fig. 6.7 shows a sharp peak at the stoichiometric composition Mg_3Bi_2 which indicates that the compound can survive melting and exists stably in the liquid. The intermediate compound Mg_3Bi_2 undergoes a polymorphic transformation at 703 ^oC and melts congruently at 821 ^oC. Egan (1959) measured the thermodynamic properties of liquid $Mg - Bi$ alloy. The activity and relative integral molar quantities as a function of composition are reproduced in Fig. 6.36 and 37, respectively. It can be seen from Fig. 6.36 that the activity of Mg is nearly zero as the concentration of Mg is increased up to about 60 $at.\%$. When the concentration of Mg approaches to and exceeds 60 $at.\%$, the activity starts going up quickly. This indicates that for the composition lower than stoichiometry the added Mg which can not exist in a state of the metallic element, reacts with the Bi to form a chemical compound and consequently the effective concentration of metallic Mg is nearly zero. When the Mg concentration exceeds the stoichiometric composition the added Mg exists as a metal in the liquid, which leads to an increase in its activity.

The entropy, enthalpy and free energy in Fig. 6.37 give further evidence for the formation of the stoichiometric compound Mg_3Bi_2. The relative integrals of entropy, enthalpy and free energy show deep minima at stoichiometry, which hints that the local structure at this composition is due to chemical ordering and is stable in energy.

All the above evidence shows that stoichiometric Mg_3Bi_2 is a chemical compound.

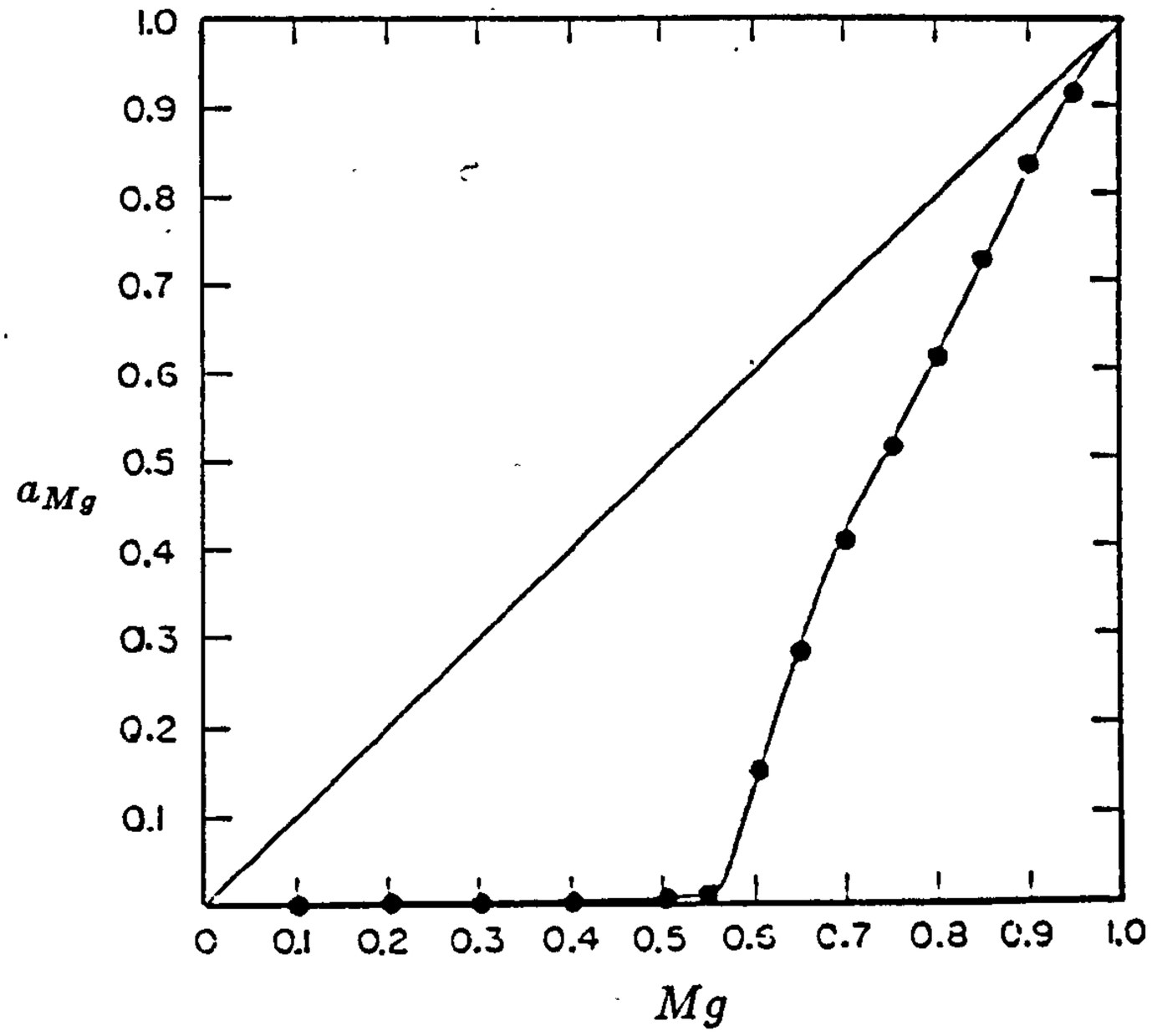

Figure 6.36: Activity of Mg in liquid $Mg - Bi$ as a function of composition at 700 ^{o}C.

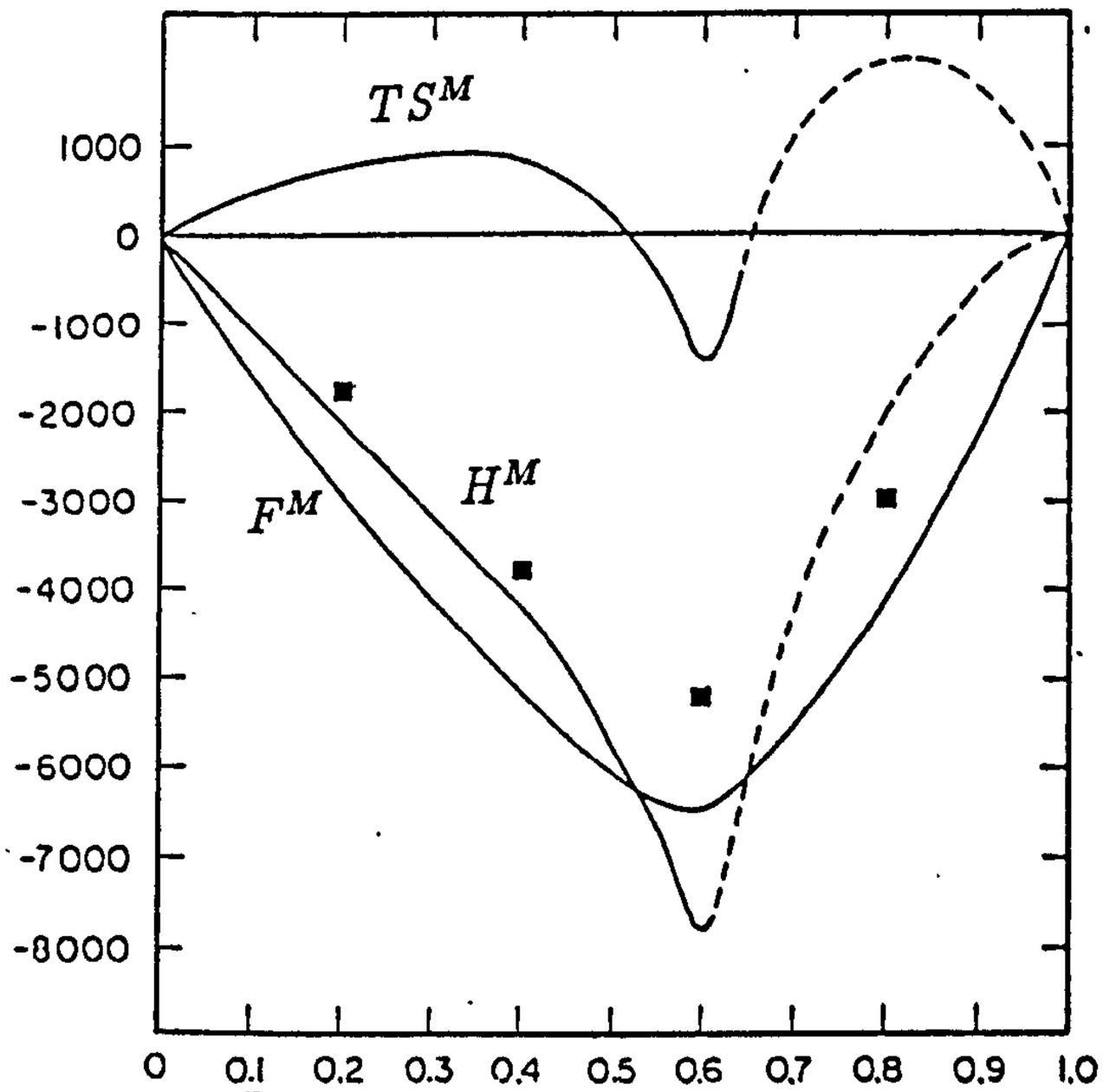

Figure 6.37: Relative integral molar quantities of liquid $Mg - Bi$ as a function of composition at 700 ^{o}C.

6.4.2.2 Structure factors and bonding properties

For ionic bonding the ionic ordering causes the ions to arrange themselves to maximise ionic screening and results in a heterocoordination. This arrangement is signalled in Q-space by a negative-going peak in $S_{+-}(Q)$ and positive peaks in $S_{++}(Q)$ and $S_{--}(Q)$ at the same value of a low Q. The combination of these three partial structure factors usually shows a small positive peak on the total structure factor. This arrangement is regarded as a bench mark of ionic bonding (Enderby *et al*, 1980, 1990a and Evans *et al*, 1980).

For the liquid Mg_3Bi_2, the arrangement of the partial structure factors $S_{Mg-Mg}(Q)$, $S_{Bi-Bi}(Q)$ and S_{Mg-Bi} which have been summarised in last section is basically in accord with the above principles, except that the peak of S_{Mg-Mg} is not pronounced enough compared with $S_{Na-Na}(Q)$ in NaCl, which is caused by the deep penetration of the first peak of $g_{Mg-Mg}(r)$ into the that of $g_{Mg-Bi}(r)$.

It is concluded that the chemical bonding of Mg_3Bi_2 is basically ionic, but it is far from a good ionic bonding.

6.4.3 The electronic structure of Mg_3Bi_2

Watson et al (1984) measured the electronic structures of crystalline Mg_3Bi_2 using soft X-ray emission and X-ray photoemission and calculated the corresponding electronic band and the density of states by the extended Huckel method, shown in Figs. 6.38 and 6.39. Sutton C M (1975) measured the optical properties of amorphous Mg-Bi alloy in the near infrared and visible spectral regions. They all agreed that amorphous Mg_3Bi_2 has a narrow band gap of E_g=0.15 eV (note: E_g=2~11 eV for alkali halides). It is known from Fig. 6.38 that the upper valence band is mainly developed from the Bi $6p$ electron orbitals and the lower conduction band principally from Mg $3s$ orbitals.

Robertson (1979) also calculated the electron band and the density of states and found the transfer of valence electrons from the Mg to the Bi.

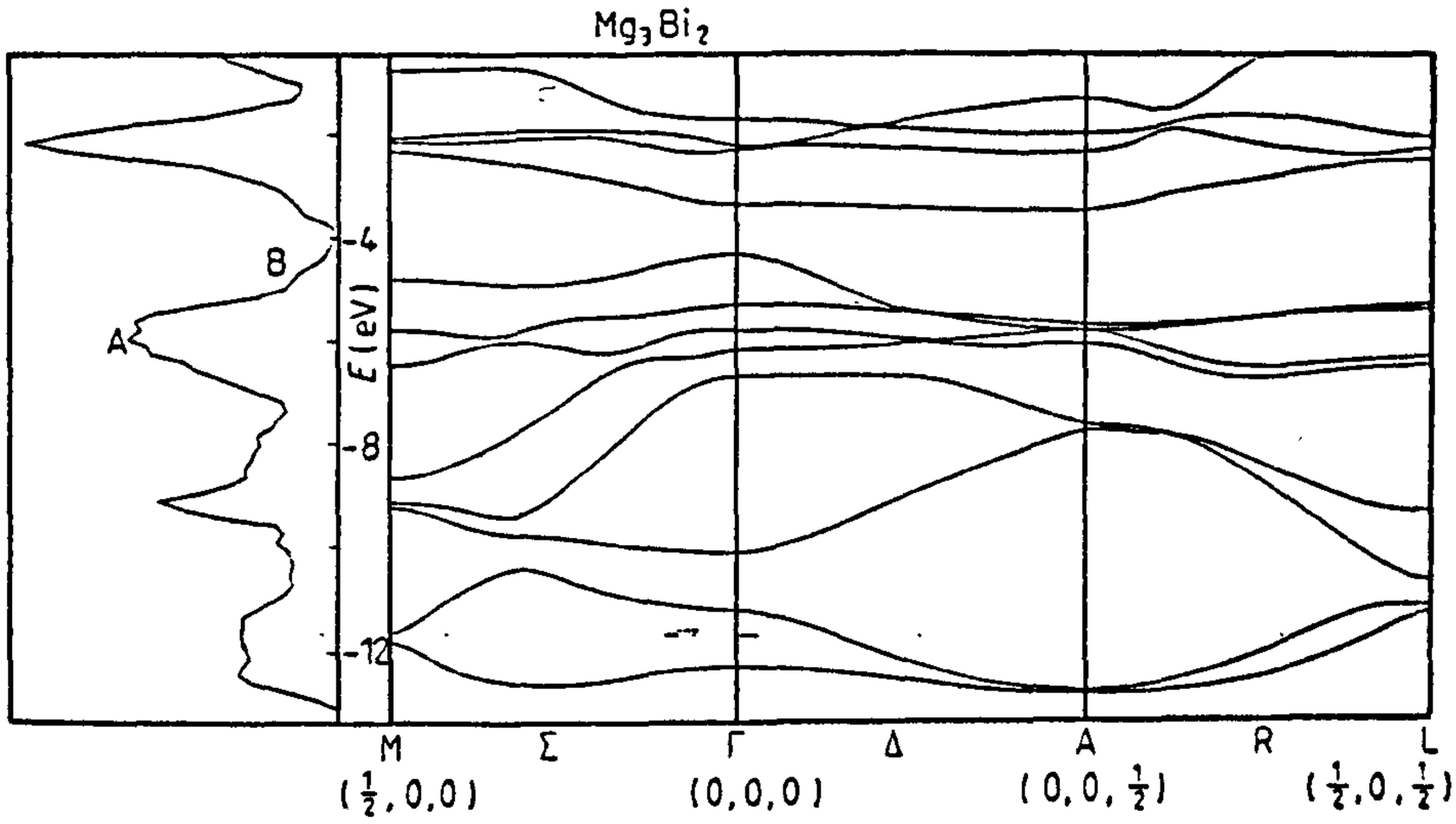

Figure 6.38: The calculated total density of states and band structure of Mg_3Bi_2. The symmetry point coordination are in dimensionless units.

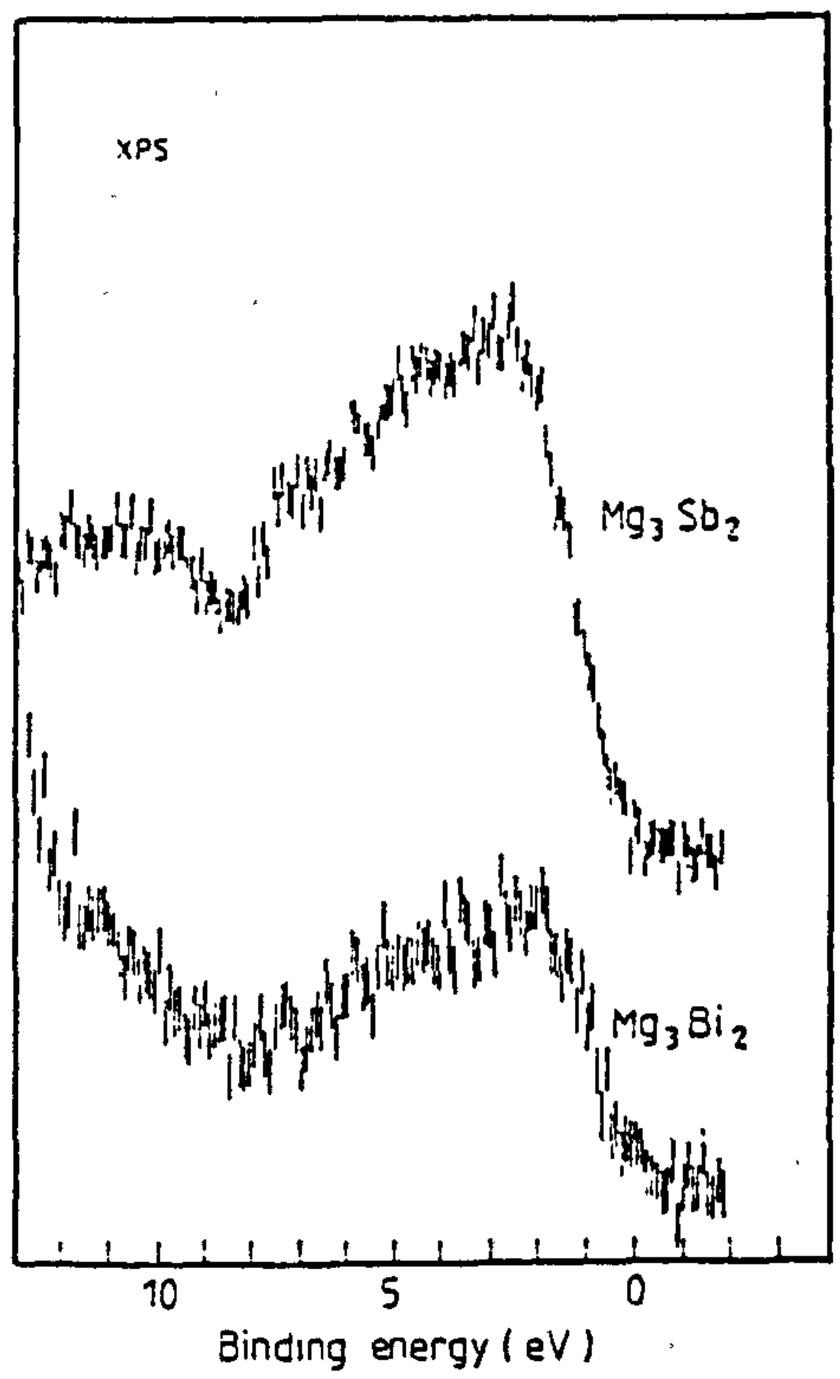

Figure 6.39: The $Mg\ K_\alpha$ excited x-ray photemission valence band spectra from Mg_3Sb_2 and Mg_3Bi_2

Both the band gap and electron transfer again demonstrate that Mg_3Bi_2 is basically ionic in bonding nature. The Madelung potential between the cation and the anion would, therefore, make a considerable contribution to the formation of the band gap. The small band gap reflects that the ionic bonding between the cation Mg and anion Bi is not strong and thus the conduction and valence band are not largely separated from each other. This is consistent with the analysis from the point of view of the interatomic structures in last section.

6.4.4 Density of states, Fermi Energy and excess electrons

We have obtained a basic picture of the intra-atomic and interatomic structures of Mg_3Bi_2 through the above discussions. If the chemical boding of Mg_3Bi_2 is regarded as essentially ionic, the band structure can be mapped out schematically in Fig.6.40(a) from the view of chemistry. At stoichiometry, the conduction band wave functions are concentrated on the Mg cations and the valence band wave functions on the Bi anions and there are no holes in the Bi-like valence band and no electrons in the Mg-like conduction band. The Fermi energy lies in the middle of the band gap E_g. The band gap originates mainly from the Madelung potential (MP).

In the case of the liquid, the fluctuation in the Madelung potential due to the disordering makes the density of states extend into the band gap and the edges of the conduction and valence band may overlap, forming a localised pesudogap in the Anderson sense. Thus any of the factors which affect the Madelung potential between the cation and the anion would influence the band gap.

We now consider the possible effects of excess electrons or holes on the density of states and Fermi energy as the compositions are slightly away from stoichiometry Mg_3Bi_2, as shown in Fig. 6.40(b). When either of the elements is in excess, changes of the density of states and Fermi energy depend on the existing states of the excess electrons or holes which are directly related to the interatomic interaction and correlation among electrons. First, let us consider some hypothetical cases.

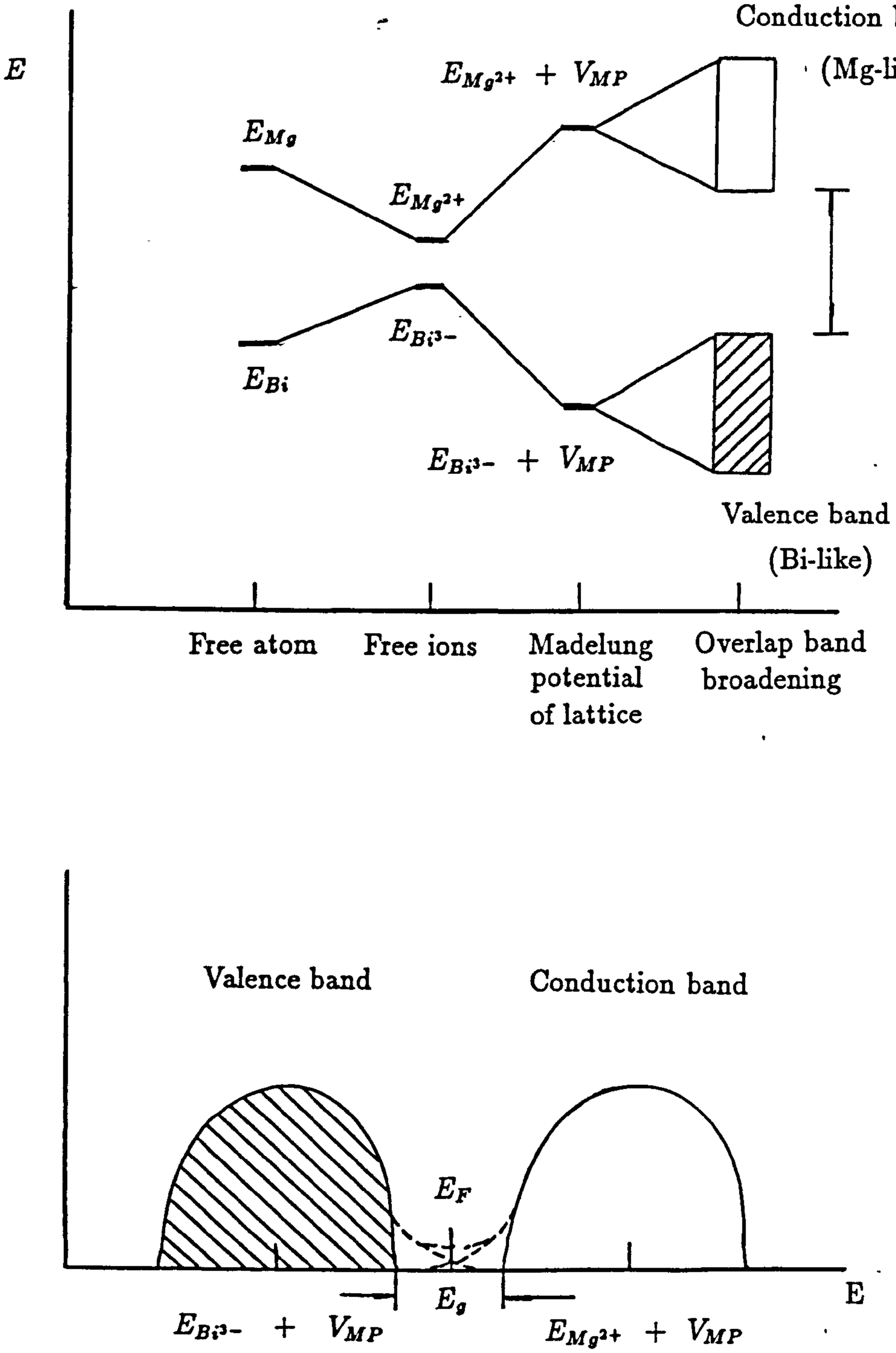

Figure 6.40: A schematic illustration of the band structure of Mg_3Bi_2. (a). crystal; (b). non-crystal with the band tails.

6.4.3.1 An ideal case - no interaction and correlation

MA (M is more electropositive than A) is basically an ionic compound. A very small amount of M (or A) is dissolved and ionised in the liquid stoichiometric compound MA. The addition of M or A does not cause a significant change in the density of states and the band is considered as 'rigid'. The orbitals of the excess electrons will lie in the M-like conduction band (the holes in the A like valence band if A is in excess). Consequently the Fermi energy shows a corresponding shift away from the middle of the band gap into the bands, and band gap remains unaffected. This process is schematically presented in Fig.6.41. The Kubo-Greenwood equations based on the rigid band model (BE theory) are applicable in this case.

6.4.3.2. The excess atoms react with the like species

If the ionised excess atoms react chemically with their like species, there is a possibility for the formation of a cluster ion $(M_n)^{1+}$ or $(A_m)^{1-}$ (m and n is greater than one). The ionic bonding between M and A does not preclude the formation of the bonds between the like species. For the case of $Mg + Mg_3Bi_2$ it can be expressed as $[(Mg_n)^{2+}]_3[(Bi)^{3-}]_2$. The chemical bonding between the like ions could be either covalent or metallic. There may be two kinds of bonding in the cluster compound, the ionic and metallic, for the system of liquid Mg-Bi. Within atomic cluster of Mg_n^{2+}, the bonding between $Mg - Mg$ is presumably metallic and similar to that of metallic Mg. The bonding between Mg and Bi is ionic, which has been discussed in last section. The energies states of the bonding electrons in the cluster compound are different from those in the stoichiometric compound. The rigid band model loses its applicability in this case. There may be two effects of the excess atoms on the density of states:

1. Reducing the Madelung potential; With ionic bonding in a compound M_aA_m each bond dipole places an effective charge $Z_m = aI$ on the M atom and $Z_a = mI$ on the A atom, where I is the Pauling ionicity.

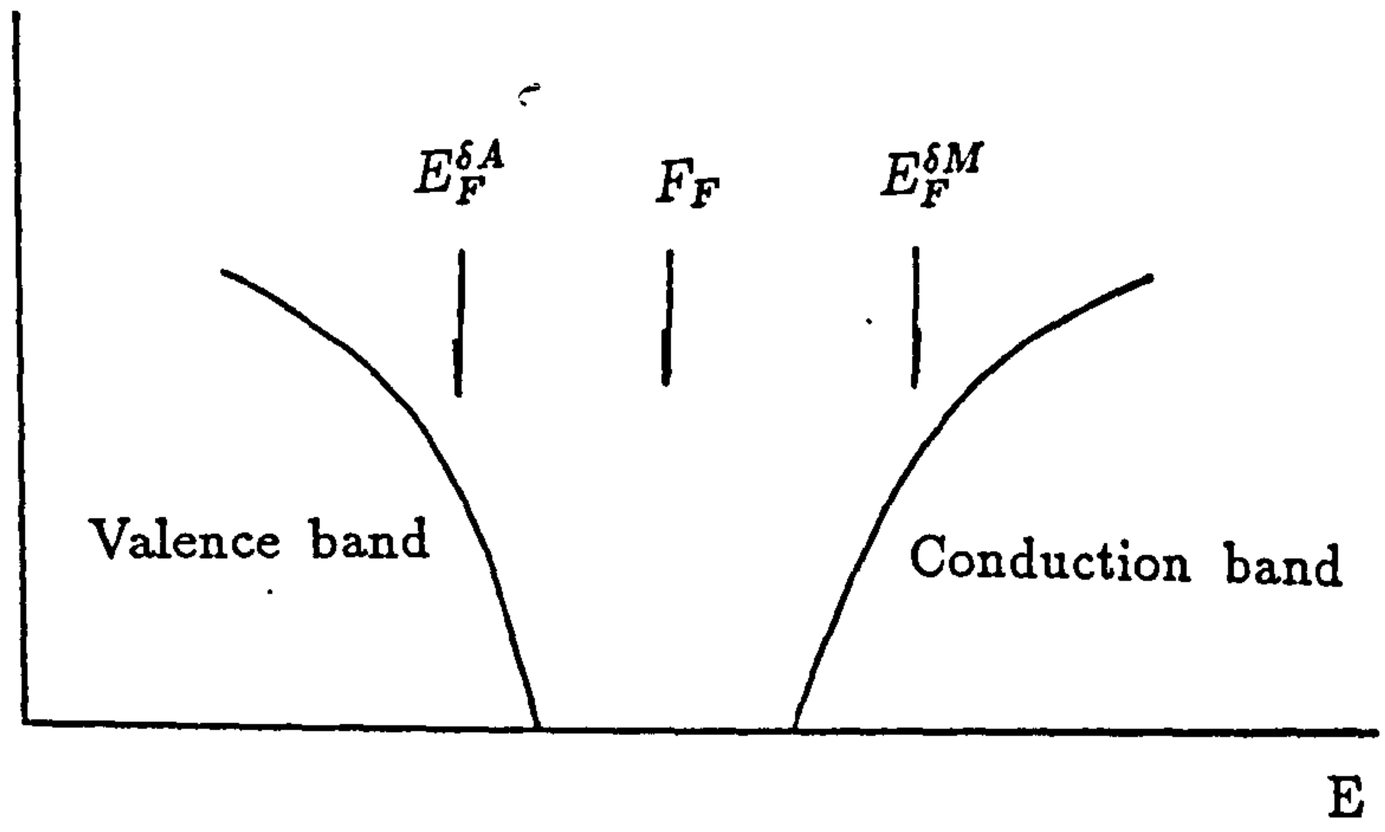

Figure 6.41: A schematic illustration of the Fermi energy shift with composition

This causes a potential difference which can be conveniently thought of as a Madelung potential (Cutler, 1977),

$$\phi = 0.8(a+m)e^2I^2/r \tag{6.7}$$

where r is the interatomic distance. For the stoichiometric compound Mg_3Bi_2, m and a are equal to 2 and 3 respectively. For the cluster compound $[(Mg_n)^{2+}]_3[(Bi)^{3-}]_2$, a will effectively be less than 3 and r in this case should be replaced with r_M which is the distance between the Bi and the mass center of the cluster ion $(Mg_n)^{2+}$ and it is generally larger than r. This will largely reduce the Madelung potential. The conduction and valence bands consequently move towards each other and the band gap diminishes, whilst the Fermi energy E_F remains close to the center of the band gap.

2. Increasing the metallicity; The metallicity of the cluster compound is enhanced due to the formation of the metallic bonding between the like species. The metallic bonding will considerably reduce the madelung potential through the electronic screening effect. The conduction ability of the electrons may effectively be improved since the electrons are delocalised by the metallic bonds. The metallicity of the cluster compound would also reduce the Madelung potential, but it would not necessarily cause a movement of the Fermi energy towards the conduction band.

Overall the effects of the excess electrons or hole would be that the band gap tends to close up and the Fermi energy E_F has a small shift relative to its original position in the stoichiometric compound. However the density of states at the Fermi energy E_F could have quite a large change as a result of the closing of the band gap, as shown in Fig.6.42.

The above analysis give a preliminary explanation why the band gap collapses and the Fermi energy has no significant shift as the composition is moved slightly away stoichiometry. It may be speculated, however, that if the band structure has

such a large change then the interatomic structures would also show an appreciable response. Such a response has not been observed in the structural studies by neutron diffraction.

It is interesting to observe that liquid semiconductors whose high temperature phases before the melting have superionic structure all show unusual electronic behaviour, for example the copper and silver chalcogenides. It has been shown in this thesis that the β-Mg_3Bi_2 has superionic structure. Ramasesha (1982) studied the interaction between mobile ions and mobile electrons in superionic conductors and found that the mobile electrons and mobile ions have an effective attractive interaction leading to a lowering of the total free energy. The creation of mobile ions favours creation of mobile electrons, which accompanies a reduction in the band gap due to the fact that the interstitial ions reduce the Madelung splitting of the band. According to this analysis it is indeed possible that the further creation of the interstitial ions by adding excess Mg in β-Mg_3Bi_2 results in a collapse of the band gap.

The conduction mechanism in liquid $Mg - Bi$ is subtle and interesting. It is clear from these studies that more theoretical work (*ie* understanding the effect of ion mobility on the electron transport and density of states) and experimental work (for example, experiment to determine electronic density of states through for example magnetic susceptibility) is needed to understand fully this system.

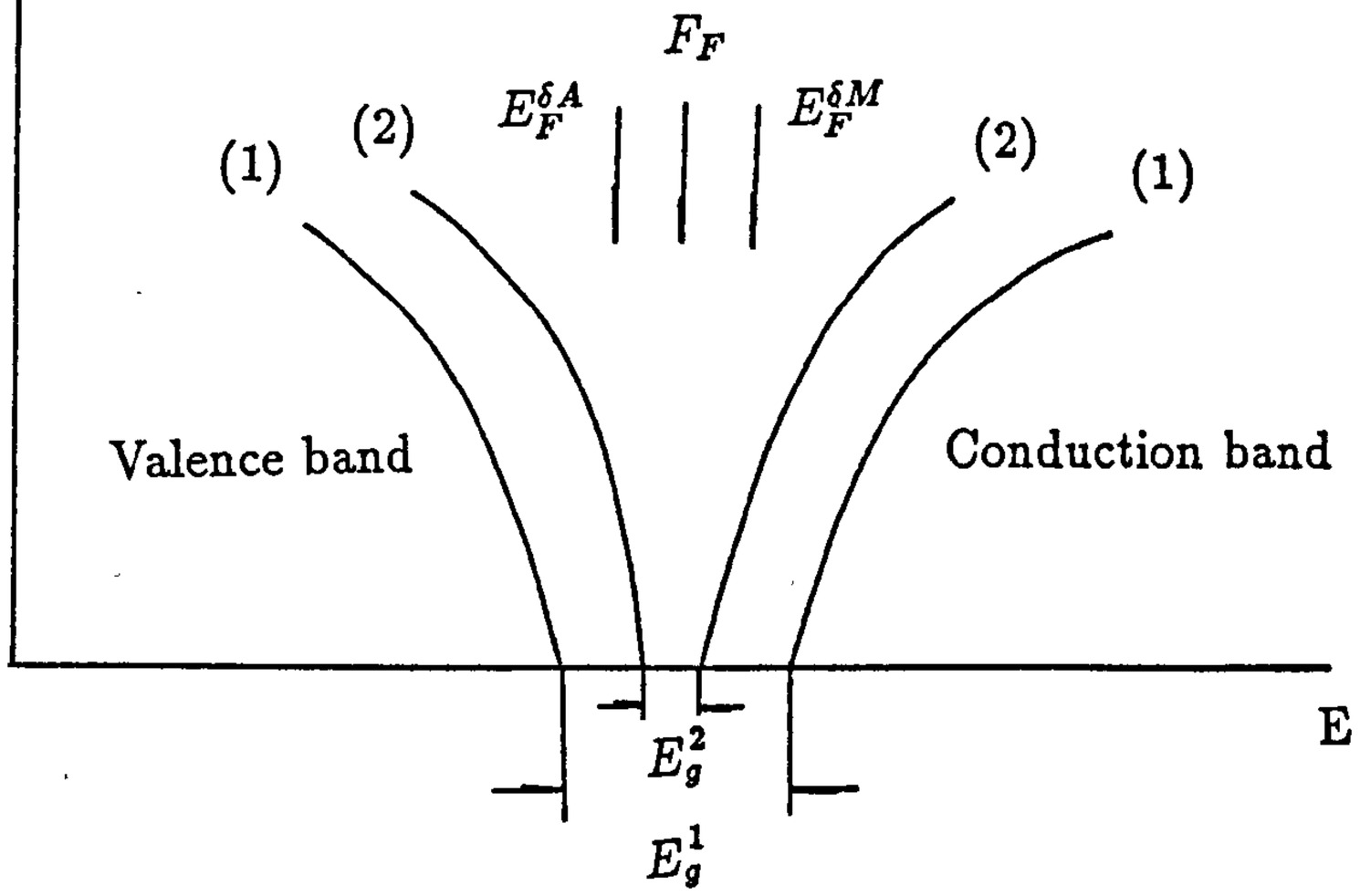

Figure 6.42: A schematic illustration of the band gap closing and the Fermi energy shift with composition. (1). The band at stoichiometry; (2). The band when adding small amount of A (or M) in the stoichiometric composition MA

Chapter 7

The Structural and Electronic Properties of Tl Chalcogenides - TlCl

7.1 Introduction

Enderby and Barnes (1987) pointed out that for $(E_F - E_v)/kT \geq 2$, the electrical conductivity (σ_s) of a liquid semiconducting sulphide M_2S (M is Ag, Cu, Tl and Sn), in the high temperature limit is given, to an excellent approximation, by

$$\sigma_s = \sigma_m exp(-q_s) \tag{7.1}$$

where q_s=$(E_F - E_v)/kT$ and σ_m is defined as

$$\sigma_m = \frac{e^2}{3\pi^2\hbar a} \tag{7.2}$$

where σ_m is characteristic conductivity, $\sigma_m \approx 350\ \Omega^{-1}cm^{-1}$ for a liquid semiconductor. In this model, when a liquid semiconductor is dissolved in a molten salt, for example Cu_2S + CuCl, $E_F - E_v$ increases, and is assumed to have a linear dependence on the mole fraction of the molten salt (c). Assuming the Fermi energy lies in the middle of the band gap E_g, $E_F - E_v$ is equal to $E_g/2$.

According to the Kubo-Greenwood equations based on a rigid band model (BE theory), the enlargement of the band gap will consequently give rise to an increase in the p-n transition (ΔS) of thermopower.

In this work, Tl_2Te - TlCl and Tl_2Se - TlCl were chosen as systems to test this theory. It has two purposes: (1) to test the above theory as the thallium chalcogenides have a good p-n transition of the thermopower as the composition is moved slightly away stoichiometry (Cutler, 1977); (2) to further test the validity of the Kubo-Greenwood equation with a rigid band model.

The careful measurements of the conductivity and thermopower in the vicinity of stoichiometry were carried out at an interval of 0.5 *at.*%. The conductivity and thermopower corresponding to the experiments have been calculated using BE theory.

In order to understand the local structures and the chemical bonding of the stoichiometric compound, neutron diffraction measurements of Tl_2Se have been performed to the partial structure factor level using isotopic substitution.

7.2 Neutron diffraction of liquid thallium selenide

7.2.1 Experimental

The neutron diffraction measurements of Tl_2Se were made using the SANDALS diffractometer at the ISIS neutron facility at the Rutherford-Appleton laboratory. The method of isotopic substitution was employed to determine the partial structure factors. The data was corrected for absorption and multiple scattering (the method described in chapter 5).

The structurally significant part of a neutron diffraction pattern can be written as

$$S(Q) = \sum_{i=1}^{N}\sum_{j=1}^{N} c_i c_j b_i b_j (S_{ij}(Q) - 1) \tag{7.3}$$

$S(Q)$ is related to the radial distribution function $g(r)$ by

$$g(r) = 1 + \frac{1}{2\pi^2\rho r}\int_0^\infty Q(S(Q)-1)sin(Qr)dQ \qquad (7.4)$$

In this work the partial structure factors of Tl_2Se was determined from three samples prepared from the pure elements using the following isotope combinations: $^{nat}Tl_2{}^{nat}Se$, $^{205}Tl_2$ ^{nat}Se, and $^{203}Tl_2{}^{76}Se$.

The data were corrected using the ATLAS analysis programmes available at ISIS. Special care was taken with the furnace corrections due to the high background scattering of the sample environment in this diffractometer. The relevant neutron parameters for the isotopes used in the experiments are shown in table 7.1.

Table 7.1 Coherent scattering length and scattering cross section

	Coherent scattering length	scattering c/s	Absorption c/s
^{76}Se	12.20	18.70	85.0
^{nat}Se	7.97	8.31	11.7
^{203}Tl	6.99	6.10	11.4
^{205}Tl	9.54	11.4	0.11
^{nat}Tl	8.785	9.70	3.43

In table 7.1, the coherent scattering length is in unit of (fm), the scattering cross-section (c/s) in (barns) and absorption cross-section (c/s) in (barns).

7.2.2 Experimental results

The $S(Q)$s for the three liquefied samples, after corrections for absorption and multiple correction are shown in Fig. 7.1. With this isotope combination it is noticeable how similar the diffraction patterns appear. The weighting, in matrix form, of the partial structure factors in the three samples is as follows:

$$\begin{vmatrix} 0.3430 & 0.0706 & 0.3112 \\ 0.4045 & 0.0706 & 0.3379 \\ 0.2172 & 0.1654 & 0.3790 \end{vmatrix} \begin{vmatrix} S_{TlTl}(Q)-1 \\ S_{SeSe}(Q)-1 \\ S_{TlSe}(Q)-1 \end{vmatrix} = \begin{vmatrix} S_{(nat,nat)}(Q) \\ S_{(205,nat)}(Q) \\ S_{(203,76)}(Q) \end{vmatrix}$$

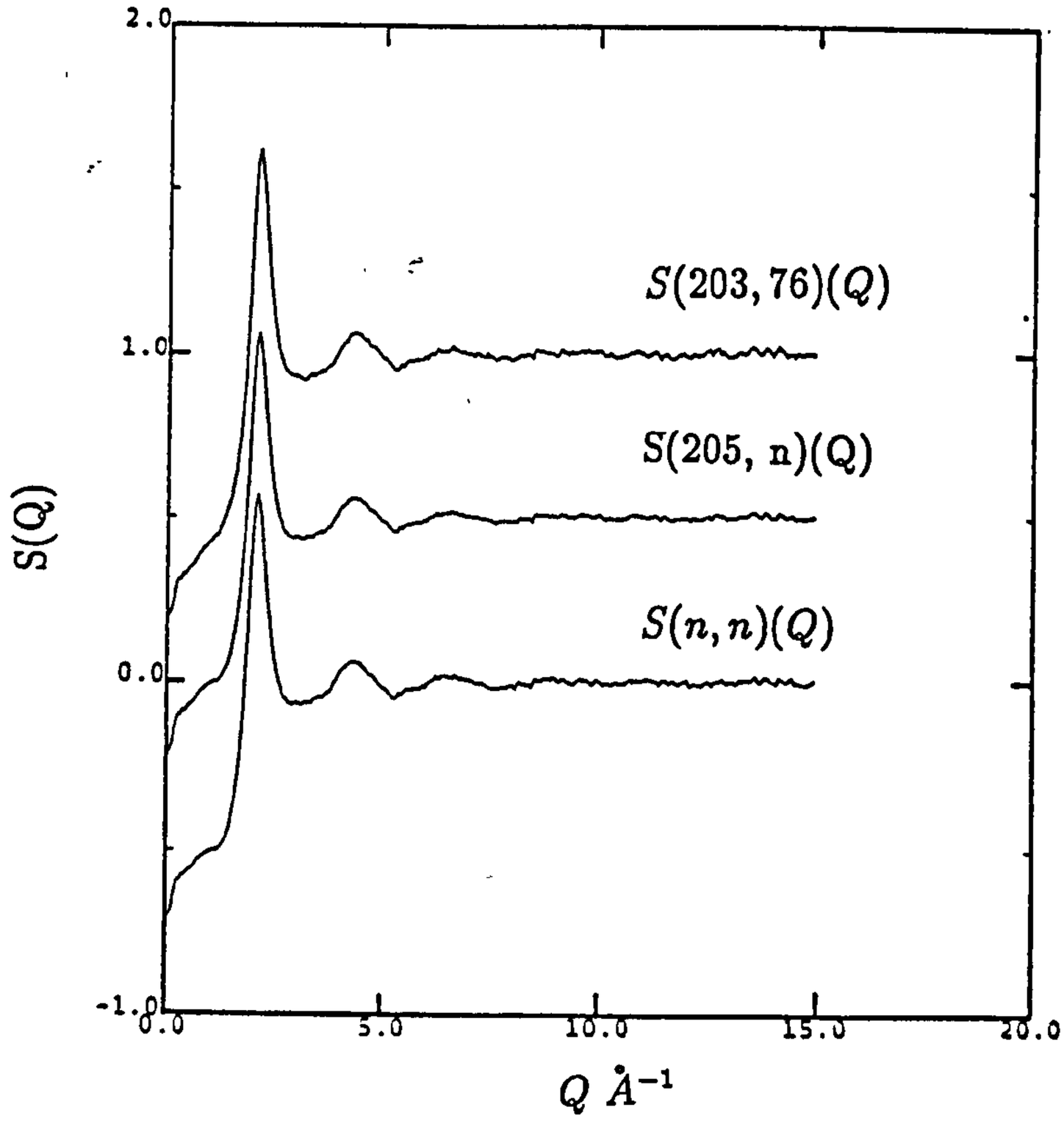

Figure 7.1: The total structure factors for liquid Tl_2Se: $S(n,n)(Q)$; $S(205,n)(Q)$ and $S(203,76)(Q)$

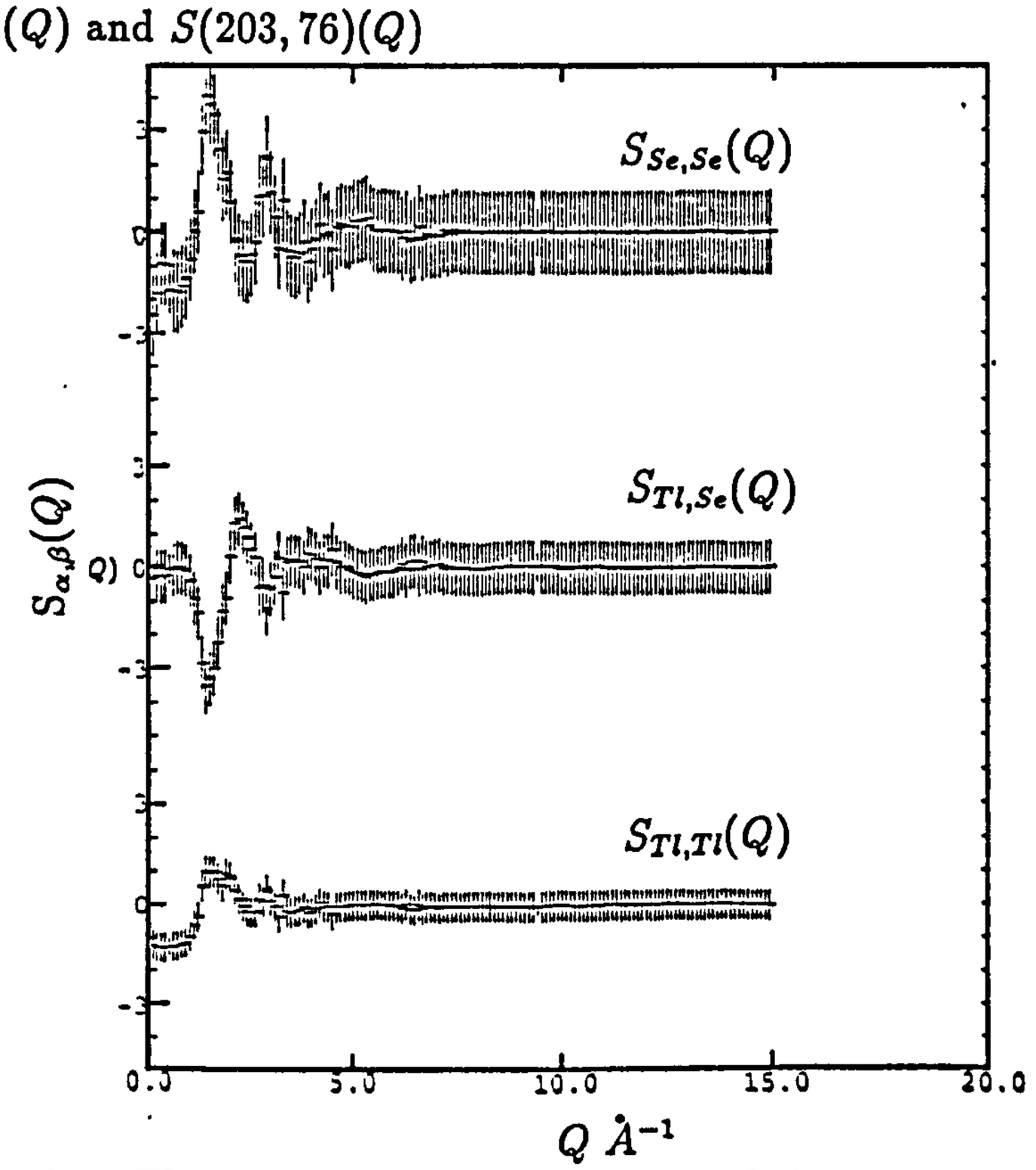

Figure 7.2: The partial structure factor $S_{\alpha,\beta}(Q)$ for liquid Tl_2Se.

0.0in which after inversion gives the partial structure factor as:

$$\begin{vmatrix} S_{TlTl}(Q)-1 \\ S_{SeSe}(Q)-1 \\ S_{TlSe}(Q)-1 \end{vmatrix} = \begin{vmatrix} -70.64 & 59.92 & 4.58 \\ -193.79 & 151.36 & 24.15 \\ 25.03 & -100.38 & -10.58 \end{vmatrix} \begin{vmatrix} S_{(nat,nat)}(Q) \\ S_{(205,nat)}(Q) \\ S_{(203,76)}(Q) \end{vmatrix}$$

It can be seen from the inverse matrix that the statistical errors in the partial structure factor will be over 100 times larger than those of the $S(Q)$'s themselves. Due to these large statistical errors in the $S_{ij}(Q)$'s, the partial $g(r)$'s could not be obtained directly from equation (7.4) because of the large termination errors produced in the Fourier transform. The $S_{ij}(Q)$s shown in Fig. 7.2 were, therefore, obtained using a refinement method similar to that described by Edwards *et al* (1975). It was shown (Enderby *et al*, 1966) that the partial structure factors for a binary alloy must satisfy the following criteria for all Q values, namely:

$$c_i + c_i^2(S_{ij}(Q)-1) \geq 0 \tag{7.5}$$

and

$$(c_1 + c_1^2(S_{11}(Q)-1)) - \frac{c_1^2 c_2^2 (S_{12}(Q)-1)^2}{c_2 + C_2^2(S_{22}(Q)-1)} \geq 0 \tag{7.6}$$

The partial structure factors determined in this experiment were constrained to obey these criteria while maintaining the condition that they should recombine to give the original $S(Q)$'s within experimental error. However, using these criteria alone the statistical errors in the data at high Q remain high. This leads to strong termination oscillations in the resulting partial $g(r)$'s. In order to reduce this problem the partial structure factors were further constrained to fit within an envelope of the form $Aexp(-BQ^2)$ where B was chosen so that each $S_{ij}(Q)$ tended to zero at high Q, while still obeying the requirement that the $S_{ij}(Q)$'s should give the original $S(Q)$'s within error. A was made large enough so that there was no rippling of the data at small Q. The values of A and B used in this analysis were 6 and 0.05 respectively. Using this procedure, the smoothing is strongest at high Q where very little structure is observable in the raw $S(Q)$'s, and is equivalent to using a window function in the data.

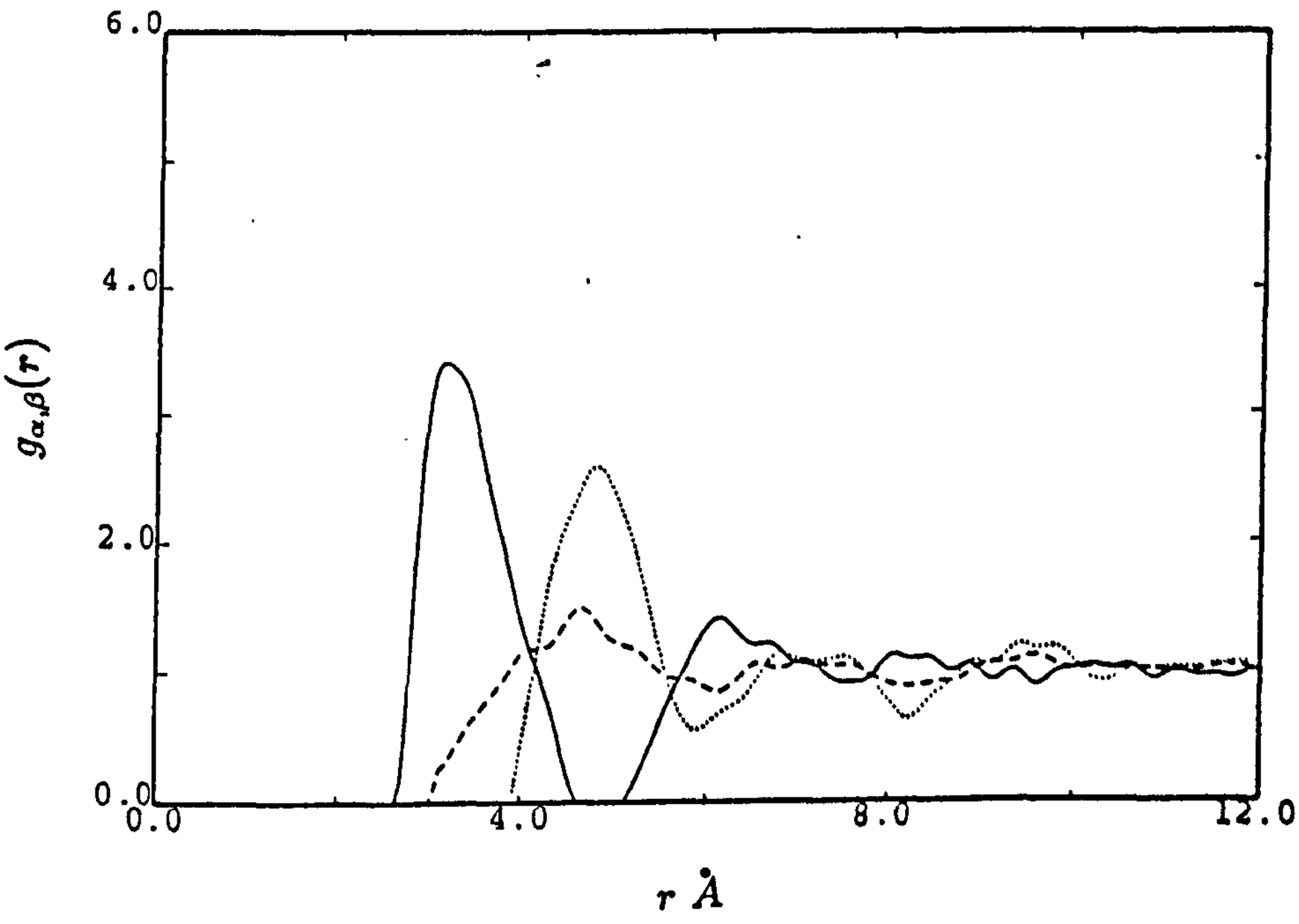

Figure 7.3: The partial radial distribution function $g_{\alpha,\beta}(r)$ for liquid Tl_2Se: Full line - $g_{Tl,Se}(r)$, Broken line - $g_{Tl,Tl}(r)$, Dotted line - $g_{Se,Se}(r)$.

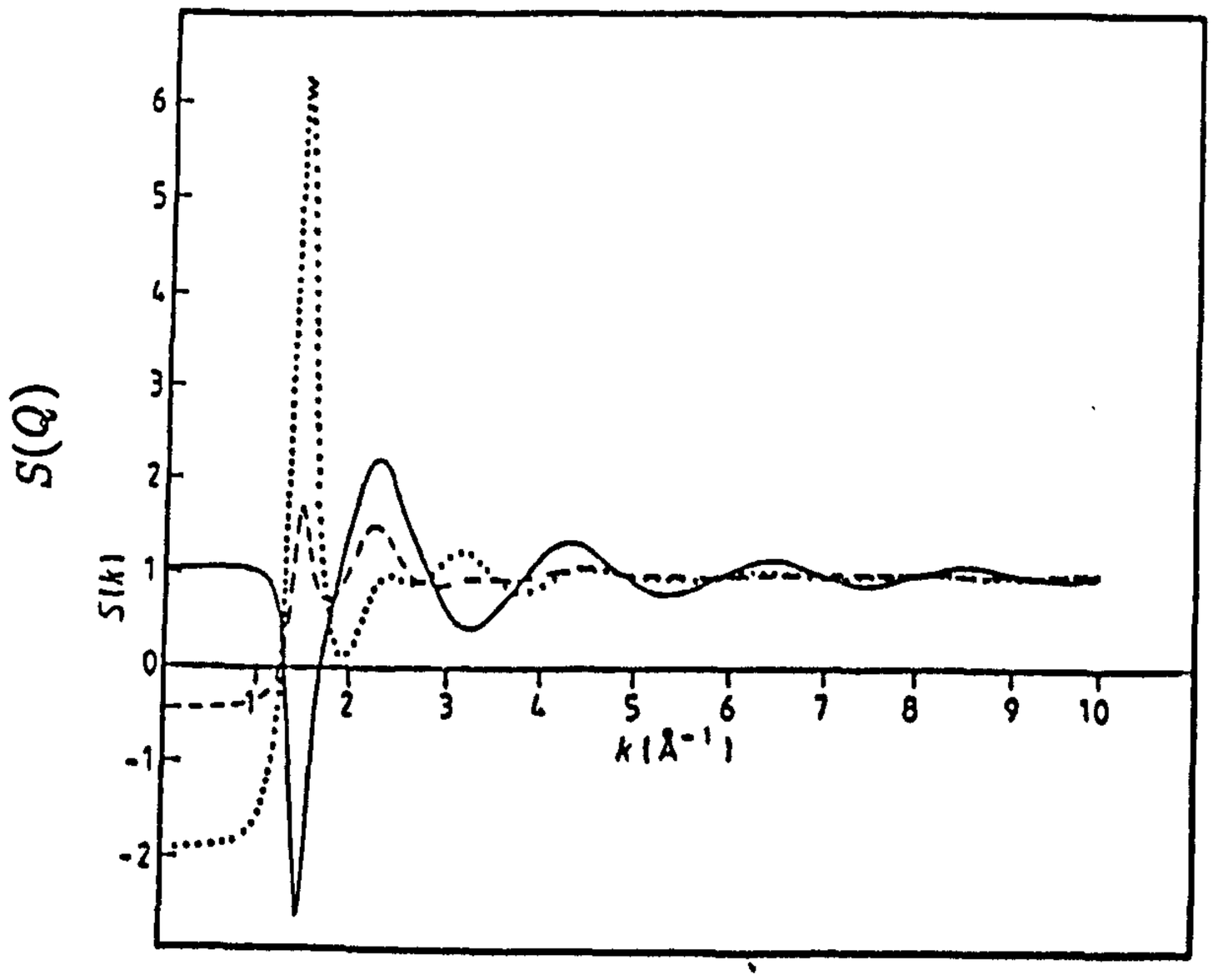

Figure 7.4: The partial structure factors for Tl_2Te obtained in the mean spherical approximation (Gay *et al*, 1982)

Comparison of the final with the original, unconstrained, $S(Q)$'s shows no systematic deviation within experimental error and we conclude that this smoothing procedure has not produced any artifacts into our final $S_{ij}(Q)$'s. The partial $g(r)$'s obtained from the constrained $S(Q)$'s are shown in Fig.7.3.

7.2.3 Interpretation of the experimental results

The partial structure factors obtained for Tl_2Se are very similar to those seen in 2:1 molten salts such as $BaCl_2$(Edwards *et al*, 1978). There is no evidence of the formation of any Se_2 pairs (with a characteristic distance of 2.34 Å) which have been seen in other (chalcogenide rich) selenides and tellurides . The $Tl-Se$ distance of 3.2 Å observed in $g_{TlSe}(r)$ is close to that expected from the sum of the ionic radii Tl^{+}(1.47Å) and Se^{2-}(1.91Å). However, there is a marked asymmetry in this first peak suggesting that the close co-ordination shell of Tl and Se is in fact quite complex with more than one characteristic distance involved. Integrating under the first peak in $g_{TlSe}(r)$ gives a coordination number of 11 that is high for this type of material (a figure of 8 would correspond to an anti-fluorite type coordination) but may also be a reflection of the complexity of the close coordination shell. This coordination number is close to figure of 9-11 obtained for Tl around Te in Tl_2Te by Gay *et al* (1982) from a total structure factor measurement. We have also obtained $S_{TlTl}(Q)$ and $g_{TlTl}(r)$. There is a broad peak in $g_{TlTl}(r)$ at approximately 4.3-4.5 Å that overlaps considerably with the first $Tl-Se$ coordination shell. This distance is close to, but slightly larger than that estimated for $Tl-Tl$ in Tl_2Te. The first peak in $g_{SeSe}(r)$ occurs at approximately 4.8 Å with a minimum distance of approach of about 4Å. This is consistent with the ionic radius of Se^{2-} that gives a minimum distance of approach of 3.8 Å.

In their work Gay *et al* (1982) show theoretical results for the structure factors of Tl_2Te using screened ionic potentials and the Mean Spherical Approximation. These are shown in Fig.7.4. The partial structure factors for Tl_2Se are very similar

apart from small differences in the position of the peaks which can be attributed to slight differences in size of the tellurium and selenium ions.

It can , therefore, be concluded that Tl_2Se and Tl_2Te are essentially ionic materials that are isostructural in the liquid phase apart from minor variations due to the slightly different sizes of the Se^{2-} and Te^{2+} ions although the high coordination numbers.

7.3 Measurements of the conductivity and the thermopower

The phase diagrams of $Tl-Te$ and $Tl-Se$ are shown in Figs.7.5 and 7.6. They show that $Tl-Te$ has no solid phase Tl_2Te unlike $Tl-Se$, and there is a non-stoichiometric phase with an approximate composition Tl_5Te_3. However, the ambipolar effects in the electronic properties occur precisely at the stoichiometric composition Tl_2Te (Cutler, 1977).

In this work, the measurements of conductivity and thermopower were made on the following three systems in the vicinity of stoichiometric composition Tl_2Te and Tl_2Se in temperature range of 560 - 580 ^oC :
(1)$(TlCl)_y$–$(Tl_2Te)_{1-y}$; (2) $(TlCl)_y$–$(Tl_xTe_{1-x})_{1-y}$; and (3) $(TlCl)_y$–$(Tl_xSe_{1-x})_{1-y}$, where, x corresponds to compositions up to ~ 5 $at.\%$ away from the stoichiometric compound $Tl_2Te(Se)$ and y is the composition of the mixtures.

7.3.1 Conductivity

The measured conductivities of the above systems are shown in Fig. 7.7 - 7.9. Figures 7.7 show the conductivities of the $(TlCl)_y - (Tl_2Te)_{1-y}$ system. The conductivities decrease rapidly with increasing thallium chloride, especially for the thallium selenide system. When the concentration of the thallium chloride is over 20 at.%, the conductivity appears to become essentially ionic.

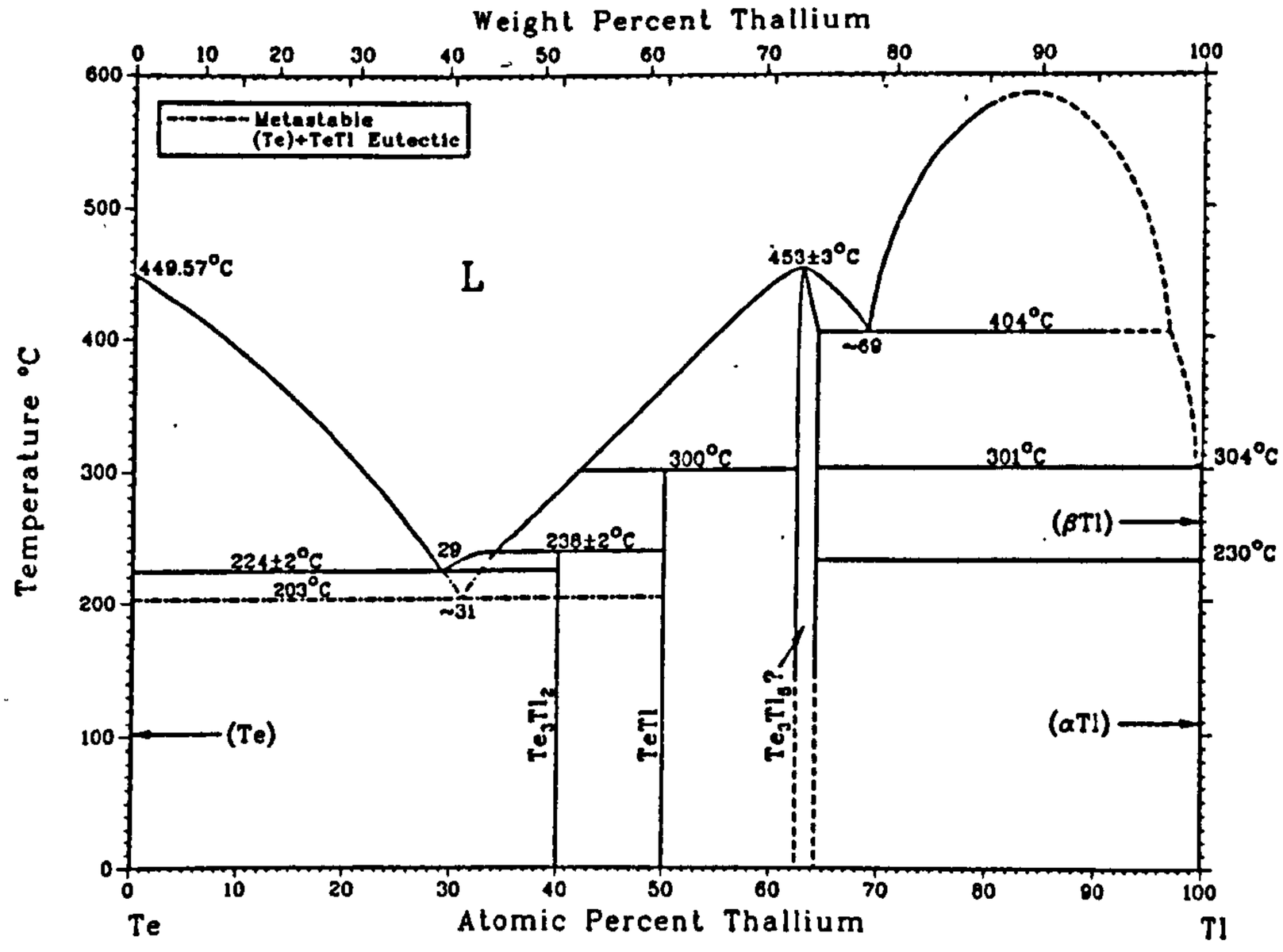

Figure 7.5: Phase diagram of $Tl - Te$.

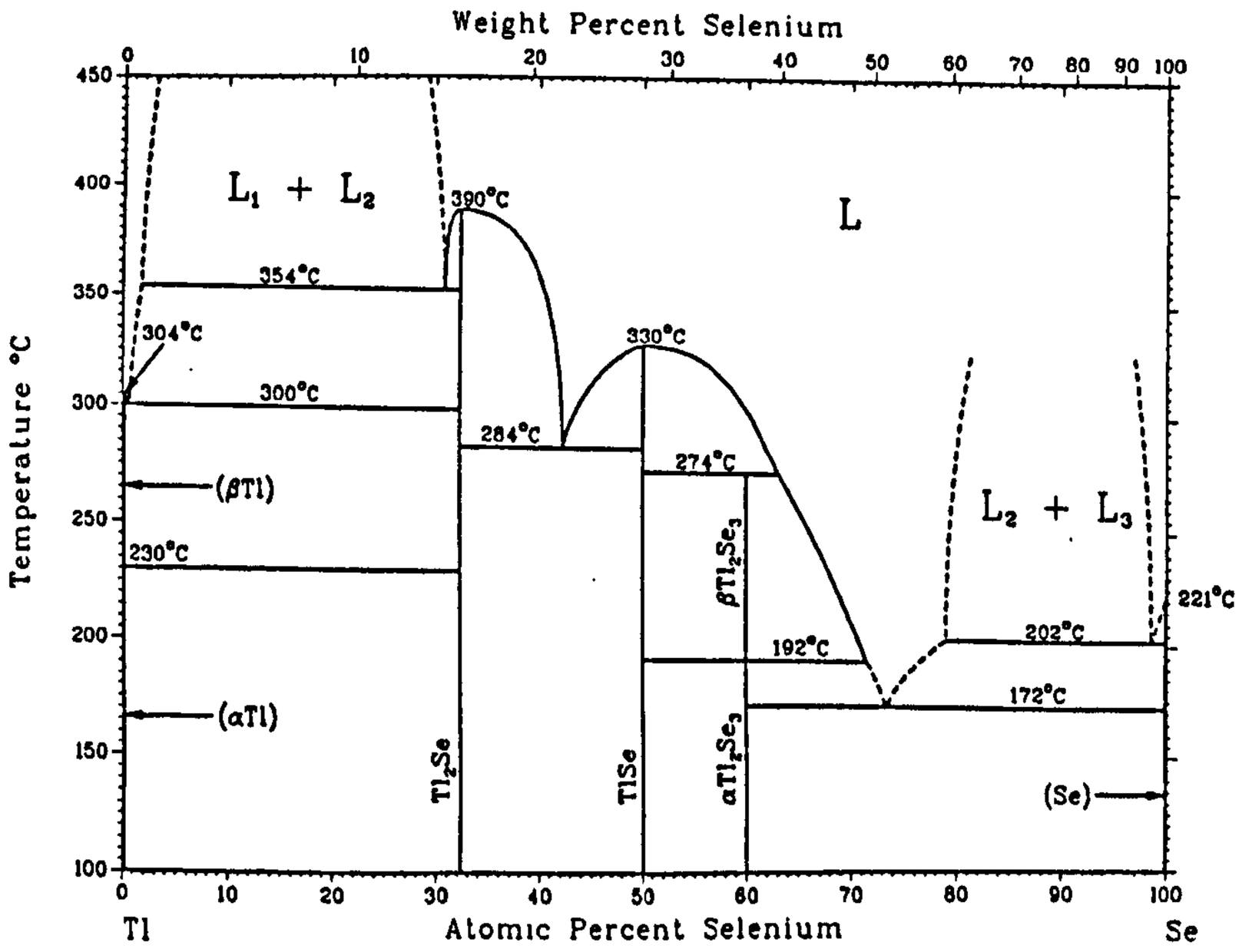

Figure 7.6: Phase diagram of $Tl - Se$.

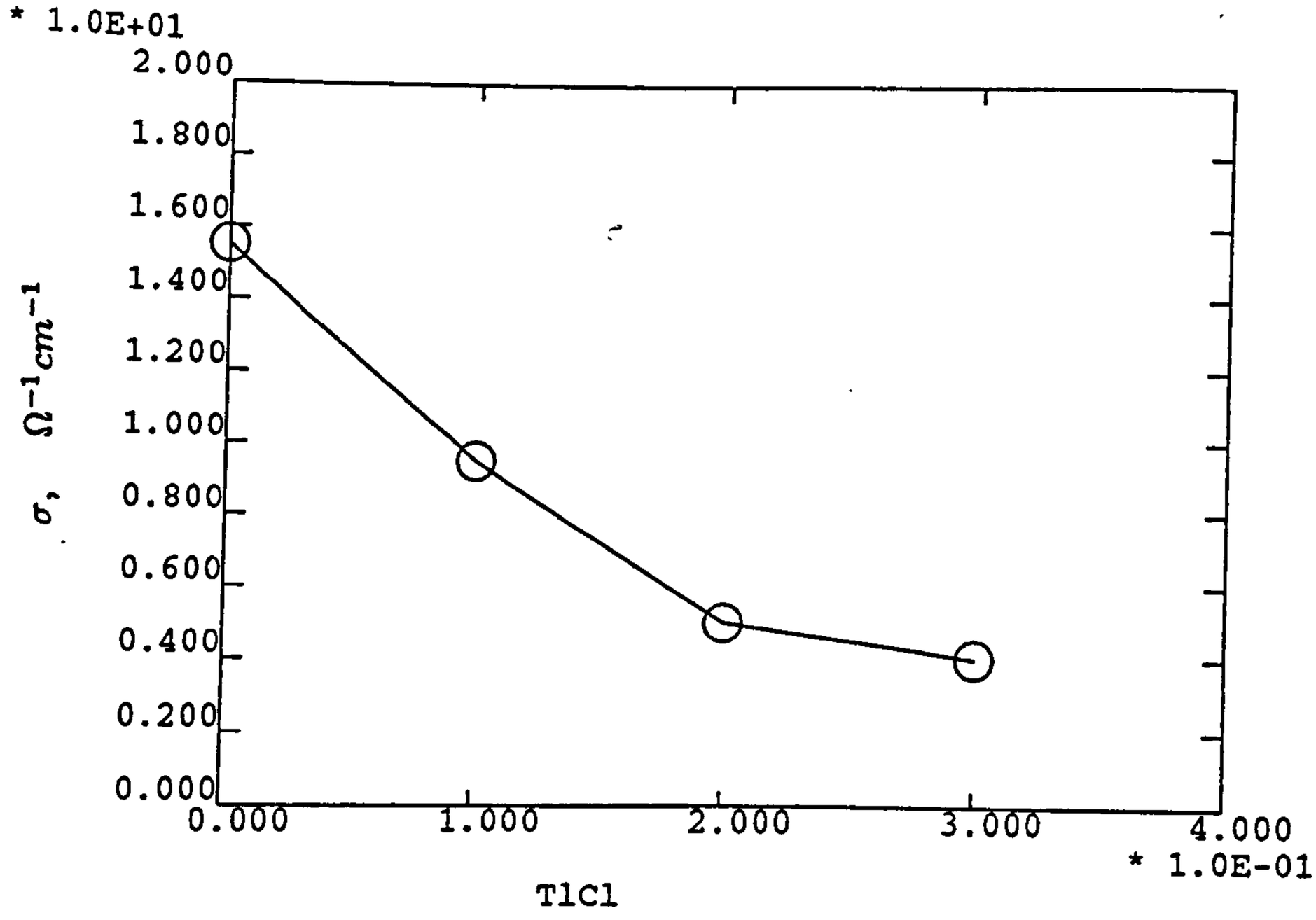

Figure 7.7: The conductivity of liquid $(TlCl)_y - (Tl_2Te)_{1-y}$.

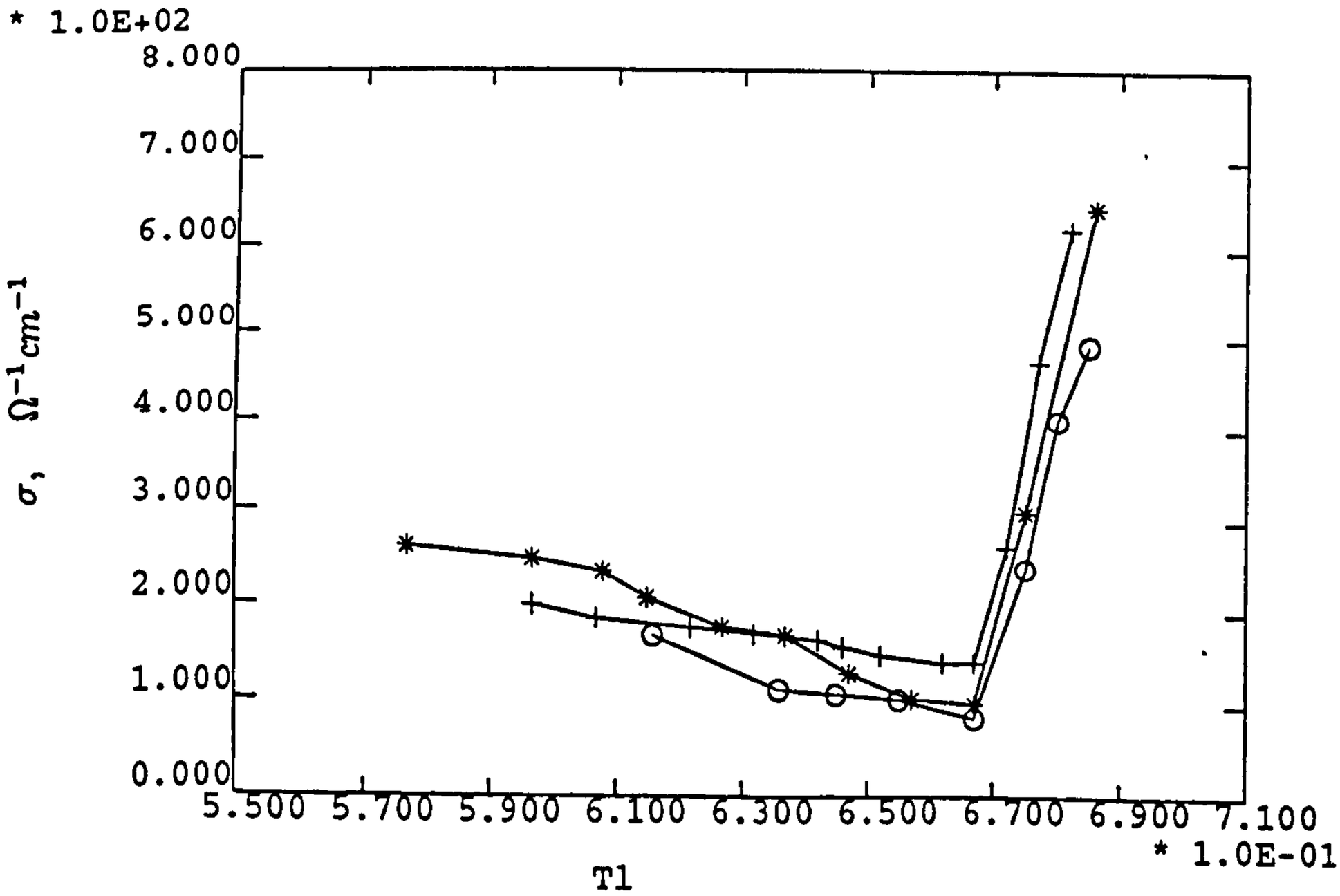

Figure 7.8: The conductivity of liquid Tl_xTe_{1-x} (+), $(Tl_xTe_{1-x})_{0.9} - (TlCl)_{0.1}$ ($\star$) and $(Tl_xTe_{1-x})_{0.8} - (TlCl)_{0.2}$ (o).

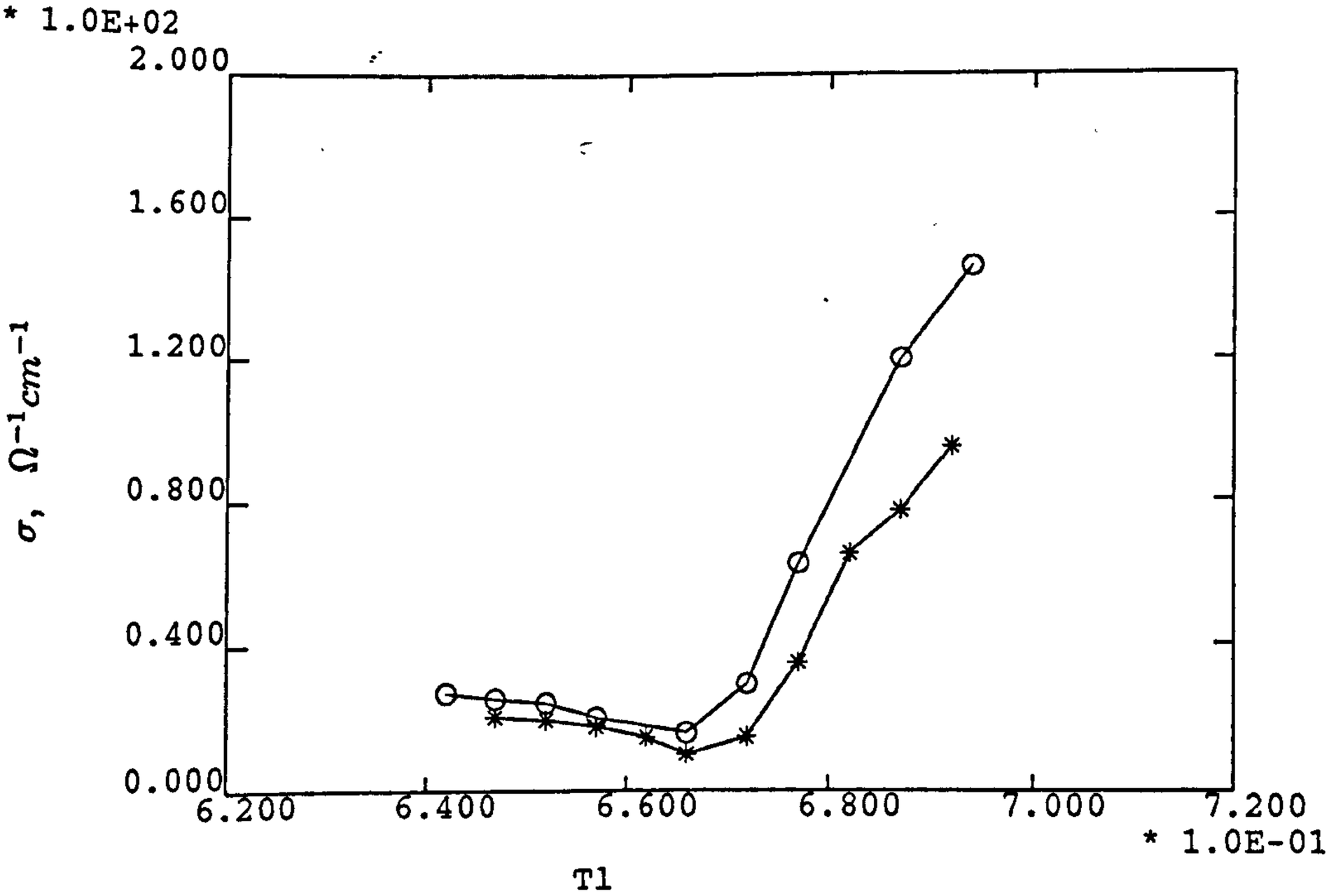

Figure 7.9: The conductivity of liquid Tl_xSe_{1-x} (o), $(Tl_xSe_{1-x})_{0.9} - (TlCl)_{0.1}$ ($\star$).

Figures 7.8 and 7.9 are the conductivities of $(TlCl)_y$–$(Tl_xTe_{1-x})_{1-y}$ and $(TlCl)_y$–$(Tl_xSe_{1-x})_{1-y}$ systems in the vicinity of the stoichiometry Tl_2Te and Tl_2Se. The conductivity of both systems shows a minimum at their stoichiometry Tl_2Te or Tl_2Se, but it is very asymmetric about the stoichiometric composition . The excess Tl increases the conductivity much more rapidly than excess Te and Se. The temperature coefficients of the both systems are shown in Figs. 7.10 and 7.11. For the Tl_2Se system (Fig. 7.11) the temperature coefficient, $d\sigma/dT$, is positive and becomes slightly smaller in the Tl-rich side of stoichiometry in the composition range of this work. For the Tl_2Te systems (Fig. 7.10) the $d\sigma/dT$s are much smaller than those of Tl_2Se and even become negative as x exceeds 0.68.

7.3.2 Thermopower

The thermopowers of $(TlCl)_y$–$(Tl_xTe_{1-x})_{1-y}$ and $(TlCl)_y$–$(Tl_xSe_{1-x})_{1-y}$ are shown in Figs.7.12 and 7.13. The p-n transition (ΔS) and ambipolar effects of the thermopower were clearly observed in both systems, ΔS is about 240 $\mu V°C^{-1}$ for the Tl_2Te system and 440 $\mu V°C^{-1}$ for the Tl_2Se. This difference is also reflected in the conductivity data. Normally, the smaller σ is, the bigger S is. The conductivity is dominated by the electrons on the Tl side showing a negative S and by the holes on the Te side showing a positive S. The region between the peaks in S corresponds to ambipolar transport. It can be seen from Fig.7.12 and 7.13 that the addition of thallium chloride does not cause an increase in the p-n transition ΔS of the thermopower which would come from an increase in the band gap as predicted by the theory proposed by Barnes and Enderby (1987)

The positive and negative maximum of the thermopower for the Tl_2Se systems in Fig.7.13 is much more symmetrical at the stoichiometric composition than those of the Tl_2Te systems in Fig. 7.12 although their conductivity behaves similarly. This reflects that the excess Te and Se behave chemically different to some extent on the chalcogen-rich side of stoichiometry.

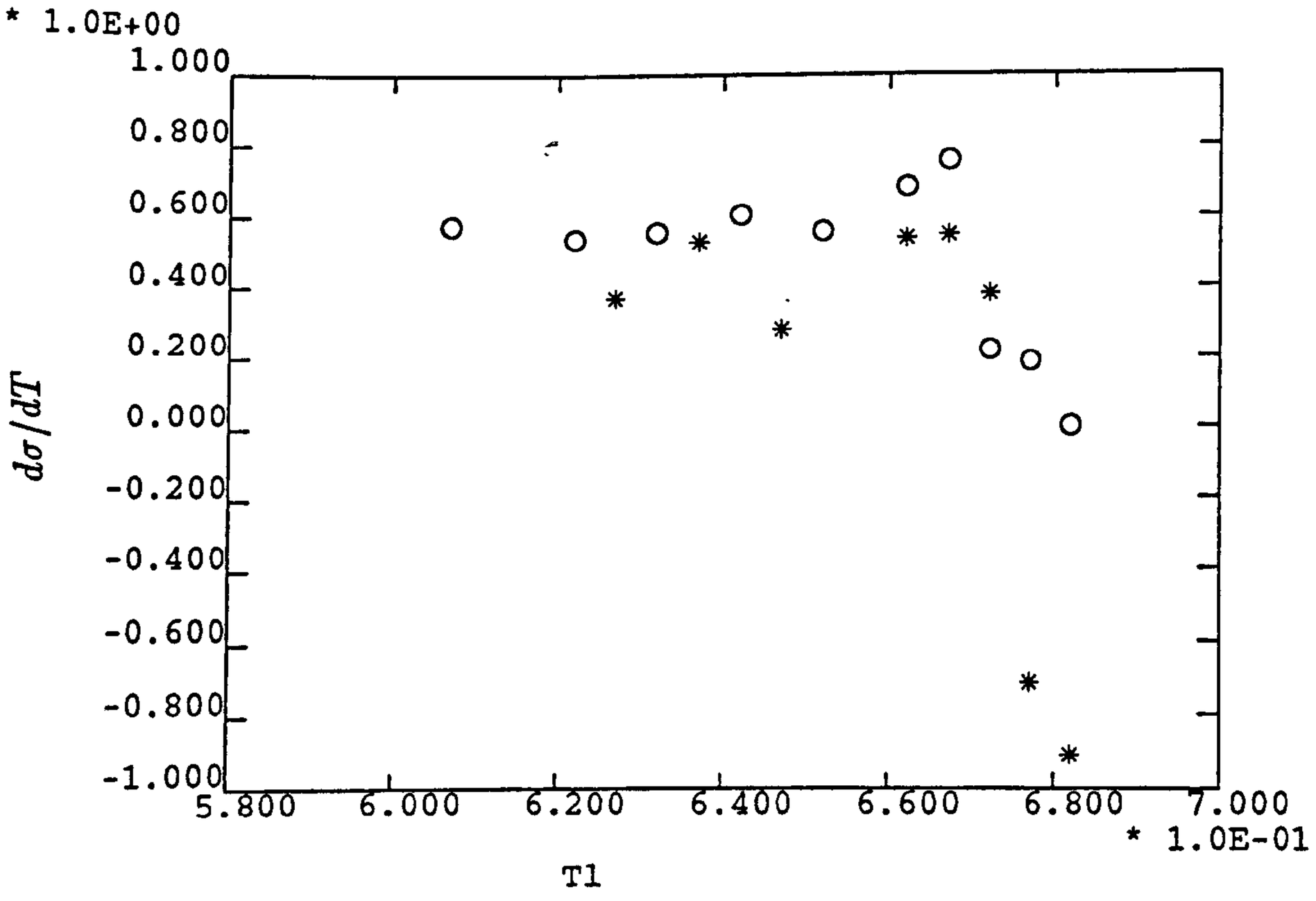

Figure 7.10: The temperature coefficient $d\sigma/dT$of liquid Tl_xTe_{1-x} (o) and $(Tl_xTe_{1-x})_{0.9} - (TlCl)_{0.1}$ (*).

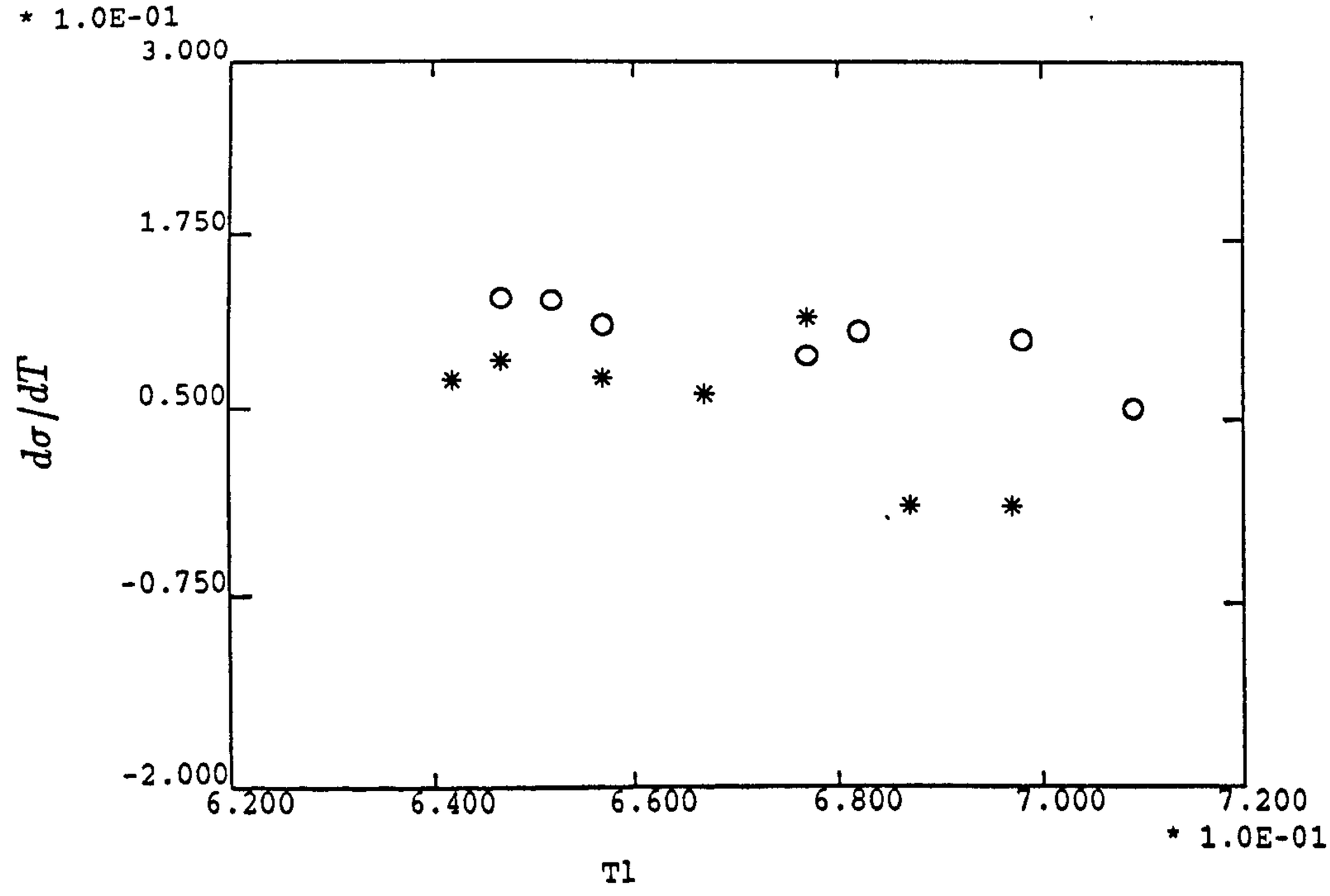

Figure 7.11: The temperature coefficient $d\sigma/dT$of liquid Tl_xSe_{1-x} (o) and $(Tl_xSe_{1-x})_{0.9} - (TlCl)_{0.1}$ (*).

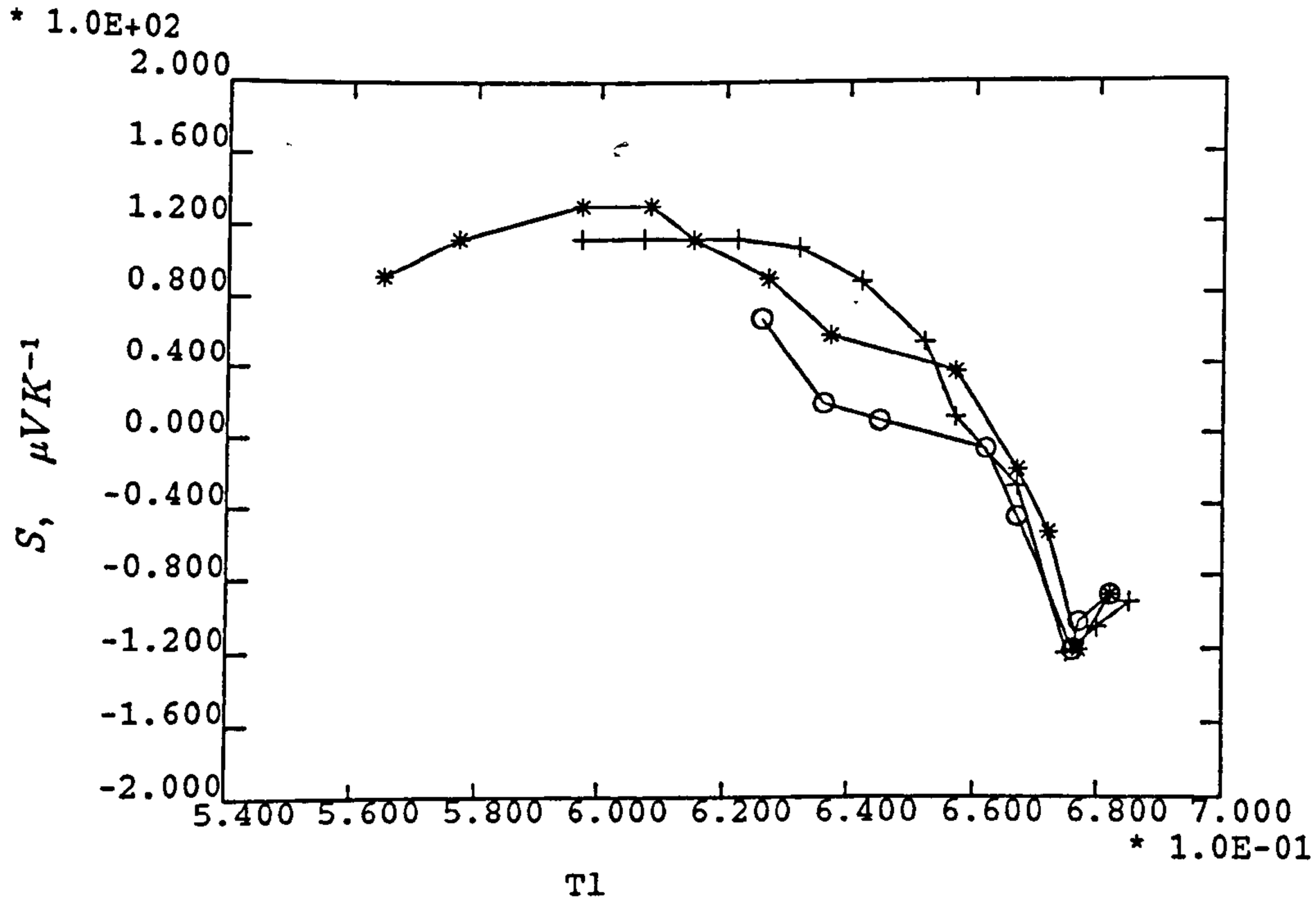

Figure 7.12: The thermopower of liquid Tl_xTe_{1-x} ,(+), $(Tl_xTe_{1-x})_{0.9} - (TlCl)_{0.1}$ (⋆) and $(Tl_xTe_{1-x})_{0.8} - (TlCl)_{0.2}$ (o).

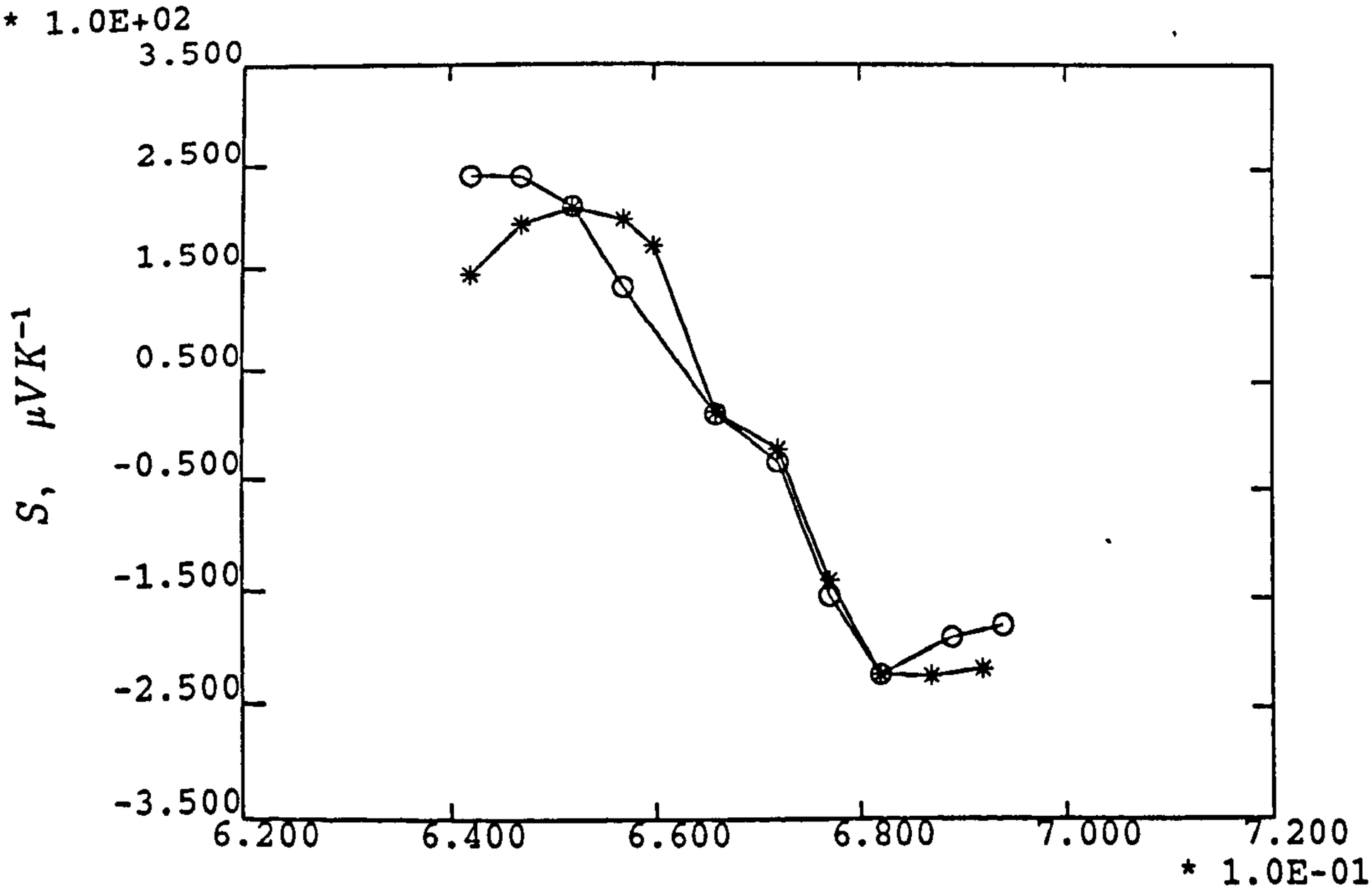

Figure 7.13: . The thermopower of liquid Tl_xSe_{1-x} (o) and $(Tl_xSe_{1-x})_{0.9} - (TlCl)_{0.1}$ (⋆) .

7.4 Theoretical calculation of conductivity and thermopower

The conductivity and thermopower of Tl_xTe_{1-x} and Tl_xSe_{1-x} have been calculated using the BE theory at a temperature 900 K. In the calculation the band gap E_g is chosen as 0.15 eV for Tl_2Te and 0.3 eV for Tl_2Se. The calculated conductivities of the both systems in the vicinity of the stoichiometric composition, compared with experimental values, are shown in Fig. 7.14 and 7.15. The corresponding thermopowers are shown in Fig. 7.16 and 7.17. It can be seen that the calculated conductivity and thermopower on the Tl-rich side are quite consistent with the measured data in the sign, magnitude and composition dependence. On the chalcogen-rich side, the calculated thermopowers are consistent with the measured magnitude of the p-n transition of thermopower, but they increase much quicker with composition, especially for the Tl_2Te system. The calculation of conductivity on the chalcogen-rich side produces rise in σ which are much faster than the measured.

It appears that BE theory can be quite successfully applicable to the thermopower, and to the conductivity on the thallium-rich side. On the chalcogen rich side the formation of chalcogenides polyanions complicates the theoretical picture. This will be discussed in later section.

7.5 Discussion

7.5.1 Local structures and chemical bonding

As stated in chapter 6, chemical bonding plays a key role in liquid semiconductors. Physicochemical and structural data provide a powerful means for inferring the existence and types of compounds in binary alloys. The thermochemical properties of the Tl_2Te and Tl_2Se have been studied by many researchers.

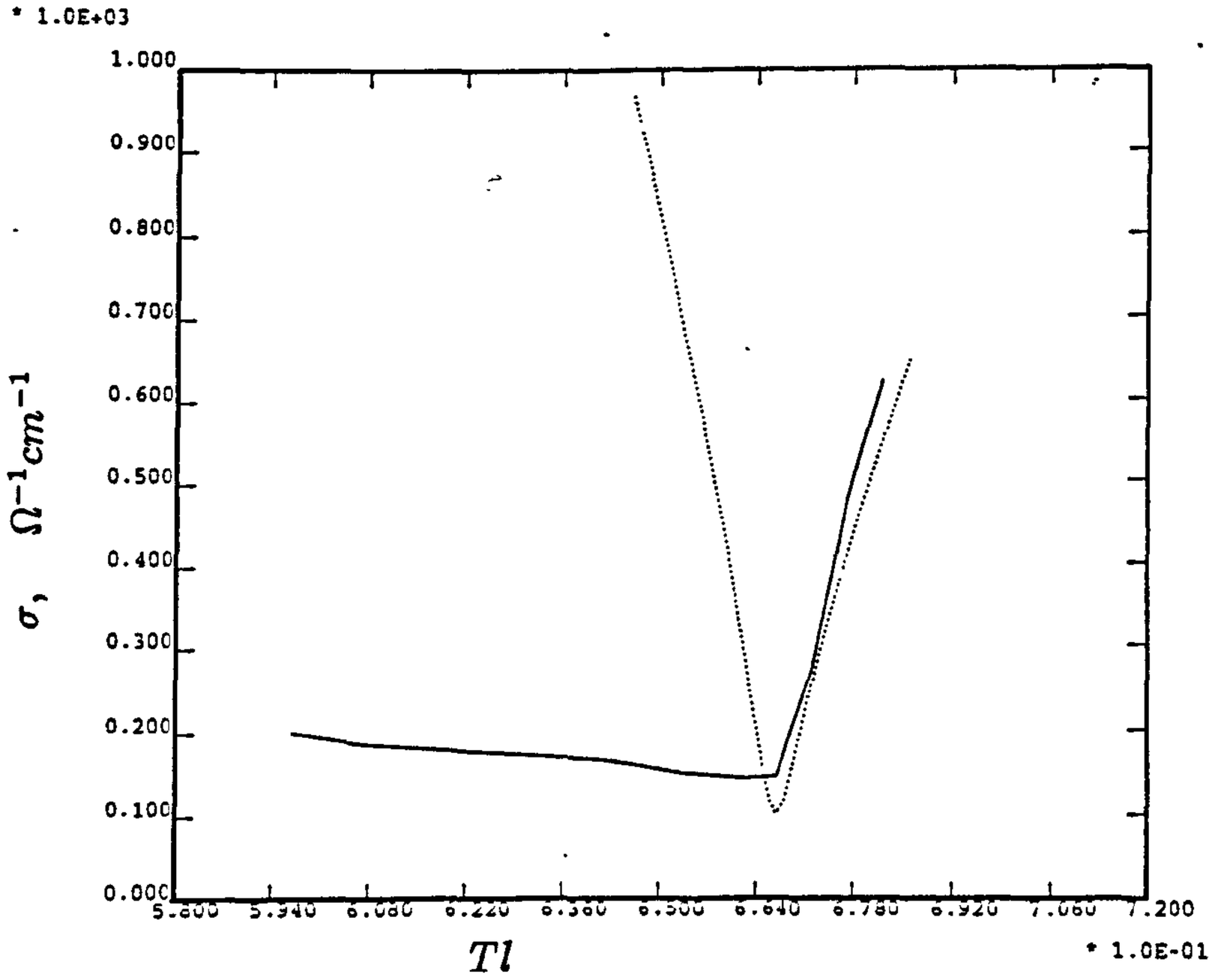

Figure 7.14: Comparison between the calculated and measured conductivity of liquid Tl_xTe_{1-x} in the vicinity of stoichiometry Tl_2Te.

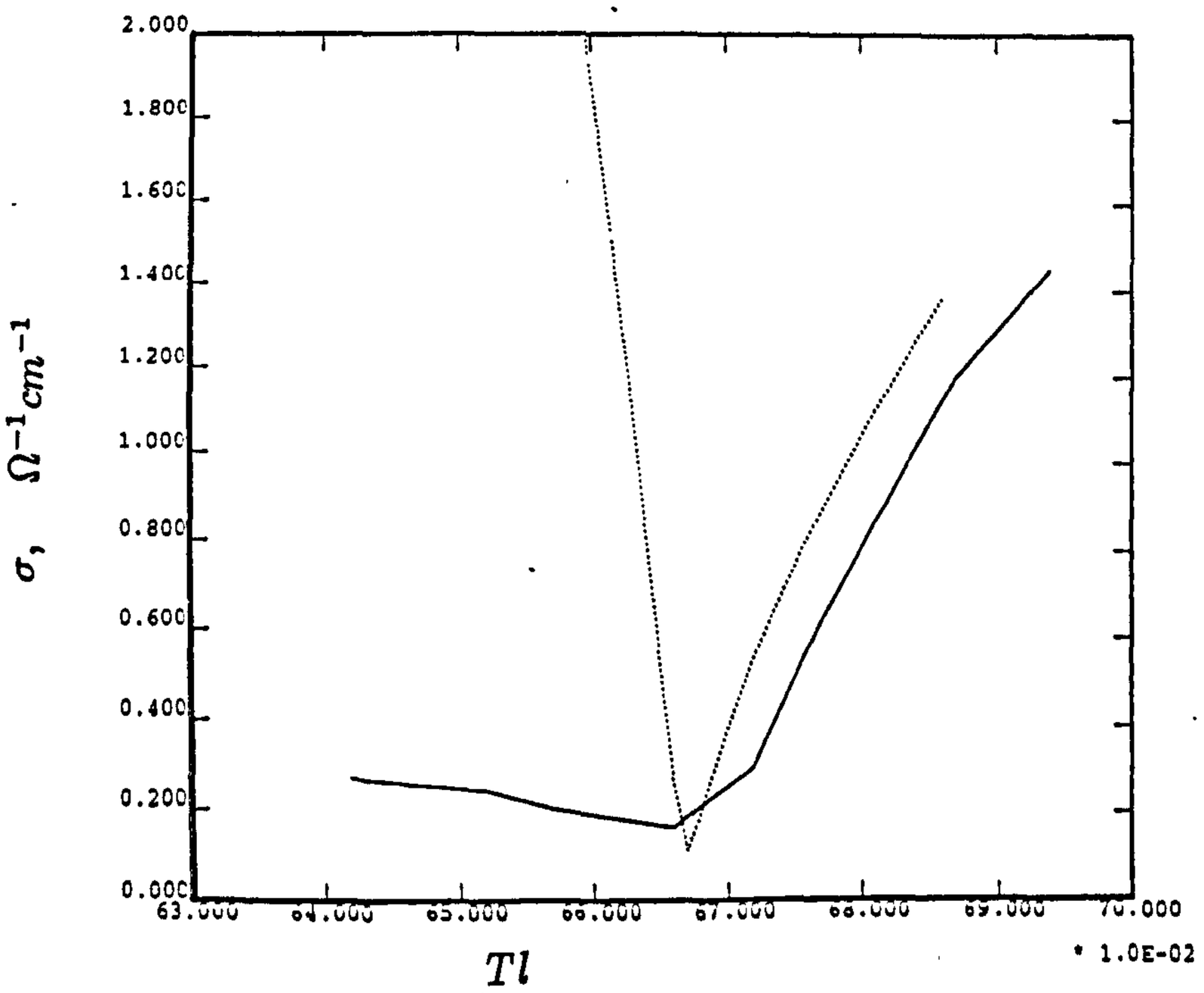

Figure 7.15: Comparison between the calculated and measured conductivity of liquid Tl_xSe_{1-x} in the vicinity of stoichiometry Tl_2Se.

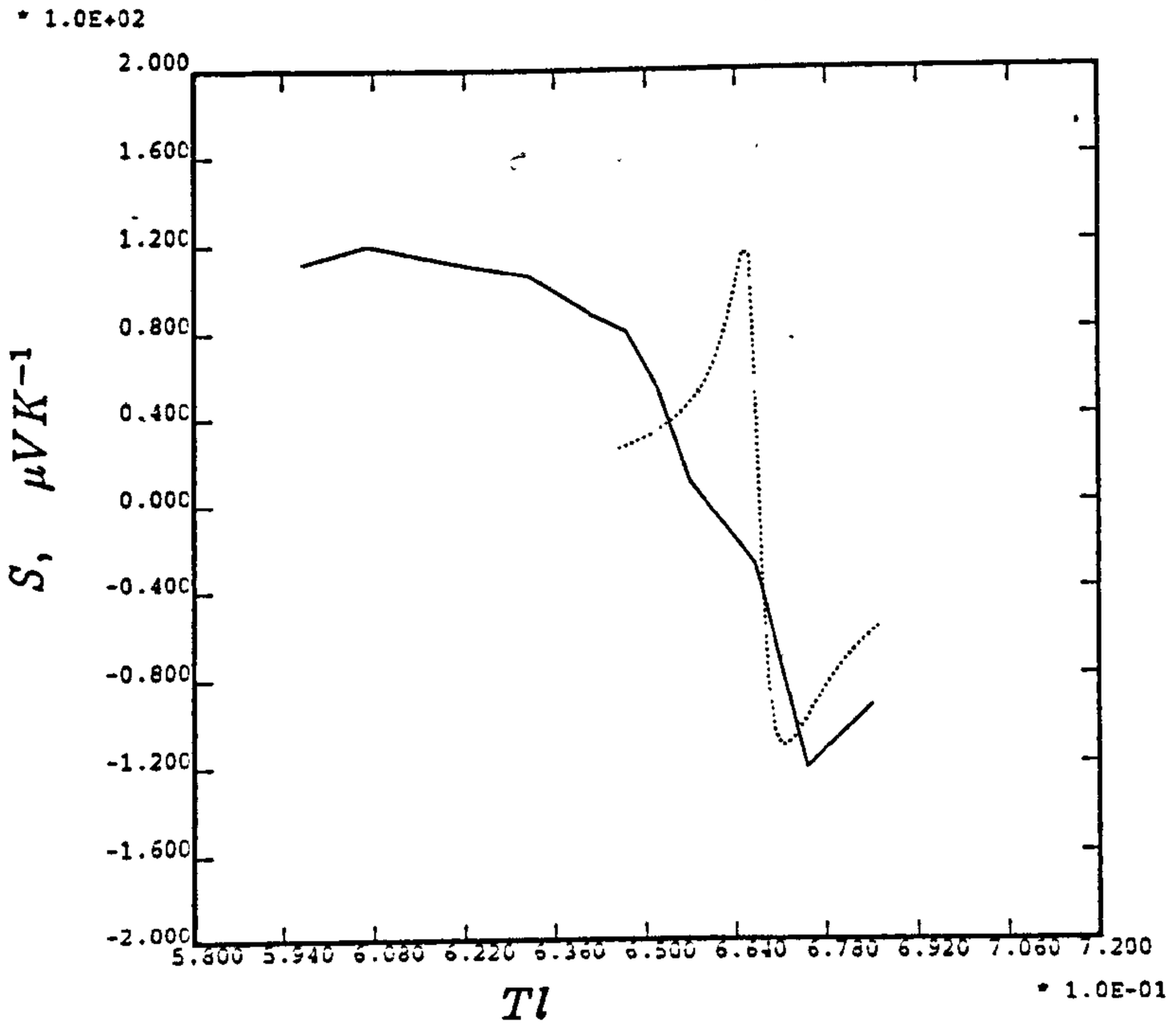

Figure 7.16: Comparison between the calculated and measured thermopower of liquid Tl_xTe_{1-x} in the vicinity of stoichiometry Tl_2Te.

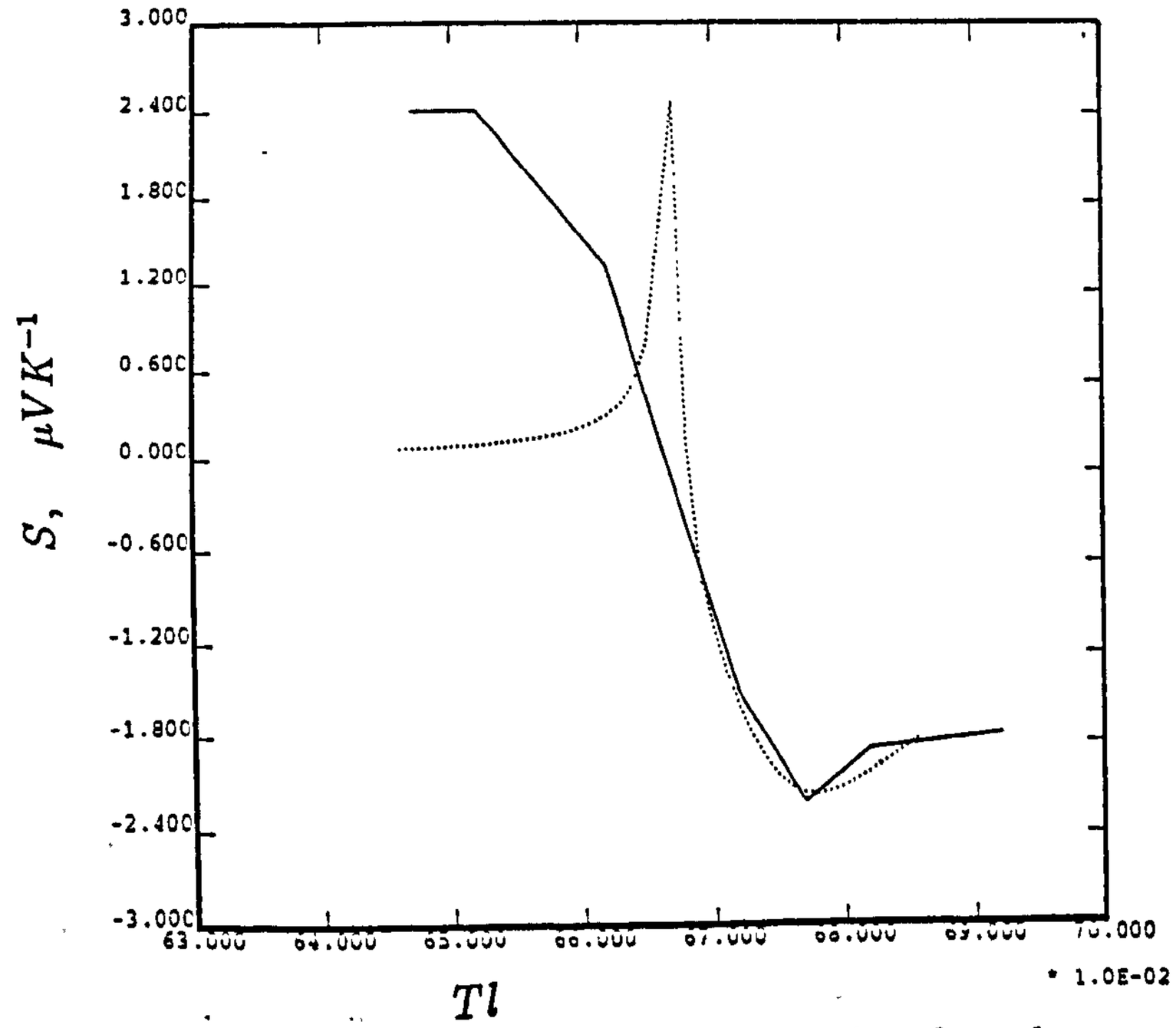

Figure 7.17: Comparison between the calculated and measured thermopower of liquid Tl_xSe_{1-x} in the vicinity of stoichiometry Tl_2Se.

Here, we quote the enthalpy of mixing ΔH^m, the entropy of mixing ΔS^{ex} and the free energy of mixing ΔG_m from the papers by Terpilowski *et al* (1963) and Nakamura and Shimoji (1971), as shown in Fig. 7.18 and 7.19. It can be seen that the excess entropy ΔS^{ex}, the enthalpy of mixing ΔH^m and the free energy of mixing ΔG_m have strong negative peaks at the stoichiometric composition. This indicates a chemically correlated ordering process which may reflect the formation of discrete molecules or ionic bonding. The fact that the minimum near stoichiometry is several times kT in magnitude implies that the dissociation constant for the reaction Tl_2Te=$2Tl$+Te is relatively small. The physicochemical properties of the compound Tl_2Se measured by Terpilowski et al (1963) are basically similar to those of the Tl_2Te.

The types of the chemical bonding of Tl_2Te and Tl_2Se can be determined by the structural data. The experimental evidence and theoretical calculations of the partial structure factors S_{ij} of both the systems which have been discussed in the section 7.2 show that the bonding between the Tl and Te or Se is essentially ionic. The transfer of the valence electrons from the Tl to Te or Se, makes the Tl the cation and the Te or Se the anion.

7.5.2 The theory of Enderby and Barnes (1987)

Enderby and Barnes (1987) predicted that the band gap of liquid semiconductor will be enlarged as molten salt is added, and thus an increase in the p-n transition of the thermopower should take place. This phenomenon was not observed in these two systems (and nor in CuCl-copper chalcogenides, see chapter 8). It suggests that the band gaps of these liquid semiconductors do not increase on adding halide. A much more detailed study is needed to further confirm this phenomenon and to give an explanation. This is beyond the scope of this thesis. However, preliminary investigations suggest that it is the parameter α (Enderby and Barnes, 1990a), that decreases on adding hahide. This leaves the p-n transition unchanged but decreases σ.

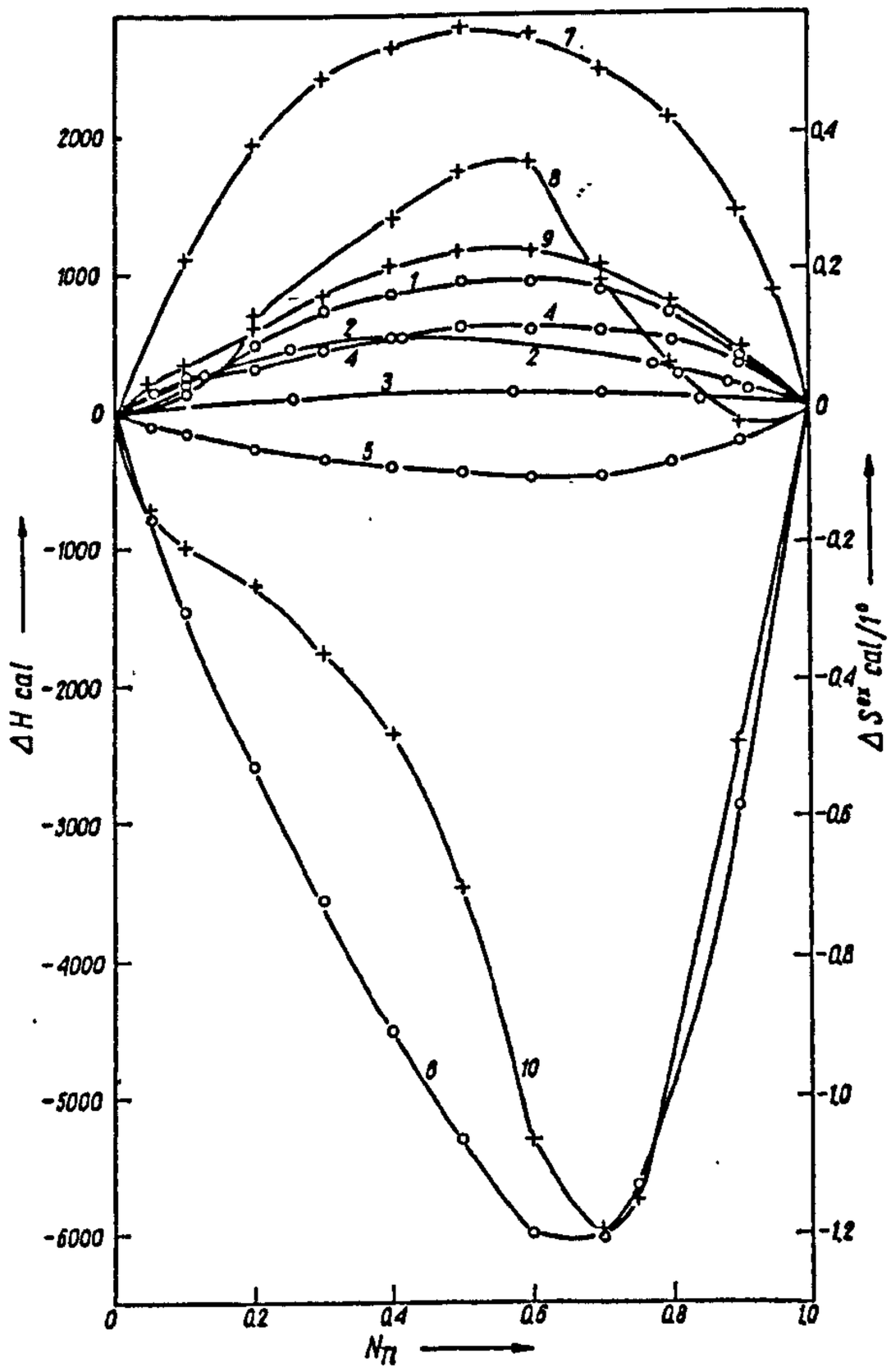

Figure 7.18: Isotherms for the enthalpy of mixing ΔH (o) and the entropy of in mixing excess of the value for ideal mixtures ΔS^{ex} (+) for a number of liquid binary alloys as a function of the atomic fraction of Tl. ΔH: (1) Ag-Tl; (2) Cd-Tl; (3) In-Tl; (4) Sn-Tl; (5) Sb-Tl; (6) Te-Tl; ΔS^{ex}: (7) Ag-Tl; (8) Sn-Tl; (9) Sb-Tl; (10) Te-Tl. (Terpilowski and Zaleska, 1963)

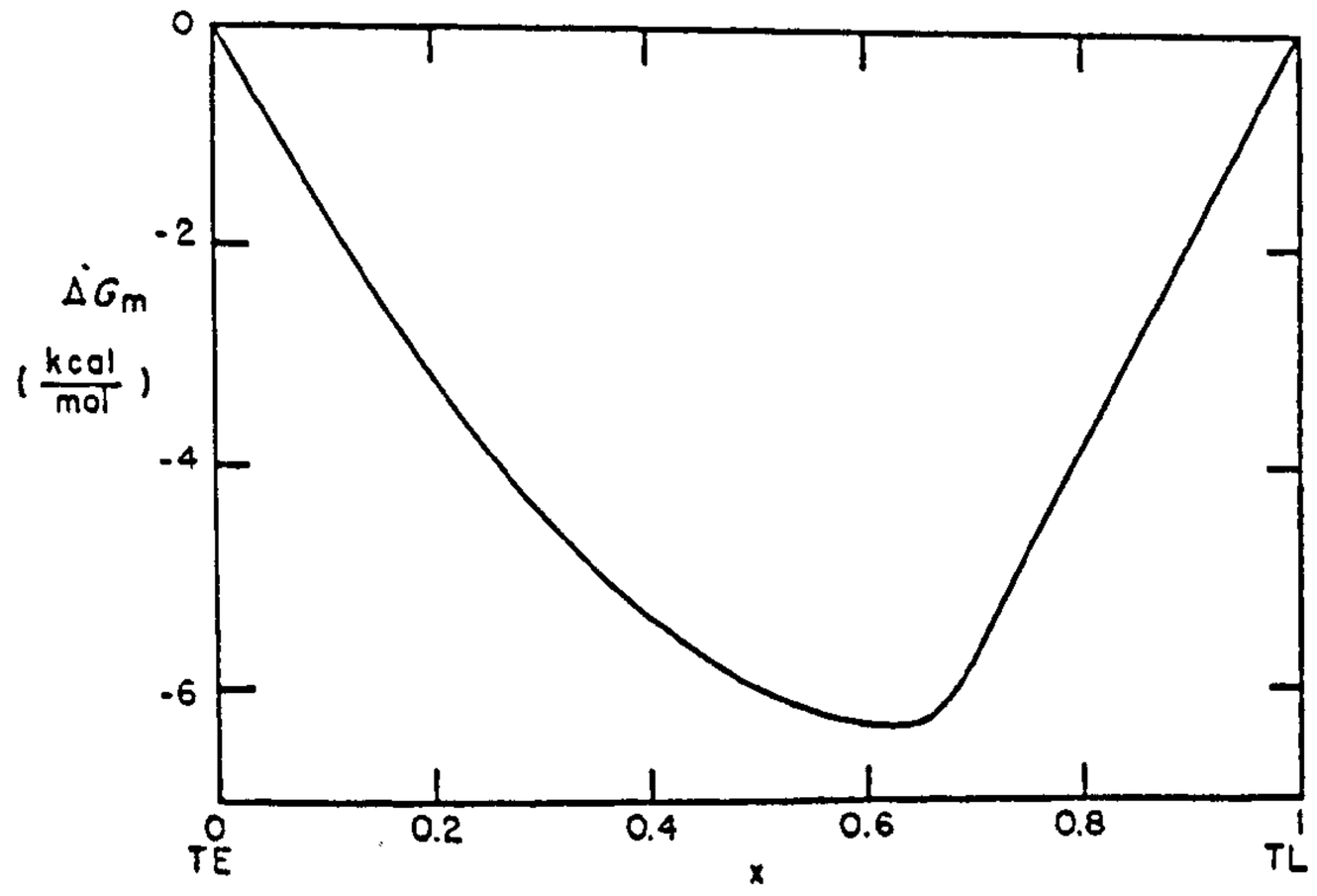

Figure 7.19: The Gibbs free energy of mixing for Tl_xTe_{1-x} at 600 $°C$. (Nakamura and Shimoji, 1971)

7.5.3 The electronic properties

From the results it is concluded that both Tl_2Te and Tl_2Se are essentially ionic in bonding nature. The electronic wavefunctions of the conduction band result mainly from the outer p orbital of the Tl and the electronic wavefunctions of the valence band from the outer p orbitals of the Te or Se at stoichiometry or in the vicinity of stoichiometry. The Fermi energy E_F lies in the middle of the band gap for the stoichiometric compound. The band structure is similar to that of Mg_3Bi_2 of Fig.6.36. Now consider the composition slightly away from stoichiometry:

(i). On the Tl-rich side - Tl_2Te+Tl and Tl_2Se+Tl

The calculation of the conductivity and thermopower based on the Kubo-Greenwood equations with the rigid band model works quite well as the composition is just off stoichiometry on Tl-rich side. This is an ideal case which has been discussed in chapter 6. Addition of excess Tl introduces ions plus the 'extra' valence electrons which enter into the conduction band, and consequently the Fermi energy E_F shifts rapidly into the conduction band. The 'extra' electrons may not create a new band and the band model remains 'rigid' and the energy-dependent conductivity can be described by $\sigma(E)$=A$[N(E)]^2$. In this case the BE theory is applicable. The density of states is schematically shown in Fig.7.20 (a).

(ii). On the chalcogen-rich side - $Tl_2Te + Te$ and $Tl_2Se + Se$

The conduction mechanism on the chalcogen-rich side is more complicated. The theoretical calculations using the BE theory cannot produce an explanation for the conductivity, but are quite successful in explanation of the thermopower. The conductivity increases very slowly with increasing chalcogens, while the ambipolar behaviour and a large p-n transition ΔS are observed. The same phenomena were reported by Cutler (1971) for Tl_xTe_{1-x}, Regel, *et al* (1970) for Tl_xSe_{1-x}, and Kazandzhan *et al* (1974) for Tl_xS_{1-x}. The conductivity becomes less sensitive to the increase of chalcogens as the nonmetallicity of the chalcogen elements increases from Te to Se to S.

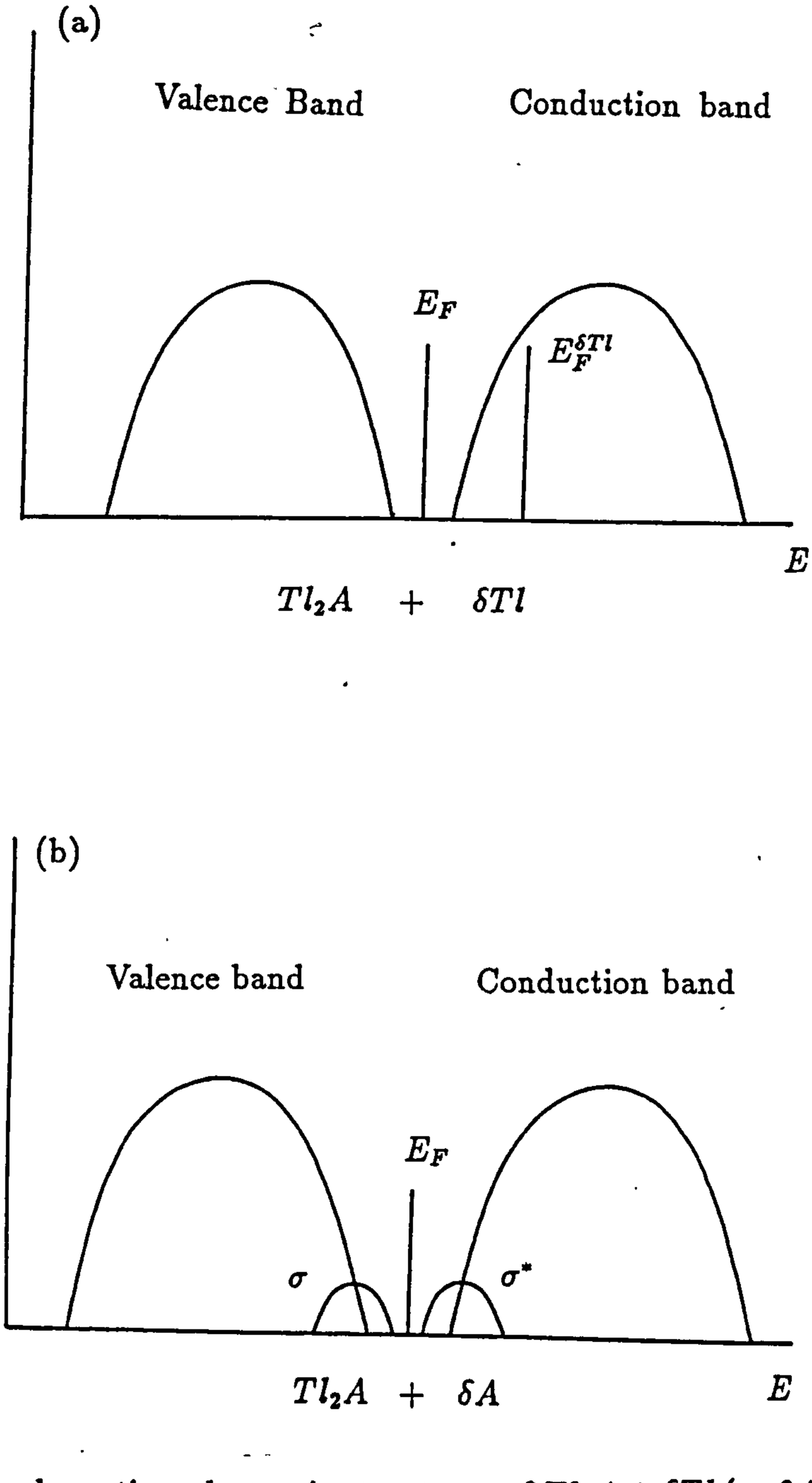

Figure 7.20: A schematic electronic structure of $Tl_2A + \delta Tl$ (or δA): where A is Se or Te, and σ is bonding states of $A-A$ and σ^* is antibonding states of $A-A$.

Now a new question is raised as to why a large p-n transition of the thermopower with increasing chalcogens can occur, while the conductivity hardly changes. I still use the concept of the cluster ions which is mentioned in chapter 6. It is assumed that the excess chalcogens are covalently bonded with themselves to form discrete or chain molecular ions of the form $(A_n)^{2-}$ (where A represents the chalcogens). The difference between the metallic and covalent bonding in the cluster is that the metallic bonding between excess metallic elements, for example Mg and Bi, holds down the thermopower as the band gap collapses, while the covalent bonding between the excess nonmetallic elements, for example the chalcogens, holds down the conductivity by keeping the Fermi energy near the mid band gap. In the case of $Tl_2A + A$, the bonding and antibonding states created by newly formed $(A_n)^{2-}$ is separately hybridised, to some extent, with valence and conduction bands of $Tl^{1+} - A^{2-}$. This band structure is schematically shown in Fig 7.20(b). The newly created density of states does not cause a change of the Fermi energy. The conductivity, therefore, does not have a significant changes as the chalcogens is in excess. This result can be tested using the Kubo-Greenwood equations on condition that the position of the chemical potential is kept at the same position. Alternatively it is possible to model the effects of ion pairing into the calculation of Barnes (1993). This should be investigated.

Chapter 8

The Structural and Electronic Properties of $Cu_2Se - CuCl$ and $Cu_2S - CuCl$

8.1 Introduction

The copper chalcogenides are of special interest because of their similarities and differences with respect to thallium-chalcogenides. Dancy *et al* (1963, 1965), Enderby *et al* (1967), Glazov *et al* (1986) and Barnes (1986) reported the experimental results of conductivity and thermopower of the liquid copper based chalcogenides. It was stated that the cuprous telluride, selenide and sulphide are true liquid semiconductors with $E_F \geq E_v$ and with the bulk of the current carried by holes. The unusual behavior of the electrical properties which have drawn much attention occurs as the composition changes from CuA to Cu_2A (A=Te, Se). The studies in the vicinity of the particular composition Cu_2A are less detailed, especially with regard to the thermopower.

The structures of the cuprous chalcogenides in solid state have received a lot of attention because of their superionic and superconductive properties. Preliminary

work by Hawker *et al* (1978), Ngugen *et al* (1982) on the liquid structure of $CuTe$ and by Hawker (1974) on Cu_2Te have been done by the technique of neutron scattering. Barnes and Enderby (1988, 1989) have determined the liquid structures of the $CuSe$ and Cu_2Se at the partial structure factor level. The conclusion drawn from these studies is that the both CuA and Cu_2A are ionic, and the common feature of these systems is that copper exists only in its monovalent form.

In this work, the emphasis is put on the studies of the electronic properties in the vicinity of stoichiometry Cu_2Se and Cu_2S, and an attempt is also made to study the effects of the addition of copper chloride on the band gap of Cu_2Se and Cu_2S.

The following work has been done in this chapter:

i) measurements of the conductivity and the thermopower of the systems: (1). $(CuCl)_y - (\mathrm{Cu_2}Se)_{1-y}$; (2). $(CuCl)_y - (Cu_2S)_{1-y}$; (3). $(CuCl)_y - (Cu_xSe_{1-x})_{1-y}$; and (4). $(CuCl)_y - (Cu_xS_{1-x})_{1-y}$ in the vicinity of stoichiometry.

ii) determination of structures of Cu_2Se-$CuCl$ systems by neutron diffraction in order to clarify the influences of the chloride on the structures of the compound Cu_2Se.

8.2 Measurement of the conductivity and the thermopower

The conductivities of $(CuCl)_y - (Cu_2Se)_{1-y}$, $(CuCl)_y - (Cu_2S)_{1-y}$, $(CuCl)_{0.2} - (Cu_xSe_{1-x})_{0.8}$ and $(CuCl)_{0.05} - (Cu_xS_{1-x})_{0.95}$ at temperature of 980 ^oC are shown in Figs.8.1 - 8.4, respectively. The thermopowers corresponding to the Figs 8.3 and 8.4 are shown in Figs.8.5 and 8.6. The temperature coefficients of the conductivity of the two systems are shown in Fig. 8.7. In order to make a comparison, the existing data (Enderby and Barnes, 1990a) are listed in table 8.1.

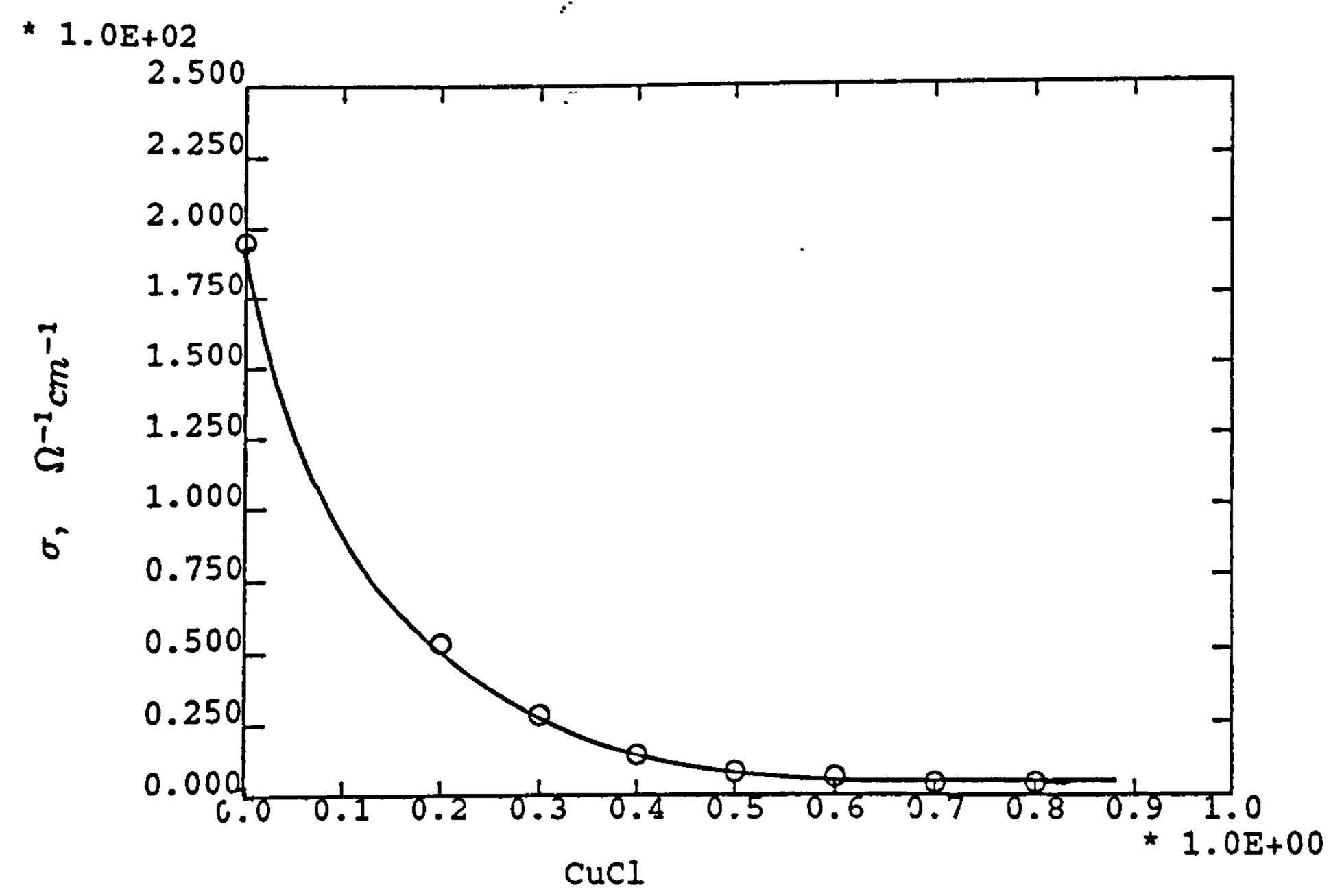

Figure 8.1: The conductivity of liquid $(CuCl)_y - (Cu_2Se)_{1-y}$ at 980 ^oC

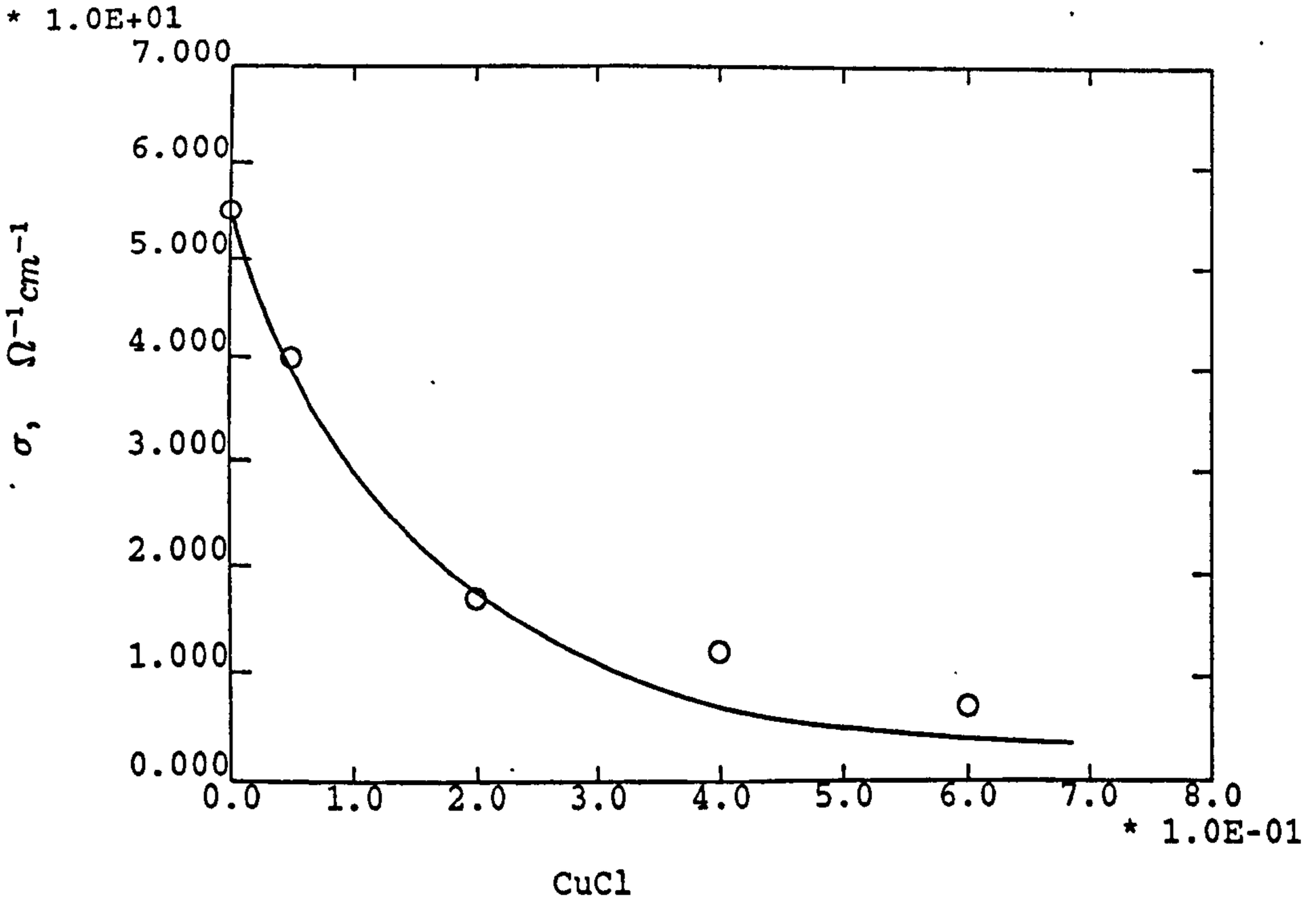

Figure 8.2: The conductivity of liquid $(CuCl)_y - (Cu_2S)_{1-y}$ at 980 ^oC.

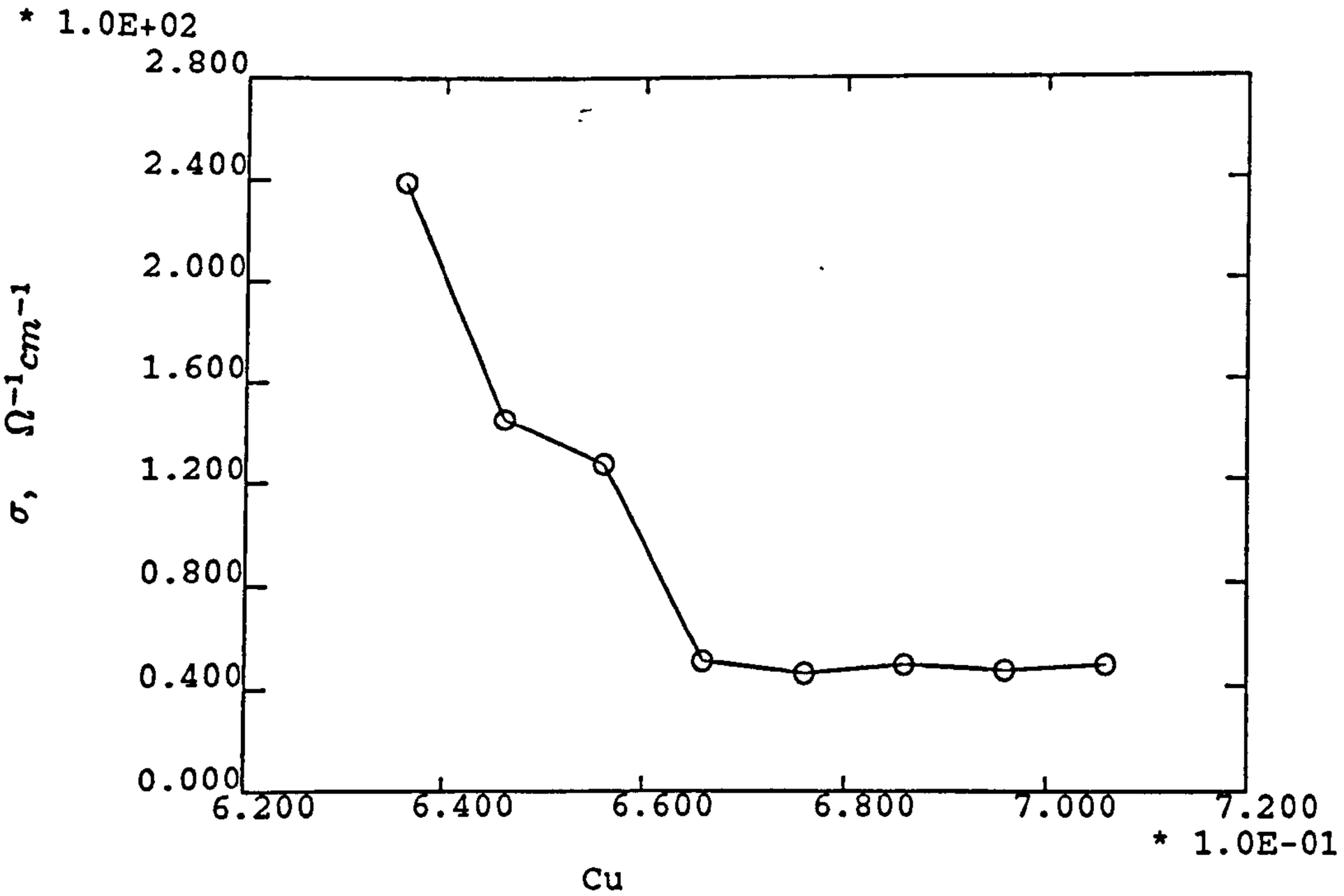

Figure 8.3: The conductivity of liquid $(CuCl)_{0.2}-(Cu_xSe_{1-x})_{0.8}$ at 980 °C.

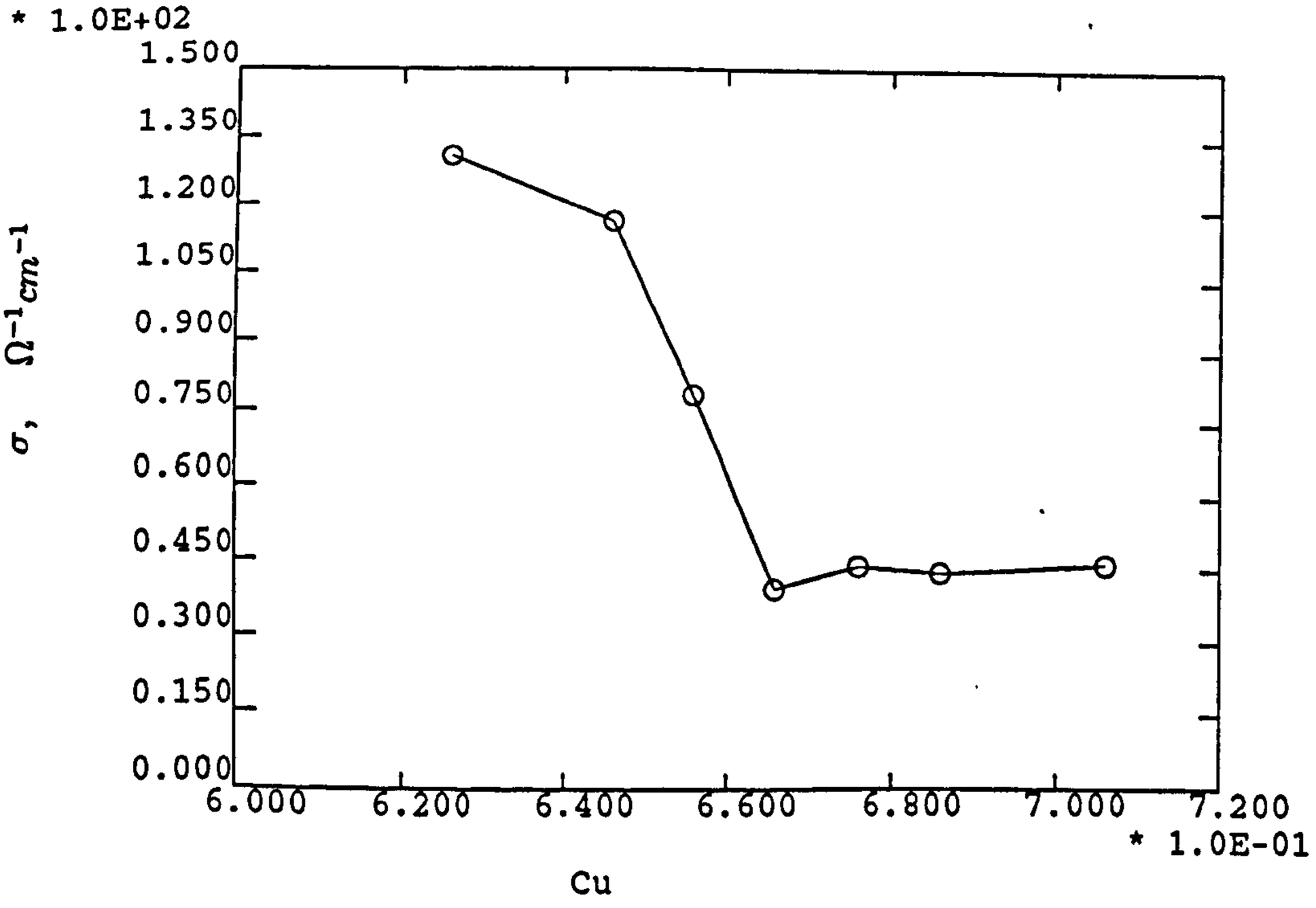

Figure 8.4: The conductivity of liquid $(CuCl)_{0.05}-(Cu_xS_{1-x})_{0.95}$ at 980 °C.

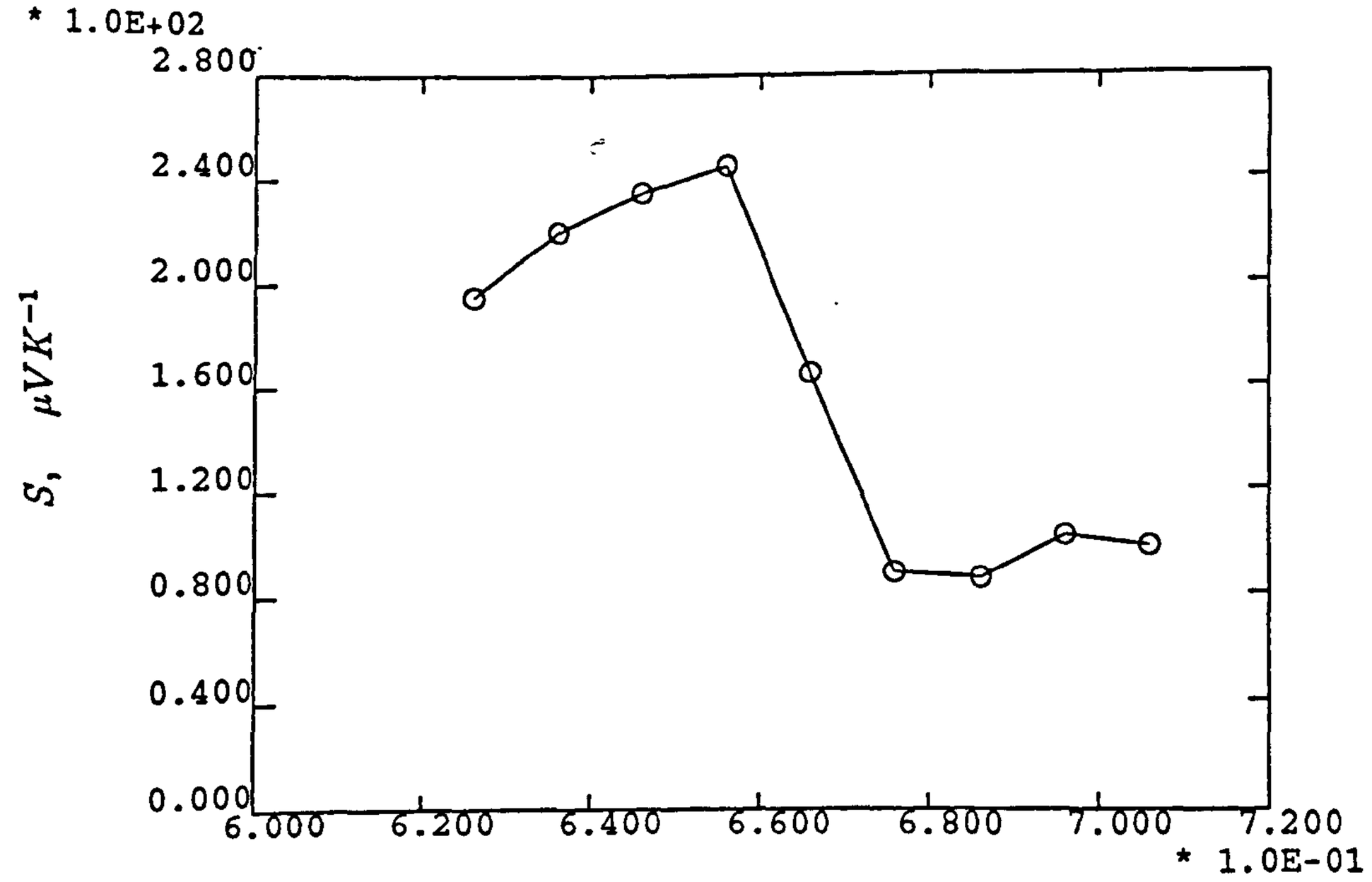

Figure 8.5: The thermopower of liquid $(CuCl)_{0.2} - (Cu_xSe_{1-x})_{0.8}$ at 980 ^oC.

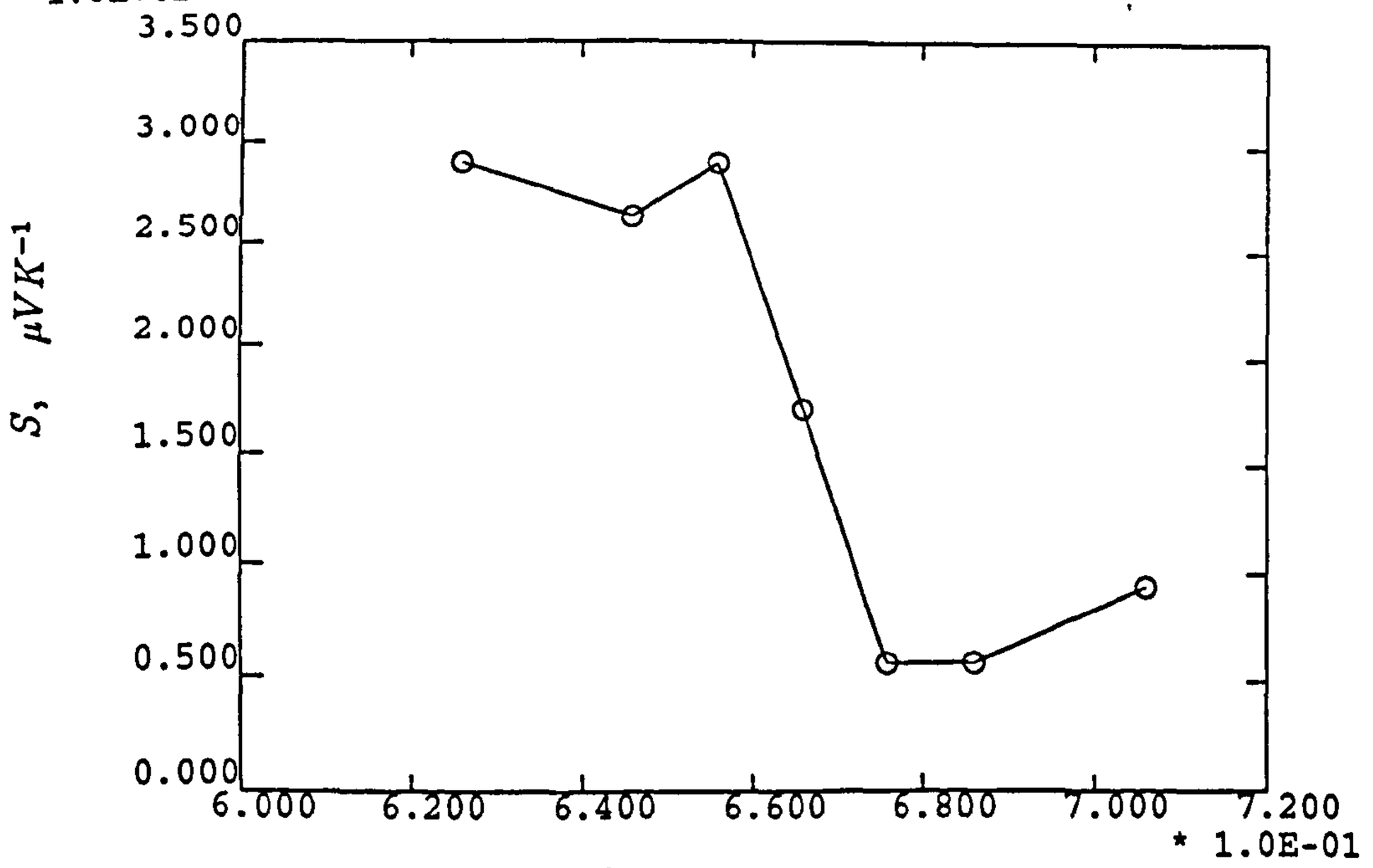

Figure 8.6: The thermopower of liquid $(CuCl)_{0.05} - (Cu_xS_{1-x})_{0.95}$ at 980 ^oC.

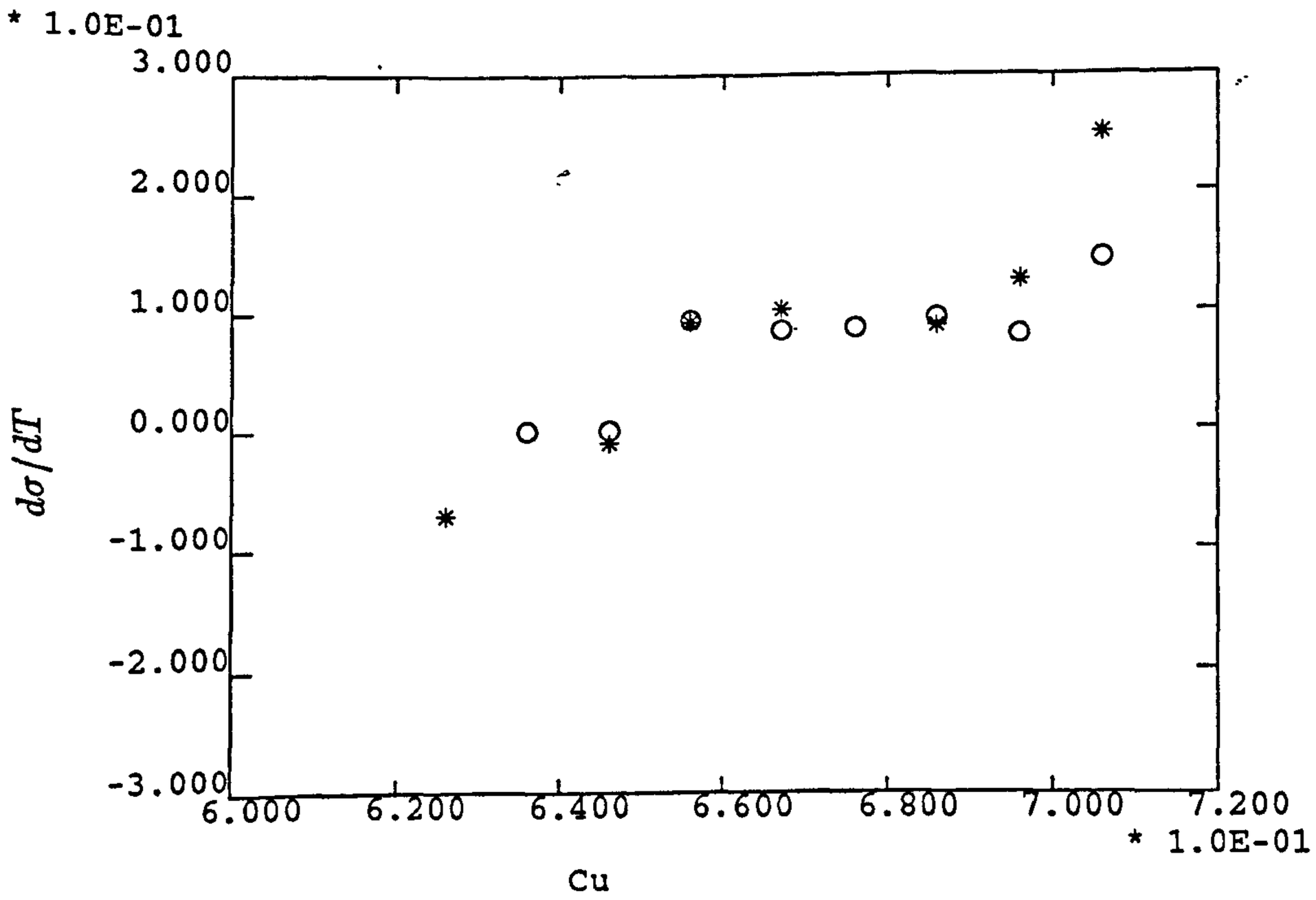

Figure 8.7: The temperature coefficient of the conductivity of liquid $(CuCl)_{0.2} - (Cu_2Se)_{0.8}$ (o) and $(CuCl)_{0.05} - (Cu_2S)_{0.95}$ (*).

Table 8.1 The existing data of the conductivity and thermopower for copper chalcogenides

Systems	Cu_2Se*	$(CuCl)_{0.2}-(Cu_2Se)^{**}_{0.8}$	Cu_2S*	$(CuCl)_{0.05}-(Cu_2S)^{**}_{0.95}$
$\sigma(\Omega^{-1}cm^{-1})$	158	50.4	38	40.3
S (μVK^{-1})	172	165	325	291

* data quoted from a review article (Enderby and Barnes, 1990a).

** data in this work

Fig.8.1 and 8.2 show that the conductivity decreases very quickly with the increase of the chloride. As the concentration of the chloride increases from 0 to 20 *at.%*, the conductivity drops from 190 to 55 $\Omega^{-1}cm^{-1}$ for the system $(CuCl)_y - (Cu_2Se)_{1-y}$. The conductivity of the system $(CuCl)_y - (Cu_2S)_{1-y}$ decreases from 55 to 40 $\Omega^{-1}cm^{-1}$ as the concentration of the chloride is increased form 0 to 5 *at.%*.

By comparing the data of this work with those of Enderby and Barnes (1990a) in table 8.1, it can be seen that the addition of copper chloride does not produce a noticeable effect on the values of the thermopower (note: this is only a preliminary conclusion because comparison to the other data usually contains considerable artificial experimental errors). This result is consistent with that of $Tl_2Te - CuCl$ and $Tl_2Se - CuCl$ systems stated in chapter 7. This indicates that although the conductivity decreases as the concentration of the chlorides increases, an increase in the value of the p-n transition ΔS of thermopower does not occur, which is expected to correspond a bigger band gap (Enderby and Barnes, 1988).

Contrary to the behaviour of the Tl_2Te and Tl_2Se systems, the conductivity of Cu_xSe_{1-x} and Cu_xS_{1-x} increases very slowly with excess metallic element Cu in the Cu_2Se and Cu_2S, while it increases quickly with the excess of the chalcogen elements Se and S, see Fig.8.3 and 8.4. Furthermore, Fig.8.5 and 8.6 show that the thermopowers behave unusually for both the systems. Only half of the p-n transition on the chalcogen-rich side was observed with the peak value 245 (μVK^{-1})

for the Cu_2Se and 290 (μVK^{-1}) for Cu_2S systems. Fig.8.7 gives the temperature coefficients of the conductivity of two systems, which show that with the increase of the non-metal chalcogen the temperature coefficients become smaller tending to the negative and more metal like. These special properties make the copper chalcogenides systems very interesting for understanding of conduction process of liquid semiconductors.

The Kubo-Greenwood equations with a rigid band model are clearly unworkable in this case. So it has not been tried.

8.3 Neutron diffraction

8.3.1 Experimental results

The above experiments have shown that when the concentration of $CuCl$ exceeds 40 *at.*%, the conductivity begins a transition from the electronic like behaviour of liquid semiconductors to the ionic like behaviour of molten salts. In order to see how this change is reflected in the underlying structure, neutron diffraction measurements of the mixtures $(CuCl)_y - (Cu_2Se)_{1-y}$ at y=0.2 , 0.4 and 0.6 have been carried out at the LAD on the ISIS facility at Rutherford-Appleton laboratory.

The structure factors corrected for the absorption and multiple scattering (the method reviewed in chapter 4), and the corresponding radial distribution functions have been produced by direct Fourier transform of the structure factors using the ATLAS analysis package, as shown in Figs. 8.8 and 8.9. Fig. 8.10 and 8.11 are the corresponding figures scaled up to the momentum transfer Q=5 $\AA^{-1}$ and r=5 Å in real space, respectively.

8.3.2 Interpretation for the experimental results

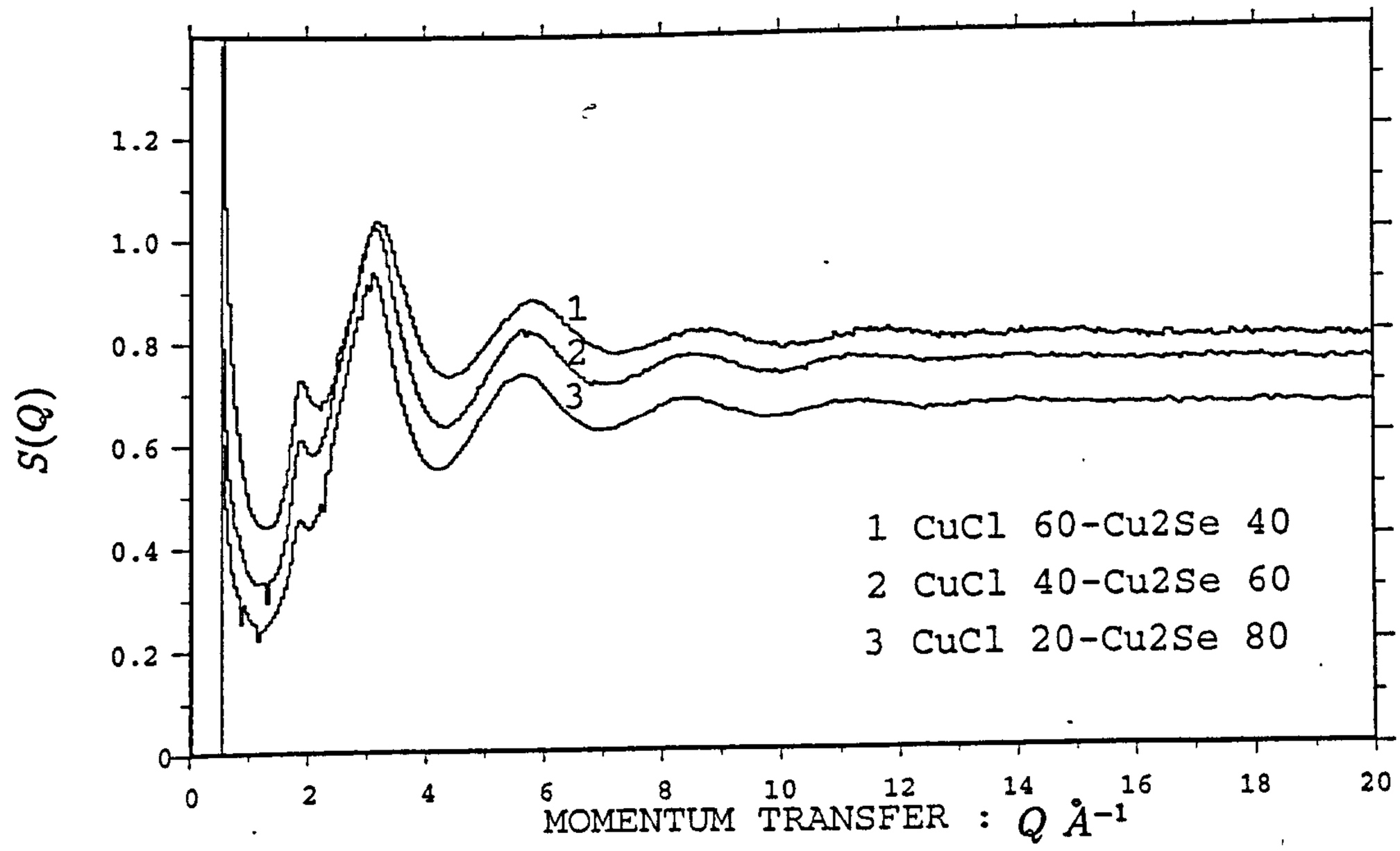

Figure 8.8: The total structure factor $S(Q)$ of liquid $(\mathrm{CuCl})_{0.6}-(Cu_2Se)_{0.4}$, $(CuCl)_{0.4}-(Cu_2Se)_{0.6}$ and $(\mathrm{CuCl})_{0.2}-(Cu_2Se)_{0.8}$ at 1050 ^{o}C.

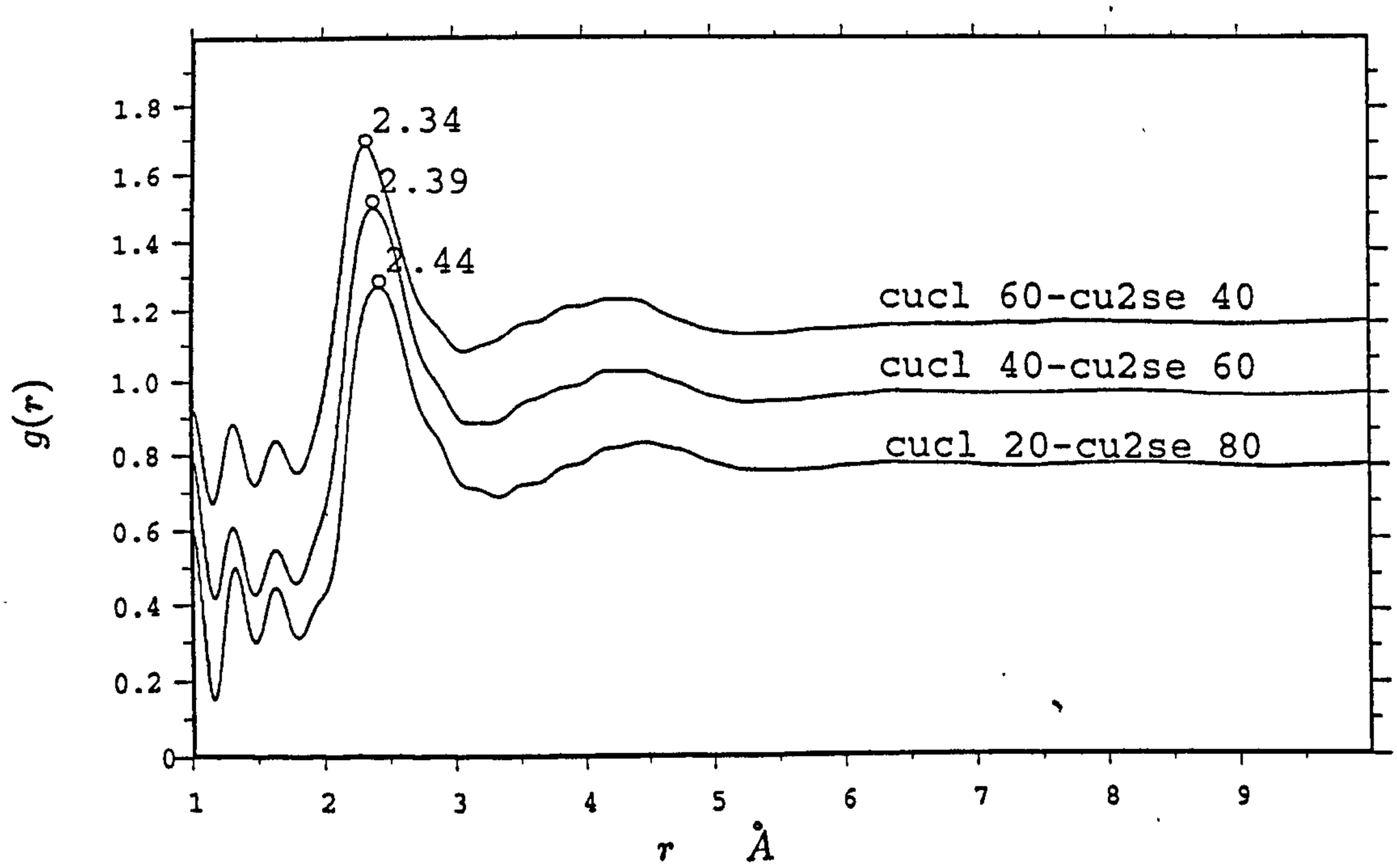

Figure 8.9: The radial distribution function $g(r)$ of liquid $(\mathrm{CuCl})_{0.6}-(Cu_2Se)_{0.4}$, $(CuCl)_{0.4}-(Cu_2Se)_{0.6}$ and $(\mathrm{CuCl})_{0.2}-(Cu_2Se)_{0.8}$ at 1050 ^{o}C.

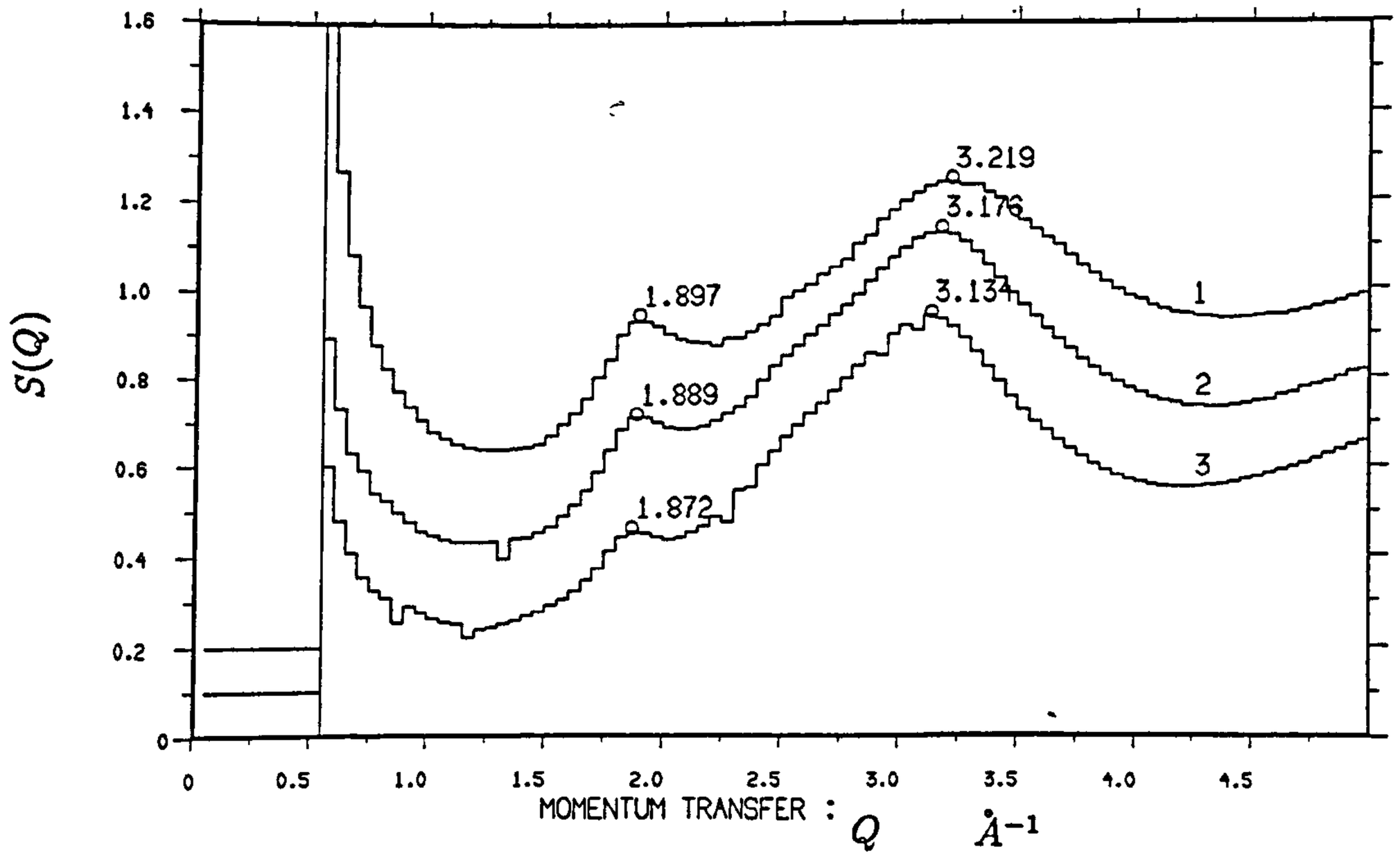

Figure 8.10: The total structure factor $S(Q)$ of liquid $(\mathrm{CuCl})_{0.6}-(Cu_2Se)_{0.4}$, $(CuCl)_{0.4}-(Cu_2Se)_{0.6}$ and $(\mathrm{CuCl})_{0.2}-(Cu_2Se)_{0.8}$ at 1050 ^oC. (in the Q-range of 0 - 5 $\mathring{A}^{-1}$)

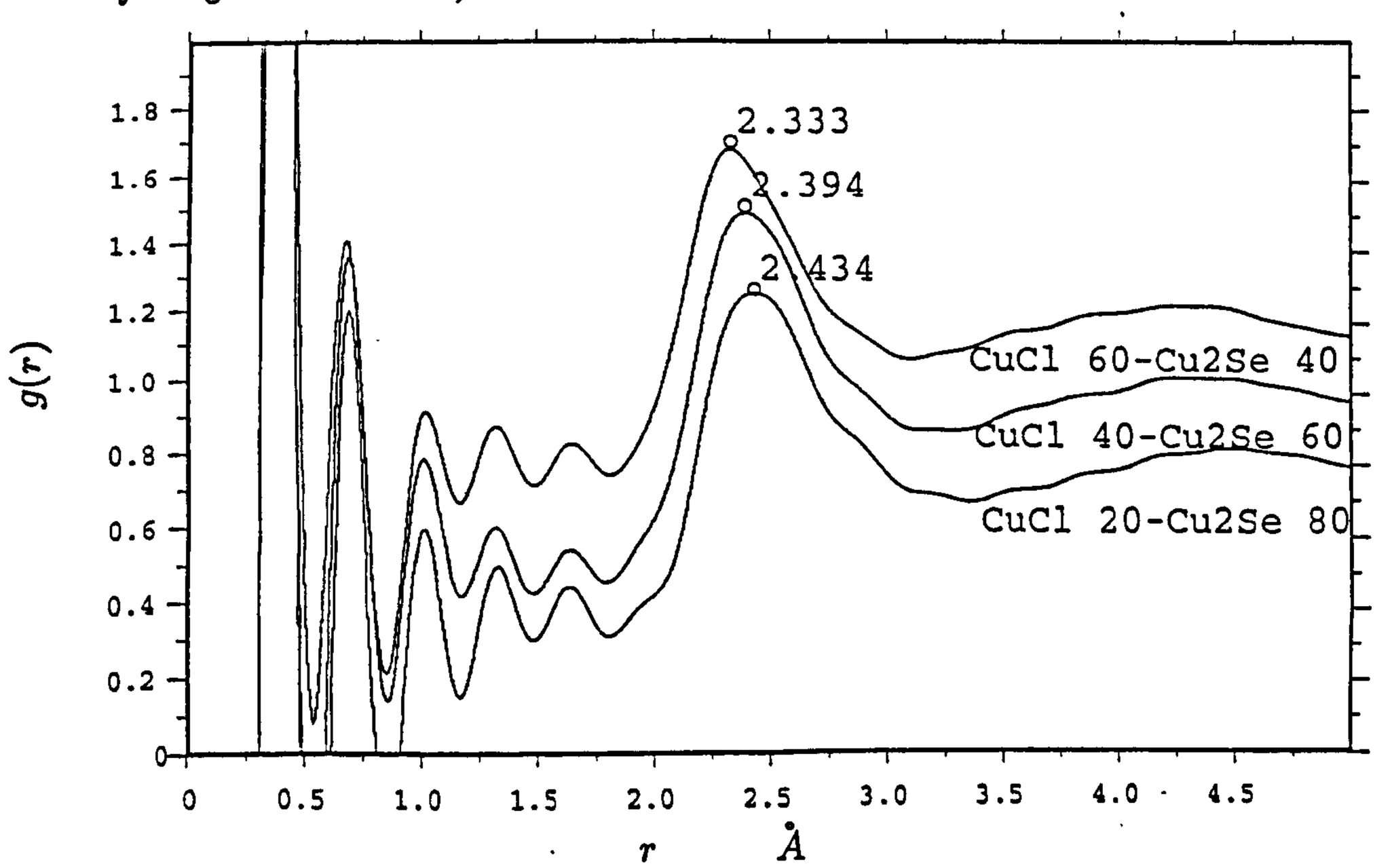

Figure 8.11: The radial distribution function $g(r)$ of liquid $(\mathrm{CuCl})_{0.6}-(Cu_2Se)_{0.4}$, $(CuCl)_{0.4}-(Cu_2Se)_{0.6}$ and $(\mathrm{CuCl})_{0.2}-(Cu_2Se)_{0.8}$ at 1050 ^oC. (in the r-range of 0 - 5 $\mathring{A}$)

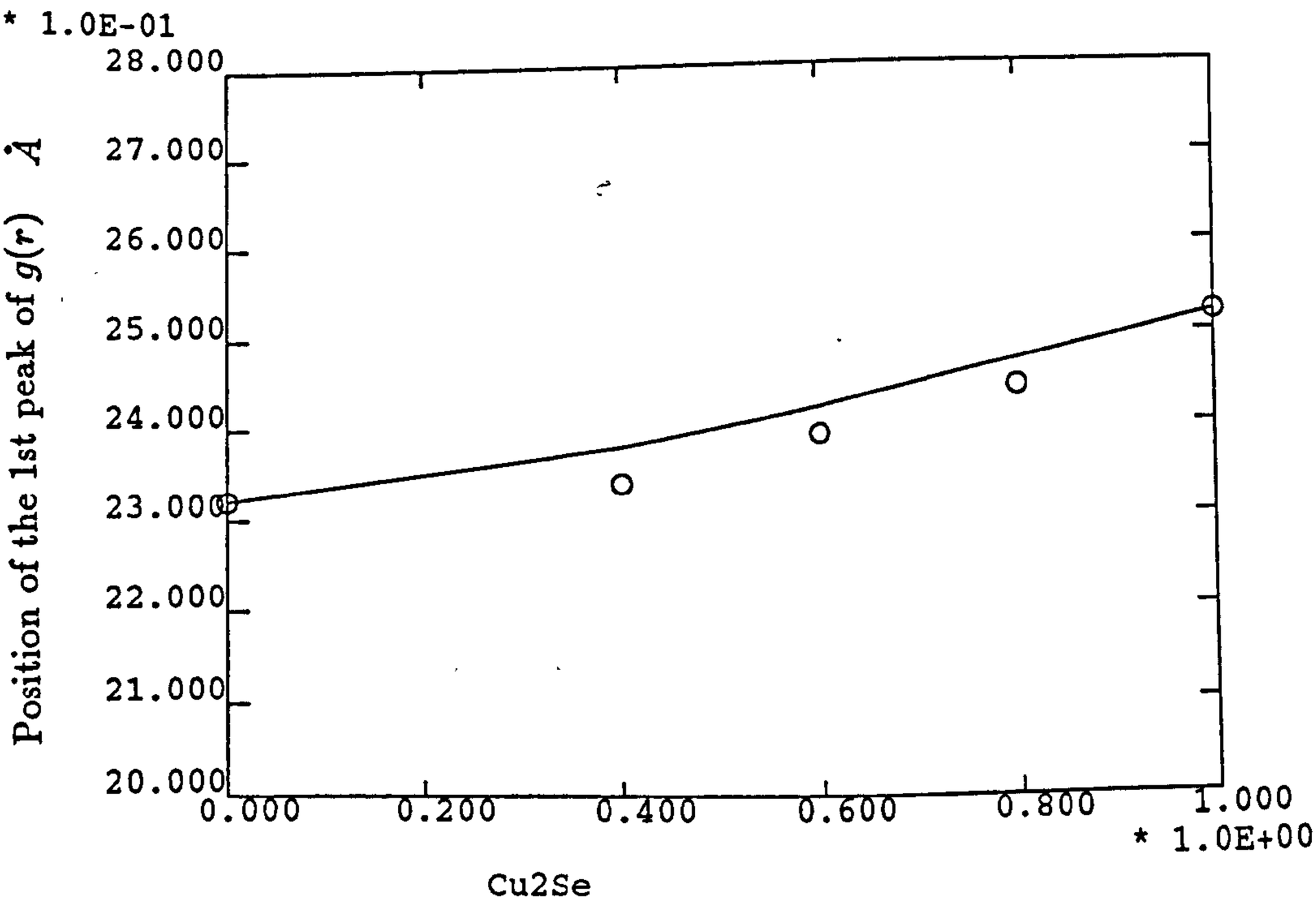

Figure 8.12: The positions of the first peak of $g(r)$ for liquid $(CuCl)_y - (Cu_2Se)_{1-y}$

It can be seen in Q-space that the structure factors are clearly characterised by a pre-peak at about 1.8 $\mathring{A}$ which is known as charge ordering shoulder and a hard sphere peak at about 3.2 $\mathring{A}$. Both the peaks shift upwards with the increase of copper chloride. The positions of the first peaks of the structure factors in this work, together with the pure Cu_2Se (Barnes, 1989) and $CuCl$ (page *et al.*, 1971) melts, are listed in table 8.2.

Table 8.2 The positions of the first peak of S(Q)s ($\mathring{A}^{-1}$) and g(r) ($\mathring{A}$)

Systems	Cu_2Se	$(Cu_2Se)0.8-(CuCl)0.2$	$(Cu_2Se)0.6-(CuCl)0.4$	$(Cu_2Se)0.4(CuCl)0.6$	CuCl
S(Q)	3.1	3.13	3.18	3.22	3.4
g(r)	2.52	2.43	2.39	2.33	2.32

It can be seen from table 8.1 that a systematic shift of the position of first main peak of the $S(Q)$ occurs with increasing the chloride. The pre-peaks in the Figs.8.8 and 8.10 get more pronounced and the first peaks become broader as the chloride is increased.

In real-space, the positions of first peak of $g(r)$s of the three samples decrease in opposition with those of $S(Q)$ in Q-space as the $CuCl$ concentration increases. The high temperature forms of both Cu_2Se and $CuCl$ are superionic conductors and the short-range order characteristic of the solid persists in the liquid phase (Barnes, 1991). The ionic radii and the mean distances of $Cu-Se$ in Cu_2Se melt (Barnes, 1989) and $Cu-Cl$ in $CuCl$ melt (page *et. al.*, 1971) are listed in table 8.3.(ionic radii quoted by Weast, 1975)

Table 8.3 Ionic radii and the mean distance of Cu-Se and Cu-Cl

$r_{Cu^{1+}}/\mathring{A}$	$r_{Se^{2-}}/\mathring{A}$	$r_{Cl^{1-}}/\mathring{A}$	$\bar{r}_{Cu-Se}/\mathring{A}$	$\bar{r}_{Cu-Cl}/\mathring{A}$
0.96	1.91	1.81	2.52	2.32

It can be seen from table 8.3 that the measured mean distances of $Cu-Se$ (2.52 Å) and $Cu-Cl$ (2.32 Å) are significantly different from the sum of the radii of the

cation and anion (2.87 Å for $Cu-Se$ and 2.77 Å for $Cu-Cl$). The ionic model in its elementary form is therefore not simply applicable in these systems. Page *et al* suggested that the association of several Cl^{1-} ions with one Cu^{1+} forms a complex ion $(Cu^{1+}Cl_n^{1-})^{(n-1)-}$. The coordination number $\overline{n}_{CuSe}$ for the Cu_2Se melt is four (Barnes, 1989), this implies that the anionic association may also occur in the Cu_2Se melt.

For an ideal ionic system the statistical distribution of the first peak position follows (Lamparter *et al*, 1976)

$$r^I_{st.} = \frac{c_A r^I_A b_A + c_B r^I_B b_B}{c_A b_A + c_B b_B} \tag{8.1}$$

where c_A and c_B are the concetration of the component A and B, b_A and b_B are their coherent scattering length, f_m and the r^I_A and r^I_B are first peak positions in their pure melt. If we assume that Cu_2Se-$CuCl$ is the simple mixture of Cu_2Se and $CuCl$ and the scattering length is the averaged scattering length (*e.g.* $b_{Cu_2Se} = c_{Cu}b_{Cu} + c_{Se}b_{Se}$ and $b_{CuCl} = c_{Cu}b_{Cu} + c_{Cl}b_{Cl}$), the r^I_{st} statistical distribution of the mixture can be calculated, shown in Fig. 8.12. A steady shift of the first peak of the measured $g(r)$ in this work from 2.32 to 2.52 Å is also plotted on Fig.8.12. It can be seen that the measured shift as the concentration of the selenide is increased is essentially consistent with the calculated one with only a small negative deviation. It is strongly suggested that the cation Cu^{1+} can have two types of the first coordination neighbours, e.g. Se^{2+} and Cl^{1-}, the number of the either neighbour depends on its concentration in the mixture. The first peak is composed of r_{Cu-Se} and r_{Cu-Cl} and consequently the shifting of the first peak position of $g(r)$ will be caused by the addition of either component, and essentially obeys the statistical distribution. The small negative deviation may hint that there exists, to some extent, a chemical correlation between the two types of the associations.

It is, therefore, suggested that the mixtures of $CuCl-Cu_2Se$ are composed of two types of associations i.e. $[(Cu^{1+}Cl_n^{1-})^{(n-1)-} + (Cu^{1+}Se_n^{2-})^{(2n-1)-}]$. The chemical bonding between Cu and Se is essentially ionic.

8.4 Discussion

The electronic properties of liquid Cu_2Se and Cu_2S are distinctly different from the thallium chalcogenides; (1) The conductivity of Cu_2Se and Cu_2S increases very slowly with excess metallic element Cu and rapidly with excess non-metallic chalcogens Se or S, which is opposite to the behavior of thallium chalcogenides; (2) The p-n transition of Cu_2Se and Cu_2S occurs only on the chalcogen-rich side, i.e. half p-n transition. The Kubo-Greenwood equations with a rigid band model (BE theory) could not be applied to give a good explanation.

8.4.1 Interatomic and intraatomic structures of Cu_2Se and Cu_2S

Copper is a transition metal with the electronic configuration [Ar]$3d^{10}4s^1$. It can exist in three oxidation states Cu^{1+}, Cu^{2+}, Cu^{3+} by losing s and d electrons in different environments. The Cu chalcogenides are remarkably complex systems existing in many phases. In Cu-Se system, there exist four stoichiometric compound $CuSe_2$, $CuSe$, Cu_3Se_2 and Cu_2Se, but the only Cu_2Se is stable in both solid and liquid states. In the solid there are two cystallographic modifications with a transition temperature of 123 ^oC. The high temperature β-phase of Cu_2Se is a superionic conductor. Barnes and Enderby (1989) measured the structures of Cu_2Se using neutron diffraction, some of the data are quoted together with some reference crystal data in table 8.4.

Table 8.4 The structure data of the crystal, β-phase and liquid of Cu_2Se

	$\overline{r}_{CuSe}$ $\mathring{A}$	$\overline{r}_{CuCu}$ $\mathring{A}$	Coordination Number
Ideal Crystal	2.50	2.88	4 (Se around Cu) 6 (Cu around Se)
High Temperature α-phase	2.35 - 2.5	2.35 - 2.88	~4+~6
Ionic Model*	2.87	3.31	
Liquid	2.52 $\pm$ 0.02	2.52 $\pm$ 0.04	4+4

* Based on the ionic radii quoted by Weast (1975) and antifluorite local order (Cu^{1+}=0.96 $\mathring{A}$ and Se^{2-}=1.91 $\mathring{A}$)

It has been known that the ionic model in its elementary form is not applicable to the liquid and the distances of Cu-Se and Cu-Cu are significantly shorter than those calculated with the ionic model. It is however clear that the short range order characteristic of high temperature superionic phase persists in the liquid phase. The mean cation-cation seperation in the superionic phase is usually smaller than that in the normal phase. Ramasesha (1981) showed using statistical thermodynamics that mobile cations in the superionic compound can cause a big increase in the concentration of mobile electrons. It could consequently be thought that the metallicity of the compound would be enhanced by the higher concentration of mobile electrons. The underlying ionic model therefore need to be corrected for covalency if we regard the metallic bonding as a 'mobile' covalent bonding.

The band structure of copper chalcogenides should however, resemble that of Mg_3Bi_2 because both of them have basically ionic bonding and their high temperature β-phases have superionic structures although Copper chalcogenide has a anionic complex structure.

8.4.2 An explanation for the electronic properties

The neutron diffraction studies of Cu_2Se show that it is possible that anionic complex ions exist in the liquid in the form of $(Cu_nA_m)^{1-}$, where A is a chalcogen. When adding copper, the large complex ions could be separated or simplified , but there is no significant effect on the electronic band structure and position of the Fermi energy because the band structure and the Fermi energy mainly depend on the intraatomic interaction. When adding chalcogens, they are ionised, but are not involved with the complex ions. The net effect is that they create mobile holes in the valence band.

(i) On the chalcogen-rich side of Cu_2Se and Cu_2S

With excess Se or S, the conductivity increases rapidly and the thermopower becomes more positive. The temperature coefficients tend to become more negative. With excess chalcogen more holes at the top of chalcogen p-like valence band are produced as a result of the deficit of electrons. Therefore, adding chalcogen to the compound Cu_2Se or Cu_2S is equivalent to creating holes in the valence band and thus the current is carried by delocalised holes in the valence band.

(ii) On the Cu-rich side of Cu_2Se and Cu_2S

The conductivity is not sensitive to the excess of metallic element Cu. The thermopower shows a similar behaviour after the slight excess. This phenomenon was also observed by Dancy (1965) in Cu-Te system, and the similar phenomenon can be found in the magnetic susceptibility (Okada, *et al*, 1983). Both the conductivity and the susceptibility depend greatly on the N(E_F). This implies that the N(E_F) does not change too much on increasing Cu. The excess coppers are involved to simplify the big complex ions and no non-bonding electrons exists in the form of 'extra' states . The Fermi energy and band structure have no large change.

Chapter 9

Summary

9.1 Liquid Mg – Bi system

a. The electronic properties

1. The conductivity of liquid $Mg - Bi$ shows a deep minimum at stoichiometry Mg_3Bi_2 and is very sensitive to small changes of the composition, while the thermopower changes slowly and steadily across stoichiometry from the negative Mg-rich side to the positive at the Bi-rich side.

2. The theoretical calculation of the electronic properties of liquid $Mg-Bi$ based on the Kubo-Greenwood equations with a generic model of $\sigma(E)$ shows that a rigid band model of the density of states is totally inadequate in explaining the electronic behaviour of liquid $Mg - Bi$. There must be a dramatic change in the band structure as the composition is moved slightly away from the stoichiometry Mg_3Bi_2.

b. The structural properties

1. The high temperature β-phase of Mg_3Bi_2 was determined to be a cubic superionic structure by neutron diffraction and reverse Monte Carlo computer simulation. The mobile species is Mg^{2+}.

2. Neutron diffraction and reverse Monte Carlo computer simulations show that Mg_3Bi_2 is essentially ionic, but with a deep penetration of the first peak of $S_{Mg-Mg}(Q)$ into the first peak of $S_{Mg-Bi}(Q)$. The Mg atoms are coordinated with both themselves and the Bi in the first coordination shell.

9.2 Liquid Tl chalcogenides – Tl chloride

a. The electronic properties

1. The conductivity of liquid $(TlCl)_y - (Tl_2Te)_{1-y}$ and $(TlCl)_y - (Tl_2Se)_{1-y}$ decreases rapidly with increasing the concentrations of the molten salt thallium chloride. When the concentration of the thallium chloride is over 20 %, the conductivity appears to become essentially ionic.

2. Liquid Tl_xTe_{1-x} and Tl_xSe_{1-x} have similar electronic properties. Their conductivities show a minimum at stoichiometry Tl_2Te or Tl_2Se, but are very asymmetric about it . The excess Tl increases the conductivity much more rapidly than excess Te. The p-n transition ΔS and ambipolar effects of the thermopower were clearly observed on both systems.

3. The Kubo-Greenwood equations with a rigid band model work well in the sign, magnitude and composition dependence on the Tl-rich side. On the chalcogen-rich side, only the calculated thermopower is consistent with the measured magnitude of the p-n transition ΔS.

b. The structural properties

1. Neutron diffraction studies in this work together with the existing structural data show that Tl_2Se and Tl_2Te are essentially ionic materials with valence states of Tl^{1+} and Se^{2-} (or Te^{2-}). They are isostructural in the liquid phase apart from minor variation due to the slightly different sizes of Tl^{1+} and Se^{2-} ions.

9.3 Liquid Cu chalcogenides – Cu chloride

a. The electronic properties

1. The conductivity of liquid $(CuCl)_y - (Cu_2Se)_{1-y}$ and $(CuCl)_y - (Cu_2S)_{1-y}$ drops quickly. When the concentration of copper chloride is over 20 at.%, the conductivity changes from liquid semiconductor like to molten salt like.

2. Contrary to the behaviour of the Tl_2Te and Tl_2Se systems, the conductivity of Cu_xSe_{1-x} and Cu_xS_{1-x} increases very slowly with excess metallic element Cu in Cu_2Se and Cu_2S, while it increases rapidly with the excess of the chalcogen elements Se and S. Only half of the p-n transition on the chalcogen-rich side was observed. Adding metallic element Copper has a much smaller effect on the electronic properties than adding the chalcogen elements.

b. The structural properties

The chemical bonding between Cu and Se for liquid Cu_2Se is essentially ionic. A complex ion $(Cu^{1+}Se_n^{1-})^{(n-1)^-}$ is suggested to exist in the melt.

9.4 Theoretical points

According to the BE theory and the nature of the states of the excess electrons (or holes), the following four cases for liquid quasi-ionic semiconductors M_aA_m are generalised as:

1. Ideal case

A very small amount of M (or A) is dissolved and ionised in the liquid stoichiometric compound M_aA_m. The addition of M or A does not cause a significant change in the density of states and the band is considered as 'rigid'. The orbitals of the excess electrons will lie in the M-like conduction band (the holes in the A like valence

band if A is in excess). Consequently the Fermi energy shows a corresponding shift away from the middle of the band gap into the bands, and the band gap remains unaffected. The Kubo-Greenwood equations based on the rigid band model (BE theory) are applicable in this regime.

2. The metallic bonding

If the added M or A is metallic element, it reacts chemically with either like or unlike species to form metallic bonding. The Madelung potential in the liquid quasi-ionic compound M_aA_m will be largely reduced by the electronic screening effect and the band gap starts closing up. The conductivity increases dramatically as the band gap collapses, while the thermopower is held down and appears to become more metal like (low thermopower).

3. The covalent bonding

If the added M or A is non-metallic element, it reacts chemically with either like or unlike species to form covalent bonding. The covalent bonding will mainly hold down the conductivity by keeping the Fermi energy near the mid band gap. In this case a clear p-n transition of the thermopower will still occur.

4. The polyanions

This case is complicated. For example in a liquid containing polyanions, the addition of metallic cations may result in the break up of some of polyanions into simpler species, e.g. $2e + Se_2^{2-} = 2Se^{2-}$, where the additional electrons come from the added cations.

For the last three cases, the BE theory using rigid band models would not be able to describe their behaviour. However, by including realistic models for the changes in N(E) in these processes, these systems might be modelled using similar methods.

Bibliography

[1] Ashcroft N W and Mermin N D, < Solid State Physics>, Holt-Saunders, 1976

[2] Anderson P W, Phys. Rev., Vol.109, 1958 p1492

[3] Armstrong R D, < Fast Ion Transport In Solids > ed Van Gool, North Holland, Amsterdam, 1972 p269

[4] Barnard R D, <Thermoelectricity in Metals and Alloys>, Taylor and Francis, London, 1972

[5] Barnes A C, <The Structureal and Electrical Properties of Some Liquid transition Metal-chalcogenide Alloys>, Ph.D Thesis, University of Bristol, 1986

[6] Barnes A C, J. Non-crystalline Solids, Vol.156-158, 1993 p675

[7] Barnes A C and Enderby J E, J. Non-Crystal. Solids, Vol.77-78, 1985 p1343

[8] Barnes A C and Enderby J E, Phil. Mag. B58, 1988, p497

[9] Barnes A C and Enderby J E, ILL Annual Report, Grenoble, ILL, 1989

[10] Barnes A C, Laundy D and Enderby J E, Phil. Mag., B55, 1987 p497

[11] Beeby J L, Phys. Rev. A, Vol.135, 1964 p130

[12] Biggin S and Enderby J E, J. Phys. C: Solid State Phys., Vol.14, 1981 p3129

[13] Biggin S and Enderby J E, J. Phys. C: Solid State Phys., Vol.15, 1982 L305

[14] Blatt F J and Schroeder P A <Thermoeletricity in Metallic Conductors>, Plenum Press, New York, 1977

[15] Boland B C, < Experimental Facilities at ISIS - User Guide >, RAL, Februry 1990

[16] Cohen M H, Fritzsche H and Ovshinsky S R, Phys. Rev. Lett., Vol.22, 1969 p1065

[17] Cohen M H and Sak J, J. Non-Cryst. Solids, Vol.8-10, 1972 p696

[18] Cohen M H, Soukoulis C M and Economou E N, < The Physics of Disordered Materials > ed. Adler D *et al*, Plenum press, New york, 1985 p305

[19] Cutler M, Phil. Mag., Vol.24, 1971 p381

[20] Cutler M, Phil. Mag., Vol.25, 1972 p173

[21] Culter M, < Liquid Semiconductors > Academic, New york, 1977

[22] Dancy E A, Trans. Metall. Soc. AIME, Vol.233, 1965 p270

[23] Dancy E A and Derge G, Trans. Metall. Soc. AIME, Vol.227, 1963 p1034

[24] Edwards F G, Enderby J E, Howe R A and Page D I, J. phys. C:solid stats phys., Vol.8, 1975 p3483

[25] Edwards F G, How R A, Enderby J E and Page D I, J. Phys. C: Solid State Phys., Vol.11, 1978 p1053

[26] Egan J J, ACTA Metallurgica, Vol.7, 1959, p560

[27] Enderby J E, < Band Structure Spectroscopy of Metals and Alloys >, Academic Press, London, 1973

[28] Enderby J E and Barnes A C, J. Electrochem. Soc., Vol.134, No.10, 1987 p2483

[29] Enderby J E and Barnes A C, < Liquid Semiconductors >, Rep. Prog. Phys., Vol. 53, 1990 p85-179 – (a)

[30] Enderby J E and Barnes A C, J. Phys. Condens. Matter, Vol 2, 1990, SA 219 – (b)

[31] Enderby J E and Collings E W, J Non-Cryst. Solids, Vol.4, 1970, p161

[32] Enderby J E and Gay A M, J Non-Cryst. Solids, Vol.35-36, 1980, p1269

[33] Enderby J E , North D M and Egelstaff P A, Adv. Phys., Vol.16, 1967 p171

[34] Evens R and Telo da Gama M M, Phil. Mag., B14, 1980 p351

[35] Faber T E, < Introduction to the theory of Liquid Metals >, Cambridge University Press, 1972

[36] Ferrier R P and Herrell D J, Phil. Mag., Vol. 19, 1969 p853

[37] Ferrier R P and Herrell D J, J. Non-Cryst. Solids, Vol.2, 1970 p278

[38] Folmer J C W and Jellinek F, J. Less-Common Met., vol.76, 1980 p153

[39] Friedman L , J. Non-Crys. Silids, Vol.6, 1971 p329

[40] Fritzsche H, Solid State Commum., No.9, 1971, p1813

[41] Gay M, Enderby J E and Egelstaff P A , Phil. Mag., Vol.14 1982, p4641

[42] Glazov V M, Koltsov V B and Kurbatov V A, Sov. Phys. Vol.20, 1986 p889

[43] Greenwood D A, Proc. Phys. Soc., Vol. 71, 1958, p585

[44] Hawker I, Ph. D. Thesis, University of Bristol, 1974

[45] Hawker I, Howe R A and Enderby J E, Proc. Int. Conf. on the Electronic and Magnetic Properties of Liquid Metals, UNAM, Mexico city, 1978 p262

[46] Howe R A and Enderby J E, Phil. Mag., Vol 16, 1967 p467

[47] Ioffe A F and Regel A R, Progr. Semicond., No.4, 1960 p238

[48] Kazandzhan B I and Tsurikov A A, Russ. J. Phys. Chem., Vol. 48, 1974 p729, 738, 746

[49] Kubo R, Canad. F. Phys., Vol.134, 1956 p1274

[50] Lovesey S W, < Theory of Neutron Scattering from Condensed Matter >, Volume I: Neutron Scattering, Oxford University Press, 1986

[51] McGreevy R L, Howe M A, Nield V M Wicks J D and Keen D A, Physica B, Vol 180-181, 1991 p801

[52] McGreevy R L and Pusztai L, Mol. Simulation, No.1, 1988 p359

[53] Michael Weber, Siegfried Steeb, and Peter Lamparter, Z. Naturforsch, Vol.34a , 1979 p1398

[54] Mott N F and Davis E A, < Electronic Processes in Non-Crystalline Materials >, Clarendon Press, Oxford, 1971

[55] Mott N F and Davis E A, < Electronic Processes in Non-Crystalline Materials >, (2nd edition), Clarendon Press, Oxford, 1979

[56] Nakamura Y and Shimoji M, Trans. Faraday Soc., Vol. 67, 1971 p1270

[57] Newport, R.J., Ph.D Thesis, University of Leicester, 1979

[58] Nguyen V T, Gay M, Enderby J E, Newport R and Howe R A, J. phys. C: Solid state phys. Vol.15, 1982 p4627

[59] Paalman H H and Pings C J, J. Appl. Phys., Vol.33, 1962, p2635

[60] Placzek G, Phys. Rev., Vol. 95, 1952 p249

[61] Okada T, Kakinuma F, and Ohno S, J. Phys. Soc. Jpn., Vol.52, 1983 p3526

[62] Ramasesha S, J. Solid state Chemistry, Vol.41, 1982 p333

[63] Regel A R *et al*, Proc. Int. Conf. Phys. Semicond. 10th, Cambridge Massachusetts, 1970 p773

[64] Robertson J, Phil. Mag. B, Vol. 39, 1979 p479

[65] Roth L, Proc. Int. Conf. on the Electronic and Magnetic Properties of Liquid Metals, Mexico, 1975 p344

[66] Salamon M B, < Physics of Superionic Conductors >, Springer, Berlin, 1979

[67] Sears V F, < Thermal Neutron Scattering Lengths and Cross Sections for Condensed-Matter Research >, AECL Report 8490, Chalk River Nuclear Laboratories, Canada, 1984

[68] Sik M J and Ferrier R P, Phil. Mag., Vol.29, 1974 p877

[69] Soper A K and Egelstaff P A, Nucl. Inst. Meth., Vol.17, 1980

[70] Soper A k, W S Howells and A C Hannon, < ATLAS - Analysis of Time-of-Flight Diffraction Data from Liquid and Amorphous Samples >, RAL, May 1989

[71] Squires G L, < Introduction to the Theory of the Thermal Neutron Scattering >, Cambridge University Press, 1978

[72] Sutton A P, < Electronic Structure of Materials>, Oxford University Press, New York, 1993

[73] Sutton C M , Solid state communications, Vol. 16, 1975 p327

[74] Terpilowski J and Zaleska E, Rocz. Chem., Vol. 37 1963 p193

[75] Thomas P, J. Non-Cryst. Solids, Vol.77-78, 1975 p121

[76] Van Hove L, Phys. Rev., Vol.95, 1954 p249

[77] Waseda Y, < Novel Application of Anomalous Scattering for Structural Characterisation of Disordered Materials >, Springer, Berlin, 1984

[78] Watson L M, Marshall C A W and Cardoso C P, J. Phys. F: Met. Phys. , Vol.14, 1984 p113

[79] Weast R C, < Hand book of Chemistry and Physics >, CRC, Florida, 1975

[80] Zintl E and Husemann E Z., Phys. Chem., B21, 1933 p138

APPENDIX

.1 Experimental data for liquid Mg-Bi

Table A-1 The conductivities and thermopowers of liquid Mg-Bi at 920 ^{o}C

Bi, *at.*%	38.0	38.5	39.0	39.5	40.0
σ, $\Omega^{-1}cm^{-1}$	1550.0	1520.0	1500.0	1417.0	63.0
S, μVK^{-1}		−5.81	−4.80	−2.60	−0.56
Bi, *at.*%	40.5	41.0	41.5	42.0	
σ, $\Omega^{-1}cm^{-1}$	943.0	1050.0	1416.0	1800.0	
S, μVK^{-1}	−0.19	0.78	1.94	2.40	

Table A-2 The temperature coefficient of liquid Mg-Bi

Bi, *at.*%	38.0	38.5	39.0	39.5	40.0
$d\sigma/dT$	3.40	3.33	4.00	3.40	3.00
Bi, *at.*%	40.5	41.0	41.5	42.0	
$d\sigma/dT$	4.20	4.50	4.60	5.00	

.2 The conductivities and thermopowers of liquid Thallium chalcogenides and chloride

Table A-3 The conductivities of liquid $TlCl - Tl_2Te$

TlCl, *at.%*	0.0	10.0	20.0	30.0
$\sigma, \Omega^{-1}cm^{-1}$	15.5	9.5	5.0	4.0

Table A-4 The conductivities and thermopowers of liquid Tl_xTe_{1-x}

Tl, *at.%*	59.7	60.7	62.2	63.2	64.2	64.6
$\sigma, \Omega^{-1}cm^{-1}$	201.0	187.0	178.0	172.0	166.0	159.0
S, μVK^{-1}	112.0	112.0	111.0	106.0	87.0	
Tl, *at.%*	65.2	66.2	66.7	67.2	67.7	68.2
$\sigma, \Omega^{-1}cm^{-1}$	151.0	144.0	145.0	270.0	475.0	623.0
S, μVK^{-1}	53.0	10.0	−29.0	−122.0	−108.0	−94.0

Table A-5 The conductivities and thermopowers of $(Tl_xTe_{1-x})_{0.9} - (TlCl)_{0.1}$

Tl, *at.%*	56.5	57.7	59.7	60.8	61.5	62.7
$\sigma, \Omega^{-1}cm^{-1}$		262.0	250.0	237.0	209.0	179.0
S, μVK^{-1}	91.0	112.0	130.0	130.0	111.0	89.0
Tl. *at.%*	63.7	65.7	66.7	67.2	67.7	68.2
$\sigma, \Omega^{-1}cm^{-1}$	170.0	130.0	105.0	100.0	309.0	648.0
S, μVK^{-1}	57.0	36.0	−20.0	−55.0	−120.0	−90.0

Table A-6 The conductivities and thermopowers of liquid $(Tl_xTe_{1-x})_{0.8} - (TlCl)_{0.2}$

Tl, *at.*%	62.6	63.6	64.5	66.2
σ, $\Omega^{-1}cm^{-1}$	169.0	113.0	108.0	104.0
S, *at.*%	66.0	18.0	8.0	−8.0
Tl, *at.*%	66.7	67.2	67.7	68.2
σ, $\Omega^{-1}cm^{-1}$	85.0	247.0	411.0	493
S, μVK^{-1}	−46.0	−120.0	−105.0	−90.0

Table A-7 The conductivities and thermopowers of liquid Tl_xSe_{1-x}

Tl, *at.*%	64.2	64.7	65.2	65.7	66.6
σ, $\Omega^{-1}cm^{-1}$	27.0	25.4	24.2	20.2	16.1
S, μVK^{-1}	242.0	241.0	212.0	135.0	16.0
Tl, *at.*%	67.2	67.7	68.7	69.4	
S, μVK^{-1}	−28.0	−150.0	−221.0	−175.0	
σ, $\Omega^{-1}cm^{-1}$	29.3	62.3	119.9	145.9	

Table A-8 The conductivities and thermopowers of $(Tl_xSe_{1-x})_{0.9} - (TlCl)_{0.1}$

Tl, *at.*%	64.2	64.7	65.2	65.7	66.2	66.6
σ, $\Omega^{-1}cm^{-1}$		20.4	19.5	17.9	15.0	10.2
S, μVK^{-1}	146.0	195.0	211.0	200.0	175.0	18.0
Tl. *at.*%	67.2	67.7	68.2	68.7	69.2	
σ, $\Omega^{-1}cm^{-1}$	15.0	35.0	65.0	77.0	95.0	
S, μVK^{-1}	−16.0	−136.0	−221.0	−222.0	−215.0	

Table A-9 The temperature coefficients of the conductivity of Tl_xTe_{1-x}

Tl, *at.%*	60.7	62.2	63.2	64.2	65.2
$d\sigma/dT$, $\Omega^{-1}cm^{-1}K^{-1}$	0.575	0.583	0.554	0.604	0.557
Tl, *at.%*	66.2	66.7	67.2	67.7	69.2
$d\sigma/dT$, $\Omega^{-1}cm^{-1}K^{-1}$	0.682	0.756	0.221	0.186	0.001

Table A-10 The temperature coefficients of the conductivity of $(Tl_xTe_{1-x})_{0.9} - (TlCl)_{0.1}$

Tl, *at.%*	61.5	62.7	63.7	65.7
$d\sigma/dT$, $\Omega^{-1}cm^{-1}K^{-1}$	0.370	0.529	0.281	0.538
Tl, *at.%*	66.7	67.2	67.7	68.2
$d\sigma/dT$, $\Omega^{-1}cm^{-1}K^{-1}$	0.547	0.380	−0.7111	−0.908

Table A-11 The temperature coefficients of the conductivity of Tl_xSe_{1-x}

Tl, *at.%*	64.7	65.2	65.7	67.7
$d\sigma/dT$, $\Omega^{-1}cm^{-1}K^{-1}$	0.131	0.130	0.113	0.093
Tl, *at.%*	68.2	69.8	70.9	
$d\sigma/dT$, $\Omega^{-1}cm^{-1}K^{-1}$	0.110	0.105	0.057	

Table A-12 The temperature coefficients of the conductivity of $(Tl_xSe_{1-x})_{0.9} - (TlCl)_{0.1}$

Tl, *at.*%	64.2	64.7	65.7	66.7
$d\sigma/dT$, $\Omega^{-1}cm^{-1}K^{-1}$	0.072	0.086	0.075	0.065
Tl, *at.*%	67.7	68.7	69.7	
$d\sigma/dT$, $\Omega^{-1}cm^{-1}K^{-1}$	0.120	−0.01	−0.01	

.3 The conductivities and thermopowers of liquid Copper chalcogenides and chloride

Table A-13 The conductivities of liquid $(CuCl)_y - (Cu_2Se)_{1-y}$ at 980 °C

CuCl, *at.*%	0.0	20.0	30.0	40.0
σ, $\Omega^{-1}cm^{-1}$	195.0	53.0	28.0	14.0
CuCl, *at.*%	50.0	60.0	70.0	80.0
σ, $\Omega^{-1}cm^{-1}$	8.0	6.0	4.0	4.2

Table A-14 The conductivities of liquid $(CuCl)_y - (Cu_2S)_{1-y}$ at 980 °C

CuCl, *at.*%	0.0	5.0	20.0	40.0	60.0
σ, $\Omega^{-1}cm^{-1}$	55.0	40.0	17.0	12.0	7.0

Table A-15 The conductivities and thermopowers of liquid $(CuCl)_{0.2} - (Cu_xSe_{1-x})_{0.8}$

Cu, *at.*%	62.6	63.6	64.6	65.6	66.6
σ, $\Omega^{-1}cm^{-1}$		239.0	144.0	127.0	50.0
S, μVK^{-1}	195.0	220.0	235.0	245.0	165.0
Cu, *at.*%	67.6	68.6	69.6	70.6	
σ, $\Omega^{-1}cm^{-1}$	45.0	48.0	46.0	48.0	
S, μVK^{-1}	88.0	86.0	102.0	98.0	

Table A-16 The conductivities and thermopowers of liquid $(CuCl)_{0.05} - (Cu_xS_{1-x})_{0.95}$

Cu, *at.*%	62.6	64.6	65.6	66.6
σ, $\Omega^{-1}cm^{-1}$	131.0	117.0	80.0	40.0
S, μVK^{-1}	291.0	265.0	291.0	174.0
Cu, *at.*%	67.6	68.6	70.6	
σ, $\Omega^{-1}cm^{-1}$	45.0	44.0	46.0	
S, μVK^{-1}	57.0	58.0	94.0	

Table A-17 The temperature coefficients of the conductivity of $(Cu_xSe_{1-x})_{0.8} - (CuCl)_{0.2}$ (#)and $(Cu_2S)_{0.95} - (CuCl)_{0.05}$ (*)

Cu, *at.%*	62.6	63.6	64.6	65.6	66.7
$d\sigma/dT$, $\Omega^{-1}cm^{-1}K^{-1}$ (*)	−0.07		−0.01	0.091	0.102
$d\sigma/dT$, $\Omega^{-1}cm^{-1}K^{-1}$ (#)		0.0	0.0	0.093	0.084
Cu, *at.%*	67.6	68.6	69.6	70.6	
$d\sigma/dT$, $\Omega^{-1}cm^{-1}K^{-1}$ (*)		0.087	0.126	0.250	
$d\sigma/dT$, $\Omega^{-1}cm^{-1}K^{-1}$ (#)	0.086	0.094	0.08	0.144	